

---

# Nonlinear Data Analysis of the CMB: Cosmological Principles put to test

Heike I. Modest

---



München 2015



---

# **Nonlinear Data Analysis of the CMB: Cosmological Principles put to test**

Heike I. Modest

---

Dissertation  
an der Fakultät für Physik  
der Ludwig–Maximilians–Universität  
München

vorgelegt von  
Heike I. Modest  
aus Lohne, Deutschland

München, den 20.04.2015

Erstgutachter: Prof. Dr. Gregor Morfill  
Zweitgutachter: Prof. Dr. Jochen Weller  
Tag der mündlichen Prüfung: 22.05.2015

# Contents

|  |            |
|--|------------|
| <b>Zusammenfassung</b>   | <b>xi</b>  |
| <b>Abstract</b>  | <b>xv</b>  |
| <b>Outline</b>   | <b>xix</b> |
| <b>1 The physics of the young Universe and CMB observations</b>              | <b>1</b>   |
| 1.1 The physics of the young Universe and the CMB                            | 1          |
| 1.1.1 Standard cosmology   | 2          |
| 1.1.2 Cosmological inflation and evolution                                   | 5          |
| 1.1.3 Anisotropies of the microwave sky                                      | 9          |
| 1.1.4 Inflationary models and alternative scenarios                          | 14         |
| 1.2 Observations   | 16         |
| 1.2.1 CMB data products from WMAP and Planck                                 | 16         |
| 1.2.2 Foreground removal – Generating maps                                   | 20         |
| 1.2.3 Anomalies in the CMB sky   | 24         |
| <b>2 Testing the Gaussian hypothesis and the cosmological principle</b>      | <b>33</b>  |
| 2.1 Representation of the data   | 34         |
| 2.2 Method of the surrogates   | 35         |
| 2.2.1 Complete sky   | 36         |
| 2.2.2 Incomplete sky   | 38         |
| 2.3 Higher-order image analysis in real space                                | 40         |
| 2.3.1 Minkowski functionals  | 40         |
| 2.3.2 Weighted scaling indices   | 42         |
| 2.3.3 Alternatives   | 44         |
| 2.3.4 Statistical interpretation   | 45         |
| 2.4 Analysis in harmonic space   | 47         |
| 2.4.1 Kuiper statistics  | 48         |
| <b>3 Publication: NGs identified by using surrogates and scaling indices</b> | <b>51</b>  |
| 3.1 Introduction   | 52         |
| 3.2 Data Sets  | 53         |
| 3.3 Generating Surrogate Maps  | 55         |
| 3.4 Weighted Scaling Indices and Test Statistics                             | 56         |
| 3.5 Results  | 58         |
| 3.6 Conclusions  | 67         |

|          |  |            |
|----------|--|------------|
| <b>4</b> | <b><i>Publication: NGs identified with MFs and Scaling Indices</i></b>           | <b>69</b>  |
| 4.1      | Introduction . . . . .   | 70         |
| 4.2      | Data Sets and Simulations . . . . .  | 71         |
| 4.3      | Method of Surrogates . . . . .   | 73         |
| 4.4      | Test Statistics . . . . .  | 75         |
| 4.4.1    | Minkowski Functionals . . . . .  | 75         |
| 4.4.2    | Weighted Scaling Indices . . . . .   | 76         |
| 4.4.3    | Statistical Interpretation . . . . .   | 77         |
| 4.5      | Results and Discussion . . . . .   | 79         |
| 4.5.1    | ILC and NILC Maps . . . . .  | 79         |
| 4.5.2    | $f_{\text{NL}}$ -dependent Simulations . . . . .                                 | 86         |
| 4.6      | Conclusions . . . . .  | 88         |
| 4.7      | Acknowledgements . . . . .   | 89         |
| <b>5</b> | <b><i>Publication: Probing non-Gaussianities on an incomplete sky</i></b>        | <b>91</b>  |
| 5.1      | Introduction . . . . .   | 91         |
| 5.2      | Methods . . . . .  | 92         |
| 5.2.1    | Cut Sky Surrogates . . . . .   | 92         |
| 5.2.2    | Measures for comparison . . . . .  | 95         |
| 5.2.3    | Statistical interpretation . . . . .   | 97         |
| 5.3      | Validation . . . . .   | 98         |
| 5.3.1    | Underlying Data Sets . . . . .   | 98         |
| 5.3.2    | Results . . . . .  | 99         |
| 5.4      | Application to WMAP data . . . . .   | 99         |
| 5.4.1    | Underlying Data Sets . . . . .   | 99         |
| 5.4.2    | Results . . . . .  | 101        |
| 5.5      | Conclusions . . . . .  | 104        |
| <b>6</b> | <b><i>Publication: Fourier phases and real-space higher order statistics</i></b> | <b>107</b> |
| 6.1      | Introduction . . . . .   | 107        |
| 6.2      | Methods . . . . .  | 109        |
| 6.2.1    | Method A – phase space . . . . .   | 110        |
| 6.2.2    | Method B – real space . . . . .  | 110        |
| 6.3      | Results . . . . .  | 113        |
| 6.4      | Conclusions & Outlook . . . . .  | 116        |
| 6.5      | Acknowledgements . . . . .   | 117        |
| 6.6      | Supplemental Material . . . . .  | 118        |
| <b>7</b> | <b>Significance of the results</b>   | <b>119</b> |
| <b>8</b> | <b>Conclusions</b>   | <b>121</b> |
|          | <b>References</b>  | <b>125</b> |
|          | <b>Acknowledgements</b>  | <b>147</b> |

# List of Figures

|      |  |    |
|------|--|----|
| 1.1  | The ingredients of the Universe . . . . .  | 4  |
| 1.2  | An illustration of the history of the Universe . . . . .   | 5  |
| 1.3  | Inflaton potential . . . . .   | 7  |
| 1.4  | Contributions to the power spectrum . . . . .  | 11 |
| 1.5  | Bianchi Model type VII <sub>h</sub> . . . . .  | 17 |
| 1.6  | WMAP scanning strategy . . . . .   | 18 |
| 1.7  | Planck scanning strategy . . . . .   | 19 |
| 1.8  | HEALPix pixelization scheme . . . . .  | 20 |
| 1.9  | The CMB sky with COBE-DMR, WMAP and Planck . . . . .   | 21 |
| 1.10 | Frequency dependence of CMB anisotropy and 3 known foregrounds . . . . .   | 22 |
| 1.11 | Nine frequency maps of Planck . . . . .  | 23 |
| 1.12 | C-R, NILC, SEVEM and SMICA map from Planck data . . . . .  | 24 |
| 1.13 | CMB anomalous cold spot . . . . .  | 26 |
| 1.14 | CMB 2p-correlation function with missing power . . . . .   | 27 |
| 1.15 | Quadrupole and octopole temperature anisotropy of the WMAP 3-year sky map . . . . .  | 29 |
|      |  |    |
| 2.1  | Sketch of the surrogatization scheme . . . . .   | 36 |
| 2.2  | Comparison of phase shuffling and replacing . . . . .  | 38 |
| 2.3  | Examples of surrogates . . . . .   | 39 |
| 2.4  | Sketch of calculating Minkowski functionals . . . . .  | 41 |
| 2.5  | Illustration of decomposition of pixels . . . . .  | 42 |
| 2.6  | Sketch of the scaling index method . . . . .   | 43 |
| 2.7  | Sketch of the hemispherical analysis . . . . .   | 46 |
| 2.8  | Sketch of the reduced cap size . . . . .   | 47 |
| 2.9  | Monotonic function $Q$ for Kuiper test . . . . .   | 48 |
| 2.10 | Illustration of characteristics of Fourier phases . . . . .  | 49 |
|      |  |    |
| 3.1  | $\sigma$ -normalized deviations $S(\langle\alpha(r_k)\rangle)$ , $r_k, k = 2, 6, 10$ , different $\Delta\ell$ , ILC7 . . . . .                   | 59 |
| 3.2  | Probability density $P(\alpha)$ for scaling indices, $r_{10}$ , $\Delta\ell = (2, 20)$ , ILC7, NILC5 . . . . .                                   | 59 |
| 3.3  | Probability density $P(\alpha)$ for scaling indices, $r_2$ , $\Delta\ell = (120, 300)$ , ILC7, NILC5 . . . . .                                   | 61 |
| 3.4  | $\sigma$ -normalized deviations $ S(r) $ over $r$ , ILC7, NILC5 . . . . .  | 63 |
| 3.5  | $\sigma$ -normalized deviations $S(\langle\alpha(r_k)\rangle)$ , $r_k, k = 2, 6, 10$ , $\Delta\ell = (2, 20)$ , different test maps . . . . .    | 66 |
| 3.6  | $\sigma$ -normalized deviations $S(\langle\alpha(r_k)\rangle)$ , $r_k, k = 2, 6, 10$ , $\Delta\ell = (120, 300)$ , different test maps . . . . . | 66 |
|      |  |    |
| 4.1  | $\sigma$ -normalized deviations $S(\chi_{M_*}^2)$ and $S(\chi_{\sigma_\alpha}^2)$ , $\Delta\ell = (2, 20)$ , ILC7, NILC7 . . . . .               | 77 |
| 4.2  | Minkowski functionals, $\Delta\ell = (2, 20)$ , ILC7 and surrogate maps . . . . .  | 81 |

|      |  |     |
|------|--|-----|
| 4.3  | Minkowski functionals, $\Delta\ell = (2, 20)$ , NILC7 and surrogate maps . . . . .   | 82  |
| 4.4  | Probability density $P(\alpha)$ for scaling indices, $\Delta\ell = (2, 20)$ , NILC7 . . . . .  | 83  |
| 4.5  | $\sigma$ -normalized deviations $S(\chi_{M_*}^2)$ and $S(\chi_{\sigma_\alpha}^2)$ at threshold value, $\Delta\ell = (2, 20)$ , NILC7                       | 84  |
| 4.6  | Mollweide projection in galactic coordinates of directions of the power distribution for different multipoles and maximal NG signal, ILC7, NILC7 . . . . . | 84  |
| 4.7  | $\sigma$ -normalized deviations $S(\chi_{M_*}^2)$ , $\Delta\ell = (120, 300)$ , ILC7, NILC7 . . . . .  | 85  |
| 4.8  | $\sigma$ -normalized deviations $S(\chi_{M_*}^2)$ and $S(\chi_{\sigma_\alpha}^2)$ , $\Delta\ell = (2, 20)$ , decreased sky area, NILC7 . . . . .           | 85  |
| 4.9  | Comparison of $f_{\text{NL}}^{\text{local}}$ simulations with NILC7, studied with Minkowski functionals  | 86  |
| 4.10 | Comparison of $f_{\text{NL}}^{\text{local}}$ simulations with NILC7, studied with scaling indices . . .  | 87  |
| 5.1  | Cut-sky surrogates, examples . . . . .   | 93  |
| 5.2  | KQ75-mask provided by WMAP, 3 additional central latitude cuts . . . . .   | 94  |
| 5.3  | Sketch of the method of surrogates on a cut sky . . . . .  | 96  |
| 5.4  | Foreground residuals of WMAP maps . . . . .  | 97  |
| 5.5  | $\sigma$ -normalized deviations $S_2(\sigma_\alpha)$ , 3 latitude cuts, simulations . . . . .  | 98  |
| 5.6  | $\sigma$ -normalized deviations $S_2(\chi_{\text{area}}^2)$ , 3 latitude cuts, simulations . . . . .   | 100 |
| 5.7  | Temperature point source mask of WMAP, original and extended version . . .   | 100 |
| 5.8  | $\sigma$ -normalized deviations $S_2(\sigma_\alpha)$ , 3 latitude cuts, NILC5 . . . . .  | 102 |
| 5.9  | $\sigma$ -normalized deviations $S_2(\sigma_\alpha)$ , 3 latitude cuts, VW7pe . . . . .  | 102 |
| 5.10 | $\sigma$ -normalized deviations $S_2(\chi_{\text{area}}^2)$ , 3 latitude cuts, NILC5 . . . . .   | 103 |
| 5.11 | $\sigma$ -normalized deviations $S_2(\chi_{\text{area}}^2)$ , 3 latitude cuts, VW7pe . . . . .   | 104 |
| 5.12 | Histograms of $S_2(\sigma_\alpha)$ , ILC7, NILC5 . . . . .   | 105 |
| 5.13 | Empirical discrete entropy $H(S_2(\sigma_\alpha))$ , ILC7, NILC5 . . . . .   | 105 |
| 6.1  | $p$ values of the Kuiper statistic for WMAP-9 ILC and Planck SMICA map after Bianchi template correction . . . . .   | 111 |
| 6.2  | $ p - 1 $ -values of ILC9 and SMICA map . . . . .  | 114 |
| 6.3  | $\chi^2$ -distribution of the surrogates of first and second order generated from Planck SMICA map . . . . .   | 115 |
| 6.4  | $\sigma$ -normalized deviations $S(\chi_{M_{\text{euler}}}^2)$ , $\Delta\ell = (2, 20)$ , SMICA . . . . .  | 115 |
| 6.5  | Same as Fig. 6.4 but for the the scaling index method. . . . .   | 116 |
| 6.6  | Mean $p$ values of the Kuiper statistic, averaged of different coordinate systems  | 118 |

# List of Tables

|     |  |     |
|-----|--|-----|
| 3.1 | Deviations $S(\langle\alpha(r_k)\rangle)$ , empirical probabilities, $r_2$ , different $\Delta\ell$ , ILC7 . . . . .                       | 62  |
| 3.2 | Deviations $S(\langle\alpha(r_k)\rangle)$ , empirical probabilities, $r_{10}$ , different $\Delta\ell$ , ILC7 . . . . .                    | 64  |
| 3.3 | Deviations $S(\langle\alpha(r_k)\rangle)$ , empirical probabilities, scale-independent statistics, different $\Delta\ell$ , ILC7 . . . . . | 65  |
| 4.1 | Deviations $S(\chi_{M_*}^2)$ and $S(\chi_{\sigma_\alpha}^2)$ , empirical probabilities, $\Delta\ell = (2, 20)$ , ILC7 . . . . .            | 80  |
| 4.2 | Deviations $S(\chi_{M_*}^2)$ and $S(\chi_{\sigma_\alpha}^2)$ , empirical probabilities, $\Delta\ell = (2, 20)$ , NILC7 . . . . .           | 80  |
| 6.1 | Combinations of $(\Delta\ell, \Delta m)$ with $p$ -values $< 0.1$ . . . . .  | 113 |



# Zusammenfassung

Das kosmologische Prinzip der Homogenität und statistischen Isotropie des Raumes ist eine fundamentale Annahme der modernen Kosmologie. Auf dieser Basis wird die Existenz einer inflationären Phase im jungen Universum postuliert, welche wiederum primordiale Gaußverteilte Fluktuationen vorhersagt, welche sich im kosmischen Mikrowellenhintergrund als Temperatur- und Polarisationsanisotropien manifestieren. Obwohl dieses derzeitige Standardmodell der Kosmologie im Allgemeinen sehr akzeptiert ist, ist es keine absolute Theorie. Ungeklärt ist zum Beispiel, wie die innerhalb des Standardmodells postulierte dunkle Materie und dunkle Energie mit dem Standardmodell der Teilchenphysik zu verknüpfen, oder wie die hochenergetischen Prozesse auf den kleinen Skalen des jungen Universums zu beschreiben sind. Abgesehen davon, gibt es eine Reihe alternativer kosmologischer Modelle, welche schwache bis starke primordiale Nicht-Gaußianitäten vorhersagen. Manche von Ihnen gehen zudem auch von einer großskaligen Anisotropie im frühen Universum aus und widersprechen somit sogar dem kosmologischen Prinzip. In dieser Arbeit werden zu diesem Thema in vier Originalpublikationen durch eine nichtlineare Datenanalyse der kosmischen Mikrowellenhintergrundstrahlung folgende Fragestellungen bearbeitet:

**1.) Temperaturkarten der kosmischen Mikrowellenhintergrundstrahlung, gemessen im Wilkinson Microwave Anisotropy Probe (WMAP) Experiment und der Planck Mission, werden unter Verwendung von Surrogaten, welche mit Skalierungsindizes und Minkowski Funktionalen analysiert werden, auf primordiale Gaußianität getestet.**

Wenn die Dichtefluktuationen einer Gaußschen Zufallsverteilung unterliegen, enthält deren Leistungsspektrum alle Information. Bei einer nicht-Gaußschen Verteilung enthalten Korrelationsfunktionen höherer Ordnung zusätzliche nichtlineare Information. Die Hypothese der primordialen Gaußianität reflektiert sich ebenso in einer unkorrelierten Verteilung der Fourier-Phasen der Hintergrundstrahlung.

Zur umfassenden Analyse der Daten benutze ich die Methode der Surrogate. Surrogate können zum Beispiel die linearen Eigenschaften des Datensatzes imitieren, und ermöglichen damit modellunabhängige Tests auf Nichtlinearitäten in diesem Datensatz. Sie werden in dieser Arbeit erzeugt, indem Korrelationen von Fourier-Phasen zerstört werden. Das Randomisieren geschieht zum Beispiel durch das Vertauschen der Phasen. Statistische Differenzen zwischen den Originalkarten und den Surrogaten zeigen dann Phasenkorrelationen in den Originalkarten auf und deuten im Falle der kosmischen Mikrowellenhintergrundstrahlung auf eine Verletzung des standardmäßigen Single Field Slow-Roll Modells der Inflation hin, wenn experimentelle Systematiken, astrophysikalische Vordergrundeffekte und eine fehlerhafte Datenanalyse ausgeschlossen werden können. Zur Quantifizierung des skalenabhängigen Korrelationsgrades der Fourier-Phasen generiere ich die Surrogatkarten auch auf verschiedenen Skalen der Multipole  $\ell$ .

Hierbei werden verschiedene  $\Delta\ell$ -Bereiche festgelegt, in welchen die Phasekorrelationen gesondert zerstört werden. Die Karten können damit in den festgelegten Bereichen auf skalenabhängige Nicht-Gaußianitäten untersucht werden.

Ich quantifiziere die in den Karten enthaltene Information höherer Ordnung mit zwei unterschiedlichen Statistiken, den Minkowski Funktionalen und den Skalierungsindizes. Im Rahmen meiner Arbeit werden damit starke Nicht-Gaußianitäten auf den größten Skalen des kosmischen Mikrowellenhintergrundes in WMAP sowie Planck Daten detektiert. Die Resultate der Minkowski Funktionalen und Skalierungsindizes für Surrogate erzeugt mit  $\Delta\ell = [2, 20]$  stimmen überein, unabhängig von Experiment, den Methoden zur Vordergrundreduktion oder der Datenversion. Im Gegensatz dazu unterliegen die Resultate der kleineren Skalen mit  $\Delta\ell = [20, 60]$ ,  $[60, 120]$  und  $[120, 300]$  schwachen bis starken Variationen in Bezug auf die zwei verschiedenen Statistiken, die Methoden zur Vordergrundreduktion und die zwei verschiedenen Experimente WMAP und Planck. Anhand von WMAP Daten wird das Ergebnis für den vollen  $\ell$ -range  $[2, 1024]$  als Superposition der Signaturen interpretiert, welche in den Bändern  $\Delta\ell = [2, 20]$  und  $[120, 300]$  gefunden werden. Eine Vielzahl an Tests zur Überprüfung auf Systematiken gibt keinen Anlass dazu, die intrinsische Natur der Anomalien im Falle von kleinem  $\ell$  auszuschließen. Jedoch wird unter anderem festgestellt, dass beispielsweise das Internal Linear Combination Verfahren zur Vordergrundreduktion und auch verbleibendes Rauschen in den Karten Nicht-Gaußianitäten auf kleinen Skalen bzw. bei großem  $\ell$  erzeugen können. Da Modelle und vorangegangene Beobachtungen die Vermutung nahelegen, dass der Mikrowellenhintergrund hemisphärische Anomalien aufweist, vergleiche ich in dieser Arbeit verschiedene Hemisphären der Mikrowellenhintergrundstrahlung miteinander. Bei der Gegenüberstellung der nördlichen und südlichen Hemisphäre werden entgegengesetzte Vorzeichen im Signal für Nicht-Gaußianität gefunden. Dies deutet auf großskalige hemisphärische Asymmetrien im Universum hin.

## 2.) Ist die standardmäßige Parametrisierung von Nicht-Gaußianität im Bisppektrum durch den $f_{\text{NL}}$ Parameter ausreichend und in Übereinstimmung mit den Beobachtungen?

In der Theorie parametrisiert der  $f_{\text{NL}}$  Parameter die Stärke der Nicht-Gaußianität, die mit dem Bisppektrum der Hintergrundstrahlung detektiert werden kann. Meine Untersuchungen zeigen, dass die oben beschriebenen Abweichungen von Gaußianität in Simulationen mit dem  $f_{\text{NL}}$  Parameter nicht reproduziert werden. Zur Interpretation der Signaturen wäre es wünschenswert, insbesondere Modelle zu untersuchen, die primordiale Nicht-Gaußianität und hemisphärische Anisotropie ähnlich den detektierten Signaturen vorhersagen. Wie in dieser Arbeit gezeigt, ist die Analyse von Bianchi Modellen mit speziellen Topologien in diesem Zusammenhang hilfreich.

## 3.) Welchen Einfluss hat die galaktische Ebene auf die Beobachtungen von Nicht-Gaußianität?

Für die Interpretation der oben genannten Ergebnisse ist es unabdingbar, den Einfluss von astronomischem Vordergrund auf den Mikrowellenhintergrund zu untersuchen. Dies geschieht in meiner Arbeit anhand eines Vergleichs verschiedener Hintergrundkarten, die sich in ihren Vordergrundreduktionsmethoden stark voneinander unterscheiden. Ich kann keinen signifikanten Unterschied zwischen den sogenannten ILC, NILC, SEVEM und SMICA Karten der WMAP bzw. Planck Daten feststellen. Die Studien zum Einfluss der galaktischen Ebene werden in Cut-Sky Analysen fortgeführt, in welchen die galaktische Ebene aus den Karten

ausgeschnitten wird. Zur Erzeugung von Cut-Sky Surrogaten werden die originalen Full-Sky Kugelfunktionen anhand von Basistransformationen in Cut-Sky Kugelfunktionen umgewandelt. Innerhalb dieser Analysen werden Signaturen von Nicht-Gaußianität auf den größten Skalen auch nach dem vollständigen Ausschneiden der galaktischen Ebene detektiert. Dies bestärkt die Annahme, dass die gefundenen Nicht-Gaußianitäten nicht vom galaktischen Vordergrund verursacht werden.

#### 4.) Welcher Zusammenhang besteht zwischen der Fourier-Phasen Information und den Statistiken höherer Ordnung im Ortsraum?

Die unter anderem in meiner Arbeit beobachteten Anomalien der Mikrowellenhintergrundstrahlung können Hinweise darauf sein, dass das Universum möglicherweise eine nicht-triviale Topologie aufweist und eventuell weder isotrop noch homogen ist. Nicht-triviale Topologien des Raumes werden beispielsweise von Bianchi Modellen beschrieben. Insbesondere Bianchi type  $VII_h$  best-fit Modelle können vermutlich Erklärungen für einige der beobachteten Anomalien wie zum Beispiel die Unterdrückung des Quadrupols, oder die bestimmte Ausrichtung kleiner Multipole liefern. Anhand meiner Analyse von Bianchi Templates können heuristische Korrelationen zwischen der Information, die in den Fourier-Phasen enthalten ist, und der Statistik höherer Ordnung ermittelt werden. Ich zeige, dass bekannte Phasenkorrelationen in den Karten durch die Subtraktion von Bianchi type  $VII_h$  Templates geschwächt werden. Die geschwächten Phasenkorrelationen führen bei der Berechnung der Minkowski Funktionale und der Skalierungsindizes im Ortsraum ihrerseits zu einer verschwindenden Signatur der hemisphärischen Anisotropie.

Die Untersuchungen in meiner Arbeit zeigen, dass Phasenkorrelationen in den WMAP und Planck Temperaturkarten der kosmischen Mikrowellenhintergrundstrahlung existieren. Nach derzeitigem Wissensstand können die Signaturen bei kleinem  $\ell$  als kosmologische Nicht-Gaußianität interpretiert werden. Die Ergebnisse widersprechen den Vorhersagen von isotropen Kosmologien mit Single Field Slow-Roll Inflation. Meine Studien eröffnen im Allgemeinen neue Wege zu einem besseren Verständnis der Signaturen von Nicht-Gaußianität in komplexen räumlichen Strukturen besonders durch das Entschlüsseln der Bedeutung von Korrelationen der Fourier-Phasen und deren Einfluss auf Statistiken höherer Ordnung im Ortsraum. Die weitere detaillierte Charakterisierung der statistischen Eigenschaften des beobachteten kosmischen Mikrowellenhintergrundes und ein fortlaufender Vergleich mit der Theorie werden die Differenzierung verschiedener kosmologischer Szenarien noch verbessern. Aufschlussreich wäre hierbei natürlich die Analyse der angekündigten Polarisationsdaten der Planck Mission mit Hilfe der innerhalb dieser Arbeit entwickelten Methoden.



# Abstract

The cosmological principle of homogeneity and statistical isotropy of space lays the foundation for modern cosmology. Based on this, cosmology assumes an inflationary scenario for the early Universe which predicts primordial Gaussian random-distributed fluctuations, imprinted on the cosmic microwave background (CMB) as temperature and polarization anisotropies. Despite its general success this current standard model is not an absolute theory. Unanswered, for example, remains the question, how to link postulated dark matter particles and dark energy with the current standard model of particle physics, or how to describe the high-energy processes on the small scales of the early Universe. Apart from that, there are a number of alternative cosmological models which predict weak up to strong primordial non-Gaussianity. Furthermore, some of them even assume large-scale anisotropies in the early Universe and therefore even contradict the cosmological principle. This work deals with the following problems in four original publications by means of a nonlinear data analysis of the CMB:

**1.) Temperature maps of the CMB, measured by the Wilkinson Microwave Anisotropy Probe (WMAP) experiment and the Planck mission, are tested for primordial Gaussianity, by means of surrogate maps, which are analyzed by the scaling indices and the Minkowski functionals.**

If the density fluctuations follow a Gaussian random distribution, then their power spectrum contains all the information. In the case of a non-Gaussian distribution, the higher-order correlation functions will provide additional nonlinear information. The hypothesis of primordial Gaussianity is also reflected in an uncorrelated distribution of the Fourier phases of the microwave background.

I use the surrogate method, which is well suited for a comprehensive analysis of the data. Surrogates can, for example, imitate the linear properties of a data set, and therefore enable model independent tests for nonlinearities in this data set. In this work, they are generated by destroying the correlations of Fourier phases. The randomization is, for example, realized by the permutation of the phases. Statistical deviations between the original maps and the surrogates disclose phase correlations in the original maps. In the case of the CMB, they indicate the violation of the standard single field slow-roll model for inflation, if experimental systematics astrophysical foregrounds and a faulty data analysis can be ruled out. To quantify a scale-dependent correlation of the Fourier phases I generate the surrogate maps on different multipole scales  $\ell$ . For this purpose, different  $\Delta\ell$  ranges are determined, in which the phase correlations are then destroyed. This method allows the maps to be checked for scale-dependent non-Gaussianities on the predefined scales.

I quantify the higher-order content of the maps with two different statistical measures, the Minkowski functionals and the scaling indices. Within the scope of my work, strong

non-Gaussianities on the largest scales of the CMB in WMAP as well as Planck data are revealed with these measures. The results of the Minkowski functionals and the scaling indices for the surrogates generated with  $\Delta\ell = [2, 20]$  agree very well, no matter which experiment, which method of foreground subtraction and which data release. A comparison of the small scale results with  $\Delta\ell = [20, 60]$ ,  $[60, 120]$  and  $[120, 300]$  shows weak up to strong variations regarding the two different measures, the methods of foreground reduction and the two different experiments WMAP and Planck. On the basis of WMAP data, the result for the full  $\ell$ -range  $[2, 1024]$  is interpreted as a superposition of the signatures detected on the ranges of  $\Delta\ell = [2, 20]$  und  $[120, 300]$ . A wide range of tests to check for systematics gives no reason to exclude the intrinsic nature of the anomalies for small  $\ell$ . However, it is, for example, found that the internal linear combination method for foreground reduction and also remaining noise in the maps can induce non-Gaussianities on smaller scales, larger  $\ell$ , respectively. Since cosmological models and previous observations suggest that the CMB features hemispherical anomalies, I compare different hemispheres of the microwave sky with each other. A comparison of the northern and southern hemisphere reveals opposite signs in the signal for non-Gaussianity. This points to large-scale hemispherical asymmetries in the Universe, imprinted on the CMB.

**2.) Is the standard parametrization of non-Gaussianity by the  $f_{\text{NL}}$  parameter in the bispectrum sufficient? Does  $f_{\text{NL}}$  comply with the observations?**

In theory, the  $f_{\text{NL}}$  parameter parametrizes the strength of non-Gaussianity that can be detected by the bispectrum of the background radiation. My studies show that the deviations from Gaussianity, as described above, cannot be reproduced by simulations with the  $f_{\text{NL}}$  parameter. For the interpretation of the observed signatures it is desirable to analyze further models that comprise primordial non-Gaussianity and hemispherical anisotropies similar to the detected signatures. As shown in this work, the analysis of Bianchi models with special topologies is helpful in this context.

**3.) How does the Galactic plane influence the observations of non-Gaussianity?**

For the interpretation of the results described above, it is indispensable to study the influence of astronomical foreground on the microwave background. In my work, this is done by a comparison of different CMB maps, that strongly differ in their foreground reduction methods. I cannot detect a significant difference in the large scale results between the so-called ILC, NILC, SEVEM and SMICA maps of WMAP and Planck data, respectively. The studies on the influence of the Galactic plane are continued in cut-sky analyses where the Galactic plane is cut out in different sizes. For the production of cut-sky surrogates, the original full-sky spherical harmonics are converted into cut-sky harmonics by means of basis transformations. Within these studies, signatures of non-Gaussianity on the largest scales are still detected when the Galactic plane is completely removed. This strengthens the assumption that the detected non-Gaussianities are not induced by the Galactic foreground.

**4.) What is the link between Fourier phase information and the real space statistics of the higher-order content?**

The detected anomalies, studied in my work and elsewhere, could point to a non-trivial topology of the Universe which is perhaps neither isotropic nor homogeneous. Non-trivial topologies of space are, for example, described by Bianchi models. Especially Bianchi type VII<sub>h</sub> best-fit models can supposedly account for some of the observed anomalies as, for example, the suppression of the quadrupole, or the alignment of small multipoles. By means of studies with Bianchi templates in my work, heuristic correlations between the information contained in the Fourier

---

phases and the higher-order statistics are determined. I show that known phase correlations in the maps are diluted by the subtraction of Bianchi type VII<sub>h</sub> templates. The weakened phase correlations result in a vanishing signal of hemispherical anisotropy when calculating the Minkowski functionals and scaling indices in real space.

The studies in this work show that Fourier phase correlations in WMAP and Planck temperature maps of the CMB do exist. Based on what is known today, the signatures at low  $\ell$  can be interpreted as cosmological non-Gaussianity. The results contradict the predictions of isotropic cosmologies with single field slow-roll inflation. In general, my studies open new roads to a better understanding of signatures of non-Gaussianity in complex spatial structures, especially through the decoding of the meaning of Fourier phase correlations and their influence on higher-order statistics in real space. Furthermore, a more detailed characterization of the statistical properties of the CMB and a continued comparison with theory will help to distinguish between different cosmological scenarios in the future. In this context, the analysis of the polarization data of the Planck mission with the methods developed within this work would certainly be revealing.



# Outline

Over the last decades, improved observing techniques and new data sets have enabled a more comprehensive analysis of our Universe and allow nowadays for profound tests on proposed axioms and theorems. In this thesis, I address new approaches of data analysis in cosmology.

In the detailed and successful cosmological concordance model we assume that the Universe starts with a Big Bang, is followed by an inflationary phase that expands the emerged scale-invariant, isotropic, Gaussian quantum fluctuations, leading to primordial nucleosynthesis and structure formation. This model is in general supported by observations. However, standard single field slow-roll inflation is not fully proven yet and remains a paradigm after all. Inflation suffers from conceptual problems such as the difficulty to embed it into the standard model of particle physics or the problem that general relativity and the theory of scalar fields, both needed for inflation, will break down on the very small scales of the young Universe. In addition to the theorem of Gaussianity for the primordial perturbations deduced from standard inflation, we generally assume that the Universe follows the axiom of the cosmological principle of homogeneity and statistical isotropy, although under the vast amount of alternative scenarios several can be found which describe anisotropic, non-Gaussian cosmologies and several might agree with observations as well as inflation does.

The statistical properties of the primordial density perturbations are imprinted on the cosmic microwave background (CMB) as tiny temperature fluctuations. Distinct anomalies violating the assumptions of statistical isotropy or Gaussianity, or both, have been detected in the linear and nonlinear regime of CMB data. Their true nature remains unclear. Understanding the CMB anomalies is important for cosmology and may modify our picture of the Universe. The anomalies might even point to new physics. However, interpreting them, we also have to be aware of yet unknown or underestimated physical effects which could be in agreement with the standard model but might still produce anomalies.

The nonlinear higher order properties of the data are reflected in the distribution of the phases in harmonic space. The null-hypothesis of a Gaussian CMB induces independent harmonic space phases, not correlated with each other. This work checks for the validity of this null-hypothesis and for the validity of statistical isotropy analyzing the nonlinear statistical properties of the data especially in phase space with a model-independent approach. First steps are taken to explain the specific CMB anomalies detected as phase correlations by studying anisotropic cosmological Bianchi models and analyzing non-Gaussian simulations. Herewith, this thesis contributes to open questions in cosmology and opens new roads in nonlinear data and image analysis along the way.

The outline of this work is as follows: In Chapter 1, I provide a short summary of the physics of the early Universe that led to the anisotropies in the cosmic microwave sky which I will study later. I give a short introduction to alternative cosmological scenarios. The recent CMB satellite missions and their data products are introduced and different methods

of foreground subtraction are compared. I will end with a list of CMB anomalies detected so far. Chapter 2 describes the nonlinear data analysis methods I use in this work. This includes the method of the surrogates and the image analysis techniques, scaling indices and Minkowski functionals, both sensitive to higher order correlations. The described Kuiper statistic, which will be applied to the phase distribution of CMB maps, provides a complementary way for the determination of the nature of the phase correlations. Chapter 3 shows the results from the analysis of *Wilkinson Microwave Anisotropy Probe* (WMAP) 3-, 5- and 7-year data with the method of the surrogates and the scaling indices. This Chapter was published as [R ath et al. \(2011\)](#) in MNRAS. The results of Chapter 3 are strengthened and extended by an analysis with the complementary technique of the Minkowski functionals in Chapter 4. In addition, a study of non-Gaussian simulations, parametrized by the local non-Gaussianity parameter  $f_{\text{NL}}$ , refines the conclusions. This Chapter was published as [Modest et al. \(2013\)](#) in MNRAS. Chapter 5 presents a cut-sky analysis of the data enabling the exclusion of Galactic plane foreground effects as cause for detected non-Gaussianities. This Chapter was published as [Rossmannith et al. \(2012\)](#) in Phys. Rev. D. Searching for the origin of the detected non-Gaussianities, Chapter 6 continues with a direct study of the phase distribution of maps that have been corrected by a cosmological Bianchi template. Bianchi models describe anisotropic cosmologies, and certain Bianchi templates are known for their ability to account for some CMB anomalies. This Chapter also addresses the connection between real-space higher order statistics and harmonic-space phase information, which is a crucial topic in nonlinear data analysis. It compares the final WMAP 9-year data with the first results of the new *Planck* mission. The Chapter is published as [Modest et al. \(2014\)](#) in Phys. Rev. D. The significance of detected CMB anomalies needs careful consideration which is discussed in Chapter 7 for our results. The thesis closes with Chapter 8 where I summarize the results and draw conclusions.

# Chapter 1

## The physics of the young Universe and CMB observations

Our Universe discloses many of its secrets through the cosmic microwave background (CMB). This relic radiation showed itself observationally to astronomers in the late 1930s and early 1940s, when [McKellar \(1940\)](#) and [Adams \(1941\)](#) tried to interpret interstellar absorption lines in the blue. They took the signal as an exciting radiation of unknown origin with a temperature less than 3 K filling the local interstellar medium. Only later [Gamow \(1946\)](#), [Alpher et al. \(1948\)](#) and [Alpher & Herman \(1950\)](#) extended the Big Bang theory of the Universe, first formulated by Georges Lemaître, and predicted that the first explosion of the Universe would have produced a uniform background radiation which Gamow expected to have a temperature of 50 K at the present time ([Gamow 1961](#)). [Alpher & Herman \(1948\)](#) had initially estimated the temperature to be 5 K. [Penzias & Wilson \(1965\)](#) accidentally detected the relic radiation as they experimented with the Bell Lab Holmdel Horn Antenna, just beating [Dicke et al. \(1965\)](#) who were in the process of building an instrument explicitly designed for finding the background radiation of the Universe and who then helped to interpret the Holmdel detection as the signature of the Big Bang. For their discovery of the CMB Arno A. Penzias and Robert W. Wilson were awarded the first of two Nobel Prizes in physics for CMB research. In the last decades many new experiments carried out with telescopes on the ground (e.g. Atacama Cosmology Telescope, POLARBEAR, South Pole Telescope), balloon missions in the sky (e.g. Archeops, BOOMERanG) and with satellites in space (COBE, WMAP, Planck) lead to highly accurate measurements of the cosmic microwave background. The discovery of the CMB black body spectrum and its anisotropies with the COBE satellite under [Smoot et al. \(1992\)](#) resulted in the second CMB Nobel Prize for John C. Mather and George F. Smoot in 2006. The radiation has a thermal black body spectrum at a temperature of  $2.72548 (\pm 0.00057)$  K today ([Fixsen 2009](#)). Its very small temperature fluctuations on the order of 1 part in 100,000 across the sky provide a detailed insight into the density field of the primordial Universe.

### 1.1 The physics of the young Universe and the CMB

*In this chapter, I will give a brief summary of our current knowledge of cosmology. For mathematical details please refer to books on modern cosmology as for example [Peacock \(1999\)](#), [Liddle & Lyth \(2000\)](#) and [Weinberg \(2008\)](#). Two reviews discussing ongoing questions in cosmology are [Bennett \(2006\)](#) and [Brandenberger \(2012\)](#). Information on the Nobel Prize*

winners and their work is provided on the Nobel Prize website<sup>1</sup>.

### 1.1.1 Standard cosmology

The basic axiom of the Universe is the **cosmological principle**, which states that the matter-energy density is homogeneous and statistically isotropic when viewed on large enough scales: The same physical laws apply throughout the Universe, and should therefore produce no imbalances in the matter-energy distribution and the large-scale structure of the Universe (e.g. [Liddle & Lyth 2000](#)). It is an extension of the Copernican principle by Nicolaus Copernicus, saying that the Earth is not in a specially favored position in the Universe and it was also Sir Isaac Newton with his formulation of the laws of motion and the principle of universal gravitation ([Newton 1687](#)) who smoothed the way for our current understanding. [Yadav et al. \(2010\)](#) calculated the appropriate length scale when looking for homogeneity to be close to  $260 h^{-1}\text{Mpc}$  in the concordance model of cosmology. In general, this is confirmed by the large-scale galaxy distribution observed with the Sloan Digital Sky Survey (SDSS) (e.g. [Ahn et al. 2012](#), SDSS 9th data release). However, in recent years different structures, for example the Sloan Great Wall ([Gott et al. 2005](#)) and a large quasar group ([Clowes et al. 2013](#)), have been detected that are not strictly compatible with the [Yadav et al.](#)-scale and challenge the cosmological principle.

Our Universe is nowadays described as sustaining a history, starting with the **Big Bang**, proceeding with different epochs of particle and structure formation over billions of years. What we need, to figure out how the Universe expands as a function of time, is an equation that relates the density and pressure of its constituents to the expansion of the Universe, and an equation that describes the energy conservation of the constituents (lecture notes [Komatsu 2011](#)). The necessary framework for this is **Albert Einstein's general theory of relativity** which generalizes special relativity and Newton's principle of universal gravitation, and describes gravitation as an apparent effect of the distortion of space and time, or spacetime, being curved by matter and energy ([Einstein 1915, 1916](#)). As said by Arthur Wheeler: "It describes how space moves matter and matter curves space" ([Wheeler & Ford 2000](#)). When Einstein applied his theory of general relativity to the Universe as a whole, he added a **cosmological constant**  $\Lambda$  to his field equations ([Einstein 1917](#)) to account for a steady and unchanging (steady state) Universe he and many other scientists believed in at that time. The resulting nonlinear Einstein field equations (EFE) can be written in the form

$$R_{\mu\nu} - \frac{1}{2}Rg_{\mu\nu} + \Lambda g_{\mu\nu} = -8\pi G T_{\mu\nu} , \quad (1.1)$$

if the speed of light is set to  $c = 1$ , where  $R_{\mu\nu}$  and  $R$  are the Ricci tensor and Ricci scalar, respectively, describing the curvature of spacetime,  $g_{\mu\nu}$  is the covariant metric tensor describing the geometry of spacetime,  $\Lambda$  the cosmological constant,  $T_{\mu\nu}$  the energy-momentum tensor and  $G$  is Newton's gravitational constant (e.g. [Weinberg 2008](#)). Only few years later, in the 1920s, observations of distant galaxies, mainly led by Edwin Hubble, showed that the Universe was expanding ([Hubble 1929](#)). Einstein began to regret the cosmological constant added by himself, and its meaning faded in the following decades. However, today the  $\Lambda$ -term is again much appreciated and  $\Lambda$  represents the energy density of the vacuum, constant in both space and time.  $\Lambda$  could stand for a form of dark energy and can account for the accelerating expansion of the Universe, a discovery made by two independent supernova Type Ia search teams in the 1990s, the High-z Supernova Search Team (HZT, [Riess et al. 1998](#)) and the Supernova

<sup>1</sup><http://www.nobelprize.org/>

Cosmology Project (SCP, [Perlmutter et al. 1999](#)). For this discovery, Saul Perlmutter, Brian P. Schmidt and Adam G. Riess have won the Nobel Prize in physics 2011.

The assumptions of homogeneity and isotropy of space motivated a certain choice of the spacetime metric in the 1920s and 1930s by the scientists Alexander A. Friedmann, Monseigneur Georges Lemaître, Howard P. Robertson and Arthur G. Walker. Their results are comprised in the so-called **Friedmann-Lemaître-Robertson-Walker (FLRW) metric**  $g_{ij}(\mathbf{x})$ , which describes a homogeneous, isotropic and expanding or contracting Universe and gives the line element  $ds^2$  of the chosen spacetime (e.g. [Weinberg 2008](#)):

$$ds^2 \equiv -g_{ij}(x)dx^i dx^j = dt^2 - a^2(t) \left[ d\mathbf{x}^2 + K \frac{(\mathbf{x} \cdot d\mathbf{x})^2}{1 - K\mathbf{x}^2} \right] \quad (1.2)$$

The speed of light is set to  $c = 1$ .  $ds$  is the proper distance between a point  $\mathbf{x}$  and  $\mathbf{x} + d\mathbf{x}$ . The scale factor  $a(t)$  in this metric describes how the size of the Universe changes with time  $t$ . It relates the distance of two objects in space at some time  $t$  to their distance at some reference time  $t_0$ . As mentioned above, observations of supernovae Type Ia have told us that the scale factor  $a(t)$  of the Universe is increasing with time. By definition, it is  $a(t) = 1$  at the present time ( $t = t_0$ ).  $K$  is describing the curvature of spacetime with

$$K = \begin{cases} +1 & \text{spherical} \\ -1 & \text{hyperspherical} \\ 0 & \text{Euclidean} \end{cases} . \quad (1.3)$$

**Hubble's law** states that the recession velocity of a distant galaxy is proportional to its distance. The time-depending factor of proportionality is called Hubble parameter  $H(t)$  and can be expressed as

$$H(t) = \frac{\dot{a}(t)}{a(t)} \quad (1.4)$$

The Hubble constant  $H_0$  stands for  $H$  measured today. It is convenient to write  $H(t)$  in the following units:  $H(t) = 100 h(t) \text{ km} * \text{s}^{-1} * \text{Mpc}^{-1}$  where  $h$  is a dimensionless quantity. The current observations suggest that the present-day value of  $h$  is  $h(0) \approx 0.7$  (see below for details). A convenient choice regarding coordinate systems in cosmology are comoving coordinates. Objects that are only moving due to the expansion of the Universe remain at fixed points on the coordinate grid, which expands with the Universe.

The FLRW metric evolves in accordance to the EFE. Together with the assumptions of the FLRW metric, the EFE give the Friedmann equation which describes the expansion of the Universe taken as a perfect fluid with a given pressure  $p(t)$  and an energy density  $\rho(t)$  (e.g. [Weinberg 2008](#)) by

$$\left( \frac{\dot{a}}{a} \right)^2 = \frac{8\pi G}{3} \rho - \frac{K}{a^2} + \frac{\Lambda}{3}. \quad (1.5)$$

Pressure and energy density depend on each other as described by the equation of state. To solve the Friedmann equation for  $a(t)$  it is only necessary to understand how  $\rho$  depends on time. The evolution of  $p(t)$  can be neglected.

Assuming  $\Lambda$  to be zero and setting the spatial curvature  $K$  equal to zero, the Friedmann equation leads to the critical density by

$$\rho_c = \frac{3H^2}{8\pi G}. \quad (1.6)$$

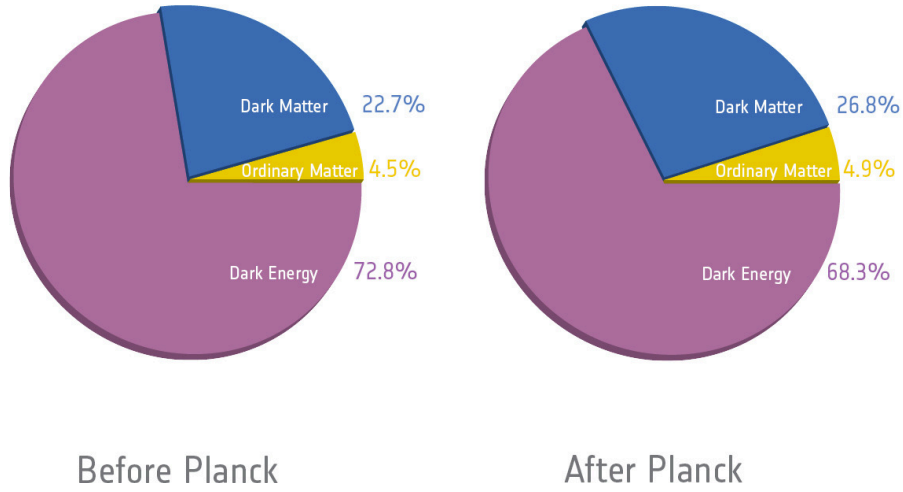


Figure 1.1: A pie chart of the ingredients of the Universe according to WMAP 9-year (left) and Planck (right) data, respectively. Source: ESA and the Planck Collaboration, ESA Planck website (<http://sci.esa.int/planck/51557-planck-new-cosmic-recipe/>)

A Universe with this mass density is flat and stops its expansion of space after an infinite time has elapsed if there is no cosmological constant.  $\Lambda$  can still lead to an accelerated expansion. The ratio between the actual density of the Universe and the **critical density** is the cosmological parameter  $\Omega = \rho/\rho_c$ . It describes the overall geometry of space. If  $\Omega = 1$  then the geometry of the Universe is flat and infinite. If the density is higher, the Universe is positively curved and closed. If the density is lower than the critical density, the Universe is negatively curved and open.

The findings of the last decades in theory and observations led to today's standard cosmological model which is called  **$\Lambda$  cold dark matter ( $\Lambda$ CDM) model**. It describes a Universe containing cold dark matter governed by the cosmological constant  $\Lambda$ .  $\Omega$  is supposed to consist of different components from baryons, cold dark matter and dark energy in the Universe whereas the geometry of space is measured to be nearly flat. The  $\Lambda$ CDM model parametrizes the Universe with six cosmological parameters, namely the physical densities of baryons  $\Omega_b h^2$  and cold dark matter  $\Omega_c h^2$  and the scalar spectral index  $n_s$ , which describes how the density perturbations vary with scale. Another parameter is the Thomson scattering optical depth  $\tau$  from reionization, which damps the temperature fluctuations of the CMB radiation and polarizes the CMB depending on its value. The acoustic scale  $\theta$  characterizes the angular size of the fluctuations in the CMB and is determined by the comoving sound horizon at the time of last-scattering and the angular diameter distance  $D_A$  at which we are observing the fluctuations. It helps determining the dark energy density. The last parameter is the log power of the primordial curvature perturbations  $\ln(10^{10} A_s)$  with the amplitude parameter  $A_s$ . The six parameters are estimated to be  $\Omega_b h^2 = 0.02207 \pm 0.00027$ ,  $\Omega_c h^2 = 0.1198 \pm 0.0026$ ,  $n_s = 0.9585 \pm 0.0070$ ,  $\tau = 0.091^{+0.013}_{-0.014}$ ,  $100\theta_{MC} = 1.04132 \pm 0.00063$  and  $\ln(10^{10} A_s) = 3.090 \pm 0.025$ , respectively (68% errors) (Planck+WP+highL, [Planck Collaboration et al. 2014e](#)). According to this model and the latest observations, we expect the Universe to be composed of 68.6% dark energy, 26.8% dark matter and 4.9% baryonic matter. These values have slightly changed compared with the WMAP data as can be seen in Figure 1.1. The value of the Hubble constant is  $H_0 = 67.3 \pm 1.2 \text{ km} \cdot \text{s}^{-1} \cdot \text{Mpc}^{-1}$ , the quadratic mean fluctuation in total matter in  $8 h^{-1} \text{ Mpc}$

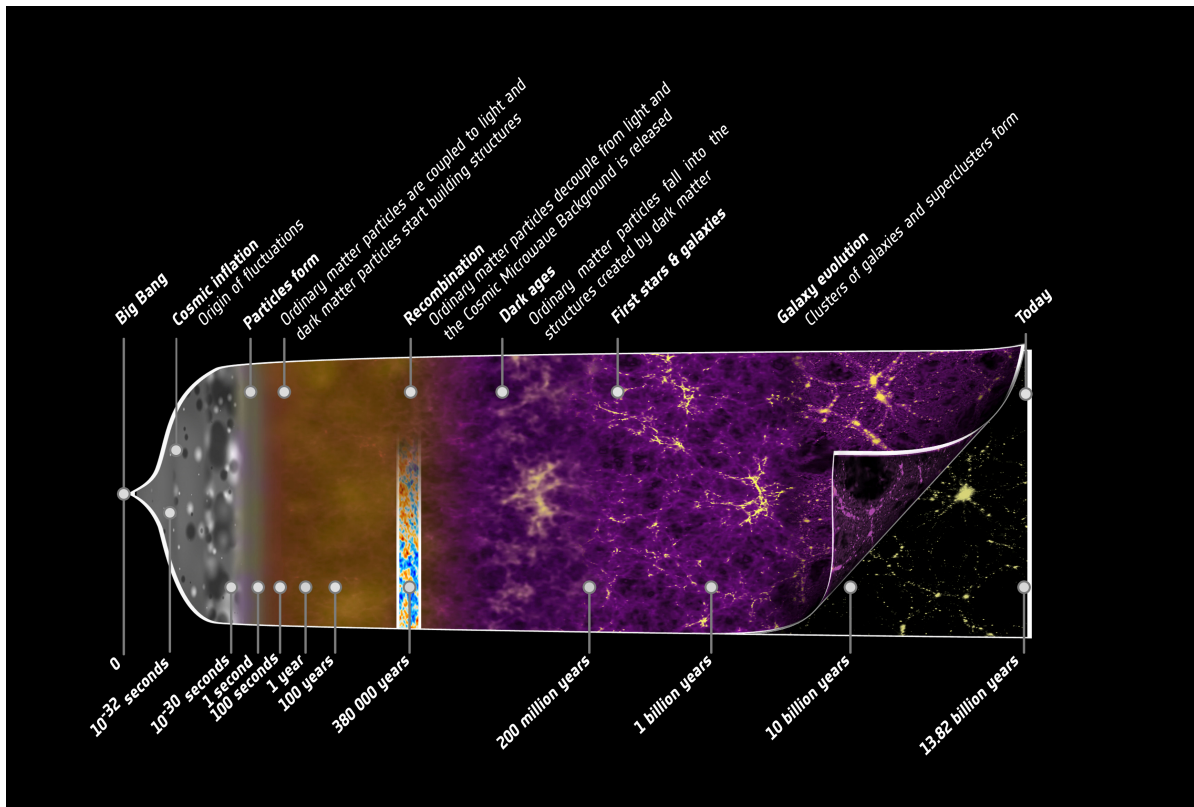


Figure 1.2: An illustration of the history of the Universe. Source: C. Carreau and ESA, ESA Planck website (<http://sci.esa.int/planck/51560-the-history-of-structure-formation-in-the-Universe/>)

spheres at  $z = 0$  is  $\sigma_8 = 0.828 \pm 0.012$ , and the reionization redshift is  $z_{\text{re}} = 11.1 \pm 1.1$ . The age of the Universe is  $13.813 \pm 0.047$  Gyr (Planck Collaboration et al. 2014e).

The  $\Lambda$ CDM model is completed by the model for cosmic inflation and comprises the idea of an initial singularity called the Big Bang. The observation of the CMB temperature anisotropies and its black body spectrum together with the determination of the abundance of hydrogen, deuterium, helium and lithium, large-scale structure measurements of the Universe and supernova Type Ia light curves for galaxy distance measurements smoothed the way to precision cosmology and confirmed the standard cosmological model in many aspects as predicted quantum fluctuations, primordial nucleosynthesis, structure formation and redshift space expansion. However, alternative models do exist and many open questions remain (for a review see e.g. Bennett 2006): What is the nature of non-baryonic dark matter? Did inflation happen and then how? What is causing the current apparent acceleration of the Universe? Although the precise measurements of the CMB provide so strong evidence for the proposed theory of inflation, the inflationary model remains a paradigm. Many details detected in the CMB maps even contradict standard inflation which will be discussed in Chapter 1.2.3.

### 1.1.2 Cosmological inflation and evolution

*The numbers of this section are taken from Liddle (2003).*

The Big Bang theory states that at its beginning the Universe was hot and dense, and has expanded from an initial singularity and adiabatically cooled ever since. As illustrated

in Figure 1.2, its content and properties evolved over time from tiny fluctuations to a rich variety of cosmic structure. However, a short epoch of accelerated expansion called **inflation** may have played an important role in the evolution of the very early Universe. Inflation can well explain how the physics of the early Universe led to the observed Universe today. During this period, the scale factor of the Universe was accelerating ( $\ddot{a}(t) > 0$ ) and the overall energy density of the Universe was first dominated by an energy of yet unknown nature with negative pressure  $p$ . Specifically predicted by Guth (1981), the spacetime of the very early Universe underwent a rapid, almost exponential expansion by a factor of  $10^{30}$  to  $10^{50}$ , finished at  $10^{-32}$  seconds after the Big Bang. The inflationary Universe is well described by a (quasi) de Sitter Universe, named after Willem de Sitter, which is a cosmological solution to Einstein's field equations. It models the Universe as spatially flat and neglects ordinary matter. The dynamics of the Universe are dominated by a positive cosmological constant. Current observations of the accelerating Universe suggest that the Universe is best described as an almost de Sitter Universe also far into the future.

Guth's **old inflation** was soon replaced by a new inflation of Albrecht & Steinhardt (1982) and Linde (1982) solving the bubble collision problem. In this so called slow-roll model, inflation occurred when one or more scalar fields slowly rolled down their potential hill. The total vacuum energy of the Universe strongly depends on the potential and kinetic energies of the scalar fields. The standard **single field slow-roll model** assumes a scalar field  $\phi$  known as the inflaton, which in the beginning took a value at which the potential  $V(\phi)$  was large but quite flat, as illustrated in Figure 1.3. The Universe must have been in a state of false vacuum meaning that it was at very high energies and was not able to rapidly lower this state. The inflaton field then slowly rolled down the potential hill and the Universe reached a state of true vacuum which corresponds to the ordinary vacuum of empty space. A false vacuum has the peculiar property of generating a negative pressure that led to the rapid expansion of space in the very early Universe due to the generation of a repulsive gravitational field. While the Universe was exponentially expanding the inflaton field reached a global minimum and its kinetic energy began to dominate the potential energy. The inflationary phase of the Universe ended and the scalar field was oscillating around that minimum. According to quantum field theory the field must then have decayed into radiation and matter particles which were able to reheat the cooled down Universe. Kofman et al. (1994) and others found that the oscillations would have driven resonances of  $\phi$  interacting with other quantum fields. A large number of particles would have been created very quickly within specific energy bands corresponding to the frequency of the oscillations and its higher harmonics (Guth & Kaiser 2005). These yet undetected fundamental particles form a testable prediction of inflation and would have to be included into the models for particle physics. Quantum field theories of spontaneous symmetry breaking in particle physics are just as well theories that describe negative pressures.

Single field slow-roll inflation produces an almost perfect Gaussian distribution of **adiabatic density perturbations**. Adiabatic fluctuations are present from the beginning and perturb both, the matter and the radiation components with the same fraction of over- and underdensities. Theory says that each perturbation originated as a quantum fluctuation of identical amplitude. The size of the perturbation depends on the time of its occurrence during the inflationary period. The size increases with time, though the power remains identical for each fluctuation. The perturbations are therefore characterized as scale-invariant regarding their power. Inflationary cosmology provides an explanation for initial quantum fluctuations to grow into macroscopic scalar density perturbations and tensor gravitational wave perturbations (Starobinsky 1980; Mukhanov & Chibisov 1981). According to standard inflation, adiabatic

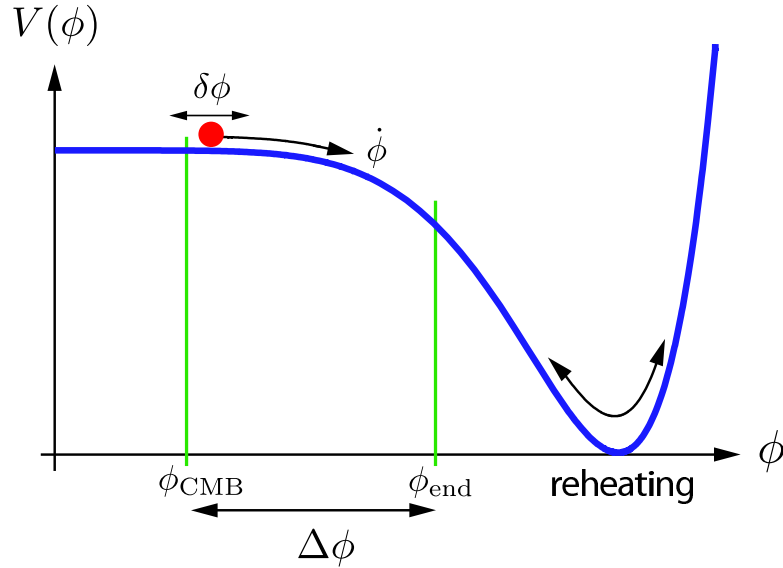


Figure 1.3: The potential of the inflaton in single field slow-roll inflation. It shows the dynamics of the scalar field during inflation. During the flat part of the potential, the Universe expands exponentially. When the field reaches the minimum, the field oscillates and decays. Source: [Yadav & Wandelt \(2010\)](#)

Gaussian fluctuations with an almost scale-invariant power spectrum are the primordial seeds for subsequent structure formation. Over time, the initial seeds accumulated more and more mass building even stronger overdensities from which first stars and finally galaxy clusters and large-scale structures have formed. The primordial perturbations are still reflected today in the all-sky CMB radiation as temperature anisotropies with tiny amplitudes. For details see e.g. [Liddle & Lyth \(2000\)](#).

It was Guth who already understood that the theory of inflation would also solve the **flatness problem**, one of the big problems in cosmology. If inflation did not happen at all, the matter-energy density of the Universe must have been extremely well fine-tuned at its beginning to evolve into the exact critical value for an almost flat Universe which we observe today, which is described by  $\Omega_{\text{tot}} = 1$ . Observations of Type Ia supernova redshift-to-distance relations (samples by [Conley et al. 2011](#); [Suzuki et al. 2012](#)) and gravitational lensing (from Planck data, [Planck Collaboration et al. 2014f](#)) plus polarization information (from WMAP data, [Bennett et al. 2013](#)) in CMB data completed by BAO measurements (6dF Galaxy Survey: [Beutler et al. 2011](#), BOSS DR9: [Anderson et al. 2012](#), SDSS DR7: [Percival et al. 2010](#); [Padmanabhan et al. 2012](#)) are consistent with a vanishing curvature parameter  $\Omega_K$  ([Planck Collaboration et al. 2014e](#)). A flat geometry in the Universe is in general unstable. A marginal deviation from flatness in the early Universe would have led to a strong curvature in the present Universe. However, it can be shown in the Friedmann equation that inflation with  $\ddot{a}(t) > 0$  brings  $\Omega_{\text{tot}}$  very close to 1.

Furthermore, the inflationary scenario was able to solve another big observational problem known as the **horizon problem**. Natural constraints of the Universe make it very difficult to explain the high degree of homogeneity and isotropy or at least of causal connection of different directions in the CMB radiation without inflation. Since the Universe has a finite age and the speed of light is very likely finite and constant, particles with a certain distance to

each other can only be in causal contact if the time is long enough for the information to be exchanged. The problem is that the Universe is in a way too big for its age, meaning that a spot in the sky is so far away from a spot in the opposite direction that light could not have traveled between these two spots during the lifetime of the Universe. The maximum distance that light has traveled since some point in the past until the finite time  $t$  is described by the comoving horizon. The horizon of the surface of last scattering at  $z_L \simeq 1100$ , where the CMB was emitted, covers a distance of only  $\approx 1.6^\circ$  on the sky today for example, which is quite small (Weinberg 2008). We can on principle not find any other physical influence after the time of last scattering, and even well before that time, that could have brought different regions of the CMB sky into causal contact. The CMB photons must have been in **thermal equilibrium** before the CMB was emitted to reach homogeneity and isotropy. A reasonable explanation for the causal connection of different CMB regions in the sky stems from inflationary theory. The idea is that a tiny patch of the early Universe had enough time to homogenize and was then inflated to an even bigger Cosmos than our observable Universe today. Inflation can thus explain why the more than 13 billion light years distant CMB patch in one direction is in causal contact with another CMB patch in the opposite direction. Alternatively, Albrecht & Magueijo (1999) suggest a time varying speed of light as a solution to this cosmological puzzle.

Models in particle physics or quantum field theory, respectively, that unify the electromagnetic, weak, and strong interactions at very high energies are called **grand unified theories (GUTs)**. They predict the existence of a larger number of elementary particles called magnetic monopoles that must have occurred after gauge symmetry breaking of the GUT's symmetry group. Despite an extensive search with huge experiments no magnetic monopole has been observed until today. In the case there simply was no gauge group to be spontaneously broken, the **monopole paradox** would be solved without the need for inflation. However, if the GUTs are true, inflation could solve this issue of the missing monopoles. Theories of cosmic inflation reduce the predicted number of magnetic monopoles by either extending the horizon or reducing the monopole to photon ratio to a density which is so small that unsurprisingly we just have not found one yet.

The inflationary scenario suffers from conceptual problems (see e.g. Brandenberger 2012). The predicted inflaton field particles have not been found yet. Theoretical expectations from particle physics for the cosmological constant  $\Lambda$  exceed observational limits by some 120 orders of magnitude. This is a problem known as the **cosmological constant problem**. Some supersymmetric theories even require a cosmological constant  $\Lambda$  that is exactly zero which makes it even more difficult. For a review see e.g. Martin (2012). How can inflation be combined with the standard model for particles physics anyway? Furthermore, inflation still suffers from a **fine-tuning problem** obtaining the correct amplitude of the perturbations. The origin of the fluctuations has to be explained on very small length scales at very high energies. Einstein gravity and quantum field theory are not sufficient here anymore. We do not yet understand the physics on these trans-Planckian scales and a new theory of **quantum gravity** is needed. Chances are that the current results are insensitive to events on the very small length scales. The very high energy scale during the period of inflation of about  $10^{16}$  GeV might necessitate correction terms for matter and gravity dependencies. A theoretical approach for these very high energy scales is string theory. The initial singularity also needs to fit to inflation. How this is achieved is not clear either. It is also unclear how exactly inflation has finished, a problem which is referred to as the **exit problem**. A phase transition must have released the potential energy of the inflation field. Amongst other models quantum gravity, **string theory**, **supersymmetry** and GUTs can shed light on these problems.

After inflation had ended, the inflaton scalar field that was driving it began to oscillate. These oscillations are thought to have led to the decay of the inflaton via matter and radiation production and eventually to a reheating of the Universe (Khlebnikov & Tkachev 1996). The Universe was now radiation dominated, in thermal equilibrium, slowly expanding and cooling. At the very early stages, when the Universe was up to  $10^{15}$  K hot (the Universe was even hotter before, but standard physics fails to explain the processes during these times), it consisted of free elementary particles such as leptons, quarks, gauge bosons and cold dark matter particles which were interacting with each other. The fundamental fermions were both matter (quarks, leptons) and antimatter (antiquarks, antileptons) particles. The highly energetic bosons were creating matter-antimatter pairs by pair production which was in equilibrium with the recombination of these particles. When the cooling Universe reached certain energy scales, particles, depending on their individual masses, were frozen-out of the pair-production processes. They became stable and for some reason there was a slight excess of matter particles over anti-matter particles. This made matter dominant over antimatter in today's Universe. The two main interpretations for this **matter-antimatter inequality** are that either the Universe started with a small preference for matter or it was originally perfectly symmetric, but somehow physical processes contributed to a small imbalance in favor of matter over time (Sakharov 1991).

Quarks combined to form baryons as protons and neutrons before the end of the first second of the Universe. The predicted cold dark matter particles were almost not interacting with other particles anymore. When the temperature had dropped below  $10^{10}$  K protons and neutrons combined to form light nuclei. After only 15 minutes, most of the hydrogen, deuterium, helium and lithium nuclei ( $H$ ,  $H^2$ ,  $He^3$ ,  $He^4$ ,  $Li^7$ ) of the Universe had been formed. At later stages, the Universe became too cold and its density was too low for more particles to form. 50000 years after the Big Bang, matter started to dominate radiation, and the nuclei combined with the electrons in a period called **recombination** at a temperature of about 3000 K at  $z \simeq 1100$  to form the first atoms and neutralize the Universe. Due to the expansion of space and the related cooling process the photons lost energy and were no longer able to ionize the forming atoms. Thereupon, the photons were no longer Thomson scattered at the free electrons and gained a longer mean free path length. Recombination did not happen instantaneously but over a certain time range during which the photons decoupled from matter and became the CMB photons we observe today. Since photons and matter had been in thermal equilibrium before recombination the photons still follow a thermal black body spectrum today. The young Universe changed from opaque to transparent during recombination. This period was followed by the **dark ages**, where the only light source was the cooling CMB radiation and the 21 cm spin line of neutral hydrogen. After that, **first stars** and quasars formed and reionized the Universe. Large volumes of matter collapsed to form galaxies and then groups, clusters and superclusters of galaxies. Today, **dark energy** is meant to dominate both radiation and matter as their densities have fallen due to the expansion of space.

### 1.1.3 Anisotropies of the microwave sky

*Details on the physics of the cosmic microwave anisotropies can e.g. be found on the website created by Prof. Wayne Hu<sup>2</sup> and in a review by Durrer (2001).*

As stated in Chapter 1.1.2, at  $z \approx 1100$  the young Universe reached a point when radiation decoupled from matter. The photons emitted at that time are observed as the CMB photons today stemming from a sphere which is almost as big as the size of the observable Universe and

---

<sup>2</sup><http://background.uchicago.edu/>

is centered on our current location. Since matter and radiation were in **thermal equilibrium** in the early Universe, the CMB photons follow a perfect thermal black body spectrum of a temperature of  $T = 3000$  K at the time of emission. Due to the expansion of space the black body spectrum evolved into a black body spectrum of  $2.72548(\pm 0.00057)$  K today (Fixsen 2009), which peaks in the microwave frequency range. The mean temperature can be seen as the CMB monopole at the multipole  $\ell = 0$ .

The solar system's peculiar motion relative to the rest frame of the CMB generates the strongest temperature anisotropy on the sky, the dipole anisotropy at  $\ell = 1$  which has been well measured for more than 30 years. Its amplitude of  $T = 3.355 \pm 0.008$  mK implies a peculiar velocity of  $v = (369 \pm 0.9) \text{ km s}^{-1}$  into the direction of  $(l, b) = (263^\circ.99 \pm 0^\circ.14, 48^\circ.26 \pm 0^\circ.03)$  (Kogut et al. 1993; Fixsen et al. 1996; Hinshaw et al. 2009; Planck Collaboration et al. 2014k). The dipole anisotropy stands apart from the rest of the CMB signal due to its large amplitude. For the purposes of CMB anisotropy studies, monopole and dipole contributions are removed from the maps.

At the higher multipoles, the CMB provides a snapshot of the Universe at the time of last scattering. The primordial density fluctuations and the successive physical effects (their contributions to the power spectrum are shown in Figure 1.4) have influenced the photon-baryon plasma before recombination and the CMB photons directly at the time of last scattering. These effects have determined the CMB temperature anisotropies and led to a wiggling angular power spectrum. The statistical properties of the CMB depend on the initial fluctuations. The CMB photons enable the extraction of the cosmological parameters and give the best insight into the early Universe so far. Almost no direct information from before recombination can reach us, except for an expected neutrino background and gravitational waves which are predicted by inflationary models. Analyzing the early stages of the Universe, studies of the 21 cm spin line of neutral hydrogen also play an important role. In the following, I shortly introduce the physical effects that affect the properties of the CMB.

The CMB anisotropies are described by a **gauge invariant perturbation theory** (Bardeen 1980; Kodama & Sasaki 1984). The general mechanism that produces primordial perturbations generates scalar, vector, and tensor modes. However, the vector modes decay with the expansion of the Universe. The CMB temperature is a scalar function whereas gravitation is a tensor interaction. Tensors also decay when they enter the horizon and therefore only contribute to angular scales larger than the horizon scale of  $1^\circ$ . This means that the low  $\ell$  signal of the CMB could contain gravity wave contributions, which can explicitly be distinguished using polarization information.

The primordial perturbations cause the first potential hills and wells in the dark matter distribution of the primordial plasma. The baryon-photon fluid is oscillating in the potential wells of dark matter but the dark matter particles are not directly coupled to the photons and baryons. The free electrons in the hot plasma act as glue between photons and baryons. Before the time of recombination the photons are Thomson scattered at the free electrons while the electrons interact with the baryons via Coulomb forces. The interactions are sufficiently rapid so that the photon-baryon system behaves as a tightly coupled fluid. The mean free path of the photons is tiny. After recombination baryons are let go from the photons and fall into the potential wells of dark matter. The radiation is free-steaming from then on.

The initial density perturbations are turned into temperature anisotropies by the (non-integrated) **Sachs-Wolfe effect** (Sachs & Wolfe 1967) occurring at the surface of last scattering which describes the gravitational redshift of the CMB photons: Photons originating from an overdense region are redshifted from climbing out of the potential well, and likewise blueshifted

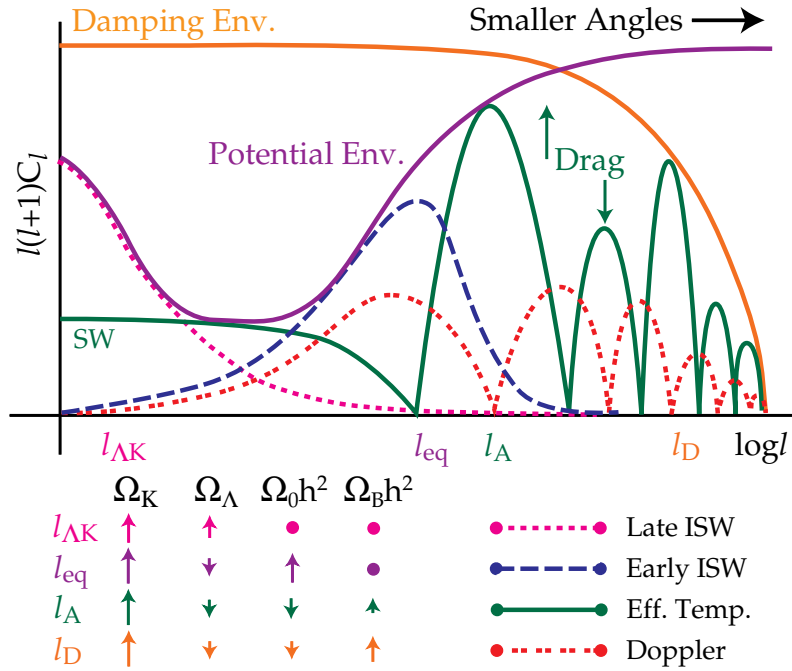


Figure 1.4: Contributions to the power spectrum from various physical processes in logarithmic multipole scale  $\ell$ . Source: [Hu et al. \(1997\)](#)

from an underdense region. The fluctuations on the largest angular scales ( $\ell \lesssim 100$ ) do not enter the horizon before recombination and hence the CMB anisotropies at  $\ell \lesssim 100$  directly reflect the initial conditions. In Figure 1.4 the Sachs-Wolfe plateau of the green curve hints at a scale-invariant nature of the primordial perturbations, in accordance with the standard inflationary model.

Fluctuations in the early Universe evolve further until the time of recombination based on the interaction between the gravitational attraction tending to collapse overdense regions and the photon pressure resisting that compression. This drives **acoustic wave oscillations** of diverse but synchronized modes to compress and rarefy the hot plasma. The frequency is determined by the sound speed of the primordial fluid. After the Universe has cooled enough to allow the formation of neutral atoms, the pattern of density variations caused by the sound waves is frozen into the CMB and can be seen in the harmonic series of peaks in the CMB power spectrum. Oscillations that reach maximal compression just in a dark matter potential well and maximal rarefaction on hill top for the first time at the time of recombination lead to the first acoustic peak. Their overtones have modes that are integer fractions of the fundamental wavelength. Oscillating two, three or more times as quickly as the fundamental wave, these overtones cause smaller regions of space to reach maximum displacement from a mean density at recombination. The angular position of the peaks is a sensitive probe of the spatial curvature of the Universe.

Recombination does not happen instantaneously, rather the last scattering surface has a finite thickness. This leads to a **damping process** of the anisotropies at the highest  $\ell$  ( $\ell \gtrsim 1000$ ) which corresponds to angular scales smaller than the surface thickness. Furthermore,

the coupling between the photons and baryons is imperfect. The diffusion between the two components will decrease the amplitudes of the oscillations with time. This is referred to as diffusion or silk damping (Silk 1968). The damping tail cuts off the anisotropies at multipoles above  $\ell \sim 2000$ , and makes smaller scale fluctuations inaccessible.

The baryons in the plasma increase the effective mass of the fluid which leads to greater compression in the potential wells during gravitational infall or so-called **baryon drag**, hence to a change of the absolute values of the maxima and minima temperature fluctuations. Modes that reach maximal compression within a potential well are enhanced over modes with maximal rarefaction within such wells which causes an alternation in the odd and even peak heights. The ratio of odd to even acoustic peaks therefore holds information regarding the ratio of baryons to dark matter.

The line-of-sight motion of the photons relative to the observer causes the **Doppler peaks** in the power spectrum. This component is out of phase with the Sachs-Wolfe component of the acoustic peaks since the fluid oscillates 90 degrees out of phases with the temperature. This doppler contribution is shown by the red dotted curve in Figure 1.4. The conversion from physical scale into angular scale depends on the curvature of the Universe and the distance of the observer to the last scattering surface. A fixed physical scale at last scattering is the sound horizon determined by the acoustic features of the CMB. The spacing between the peaks provides a good test of the curvature. However, the diffusion damping scale provides a further model-independent test.

The CMB radiation shows a residual polarization that complements the information we get from the temperature anisotropies. By providing directional information on the sky, the polarization pattern carries additional information about the very early Universe and the origin of structure. It provides a strong test of our inflationary paradigm by enabling a consistency check on our interpretation of acoustic peaks in the power spectrum, since shape and amplitude in the polarization acoustic peaks can be precisely predicted from the temperature peaks under the standard theory. Furthermore, primordial gravitational waves that are predicted for inflation cause specific polarization patterns that could be detected with today's experiments. The primordial **polarization** of the CMB radiation is generated by scattering processes at the last-scattering surface and is then influenced by the first stars during the reionization epoch of the Universe. The CMB is first polarized by Thomson scattering at free electrons during the time of decoupling. A linear net polarization arises when radiation with different intensities from different directions meets at the scattering electron. The polarization pattern of the CMB is therefore a projection of the quadrupole anisotropies. These quadrupole anisotropies can be caused by density fluctuations, a vorticity in the primordial plasma or gravitational waves. The individual contributions can be distinguished by the symmetry properties of the polarization pattern. The movement of the photons due to streaming and diffusion effects of the temperature perturbations produces a symmetric quadrupole moment. Vorticity vector perturbations are predicted to be negligible at recombination. Passing gravitational waves cause an anisotropic stretching of space and herewith change the frequency of the CMB photons. This quadrupolar variation is not symmetric and causes a curly handedness in the polarization pattern. The polarization pattern is described by the Stokes parameters  $Q$  and  $U$  or by its  $E$ - and  $B$ -modes. Density perturbations only produce  $E$ -mode polarization. Gravitational waves generate both modes. The  $B$ -mode component caused by gravitational wave anisotropies is very small and its detection and interpretation therefore requires a detailed understanding of foregrounds and secondary effects as for example gravitational lensing that can also cause  $B$ -mode contributions. However, Hanson et al. (2013) have claimed the first detection of grav-

itational lensing  $B$ -modes, using first-season data from the polarization-sensitive receiver on the South Pole Telescope. The BICEP2 collaboration reported first results on their search for a gravitational wave signal in the B-mode power spectrum of the CMB (Ade et al. 2014) that pointed to a detection of a gravitational wave signal. But they have stated that further experimental results, as for example those from the Planck experiment, are necessary to account for polarized foreground dust contributions to the B-mode signal. Colley & Gott (2015) have studied the genus topology of the B-modes of the BICEP2 experiment in an independent study and also think of a gravity wave signal. A combined study of BICEP2/Keck Array and Planck data has detected lensing B-modes with a very high significance but no contribution of gravity waves yet (BICEP2/Keck and Planck Collaborations et al. 2015). Upcoming Planck data releases on CMB polarization in 2015/2016 will provide further insight into the polarization properties of the CMB, and therefore will give more information about both, structure formation and the inflationary epoch. The theory of the cosmic microwave background polarization is, for example, described in Cabella & Kamionkowski (2004).

Intervening effects between the time of recombination and today contribute to the measured CMB signal and alter the primary anisotropies. The **secondary anisotropies** are caused by several different known physical processes modifying the CMB temperature fluctuations. As described by Wayne Hu, the effects basically divide into two categories namely gravitational effects from metric distortions and rescattering effects from reionization. The **integrated Sachs-Wolfe effect** (ISW) causes a net redshift or blueshift for CMB photons traversing time-varying gravitational potentials. If the depth of the potential well changes as the photon crosses it, the blueshift from falling in and the redshift from climbing out no longer cancel. In addition, the wavelengths of the photons are stretched and contracted with spacetime which amplifies the effect described above. The ISW effect can be separated into two contributions, the **early-time** and **late-time ISW**. The early ISW effect arises right after the non-integrated SW effect at last-scattering, when radiation pressure still makes the potentials decay. The late ISW effect arises at the end of matter domination when the cosmological constant starts to govern the cosmological expansion. Once fluctuations enter the nonlinear regime and the decaying potential wells and hills have become large-scale structure superclusters and voids, the full (linear and nonlinear) late-time ISW effect is described by the **Rees-Sciama effect** (Rees & Sciama 1968). **Gravitational lensing** of the CMB by intervening large-scale structure slightly decreases the amplitude of CMB acoustic peaks, and tends to redistribute some of the CMB power towards smaller scales.

After recombination the Universe underwent a phase of reionization until  $z \sim 5$  which was detected by the observation of absent **Gunn-Peterson troughs** in quasars. The free high-energy electrons, mostly present in galaxy clusters, distort the CMB photons through inverse Compton scattering. This so-called **Sunyaev-Zel'dovich effect** (SZ effect) (Sunyaev & Zel'dovich 1972), predicted by Rashid Sunyaev and Yakov Zel'dovich, can be divided into thermal and kinematic effects, depending on the energy properties of the electrons. The kinematic effect, where CMB photons interact with electrons that have high energies due to their bulk motion is also called **Ostriker-Vishniac effect** (Ostriker & Vishniac 1986). The topological inhomogeneity of a patchy reionization causes further effects on the polarization (Doré et al. 2007) and temperature anisotropies (Santos et al. 2003). Also, discrete sources and the Galactic ISM generate an extensive foreground of **synchrotron radiation**, **free-free radiation** and/or **thermal dust emission**. It is one of the major concerns in CMB anisotropy analysis to determine correctly the fraction of the foreground contamination to the observed signal.

### 1.1.4 Inflationary models and alternative scenarios

Trying to describe the beginning of the Universe, inflationary models generically predict distinct features for our Cosmos as presented in e.g. Guth & Kaiser (2005). The features of the inflationary models are currently tested by a new generation of high-precision astronomical experiments as the CMB satellite missions. Inflation has passed more and more stringent tests, but over decades now theoreticians explore its meaning and its implications. Such as what has been there before the inflationary epoch, how did inflation end, how do the characteristics of inflation agree with the structure of spacetime and matter, and, last but not least, with the statistics of the primordial density fluctuations studied in this work.

One of the generic predictions from the simplest inflationary **single field slow-roll model** is that the primordial fluctuations are adiabatic and exactly Gaussian in linear order. Weak gravitational interactions of the inflaton potential cause nonlinearities that can in principle be detected as weak non-Gaussianity. The current CMB or large-scale experiments are not sensitive enough thought to detect these weak nonlinearities (Komatsu & Spergel 2001; Acquaviva et al. 2003; Maldacena 2003; Planck Collaboration et al. 2014h). Interestingly, several tests have identified strong anomalies and/or deviations from Gaussianity in the primordial perturbations and hence suggest a violation of standard inflation. The detection of primordial non-Gaussianity (NG) provides a powerful means to study the nonlinear physics of the very early Universe at extremely high energy scales. Measuring the amplitude, shape and scale dependence of NG will help to distinguish between various inflationary scenarios with the ultimate goal to constrain the shape of the potential and/or the dynamics of the inflaton field(s) and their possible (self-)interactions (for a review see e.g. Komatsu 2010). Even alternative models without a need for an inflationary phase are discussed in cosmology and would benefit from a quantitative and qualitative measurement of non-Gaussianity (for a review see e.g. Brandenberger 2013). In Chapter 1.1.2, I have given a short summary of the standard single field slow-roll inflationary scenario which predicts nearly Gaussian fluctuations. Here, I will introduce a few models from a variety of examples that predict deviations from Gaussianity. Single-field inflation means those inflationary models in which one field is solely responsible for the accelerated expansion and the creation of density perturbations. In general, density perturbations can either be adiabatic (as described in Chapter 1.1.2) or in isocurvature mode. Isocurvature perturbations would arise from stresses in the matter distribution and are more likely to be found with **multiple-field** inflationary models by the vacuum fluctuation of a field other than the inflaton. Multiple-field inflation refers to inflationary models in which multiple fields interact with each other (e.g. Wands 2007). Isocurvature perturbations can lead to non-Gaussian fluctuations in the early Universe (e.g. Linde & Mukhanov 1997).

Inflationary models that involve additional fields different from the inflaton can generate a high level of NG of the local type, e.g. **curvaton-type models**, where the late-time decay of a scalar field induces curvature perturbations (Linde & Mukhanov 1997; Moroi & Takahashi 2001; Lyth et al. 2003), and **two-field** (Vernizzi & Wands 2006) or multiple-field models (Bernardeau & Uzan 2002; Bartolo et al. 2002). For a review see e.g. Byrnes & Choi (2010).

Models in which the Lagrangian is a general function of the inflaton  $\phi$  and of powers of its first derivative, even in absence of any potential energy term, can kinetically drive inflationary evolution of the same type as the usually considered potential driven inflation. These models are called **k(inetical)-inflation** (Armendáriz-Picón et al. 1999; Garriga & Mukhanov 1999) and can lead to scale-dependent NGs, if the sound speed varies during inflation (Chen et al. 2007).

**Brane inflation** (Dvali & Tye 1999) is a widespread idea to construct inflationary models in string theory. Its dynamics can be described by the Dirac-Born-Infeld action leading to DBI inflationary models (Alishahiha et al. 2004; Silverstein & Tong 2004; Chen 2005*a,b*). These string theory models give rise to equilateral NG with a natural scale dependence (e.g. Lo Verde et al. 2008). Also **ghost inflation** (Arkani-Hamed et al. 2004) predicts equilateral NG and features an alternative way of having de Sitter phases in the early Universe differing from the cosmological constant explanation. **Warm inflation** (Berera 2006) occurs when there is a significant amount of particle production during the inflationary era and predicts local NG in the squeezed limit (Moss & Xiong 2007).

Another important alternative to the inflationary paradigm is the striking **ekpyrotic Universe** (Khoury et al. 2001), motivated by superstring theory. It predicts that the Big Bang Universe was produced by the collision of two brane worlds. For a review see Lehnert (2010). Superstring theory promises to synthesize general relativity with the other fundamental forces of nature. The ekpyrotic model addresses the cosmological horizon, flatness and monopole problems and generates a nearly scale-invariant spectrum of density perturbations without the need for inflation. It relies on a phase of slow contraction before the Big Bang, called ekpyrosis, in which isocurvature perturbations are converted into curvature perturbations. Khoury et al. (2001) predict a strongly blue gravitational wave spectrum implying consequences for CMB polarization. Ekpyrotic cosmology predicts local NG. Through a shape dependence of the correlation functions and the strength of detected NG, the model is distinguishable from other alternative scenarios that can yield large non-Gaussianity, such as DBI inflation and curvatonlike models (Buchbinder et al. 2008; Lehnert & Steinhardt 2008). It is complemented by the **cyclic model** (Steinhardt & Turok 2002*a,b*) in which the Universe undergoes a periodic sequence of expansion and contraction. Each cycle begins with a Big Bang and ends in a Big Crunch.

The **pre-Big Bang scenario** in string cosmology (Gasperini & Veneziano 1993, 2003) represents an alternative to the classical initial Big Bang singularity scenario. It is an attempt to derive the standard FLRW cosmology from a fundamental theory of quantum gravity. Enqvist & Sloth (2002) consider the emergence of adiabatic CMB perturbations in this scenario. A problem with this model is the transition phase between pre- and post-Big Bang times. Vernizzi et al. (2001) state that this model generates non-Gaussian perturbations.

Brandenberger (2013) notes that any theory which yields an approximately scale-invariant spectrum of adiabatic primordial fluctuations is an alternative to the standard inflationary paradigm. He introduces two examples, namely the **emergent Universe paradigm** (Ellis & Maartens 2004) and the **bouncing scenario** (Wands 1999; Finelli & Brandenberger 2002; Novello & Bergliaffa 2008), that both avoid an initial singularity. The emergent scenario describes a cosmology with positive curvature, that originates as an Einstein static Universe and is inflating and later reheating into a hot Big Bang era. These two cosmologies neither have a beginning-of-time nor a horizon problem. If the initial radius is chosen to be above the Planck scale, then they also have no quantum gravity era, and are described by classical general relativity throughout their history. It is so far unknown whether these models can naturally produce non-Gaussianities. The bouncing scenario involves a single scalar field coupled to gravity and a contracting phase which is smoothly connected at some high density to the expanding phase of standard cosmology. New physics is required to obtain a smooth transition from contraction to expansion. Li et al. (2012) claim that the discrete spacetime geometry in loop quantum cosmology scenarios predicts a nonsingular bouncing universe that could generate non-Gaussian features. For an overview on supersymmetry and supergravity in

cosmology please refer to [Feng \(2005\)](#).

Einstein's theory of general relativity is a theory of geometry but does not directly predict homogeneity, isotropy or any global topology. Perhaps the Universe has no trivial topology. It is possible that it is neither isotropic nor homogeneous. The power asymmetry, observed in CMB data (described in Chapter 1.2.3), could indicate a preferred direction in the Universe which is either inherited from some pre-inflationary state or might be generated spontaneously during inflation (e.g. [Wands 2009](#)). [Gordon \(2007\)](#) and [Erickcek et al. \(2008\)](#) argue that such a power asymmetry could be produced in curvaton-like models. However, the assumption of homogeneity simplifies the Einstein field equations. A set of homogeneous three-dimensional geometries was completely classified by [Bianchi \(1898\)](#) and led to the cosmological **Bianchi models** for a homogeneous and anisotropic 3+1 spacetime. If isotropy is assumed in addition, just two integrable equations of the EFEs remain and their solution gives the FLRW cosmological models as special cases of the Bianchi models of type I and VII<sub>0</sub> (flat space), V and VII<sub>h</sub> (open space) and IX (closed space) ([Barrow & Sonoda 1986](#)) (see also Chapter 1.1.1). The Bianchi models VII<sub>h</sub>, VII<sub>0</sub> and IX are the most general solutions for a homogeneous and anisotropic Universe ([Kogut et al. 1997](#)). The Bianchi type VII<sub>h</sub> model contains the Bianchi I, V, and VII<sub>0</sub> models in the appropriate limits. The metric anisotropy in these models is characterized by a vorticity and shear of space. In the Bianchi model of type VII<sub>h</sub> the combined effect of vorticity and shear introduces a swirly pattern into the density field. The geodesics are caused to spiral due to an intrinsic handedness which leads to a rotating Universe. Following [Barrow et al. \(1985\)](#), [Bunn et al. \(1996\)](#) and [Kogut et al. \(1997\)](#), it is necessary to study general models of **rotating Universes** especially in the framework of certain types of Bianchi models, such as type V, VII, and IX. It is under current debate whether detected large-scale CMB anomalies such as the suppression of the quadrupole and the alignment of some multipoles originate in a rotation of the Universe. It has been shown that the subtraction of Bianchi type VII<sub>h</sub> templates from CMB maps, as illustrated in Figure 1.5 for the Planck SMICA map, can significantly reduce some of the detected large-scale CMB anomalies (e.g. [Jaffe et al. 2005](#); [McEwen et al. 2006](#); [Jaffe et al. 2006a](#); [McEwen et al. 2013](#)). The authors have tried to place limits on the global rotation and shear of the Universe and concluded that the large-scale anisotropy is described at least in part by a low-density Bianchi model. Known phase correlations in WMAP and Planck data are also diminished by subtracting Bianchi templates from the maps, as shown in Chapter 6 ([Modest et al. 2014](#)).

## 1.2 Observations

### 1.2.1 CMB data products from WMAP and Planck

On November 18th in 1989 the National Aeronautics and Space Administration (NASA) launched the Cosmic Microwave Background Explorer (**COBE**) satellite in order to observe the predicted density anisotropies of the Universe in the CMB temperature distribution of the full sky with an angular spatial resolution of 10°. As a consequence of the successful detection of temperature anisotropies in the COBE-DMR (Differential Microwave Radiometer) data ([Smoot et al. 1992](#)) Nasa launched a follow-up mission, called the Wilkinson Microwave Anisotropy Probe (**WMAP**) satellite<sup>3</sup> on June 30th, 2001. WMAP orbited the **Sun-Earth Lagrange point** L2 at a distance of 1.5 million kilometers from Earth before it finished its observations in 2010 and left L2 for a parking position in orbit. The observatory contained 20 different **radiometers** that translated the CMB signal which was observed by a dual Gregorian telescope

<sup>3</sup><http://map.gsfc.nasa.gov/mission/observatory.html>

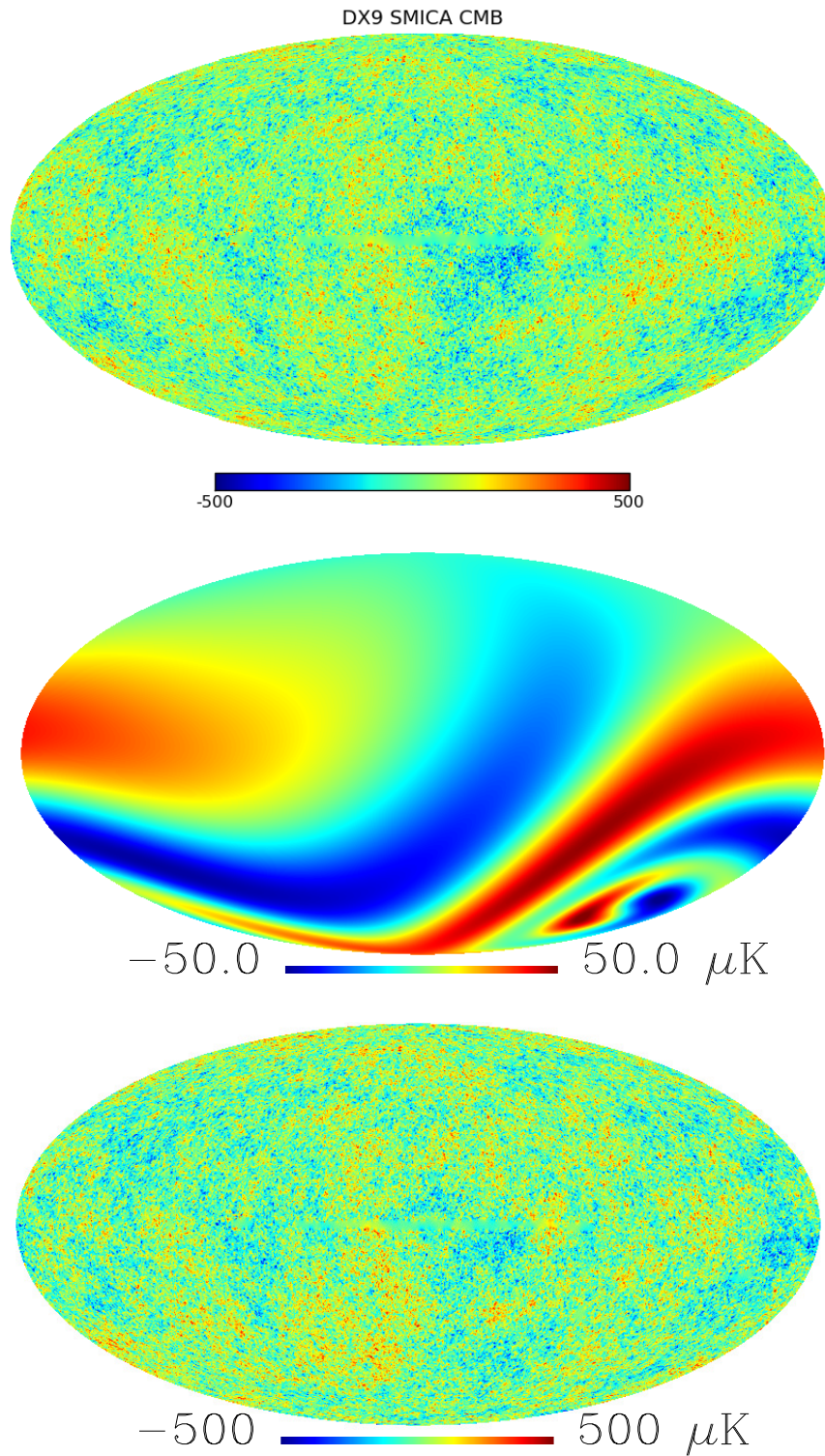


Figure 1.5: Subtracting a best fit Bianchi type  $\text{VII}_h$  template (middle) from the Planck SMICA map (top) reduces some of the large-scale anomalies of the SMICA map in the resulting map (bottom). The SMICA map shows remaining Galaxy bias.

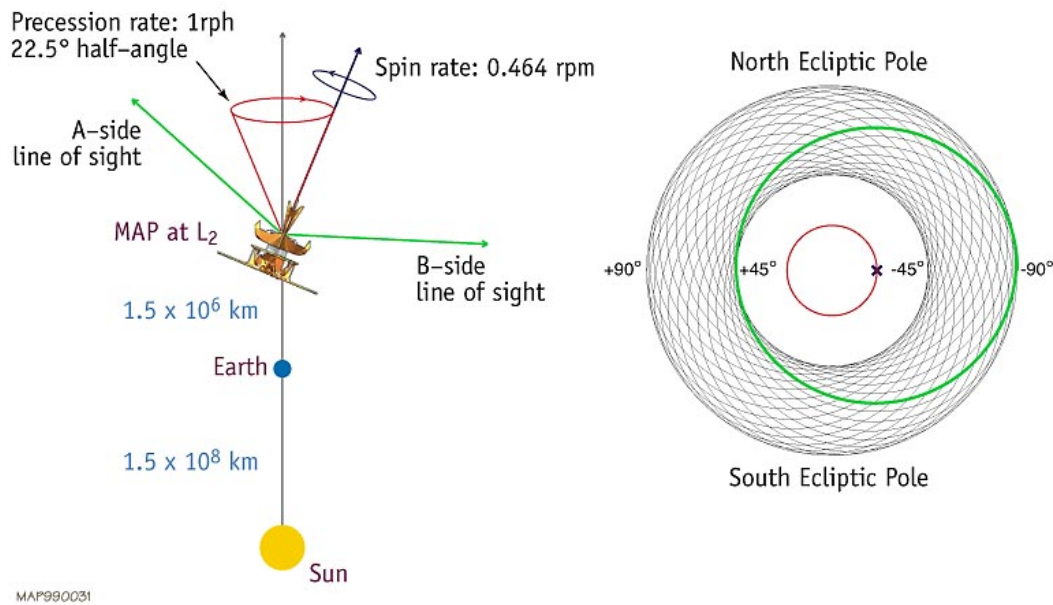


Figure 1.6: The scanning strategy of WMAP. Source: Nasa and the WMAP Collaboration, NASA WMAP website ([http://map.gsfc.nasa.gov/mission/observatory\\_scan.html](http://map.gsfc.nasa.gov/mission/observatory_scan.html)).

into temperature values. They were constructed as so-called pseudo-correlation-radiometers, each from two back-to-back radiometers roughly  $140^\circ$  apart that ignored the signal that was identical for both radiometers. These radiometers measured the temperature difference between two opposite points in the sky at a time  $t$ , which resulted in time-ordered CMB data. Passive radiator sunscreens cooled down the instruments to 95 K. Solar panels and diffraction shields limited the diffraction signal from sun, earth and moon to less than  $0.5\mu\text{K}$ . For years, WMAP was able to measure the entire sky every six months. Its angular resolution of  $0.3^\circ$  was 33 times higher compared to COBE, providing a much greater sensitivity to the angular power spectrum. In October 2013, the final WMAP data was released after nine years of observation (Bennett et al. 2013). Foreground signals (milky way, extra-Galactic sources, etc.) are distinguishable from the CMB anisotropy by differing spectra and spatial distributions. Therefore, multiple frequency coverage is needed to reliably separate the Galactic foreground signal from the CMB anisotropy: WMAP has observed with five frequency bands with center frequencies of 23, 33, 4, 61 and 93 GHz in the **K, Ka, Q, V and W band**, respectively. The K-band and Ka-band are measured with one differencing assembly each. The Q- and V-band need two differencing assemblies each: Q1, Q2 and V1, V2. The W-band has four: W1-W4. The larger number of channels at the higher frequencies is necessary to provide roughly equal sensitivity at each frequency. The resolution of the instrument depends on the frequency band and is smaller than 13.8 arcmin full width at half maximum (FWHM) for the W-band.

To complement and improve upon WMAP observations with an even higher resolution of up to 5 arcmin and higher sensitivity, the **Planck space observatory**<sup>4</sup> was launched on May 14th, 2009, alongside the Herschel space observatory. A comparison of the resulting maps from the three different experiments COBE, WMAP and Planck is shown in Figure 1.9. Planck is operated by the European Space Agency (ESA) with NASA participation. During its five

<sup>4</sup><http://sci.esa.int/planck/34729-spacecraft/>

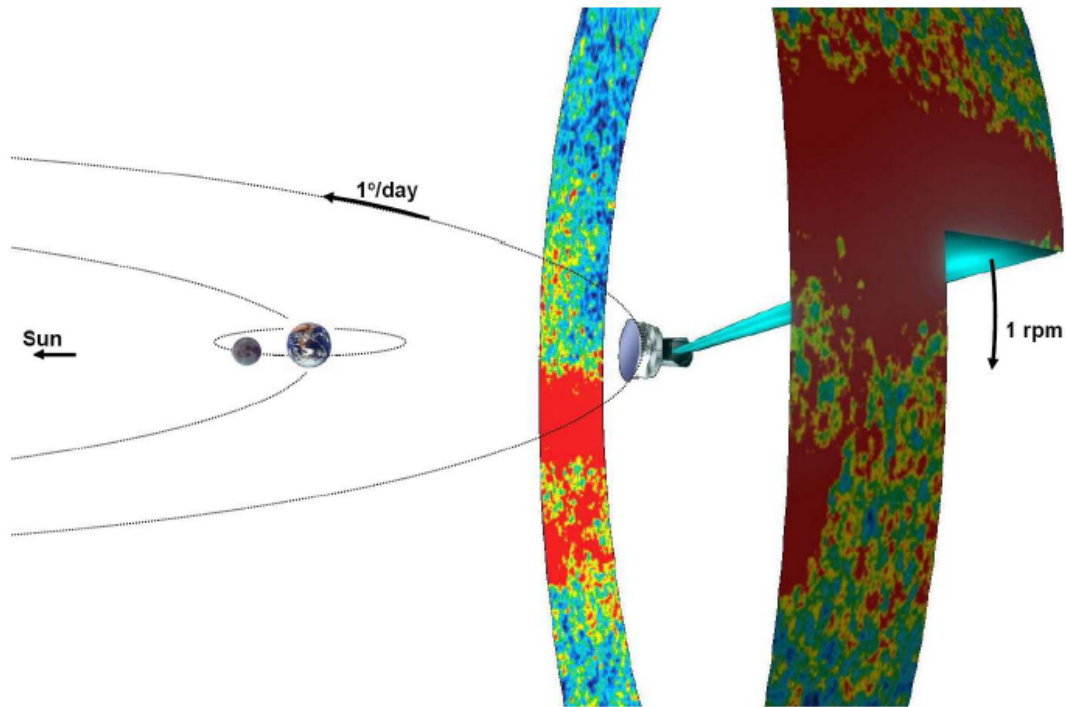


Figure 1.7: The scanning strategy of Planck. Source: ESA and the Planck Collaboration, ESA Planck website (<http://www.sciops.esa.int/index.php?project=PLANCK&page=Pointing>)

observation periods it was orbiting on the Sun-Earth L2 point similar to the WMAP satellite, until its operations ended on October 23rd, 2013, and Planck was placed into a heliocentric orbit to die. The whole sky is scanned in a little more than 6 months. The observatory carries a single off-axis tilted Gregorian telescope which feeds two high-sensitivity, multi-frequency instruments, namely the low frequency instrument (LFI) and the high frequency instrument (HFI). The LFI is designed to produce measurements of the microwave sky in the frequency range 27 to 77 GHz with 22 radiometers. The HFI is designed to measure the diffuse sky radiation in the frequency range 84 GHz to 1 THz using bolometer arrays. Planck observes nine frequency channels as shown in Figure 1.11. The passive and active cooling systems maintain a very low temperature of 0.1 K for the two instruments.

A well-defined **scan strategy** of the satellites is necessary for high quality data. **Full-sky coverage** is required in order to enable the accurate determination of the low-order spherical harmonic moments. The **beam response** has to be almost symmetric which is guaranteed by scanning a given point in the sky at many angles. A given pixel needs to be observed on **different time scales** from minutes to months. The **angular velocity** of a given line of sight has to be nearly constant on the sky. The instrument has to observe a large fraction of the sky each day; and the time-average of the differential data has to be approximately zero over an hourly calibration period, allowing for a robust initial baseline estimation (Hinshaw et al. 2003). The WMAP and Planck missions follow different scanning strategies (Dupac & Tauber 2005; Tauber et al. 2010; Planck Collaboration et al. 2011) as shown in Figures 1.6 and 1.7. WMAP has scanned the entire sky by spinning around the spacecraft symmetry

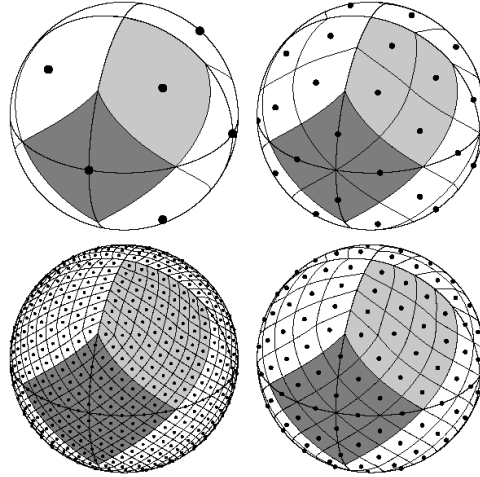


Figure 1.8: HEALPix pixelization scheme. Source: HEALPix website (<http://healpix.sourceforge.net/>)

axis with a slow precession at  $22.5^\circ$  off the Sun-WMAP line. Since the line-of-sights of the dual telescopes are off the symmetry axis, the path of one line-of-sight on the sky resembles a spirograph pattern. WMAP has observed more than 30% of the sky each day and each ecliptic pole every day. Planck has observed the sky by continuously scanning nearly great circles on the celestial sphere. The spin axis of the satellite followed a cycloidal path on the sky, by step-wise displacements of  $1^\circ$  a day to avoid pointing into the Sun's direction. The detector's line-of-sight has an axis offset of  $85^\circ$ . Both scanning strategies result in an inhomogeneous depth of integration time across the sky. The areas near the ecliptic poles are observed with greater depth than all the others.

The resulting maps are provided as **pixelized sky maps** following the HEALPix pixelization scheme (Górski et al. 2005). HEALPix divides the sky into  $N_{\text{pix}}$  (minimum 12) exactly equal area quadrilaterals of varying shape (see Figure 1.8), where  $N_{\text{pix}} = 12 * N_{\text{side}} * N_{\text{side}}$  with  $N_{\text{side}}$  being a power of two. The pixel size depends on the HEALPix resolution parameter of the grid. For WMAP the maximum  $N_{\text{side}}$  is 1024, for Planck it is 2048. The standard maps have a resolution of  $N_{\text{side}}^{\text{WMAP}} = 512$  and  $N_{\text{side}}^{\text{Planck}} = 2048$  which corresponds to a pixel number of  $N_{\text{pix}}^{\text{WMAP}} = 3,145,728$  and  $N_{\text{pix}}^{\text{Planck}} = 50,331,648$ , respectively. The specific geometrical properties allow HEALPix to support two different numbering schemes for the pixels. The ring scheme counts the pixels moving down from north to south along the isolatitude rings. The nested scheme arranges the pixels in twelve tree structures.

### 1.2.2 Foreground removal – Generating maps

The CMB maps are contaminated by foreground emission. The differences between the spectral and spatial characteristics of the CMB and the foregrounds allow for a separation of the CMB from the different foreground components. There are three foreground emissions that strongly affect the CMB radiation. These are **Galactic synchrotron radiation** and **free-free emission**, dominating the lower frequencies, and **Galactic dust emissions**, dominating the higher frequencies. The spectral properties of these emissions contribute different amounts to the different frequency bands of the experiments as can be seen in Figure 1.10. Further foreground signals and distortions of the primordial CMB stem from extra-Galactic and far-IR point sources, the SZ effect, ISW contributions and gravitational lensing. Extra data sets

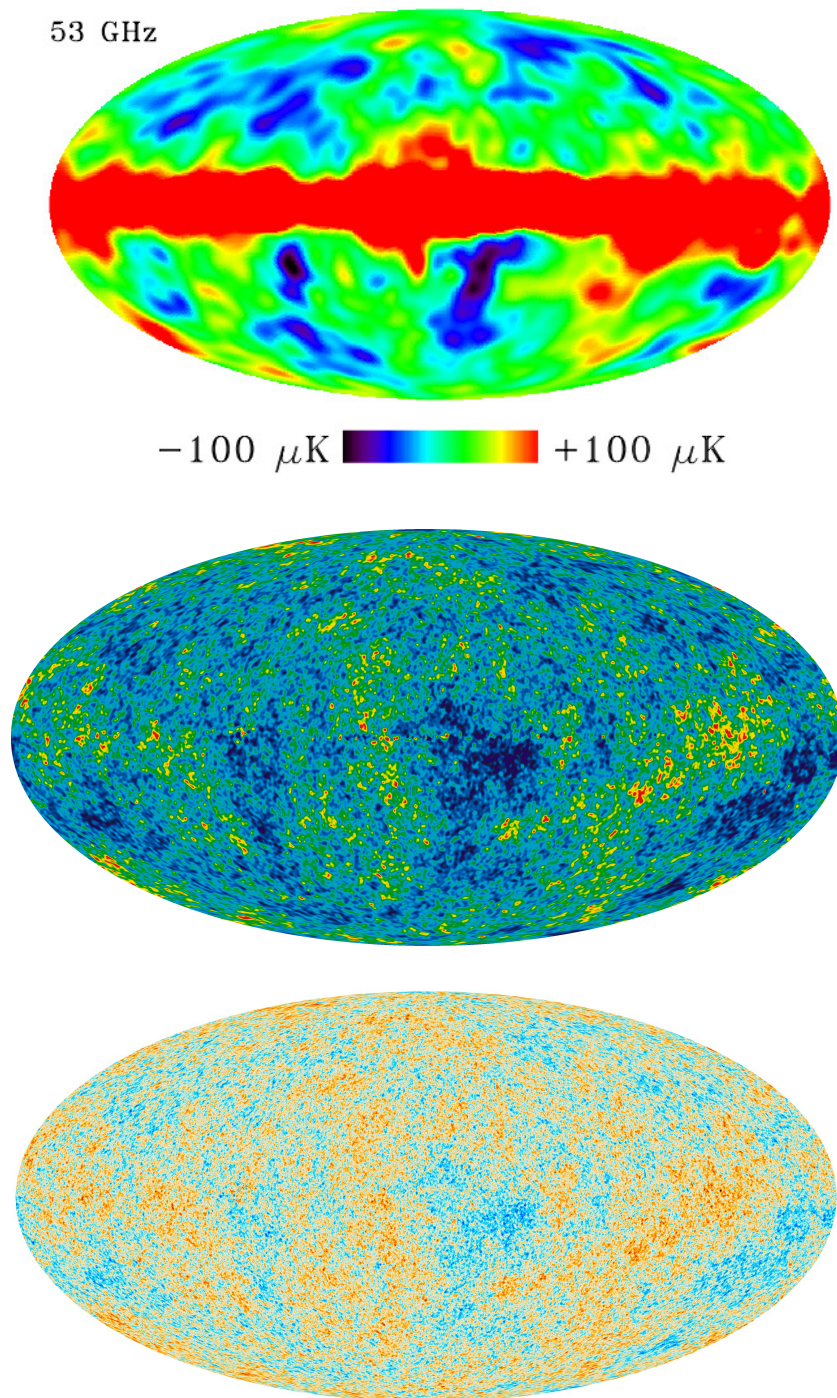


Figure 1.9: The CMB sky observed with increasing resolution by COBE in the range from  $-100$  to  $+100 \mu\text{K}$ , WMAP (ILC map, 9-year data release) in the range from  $-200$  to  $+200 \mu\text{K}$  and Planck (SMICA map, first data release) in the range from  $-500$  to  $+500 \mu\text{K}$ . The latter is generated with the Planck color coding and shows the inpainted full-sky version of the SMICA map. Figure 1.5 shows the SMICA map with remaining Galaxy bias and in a different color coding which resembles the WMAP coding.

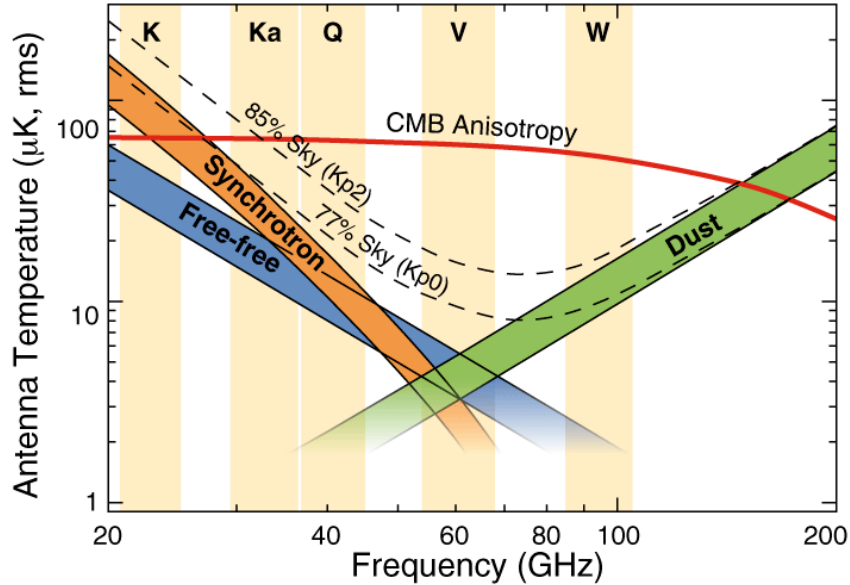


Figure 1.10: Frequency dependence of the expected CMB anisotropy (red band) and of three known sources of foreground emission from our Galaxy, in units of antenna temperature. Source: NASA WMAP website ([http://map.gsfc.nasa.gov/mission/observatory\\_freq.html](http://map.gsfc.nasa.gov/mission/observatory_freq.html))

are used to subtract Galactic emission and **point sources**. Highly contaminated regions are excluded for generating the maps and different component separation methods are developed to achieve the primary goal of CMB experiments which is to provide a clean map of the CMB suitable for a cosmological analysis.

Generating the WMAP CMB maps, [Hinshaw et al. \(2007\)](#) developed the **Internal Linear Combination (ILC)** method which linearly combines the multifrequency sky maps using weighted coefficients that approximately cancel the Galactic signal while preserving the CMB signal. The weights are determined by minimizing the variance of the measured temperatures with the additional constraint that the sum of the weights is equal to 1. To account for the spatial dependence of the various foreground components across the sky and in particular in the Galactic plane, the sky is divided into 12 regions and the weights are computed for each of these 12 different regions. If calculated in pixel space, the ILC map does not take into account the fact that noise dominates at high  $\ell$ -modes (small scales), while foreground emission dominates on low  $\ell$  (large scales). Calculated in harmonic space, the fact that noise is the dominant source at high Galactic latitude, while foreground signals dominate at low Galactic latitude would not be incorporated. With the aim of generating CMB maps that show even weaker contamination by Galactic and extra-Galactic foreground emissions or instrumental noise, [Delabrouille et al. \(2009\)](#) and [Basak & Delabrouille \(2012\)](#) developed a new method for generating ILC maps based on spherical wavelets called needlets. Needlets allow for a localized filtering in both pixel and harmonic space and hence generate weights varied over the sky and the full multipole range. The **Needlet-based Internal Linear Combination (NILC)** can therefore overcome the problems of the original ILC maps. However, in consideration of certain limits the full-sky ILC and NILC maps are both suitable for a cosmological analysis.

For the new Planck data, even more component separation methods have been developed

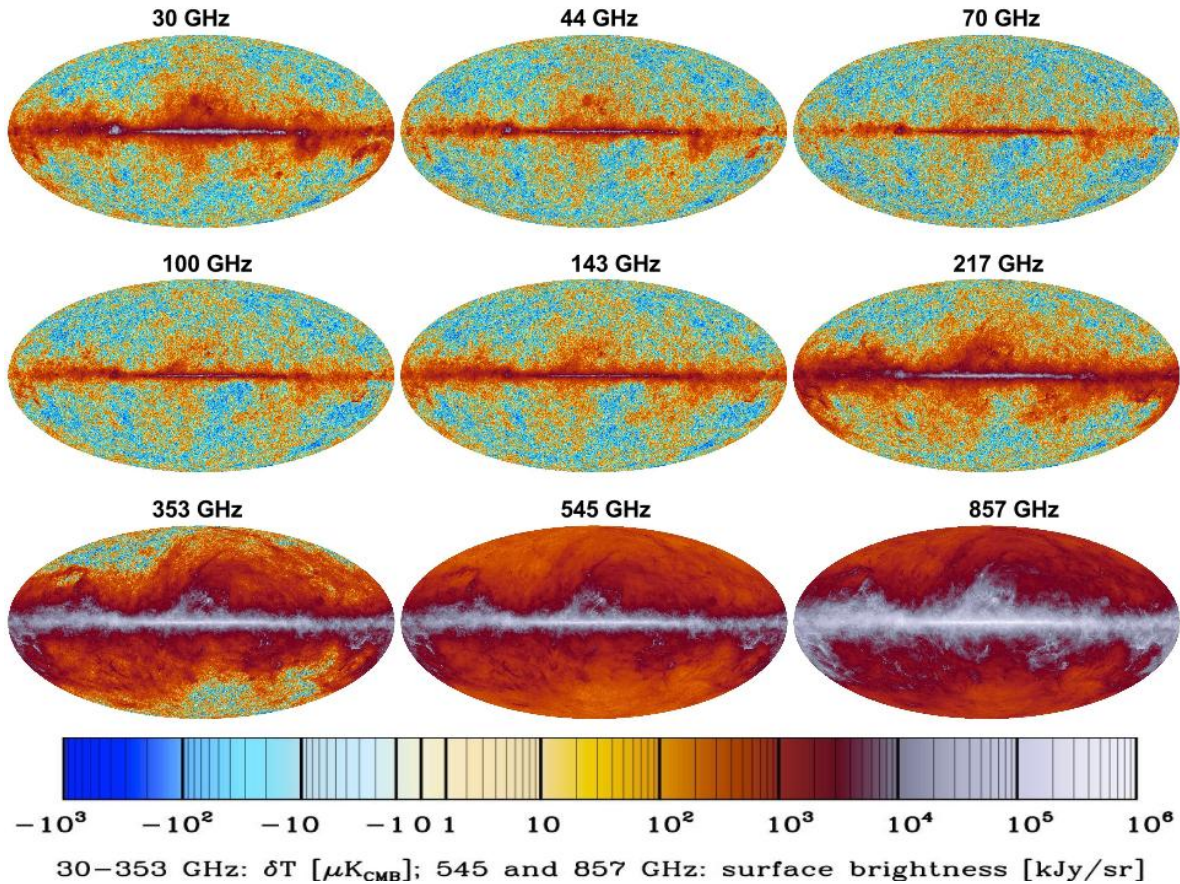


Figure 1.11: The nine Planck frequency maps show the broad frequency response of the individual channels. The color scale has been tailored to show the full dynamic range of the maps. Source: [Planck Collaboration et al. \(2014a\)](#).

and evaluated. For an overview see [Leach et al. \(2008\)](#). For the first Planck data release four well-performing methods out of 12 examples ([Planck Collaboration et al. 2014b](#)) have been used for cosmological studies on statistics and isotropy ([Planck Collaboration et al. 2014g](#)), primordial non-Gaussianity ([Planck Collaboration et al. 2014h](#)), gravitational lensing ([Planck Collaboration et al. 2014f](#)), the ISW effect ([Planck Collaboration et al. 2014c](#)), background geometry and topology ([Planck Collaboration et al. 2014j](#)), searches for cosmic strings and other defects ([Planck Collaboration et al. 2014i](#)) and the CMB power spectrum ([Planck Collaboration et al. 2014d](#)). The resulting foreground-reduced maps are shown in Figure 1.12.

The NILC map in needlet-space makes minimal assumptions concerning the foregrounds. The pre-processing steps include the subtraction/masking of point sources. If a point source is masked, the remaining hole is inpainted by a simple diffusive filling process. A second non-parametric method, that does basically not use foreground models, is the method of **Spectral Estimation Via Expectation Maximization (SEVEM)** in pixel space ([Martínez-González et al. 2003](#); [Fernández-Cobos et al. 2012](#)). In this approach the foreground templates are constructed from the lowest and highest frequency channels of the experiment without considering external data sets. The **Commander-Ruler** algorithm estimates the joint foreground-CMB posterior distribution by Bayesian Gibbs Sampling ([Eriksen et al. 2008](#)) in

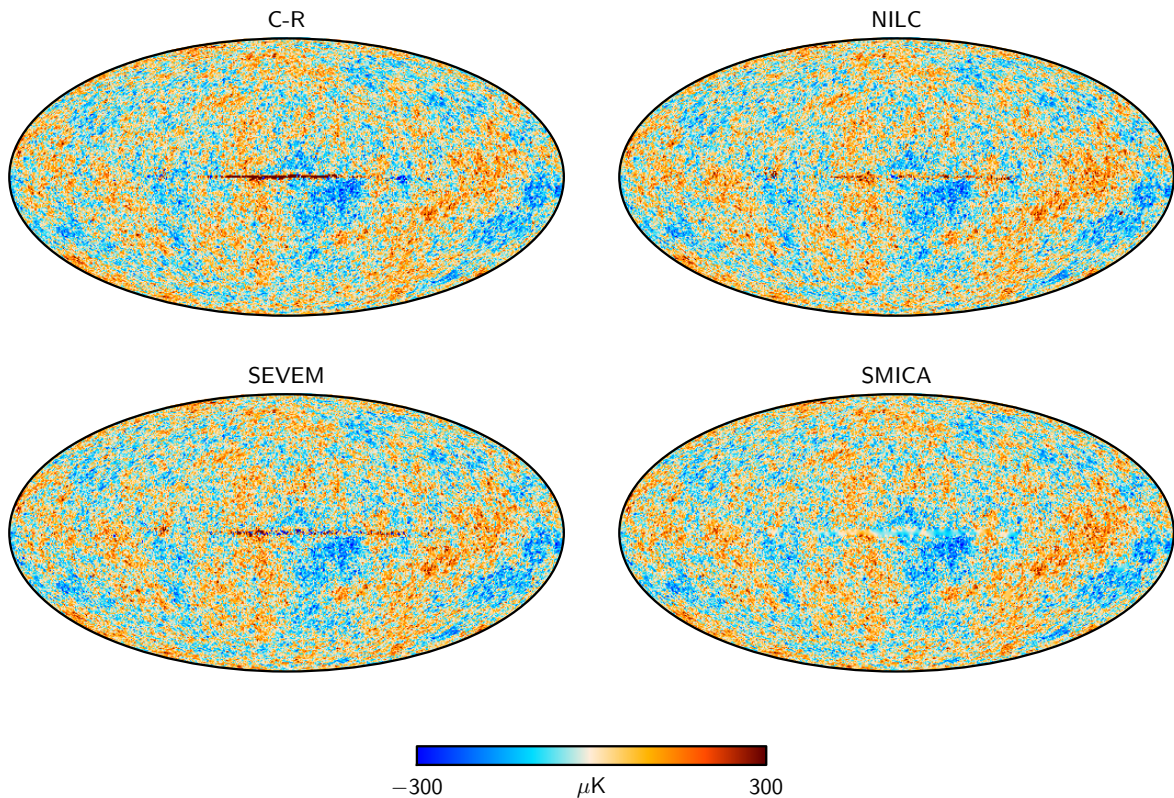


Figure 1.12: Foreground-cleaned Planck CMB maps derived by Commander-Ruler, NILC, SEVEM and SMICA. Note that the SMICA map has been filled in smoothly inside a 3% Galactic mask. Source: [Planck Collaboration et al. \(2014b\)](#)

pixel space. This method needs a parametric model of the foreground signal and assumes identical beam responses at each frequency band. It is therefore limited to the lowest angular resolution of the given data set. The **Spectral Matching Independent Component Analysis (SMICA)** ([Delabrouille et al. 2003](#); [Cardoso et al. 2008](#)) uses a CMB-oriented parametric approach that fits the amplitude and spectral parameters of the CMB and the foregrounds in the harmonic domain. The pre-processing steps here resemble the steps for the NILC map making. Most inpainted areas lie in the Galactic plane, but a few bright regions like the Large Magellanic Cloud are included as well.

### 1.2.3 Anomalies in the CMB sky

The data release of the first WMAP maps in 2003 ([Bennett et al. 2003](#)) opened a unique window to the physics of the early Universe and enabled tests of the standard inflationary picture (e.g. [Peiris et al. 2003](#); [Komatsu et al. 2003](#)). Consequently, it led to systematic checks on the predicted isotropy and Gaussianity of the CMB by several independent research groups. The detection of different anomalies gave evidence for a **departure from either Gaussianity or statistical isotropy or both**. Many of these anomalies were confirmed by later WMAP data releases and by the latest Planck data ([Planck Collaboration et al. 2014g](#)). Therefore, the standard assumption of statistical isotropy and Gaussianity of the CMB has to be regarded as a paradigm.

A satisfactory explanation for a violation of statistical isotropy and a departure from Gaus-

sianity based on physically motivated models is still lacking. As stated in [Hinshaw et al. \(2007\)](#) the most compelling development in cosmological science would be introducing a new model that explains a number of cosmological phenomena (such as the behavior of the low- $\ell$  CMB modes or the nature of dark energy), while also making testable predictions for the experiments. Understanding the origin of CMB anomalies remains one of the most important tasks when studying the very early Universe.

A cosmological nature of the anomalies is definitely possible but in general four different classes of potential explanations have to be considered (see e.g. [Copi et al. 2010](#)):

- 1) faulty data analysis
- 2) instrumental/experimental systematics
- 3) astrophysical foregrounds
- 4) theoretical/cosmological justification

Of course, faulty data analysis is an imminent danger in every complex study. The detection methods in CMB data analysis are for sure ambitious due to the complexity of nonlinear data analysis. They are very different from each other and individually sensitive to different kinds of anomalies. However, most of the complex methods used for the check on anomalies have withstood the critics over the recent years. The fact that the CMB temperature anisotropies are the only information of the early Universe available to us makes it much harder to trust in the found results. A second data set of the early Universe such as the CMB polarization would be of great value.

The operation methods of the satellites clearly differ between the WMAP and the Planck mission as described in Chapter 1.2.1. The similarity of the detected anomalies in the different experiments though establishes the credibility of the results and restricts the danger of strong experimental systematics. [Liu & Li \(2011\)](#) for example have claimed that a timing error in the WMAP observational scan had induced artificial CMB anisotropy. They suggested that the WMAP quadrupole is not primordial in its origin, and arises from incorrect Doppler dipole subtraction because of incorrect satellite pointing. This was neither confirmed by e.g. [Roukema \(2010\)](#) and [Moss et al. \(2011\)](#) nor by the Planck results. To our knowledge there is no experimental systematic in WMAP or Planck that could have caused the detected anomalies.

The WMAP and Planck data maps are carefully reduced by the subtraction of known Galactic foregrounds and secondary anisotropies as SZ, ISW, and gravitational lensing (see Chapter 1.1.3). However, the correct subtraction remains sophisticated and is subject of ongoing research. We therefore cannot fully exclude a contamination even by known foregrounds, not to mention the possible influence of unknown foregrounds (see e.g. [Rassat & Starck 2013](#), for ISW induced foregrounds). However, in most studies a contamination by foregrounds is – depending on the angular scales of the anomalies though – more or less neglected.

The correlation of different anomalies is subject to discussion. The different anomalies might stem from different physical origins but could as well be identified as different implications of the same cosmology. If they emerge to be truly cosmological in nature some of them are seriously inconsistent with the predictions of standard cosmology. The significance of the detected anomalies usually lies in the 2 to  $3\sigma$  range. See also Chapter 7 for a discussion on the significance for the method of the surrogates. Therefore, the results are not ruling out statistical isotropy or Gaussianity for good but the findings are certainly peculiar. In the following, I will list the most important examples from a variety of anomalies.

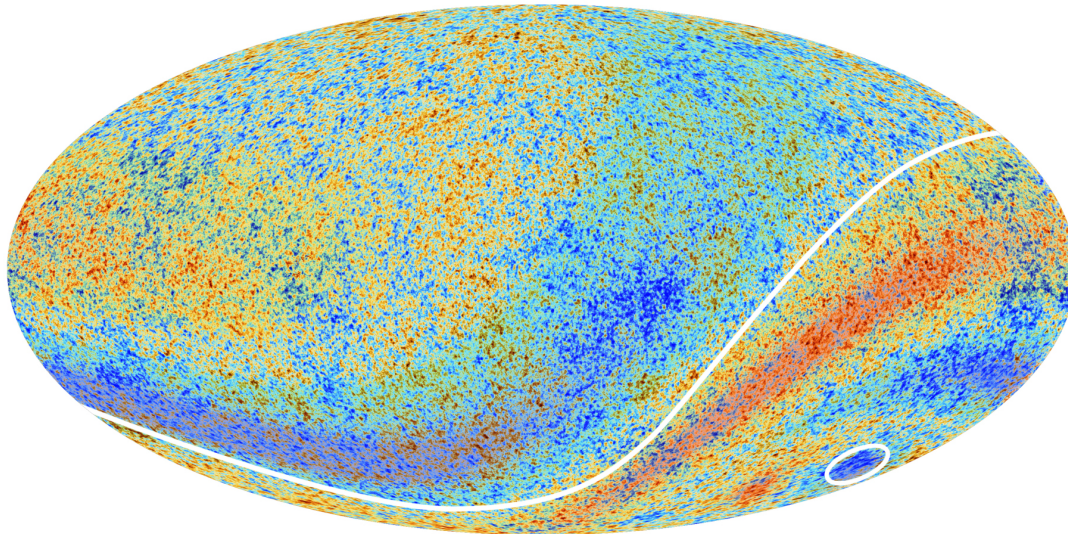


Figure 1.13: Planck data confirms an asymmetry in the average temperatures on opposite hemispheres of the sky (indicated by the curved line), with slightly higher average temperatures in the southern ecliptic hemisphere and slightly lower average temperatures in the northern ecliptic hemisphere. The cold spot, also detected with WMAP, is indicated by the circle. The anomalous regions have been enhanced with red and blue shading to make them more clearly visible. Source: ESA and the Planck Collaboration, ESA Planck website (<http://sci.esa.int/planck/51551-simple-but-challenging-the-universe-according-to-planck/>)

### Cold spot

Vielva et al. (2004) reported a non-Gaussian detection in the WMAP 1st-year data with a size of around  $10^\circ$  in the southern sky (Figure 1.13) using the spherical wavelet technique that has been shown to be very powerful for detecting non-Gaussianity in CMB data. A continuation of their work with the spherical Mexican hat wavelet (SMHW) and the non-Gaussian skewness and kurtosis estimators identified the source of the non-Gaussian detection as an extremely cold and big spot at  $b = -57^\circ$ ,  $l = 209^\circ$  (see also Mukherjee & Wang 2004; Cruz et al. 2005). In all likelihood, systematics or Galactic foregrounds are not responsible. The shape of the cold spot is found to be almost circular and Gaussian simulations of the CMB have a probability of less than one per cent to contain such a big cold spot (Cruz et al. 2006). Follow-up studies with different analysis techniques and also later WMAP data releases as well as the Planck data confirmed this detection (McEwen et al. 2005; Cayón et al. 2005; R ath et al. 2007; Cruz et al. 2007a; Vielva et al. 2007; Rossmannith et al. 2009; Planck Collaboration et al. 2014g). New methods, as for example the Kolmogorov maps measuring the degree of randomness in the CMB, confirmed the detected cold spot and revealed even more detections of anomalous spots in the sky (e.g. Gurzadyan et al. 2009). In addition to the cold spot, Pietrobon et al. (2008) found evidence for anomalously hot spots in the WMAP sky using spherical needlets. The hot spots contribute to other multipoles of the CMB power spectrum than the cold spot does. Hou et al. (2009) confirmed these results with an extensive frequentist analysis.

Naselsky et al. (2010) inferred that the mystery of the cold spot directly reflects the pecu-

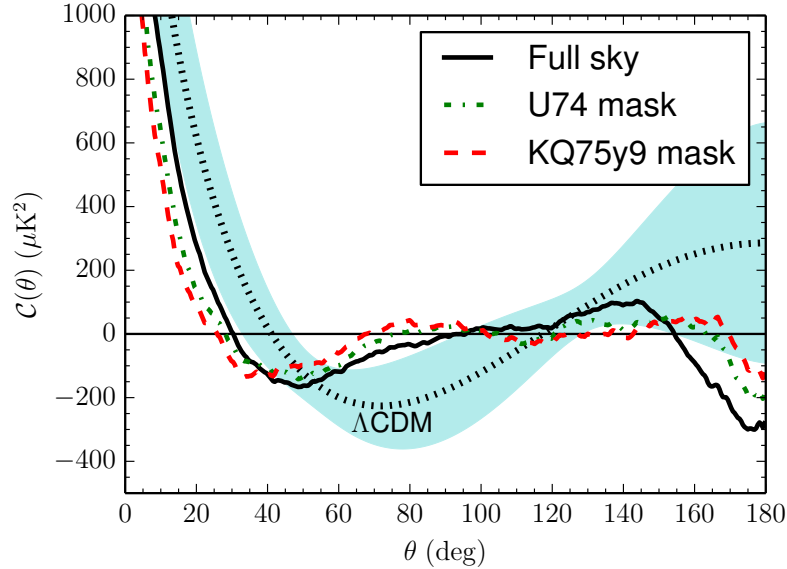


Figure 1.14: Near vanishing of two-point angular correlation function at angular scales between  $60^\circ - 120^\circ$ , from the inpainted Planck SMICA map. Source: Copi et al. (2013a)

liarities of low multipoles of the CMB signal (see next paragraph) rather than a single local defect. An extremely large void, extremely unlikely in  $\Lambda$ CDM cosmology, and a cosmic texture, a remnant of a phase transition in the early Universe holding important implications for the study of high-energy theories, are possible explanations for the cold spot (Cruz et al. 2007b, 2008; Bridges et al. 2008; Feeney et al. 2013; Kovetz & Kamionkowski 2013).

### Multipole anomalies and alignment

A multipole expansion with a series of spherical harmonics is most useful to describe the spherical CMB sky. The multipole moment  $a_{\ell m}$  with  $\ell = 1$  corresponds to the CMB dipole. Its orientation tells us about the solar system's motion through the Universe. Estimates of the CMB quadrupole, where  $\ell = 2$ , require a very careful foreground reduction since they are very sensitive to foreground contamination from the Galactic plane. However, with a cut applied to the sky masking out the Galactic plane residuals, the foreground contamination of the quadrupole is determined to be insignificant (Gold et al. 2011; Jarosik et al. 2011). The first data from the COBE-DMR experiment already suggested that the amplitude of the quadrupole power of the maps is unexpectedly low compared to best-fit models (e.g. Hinshaw et al. 1996; Bennett et al. 1996). This **lack of power** was confirmed by WMAP data (Bennett et al. 2003; Spergel et al. 2003; de Oliveira-Costa et al. 2004; Copi et al. 2009) and with the Planck maps (Planck Collaboration et al. 2014g). The suppression is seen in both, the correlation function which lacks in a correlated signal on angular **scales larger than  $60^\circ$**  (e.g. Copi et al. 2007, 2013a), shown in Figure 1.14, and it is seen in the behavior of the low-order multipoles with  $\ell = 2, 3, 4, 5$ . It is claimed to be inconsistent with statistical isotropy and Gaussianity. The significance of these results is less clear. Others, as Bond et al. (1998) with COBE-DMR data and Land & Magueijo (2005a) with WMAP data, interpreted the low quadrupole as statistically not significant and as consistent with cosmic variance uncertainties and the best-fit  $\Lambda$ CDM model.

Tegmark et al. (2003) and de Oliveira-Costa et al. (2004) first argued that the octopole ( $\ell = 3$ ) is anomalous by being very planar and that the **quadrupole and octopole planes** are aligned with each other. They tested different cosmic topologies but did not find an explanation for the anomaly. The usual representation of spherical CMB data by the spherical harmonic basis is complemented by the multipole vector framework established by Copi et al. (2004) who also indicated a strong violation of statistical isotropy and Gaussianity. Multipole vectors enable well suited tests of orientation, planarity and alignments of the CMB anisotropies. Schwarz et al. (2004) and Copi et al. (2006, 2007) investigated the quadrupole-octopole shape and orientation in WMAP 1st- and 3-year data using the multipole vector framework. In the combined quadrupole and octopole map, they found that the one quadrupole and three octopole planes are aligned within about  $1^\circ$ , that the planes are orthogonal to the ecliptic, the normals to these four planes are aligned with the direction of the CMB dipole, and that the ecliptic separates a hot and a cold extrema and the three strong extrema from the three weak extrema of the map (Figure 1.15). Furthermore, they found unusually low angular correlations at the largest angular scales. These results are inconsistent with Gaussian random, statistically isotropic skies. An analysis of a cut sky by Bielewicz et al. (2005) revealed that the anomalies are robust with respect to sky cut. The  $\ell$ -alignment was dubbed the **Axis of Evil** (AoE) by Land & Magueijo (2005a) who improved their previous statistics and compared a Bayesian and a Frequentist approach for WMAP 3-year data which resulted in lower significances (Land & Magueijo 2007).

For their 7-year data release the WMAP team explicitly discussed several CMB anomalies in Bennett et al. (2011). They argued that for the alignment of low multipoles the integrated Sachs-Wolfe effect could be held responsible and blamed the missing power on large angular scales (e.g. Copi et al. 2007) on posterior statistical bias in the choice of statistics. Copi et al. (2010) provided a review on the large-angle anomalies in the CMB and claimed that the arguments from the WMAP team offered no convincing explanations of the observed anomalies and produced new problems on the way. They stated, that at best they (the WMAP team) have replaced one set of anomalies by another.

A legitimate question is whether the lack of angular correlation on scales larger than  $60^\circ$  and the alignment of the quadrupole and octopole are correlated with each other. Rakić & Schwarz (2007) on a full sky and Sarkar et al. (2011) on a cut sky demonstrated the absence of such a correlation between these two different features. The WMAP 9-year data release and the Planck data revealed the same multipole alignment. However, an increasing misalignment between quadrupole and octopole of  $3^\circ$  and  $9^\circ - 13^\circ$ , respectively, is also suggested.

The relations between the quadrupole, the octopole and the ecliptic have long been known. What remains unestablished is whether these are signatures of a non-trivial cosmic topology or coincidences or experimental artifacts. When people have first detected the unexpected alignment of the quadrupole and the octopole and their perpendicular alignment with the direction of motion of the Solar system they argued that these results strongly suggest either an additional, unexplained foreground contamination of the microwave background or an unexpected systematic error in the WMAP maps. As stated in Copi et al. (2013a): “After twenty years, we still await a satisfactory explanation.” Other ideas are that the multipole anomalies might result from anisotropic expansion (Jaffe et al. 2005), intrinsic cosmic inhomogeneity (Moffat 2005) or spontaneous isotropy breaking (Gordon et al. 2005). Inoue & Silk (2006, 2007) hold local voids and their asymmetric distribution around the sky responsible for the cold spot as well as for the planarity of the octopole, for the alignment between the quadrupole and the octopole and for the north-south power asymmetry (explained below). Rakić et al. (2006)

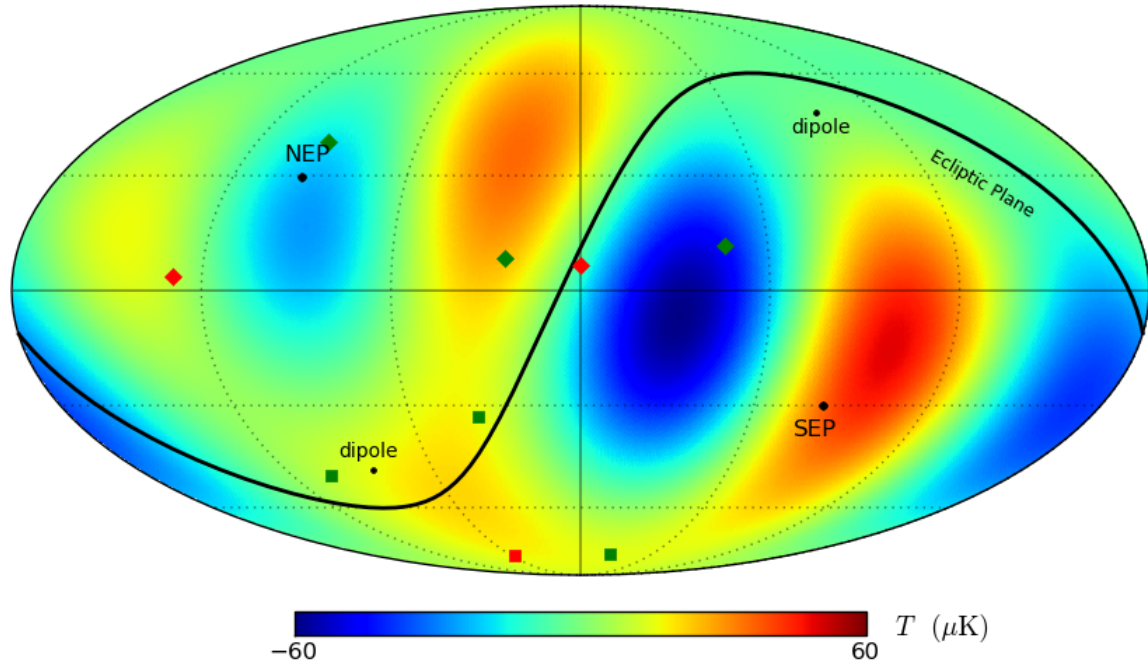


Figure 1.15: Quadrupole and octopole ( $l = 2$  and  $3$ ) temperature anisotropy of the WMAP 3-year sky map in Galactic coordinates, shown with respect to the ecliptic plane, the northern and southern ecliptic poles (NEP and SEP) and the CMB dipole. The four normals (solid squares) to the planes defined by vectors that describe the quadrupole and octopole temperature anisotropy are shown as well; one normal is defined by the quadrupole (red square) and three by the octopole (green squares). Note that three out of four normals lie very close to the dipole direction. Source: Copi et al. (2010)

studied the contribution of the local Rees-Sciama effect on the detected anomalies and found alignments among low multipoles, but concluded that they do not agree with the type of correlations revealed by the other data. Land & Magueijo (2005b) found that the detected preferred axis is associated with positive (even) mirror parity and according to Rassat & Starck (2013), removing the ISW effect reduces the significance of the Axis of Evil statistic and even/odd mirror parity in WMAP data.

### Parity asymmetry

The examination of CMB properties under parity transformations yields further insight into the nature of the topology of the Universe. Given that the Universe is homogeneous and isotropic, a cosmological signal should neither be exactly symmetric nor asymmetric but random in its angular distribution on the sky. Several authors studied the parity properties of the large angle CMB considering two types of parity transformations: **mirror reflections** and **point reflections**. Mirror reflection parity is related to the emergence of a preferred axis of the Universe. Point-parity handedness accounts for focal points of space symmetry and implies almost certainly a high level of galactic contamination. Land & Magueijo (2005b) did not find

significant odd point-parity, but claimed that the detected preferred axis of evil is associated with positive (even  $\ell$ ) mirror parity. Kim & Naselsky (2010*a,b*) found a preference of odd point-parity (odd  $\ell$ ) in WMAP data and suggested that the low quadrupole power is associated with parity asymmetry. They furthermore claimed that the odd-parity preference at low multipoles is in fact a phenomenological origin of the lack of large-angle correlation. Ben-David et al. (2012) reported a significant detection of odd mirror parity in WMAP data, and also found even parity in a perpendicular direction, although with a low significance.

### General non-Gaussianities

While some of the symmetry anomalies, described in this chapter, are detected in the linear part of the data, general non-Gaussianities manifest themselves in the nonlinear regime. Deviations from the random phase hypothesis were already detected in the WMAP 1st-year data release through a phase-mapping technique by Chiang et al. (2003). A study based on the three Minkowski functionals and the length of the skeleton calculated for WMAP 1st-year data also revealed a deviation from Gaussianity and a north-south power asymmetry in the genus statistic (Eriksen et al. 2004*b*). This study confirmed the results of Park (2004) who also used the genus statistic. The genus statistic  $g$  can be defined in terms of the Euler characteristic  $M_2$ , which is calculated in this work, via  $M_2 = 2 - 2g$ . Vielva et al. (2004) reported a non-Gaussian detection as well as north-south asymmetry using spherical wavelets in their analysis. They carefully studied foreground contamination and systematic effects but excluded these as causes for the detected non-Gaussianity. However, Slosar & Seljak (2004) held foreground contamination responsible for WMAP anomalies. Bernui et al. (2007) excluded a Gaussian distribution for WMAP 3-year data at the 99% confidence level. The application of the needlet formalism to WMAP 5-year data confirmed earlier findings of north-south asymmetries and found the bispectrum to be more significant on large scales and in the more co-linear configurations and in the “squeezed” configurations (Pietrobon et al. 2010). These anomalies do not appear to affect the estimate of the nonlinear non-Gaussianity parameter  $f_{\text{NL}}$ . This is similar to the results in Chapter 4 where it is concluded that the parametrization of non-Gaussianity by  $f_{\text{NL}}$  cannot account for the detected deviations from Gaussianity.

### Power asymmetry

Great attention has been devoted to the hemispherical power asymmetry of the CMB as detected in COBE-DMR, WMAP and Planck data. Measurements of the power spectrum in the northern and southern ecliptic hemisphere have revealed a statistically significant lack of power in a region associated with the north ecliptic pole. The asymmetry has been originally found in WMAP 1st-year data and appears to lay on an axis nearly orthogonal to the ecliptic plane (Eriksen et al. 2004*a*; Hansen et al. 2004). It is inconsistent with the statistical isotropy of the  $\Lambda$ CDM concordance model and also questions the Gaussianity of the data. It has been confirmed in the WMAP 3- and 5-year release (Eriksen et al. 2007; Hansen et al. 2007; Hoftuft et al. 2009). Hansen et al. (2009) found that the power asymmetry is not only evident for low multipoles of  $\ell = 2 - 40$  but also extends to much smaller scales in the full multipole range of  $\ell = 2 - 600$ . Moreover, in Bernui (2008) it was also shown that this hemispherical asymmetry is unlikely due to systematics or foreground contaminants, because it is present in single-frequency, multifrequency, and cleaned ILC-type CMB maps. The dipolar power asymmetry was found to persist in the Planck data to much smaller angular scales, and can be described in the low- $\ell$  regime by a phenomenological dipole modulation model (Planck Collaboration et al. 2014*g*). The deficit in power in one hemisphere may be related to the parity violation

and phase correlations also detected in the data. No significant asymmetry on the polarized spectra is detected analyzing WMAP 7-year polarization maps (Paci et al. 2013). It remains to be seen whether Planck polarization data with higher sensitivity will reveal signatures of dipole modulations.

### Phase correlations/non-Gaussianities

Second-order-only measurements as the power spectrum are blind to the distribution of the Fourier phases and are throwing away the fine details of cosmic structure. The power spectrum contains the full information of the underlying distribution only if this distribution is Gaussian. The standard assumption is that primordial density fluctuations constitute a statistically homogeneous and isotropic Gaussian random field, which then exhibits phases that are uniformly random on the unit circle. A non-Gaussian signal, whether primordial or not, leads to highly **coupled Fourier phases** in the nonlinear regime of the data. To describe the data it is then necessary to analyze the higher-order correlation functions. Coles & Chiang (2001) have compared a number of methods that can be used to test the standard paradigm of random-phase fluctuations, and even provide direct tests for the presence of initial non-Gaussianity. They showed that the bispectrum measures the phase coupling induced by quadratic nonlinearities. Coles et al. (2004) analyzed COBE DMR and WMAP CMB maps with a method that checks for the uniformity of the distribution of the Fourier phases based on the Kuiper statistic which is also described in Chapter 2.4.1. They found departures from uniformity in both experiments. However, they interpreted the results as Galactic contamination and experimental systematics rather than primordial non-Gaussianity. Another method, introduced by Naselsky et al. (2005), based on the trigonometric moments of phases, also demonstrated the existence of non-Gaussian signal among different WMAP 1st-year maps derived with different methods of foreground cleaning. The phases of spherical harmonic modes from WMAP 3-year data were tested for uniformity, randomness, and the correlation with phases of the foreground maps (Chiang et al. 2007). An alignment between the CMB temperature pattern and Galactic foreground morphology was detected. The authors pointed out that this alignment could also just be coincidental.

As pointed out in this work, studies using the methods of the surrogates with the aid of scaling indices and Minkowski functionals based on the WMAP 3-, 5- and 7-year data (Räth et al. 2009; Rossmannith et al. 2012; Modest et al. 2013) showed significant evidence for intrinsic phase correlations at the low- $\ell$  values in the CMB. The signal was demonstrated to be robust with respect to the WMAP data release, to the component separation methods and to the selected test statistics. An application of these methods to the Planck component separated data sets also reveals phase correlations at low  $\ell$  (Planck Collaboration et al. 2014g).



## Chapter 2

# Methods for testing the Gaussian hypothesis and the cosmological principle

According to the standard inflationary theory, the initial fluctuations of the Universe obey Gaussian statistics, i.e. the  $a_{\ell m}$  harmonic coefficients are Gaussian distributed. This implies a Gaussian distribution of the temperature fluctuations as well as the non-existence of phase correlations in harmonic space. Testing these predictions, a determination of primordial non-Gaussianity (NG) would rule out single field slow-roll inflation and would help to constrain parameters of alternative scenarios as outlined in Chapter 1.1.2.

Research in this area of cosmology has to deal with the major problem that NG is not specifically defined. It can be anything except Gaussianity. This introduces a variety of stumbling blocks: The number of possible investigation methods is almost infinite. The methods chosen to analyze the data are naturally at risk of depending on the specific characteristics of the data sets. They share the difficulty of adequately accounting for a posteriori bias in the analysis (Bunn 2010; Bennett et al. 2011). Even if attention is paid to preselection effects on the data, and a posteriori choices are avoided as far as possible, many uncertainties remain. Moreover, there is also the danger that statistical flukes in the data are mistaken for the detection of non-Gaussianity. Not to mention that a non-detection of an anomaly is neither a proof of its non-existence nor does it prove Gaussianity.

An anisotropic behavior of the data has been repeatedly verified in terms of hemispherical asymmetries in real space. If anything, these detections strongly challenge the cosmological principle of statistical isotropy and homogeneity. A test for non-Gaussianity is not necessarily a test for the cosmological principle and vice versa, since non-Gaussian signals observed in harmonic space are not necessarily localized in real space, and therefore do not automatically allow for any conclusions on the isotropy of space. However, if an analysis that is performed in harmonic space as well as in real space, comparing different patches of the sky with each other, detects NG, it can enable conclusions on the isotropy of space.

A primary goal of observational cosmology is to understand the physics of the predicted epoch of inflation. This work will test the validity of the Gaussian and isotropic hypothesis of the standard model. The technical approach is fully data driven and model-independent, and the approach is simple in a way: If the Gaussian prediction holds, the harmonic-space phases must be uncorrelated. With the detection of primordially correlated phases the standard model

would be ruled out.

If the Gaussian hypothesis could be excluded via data analysis, it would stimulate research on alternative cosmological scenarios. The qualification and quantification of non-Gaussianity would allow for a parametrization of NG and would enable to distinguish between different cosmological models. In the near future, polarization data will be used as a second independent sample when testing for the Gaussian hypothesis (Komatsu et al. 2011; Munshi et al. 2011; Vielva et al. 2011).

## 2.1 Representation of the data

The basic observable of the CMB is its intensity as a function of frequency and direction on the sky  $\mathbf{x}$ . The CMB temperature map originally presents temperature deviations  $\Delta T(\mathbf{x}) = T(\mathbf{x}) - \langle T(\mathbf{x}) \rangle$  from the average temperature, where  $\mathbf{x}$  is representing the direction in which the temperature is measured. Since the microwave radiation reaches us from every direction in the sky, the full-sky CMB temperature anisotropy map of the celestial sphere  $\mathbb{S}^2$  with  $\Delta T/T(\mathbf{x}) \equiv \Delta T/T(\theta, \phi)$  ( $\theta$  being the Galactic latitude and  $\phi$  being the azimuth) can be expressed via a multipole-decomposition with complex valued orthonormal spherical harmonics  $Y_{\ell m} : \mathbb{S}^2 \Rightarrow \mathbb{C}$  as

$$\Delta T/T(\theta, \phi) = \sum_{l=0}^{\infty} \sum_{m=-l}^l a_{\ell m} Y_{\ell m}(\theta, \phi) \quad (2.1)$$

with the complex spherical harmonic coefficients

$$a_{\ell m} = \int d\mathbf{n} T(\mathbf{n}) Y_{\ell m}^*(\mathbf{n}) \quad (2.2)$$

where  $\mathbf{n}$  is the unit direction vector,  $a_{\ell m} = |a_{\ell m}| e^{i\varphi_{\ell m}}$  in polar coordinates and  $\ell \geq 0$ ,  $-l \leq m \leq l$ . The phases  $\varphi_{\ell m}$  can be computed as  $\varphi_{\ell m} = \arctan(\text{Im}(a_{\ell m})/\text{Re}(a_{\ell m}))$ . The index  $m$  describes the angular orientation of the spherical harmonic, while the multipole  $\ell$  describes its characteristic angular size. The bigger  $\ell$ , the smaller the scale. The resolution of the experiment constrains the original term  $\ell = \infty$  to some maximum number  $\ell_{\max}$ . For WMAP, most maps hold  $\ell_{\max} = 1024$ . For Planck data with a higher resolution, the CMB maps are constrained by  $\ell_{\max} = 2048$ . The number of summands in equation (2.1) is  $(\ell_{\max} + 1)^2$ .

The linear properties of the underlying density field are contained in the absolute values  $|a_{\ell m}|$ , whereas all higher-order correlations (HOCs) - if existent - are encoded in the phases  $\varphi_{\ell m}$  and the correlations among them. Equivalently, higher-order n-point correlation functions can account for the HOCs as well. The phases are highly sensitive to the morphology of the temperature pattern and the phase information can also be used to diagnose departures from statistical homogeneity over the celestial sphere.

If the spherical harmonic coefficients are independent Gaussian random variables their probability density is

$$P(a_{\ell m}) da_{\ell m} = \frac{1}{\sqrt{2\pi C_{\ell}}} e^{-\frac{a_{\ell m}^2}{2C_{\ell}}} da_{\ell m} \quad (2.3)$$

(e.g. Rubakov & Vlasov (2012)) and the orthonormality relation

$$\langle a_{\ell m} a_{\ell' m'}^* \rangle = \delta_{\ell\ell'} \delta_{mm'} C_{\ell} \quad (2.4)$$

holds, where  $C_{\ell}$  is the angular power spectrum and  $\delta$  is the Kronecker delta. In this case, the amplitude  $|a_{\ell m}|$  would be Rayleigh-distributed and the phase  $\varphi_{\ell m}$  would be independent and

identically distributed (i.i.d.) and follow a uniform distribution in the interval  $[-\pi, \pi]$ . The temperature values themselves would be normally distributed as well. The measured angular power spectrum  $C_\ell^{\text{obs}}$  depends on the  $a_{\ell m}$  coefficients by

$$C_\ell^{\text{obs}} = \frac{1}{2\ell + 1} \sum_{m=-\ell}^{\ell} |a_{\ell m}|^2, \quad (2.5)$$

where  $\langle C_\ell^{\text{obs}} \rangle = C_\ell$ . In case the CMB variables  $a_{\ell m}$  are independent and Gaussian distributed and their phases are therefore i.i.d. and consequentially uncorrelated, it is adequate (Komatsu et al. (2009b) and references therein) to only investigate the linear properties of the data described by the power spectrum  $C_\ell$ . In this work, I focus on the nonlinear information and test for possible phase correlations of  $\varphi_{\ell m}$  in the data, which I define as non-Gaussianities of the CMB. This is done by checking if the requirements of Gaussianity and randomness from above are fulfilled.

As described in Chapter 1.2.1, the temperature maps for the WMAP and Planck missions are available as pixelized data maps  $\Delta T(\mathbf{x}_i)$ ,  $i = 1, \dots, N_{\text{pix}}$ , where  $N_{\text{pix}}$  denotes the number of pixels and is related to the chosen HEALPix resolution. The spherical harmonics representation with  $\mathbb{S}^2 \Rightarrow \mathbb{C}$  is similar to the Fourier series with  $\mathbb{S}^1 \Rightarrow \mathbb{C}$ . Hence, the spherical harmonic coefficients are the analogues of the Fourier coefficients. In this work, I will equivalently use *Fourier coefficients* and *Fourier phases* meaning spherical harmonic coefficients and their phases, respectively.

## 2.2 Method of the surrogates

The method of the surrogates is one of the key concepts of nonlinear data analysis and originates from the field of time series analysis (Theiler et al. 1992). It enables model-independent tests on weak nonlinearities in data sets. The idea behind is to define some linear process in a given data set as the null hypothesis and to construct surrogate maps from the data set, which mimic the linear properties of the original data. If discriminating statistics, sensitive to nonlinearities, observe significant differences between the original data set and the surrogates, then the null hypothesis is rejected and nonlinearity is detected. The method of the surrogates can be applied to complex systems in general, for example also to the climate, stock-market or heart beat variability as pointed out in Bunde et al. (2002). It was introduced into cosmology by Pompilio et al. (1995) analyzing non-Gaussian effects of cosmic strings on the CMB with a multifractal formalism and by R ath et al. (2002) and R ath & Schuecker (2003) analyzing the large-scale structure of the Universe and the CMB. The method of the surrogates was continuously developed (Schreiber & Schmitz 1996; Schreiber 1998; R ath et al. 2012) and has found numerous applications in a huge variety of research fields ranging from geophysical and physiological time series analysis (Schreiber & Schmitz 2000) to econophysics on the stock market (Wang et al. 2008), astrophysics (Gliozzi et al. 2010) and cosmology (R ath et al. 2009, 2011; Rossmanith et al. 2012; Modest et al. 2013). Its applications to cosmology are partly represented in this work.

The data set of the CMB is a complex system which is perfectly well suited for being studied with the method of the surrogates. A null hypothesis of the CMB is the Gaussianity of the spherical harmonic coefficients which implies random Fourier phases. If the CMB harmonic phases are randomized while generating surrogate maps, these surrogates will only contain the linear properties of the data. The surrogates allow to test for the given null hypothesis of a Gaussian CMB. For this check, it is necessary to apply image analysis techniques to the data

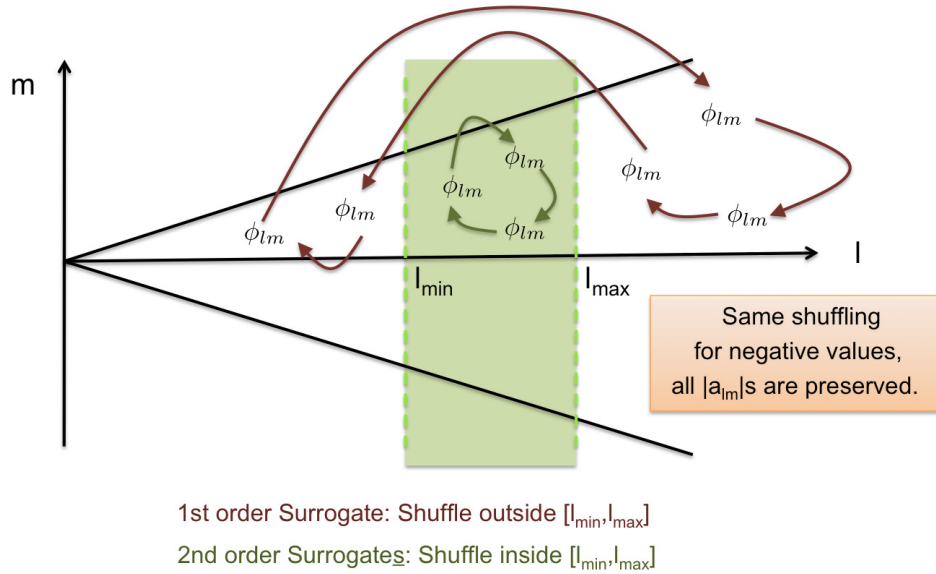


Figure 2.1: Sketch of the surrogatization scheme generating first and second-order surrogates for a given range of interest with  $\Delta\ell = [l_{\min}, l_{\max}]$ .

set that are sensitive to higher-order correlations. I make use of the Minkowski functionals and the scaling indices in this work which I explain in more details in Chapter 2.3.

### 2.2.1 Complete sky

To constrain possible phase correlations of the Fourier phases of the cosmic microwave background, surrogate maps are generated as proposed in R ath & Schuecker (2003). Possible phase correlations in the data are destroyed by applying a shuffling scheme to the phases. To test for the scale-dependence of non-Gaussianity this is done with a two-step procedure.

To prepare the CMB data for a test on the hypothesis of independent Fourier phases and to ensure that the results will not be falsified, it is necessary to exclude data artifacts due to experimental constraints and data outliers that do not follow the assumed probability distribution as described in Chapter 2.1. The data has to meet the following two requirements before generating the surrogate maps: The temperature distribution is Gaussian and the set of phases is uniformly distributed in the interval  $[-\pi, \pi]$ . To fulfill these conditions two preprocessing steps are performed. First, the almost Gaussian distributed temperature values  $T(\mathbf{x})$  of the original map in real space are replaced by an exact Gaussian/normal distribution  $\mathcal{N}$  in a rank-ordered way, i.e. the lowest value of the original distribution is replaced with the lowest value of the Gaussian distribution etc., so that

$$T_{\text{new}}(\mathbf{x}_i) = D^{(k)} \quad (2.6)$$

is obtained, with  $D(\mathbf{x}) = \mathcal{N}(\mu, \sigma^2)$  and  $\mathcal{N}(\mu, \sigma^2)$  being the normal distribution with the expected value  $\mu$  and the variance  $\sigma^2$ ,  $i = 1, \dots, N_{\text{pix}}$ .  $k$  characterizes the position of the temperature values after rank ordering of  $T_{\text{old}}(\mathbf{x}_i)$  with  $T_{\text{old}}^{(k=1)} < T_{\text{old}}^{(k=2)} < \dots < T_{\text{old}}^{(k=N_{\text{pix}})}$ . The real-space temperature maps are then transformed into Fourier phase space via a multipole-decomposition to enable the calculation of the phases.

Second, to guarantee that the Fourier phases  $\varphi_{\ell m} = \varphi(i_{\ell m})$  are identically distributed the phases are remapped onto a set of uniformly distributed ones with a similar rank ordering, so

that

$$\varphi_{\text{new}} = D^{(k)} \quad (2.7)$$

with  $D = \mathcal{U}([-\pi, \pi])$  and  $\mathcal{U}([-\pi, \pi])$  being the uniform distribution between  $-\pi$  and  $\pi$ ,  $i = 1, \dots, i_{\text{max}}$ .  $k$  represents the position of the phases after rank ordering of  $\varphi_{\text{old}}(i)$  with  $\varphi_{\text{old}}^{(k=1)} < \varphi_{\text{old}}^{(k=2)} < \dots < \varphi_{\text{old}}^{(k=i_{\text{max}})}$ . No significant dependence on the specific Gaussian or uniform realization, respectively, was found in these preprocessing steps. The two steps are not affecting possible phase correlations in the data. The maps are additionally monopole and dipole reduced. Therefore, harmonic modes with  $\ell = 0, 1$  are not considered in the following shuffling procedures.

In the scale-dependent analysis, individual  $\ell$ -ranges can be tested for Gaussianity. The  $\ell$ -range can be chosen arbitrarily but throughout this work  $\Delta\ell_1 = [2, 20]$ ,  $\Delta\ell_{1b} = [2, 10]$  and  $\Delta\ell_2 = [120, 300]$  are of particular interest. The interval  $\Delta\ell_1$  covers the largest spatial scales of the CMB, while the first peak of the power spectrum lies in the interval  $\Delta\ell_2$ . The results in Chapter 3 will show that findings of an almost scale-independent analysis with a shuffling range  $\Delta\ell = [2, 1024]$  are only the superposition of signals from the analysis with  $\Delta\ell_1$  and  $\Delta\ell_2$  shuffling ranges (Räth et al. 2011). The scale-dependent surrogate maps that are later analyzed are obtained as follows: Firstly, a first-order surrogate map is generated, in which any correlation of phases  $\varphi_{\ell m}$  with  $\ell$  outside the particular  $\Delta\ell$ -range of interest is destroyed: The phases  $\varphi_{\ell m}$  with  $2 \leq \ell \leq 1024$  and  $\ell \notin \Delta\ell = [\ell_{\text{min}}, \ell_{\text{max}}]$ ,  $0 < m \leq \ell$ , are randomized through a shuffling procedure. In a second step,  $N$  ( $N = 500$  throughout this work unless stated otherwise) realizations of second-order surrogate maps are generated from the first-order surrogate map: The remaining phases  $\varphi_{\ell m}$  with  $\ell \in \Delta\ell = [\ell_{\text{min}}, \ell_{\text{max}}]$  are shuffled, while the already randomized phases in the first-order surrogate for the scales not under consideration are preserved. The surrogatization process is illustrated in Figure 2.1. Due to the real valued temperatures, the coefficients need to satisfy  $a_{l,m}^* = a_{l,-m}$ . Otherwise, the imaginary parts of the  $a_{\ell m}$  coefficients and spherical harmonics  $Y_{\ell m}$  would not cancel each other out. Phases  $\varphi_{\ell m}$  with a negative  $m$ -value are shuffled identically to the corresponding phases with  $m > 0$ . The phases of  $a_{l,0}$  coefficients are not shuffled. Note that the Gaussian properties of the maps, which are given by  $|a_{\ell m}|$ , are exactly preserved for all surrogate maps, i.e. the surrogate maps have exactly the same power spectrum as the original map.

The first-order surrogate preserves phase correlations in the  $\Delta\ell$  range, if they are present in the original maps. In the second-order surrogate map, where all phases have been randomized, all original correlations are completely destroyed. The statistical comparison of the two classes of surrogates by means of suitable measures will thus reveal possible higher-order correlations in the original maps on defined ranges of Fourier modes, and thus uncover signatures for deviations from Gaussianity. A special case of the shuffling procedure occurs if one chooses the  $\ell$ -range of  $[2, \ell_{\text{max}}]$ . Since this interval covers the complete range of available multipoles, generating a first-order surrogate map is redundant. In a comparison between the original map and the second-order surrogates, signatures cannot be traced back to individual modes but show deviations from Gaussianity on all scales in total. It is also possible to construct surrogates of first- and of second-order by replacing the respective Fourier phases with a set of random values. This replacement approach is tested in this work by constructing surrogates with replacing the original phases by a completely new set of uniform distributed values in the interval  $[-\pi, \pi]$ . With this approach new values are added to the data, instead of purely relying on the information given in the underlying data set. The comparison of the shuffling procedure with the replacement technique does not reveal any significant difference between

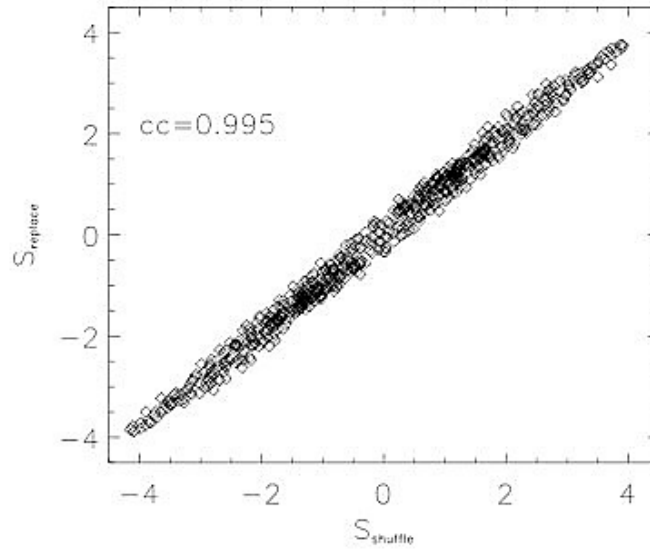


Figure 2.2: A comparison of the  $S$ -values after replacing and shuffling of the phases, respectively. The values show a cross correlation of 0.995. The comparison was done with the WMAP ILC map. Source: Christoph R ath, private communication

the two methods as can be seen in Figure 2.2 and also in Chapter 4.

Before analyzing the maps with different image analysis techniques, the  $a_{\ell m}$ s are converted back to temperature maps and their HEALPix resolution is decreased from  $N_{\text{side}}^{\text{WMAP}} = 512$  and  $N_{\text{side}}^{\text{Planck}} = 1024$  to  $N_{\text{side}} = 256$ . This is done to save computational time, and does not introduce any difficulties for the analysis of CMB data on the largest scales. Figure 2.3 shows examples of surrogates of the first and second order. The method of the surrogates requires a complete sphere to ensure that the spherical harmonics are orthogonal. An incomplete sphere can cause coupled phases and thus induce phase correlations in the map. For this reason full-sky maps, where the foreground influence of the Galactic plane is reduced to a minimum (e.g. ILC, NILC, SEVEM and SMICA of WMAP and/or Planck data), are well suited for the studies in this work as can be seen in Chapter 3 and 4. To enable advanced studies of foreground affected maps, new ways of constructing new sets of orthogonal harmonics for incomplete skies are developed in Chapter 5, and introduced shortly in the following section.

### 2.2.2 Incomplete sky

Parts of the CMB maps are heavily affected by foregrounds, particularly stemming from the Galactic plane as also shown in Chapter 1.2.2. In CMB studies it is therefore desirable to cut out these affected regions from the maps to minimize this influence. But the method of the surrogates is then much harder to apply and needs careful supplementation. The spherical harmonics form an orthonormal basis set on the complete sphere  $\mathbb{S}^2$  in ordinary space, expressed by

$$\int_{\mathbb{S}^2} Y_{\ell m}(\mathbf{x}) Y_{\ell' m'}(\mathbf{x}) d\Omega = \begin{cases} 1 & \text{for } \ell = \ell' \text{ and } m = m' \\ 0 & \text{else} \end{cases} \quad (2.8)$$

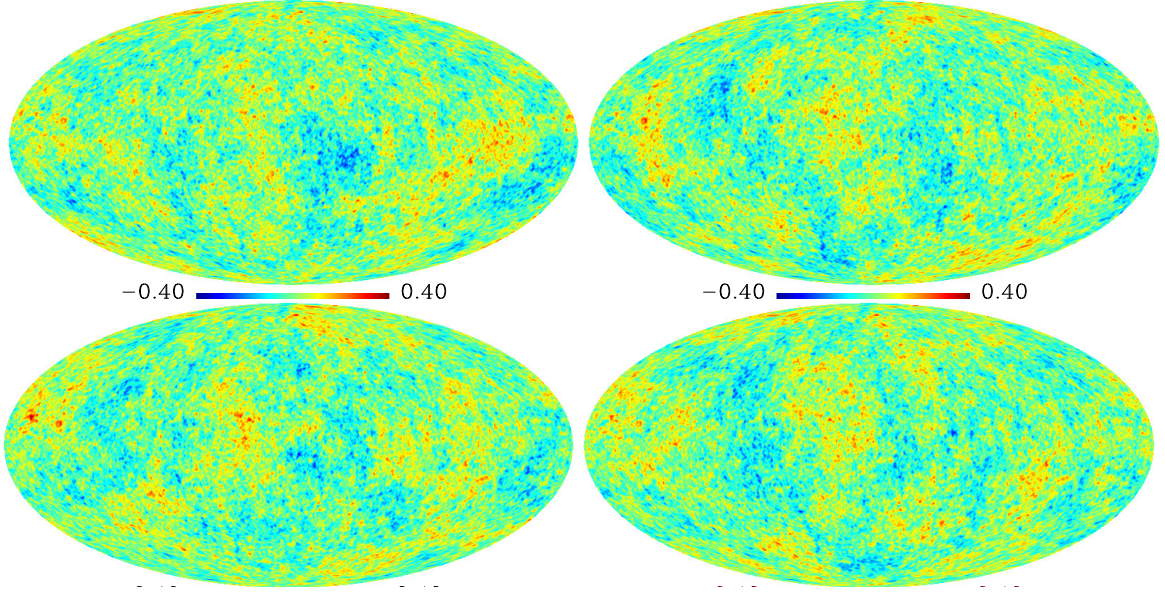


Figure 2.3: Examples of surrogates of one first-order (upper left) and three second-order (upper right, lower left, lower right), generated from the ILC9 map. The scale range is from  $-0.4$  to  $+0.4\text{mK}$ .

where  $Y_{\ell m}, Y_{\ell' m'}$  represent two harmonic functions with  $\ell, \ell' \geq 0, -\ell \leq m \leq \ell, -\ell' \leq m' \leq \ell'$ . Only if orthogonality holds, the coefficients  $a_{\ell m}$  of the map are unique. If the full sphere  $\mathbb{S}^2$  is replaced by an incomplete sphere  $\mathbb{S}^{2,\text{cut}}$ , the orthogonality of the spherical harmonics vanishes which leads to a coupling of the  $a_{\ell m}$  coefficients and the phases  $\varphi$  themselves. The method of the surrogates from the section above is no longer applicable.

It is necessary to express any CMB temperature map on an incomplete sky  $\mathbb{S}^{2,\text{cut}}$  by means of new cut sky coefficients  $a_{\ell m}^{\text{cut}}$  and new cut sky spherical harmonics  $Y_{\ell m}^{\text{cut}}$  ( $\mathbb{S}^{2,\text{cut}} \Rightarrow \mathbb{C}$ ) as

$$\Delta T/T(\theta, \phi) = \sum_{l=0}^{\infty} \sum_{m=-l}^l a_{\ell m}^{\text{cut}} Y_{\ell m}^{\text{cut}}(\theta, \phi) \quad (2.9)$$

where  $Y_{\ell m}^{\text{cut}}$  is an orthogonal basis set on  $\mathbb{S}^{2,\text{cut}}$  again, and thus  $a_{\ell m}^{\text{cut}}$  being unique.  $\ell = \infty$  is constrained again by the experiment to some maximum  $\ell_{\text{max}}$ . The vectors  $Y(\mathbf{x}), Y(\mathbf{x})^{\text{cut}}, a$  and  $a^{\text{cut}}$  are created containing all harmonics and coefficients with  $m \geq 0$ . The idea is to determine two transformation matrices  $B_1, B_2 \in \mathbb{C}^{i_{\text{max}} \times i_{\text{max}}}$ , that fulfill the following equations:

$$\begin{aligned} Y^{\text{cut}}(\mathbf{x}) &= B_1 Y(\mathbf{x}) \\ a^{\text{cut}} &= B_2 a. \end{aligned} \quad (2.10)$$

To identify them it is necessary to define the coupling matrix

$$C := \int_R Y(\mathbf{x}) Y^*(\mathbf{x}) d\Omega \quad (2.11)$$

as well as its counterpart  $C^{\text{cut}}$ , with  $R$  being a given region on the sphere.  $Y^*$  denotes the Hermitian transposed of  $Y$ . A set of harmonics  $Y_{\ell m}^{\text{cut}}$  which are orthonormal, needs to fulfill the condition  $C^{\text{cut}} = I_{i_{\text{max}}}$  with  $I_{i_{\text{max}}}$  being the unit matrix of size  $i_{\text{max}}$ . Equation (2.10) on

$C^{\text{cut}}$  changes this condition to  $B_1 C B_1^* = I_{i_{\text{max}}}$ . Different matrix decompositions of  $C$ , as for example the Cholesky, the Eigenvalue and the singular value decomposition, can help to obtain  $C = A A^*$  with  $A \in \mathbb{C}^{i_{\text{max}} \times i_{\text{max}}}$ . The above equation then reads as  $(B_1 A)(B_1 A)^* = I_{i_{\text{max}}}$  and offers the solution  $B_1 = A^{(-1)}$ . It follows from above  $B_2 = A^T$ . For the details on the different matrix decompositions and more please refer to [Rossmanith et al. \(2012\)](#).

The new cut sky harmonics enable to generate surrogates on a cut sky. The phases  $\phi_{\ell m}^{\text{cut}}$  are shuffled as well, the newly obtained sets of  $a_{\ell m}^{\text{cut}}$ s are transformed back to pixel space to form the cut sky surrogate maps. It is important to note that a cut sky transformation still induces phase correlations. To account for this systematic effect, a number of full-sky surrogate maps is created as well. The cut-sky algorithm is then applied to these full-sky surrogates. The results of the cut-sky surrogate analysis from the original map and via full-sky surrogates are compared. Since original map and full-sky surrogates undergo the same cut sky transformations systematics are circumvented and intrinsic signatures of phase correlations in the original map can be detected.

## 2.3 Higher-order image analysis in real space

Natural images can feature any kind of unknown structure. In the majority of these images, any interesting structure is characterized by its higher-order statistics. Arbitrarily oriented lines, edges or corners, for instance, can only be described by third- or fourth-order statistics. Only those specific images that do not contain higher-order correlations are fully described by pairwise statistics such as the power spectrum or the autocorrelation function. In order to interpret the CMB maps in these studies, measures are necessary that can quantify and compare the higher-order content of the original maps and their surrogates. Classically, higher-order correlations are computed by higher-order spectra such as the bispectrum (three-point correlation) and trispectrum (four-point correlation). Due to the huge amount of terms their computation is difficult to estimate and to interpret. Alternatively, it is possible to use the two different global measures, the Minkowski functionals and the scaling indices.

### 2.3.1 Minkowski functionals

The Minkowski functionals (MFs) describe the morphological properties of random fields in real space: A full morphological specification of an image requires geometrical as well as topological descriptors to characterize not only the shape and content but also the connectivity of spatial patterns. Hadwiger's theorem ([Hadwiger 1957](#)) in the field of integral-geometry states that any complete morphological descriptor of a set  $Q$  in  $d$ -dimensional Euclidian space  $\mathbb{E}^d$  is a linear combination of only  $d + 1$  functionals which meet some simple requirements; these functionals are given by the Minkowski functionals  $M_j$  with  $j$  ranging from 0 to  $d$ , calculated for given thresholds  $v$ . Functional  $M_0$  and  $M_1$  in two-dimensional space can be interpreted as the familiar geometric quantities surface area and perimeter, respectively. Functional  $M_2$  is the Euler characteristic and measures the topology of the field by giving the number of hot spots minus the number of cold spots. The Euler characteristic is very similar to the genus statistics ([Gott et al. 1986](#)) which differs only by the numerical coefficient of  $-1/2$ . The Minkowski functionals have been introduced into cosmology as descriptors for the morphological properties of large-scale structure by [Mecke et al. \(1994\)](#) and of CMB sky maps by [Winitzki & Kosowsky \(1998\)](#) and [Schmalzing & Górski \(1998\)](#). They embody information from every order of the correlation functions and yield global as well as local morphological information. Furthermore, they are additive measures which enables to calculate them efficiently by summing up their local contributions. In spherical, two-dimensional CMB space  $\mathbb{S}^2$  of radius  $R$  and a constant

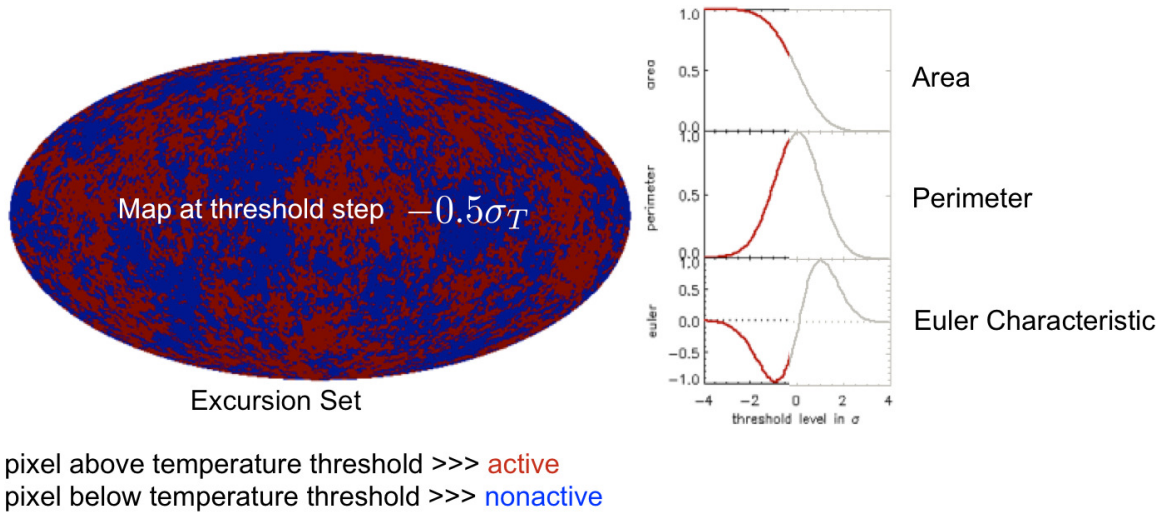


Figure 2.4: Sketch for calculating Minkowski functionals. The red and blue map shows active (red) and non-active (blue) temperature values at a threshold step of  $0.5\mu\text{K}$ .

curvature  $K = R^{-2}$  they are defined as

$$\begin{aligned}
 M_0 &= \int_Q da \\
 M_1 &= \frac{1}{4} \int_{\partial Q} dl \\
 M_2 &= \frac{1}{2\pi} \int_{\partial Q} dl k_g,
 \end{aligned} \tag{2.12}$$

where  $da$  and  $dl$  denote the surface element of  $\mathbb{S}^2$  and the line element along the smooth boundary  $\partial Q$ , respectively, as explained in [Schmalzing & Górski \(1998\)](#). The factor  $k_g$  is the geodesic curvature.

To study the morphology of the temperature anisotropies  $\Delta T/T(\mathbf{n})$ , which can be considered as a smooth scalar field on  $\mathbb{S}^2$ , the three MFs of the excursion sets  $Q_\nu$  are calculated in the pixelized spherical two-dimensional CMB maps (original data, surrogates or simulations).  $Q_\nu$  is here defined as the set of all pixels with value of  $\Delta T/T$  greater than or equal to some temperature threshold  $\nu$ , given by  $Q_\nu = \{\mathbf{n} \in \mathbb{S}^2 | \Delta T/T(\mathbf{n}) \geq \nu\}$ . The surface integrals of equation (2.12) are replaced by sums over all pixels.

To compute the Minkowski functionals of the pixelized two-dimensional maps I have adapted an algorithm of [Michielsen & De Raedt \(2001\)](#). Conceptually, each active pixel is decomposed into 4 vertices, 4 edges and the interior of the pixel as illustrated in Figure 2.5. The temperature maps are divided into an active and a non-active part by running over 200 threshold steps  $\nu_i$  with  $-4\sigma_T \leq \nu_i \leq +4\sigma_T$ , as illustrated in Figure 2.4. At the first threshold step  $\nu_0$ , nearly every pixel is included in the active part besides few outliers with  $T < -4\sigma_T$ . The last step  $\nu_{199}$  excludes most of the pixels. For each threshold step the total number of active squares  $n_s$  and edges  $n_e$  as well as vertices  $n_v$  of active pixels is counted to compute the area  $M_0$ , the

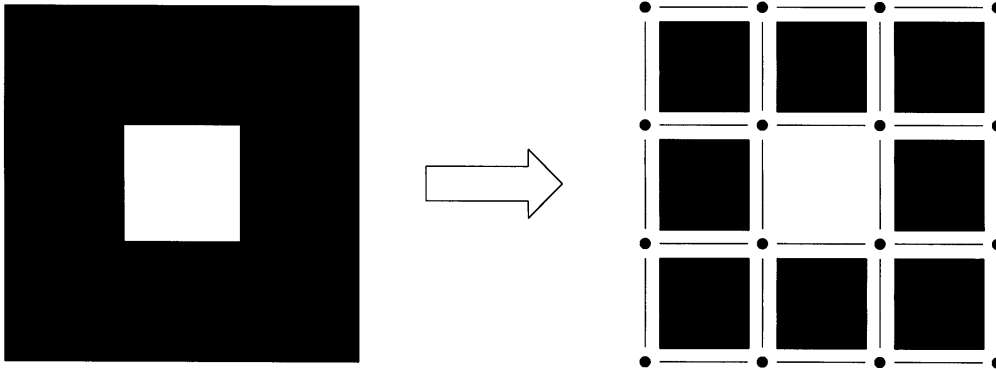


Figure 2.5: Decomposition of pixels into squares, edges, and vertices. Source: [Michielsen & De Raedt \(2001\)](#)

integral mean curvature/ perimeter  $M_1$  and the Euler characteristic  $M_2$  from

$$\begin{aligned}
 M_0 &= n_s \\
 M_1 &= -4n_s + 2n_e \\
 M_2 &= n_s - n_e + n_v.
 \end{aligned}
 \tag{2.13}$$

Neighboring pixels share edges and vertices. A technical difficulty with this procedure is to avoid counting an edge or vertex more than once. To avoid this, the original image is built up by adding active pixels to an initially empty temporary image one by one as suggested by [Michielsen & De Raedt \(2001\)](#). Depending on whether the surrounding pixels have already been activated in the temporary image or not, edges and vertices are added up to their total numbers. The number of arithmetic operations required to compute  $M_0$ ,  $M_1$ , and  $M_2$  scales linearly with the number of active pixels, threshold steps and the total number of pixels of the image.

### 2.3.2 Weighted scaling indices

For comparison, phase correlations in the CMB are assessed with the scaling indices method (SIM). This method represents another way to estimate the morphological and topological properties of an image. It can discriminate point-like, ring-like and sheet-like structures from each other and from a random background.

The scaling indices have been used for texture discrimination ([Räth & Morfill 1997](#)) and feature extraction ([Jamitzky et al. 2001](#); [Räth et al. 2008](#)), time series analysis of stock exchanges ([Monetti et al. 2004](#)) and active Galactic nuclei ([Gliozzi et al. 2002](#)) ([Gliozzi et al. 2006](#)) ([Gliozzi et al. 2010](#)) as well as structure analysis of bone images ([Mueller et al. 2006](#)) and other medical data sets as biological specimens, skin cancer, computed tomographic images, and beat-to-beat sequences from electrocardiograms ([Bunde et al. 2002](#)). The scaling indices were first applied to CMB data analysis in [Räth & Schuecker \(2003\)](#) and [Räth et al. \(2007\)](#).

The basic idea for this test statistic comes from the calculation of the dimensions of attractors in nonlinear time series analysis ([Grassberger & Procaccia 1983](#)). The scaling indices have been extended to the field of image processing for texture discrimination. If the image data is

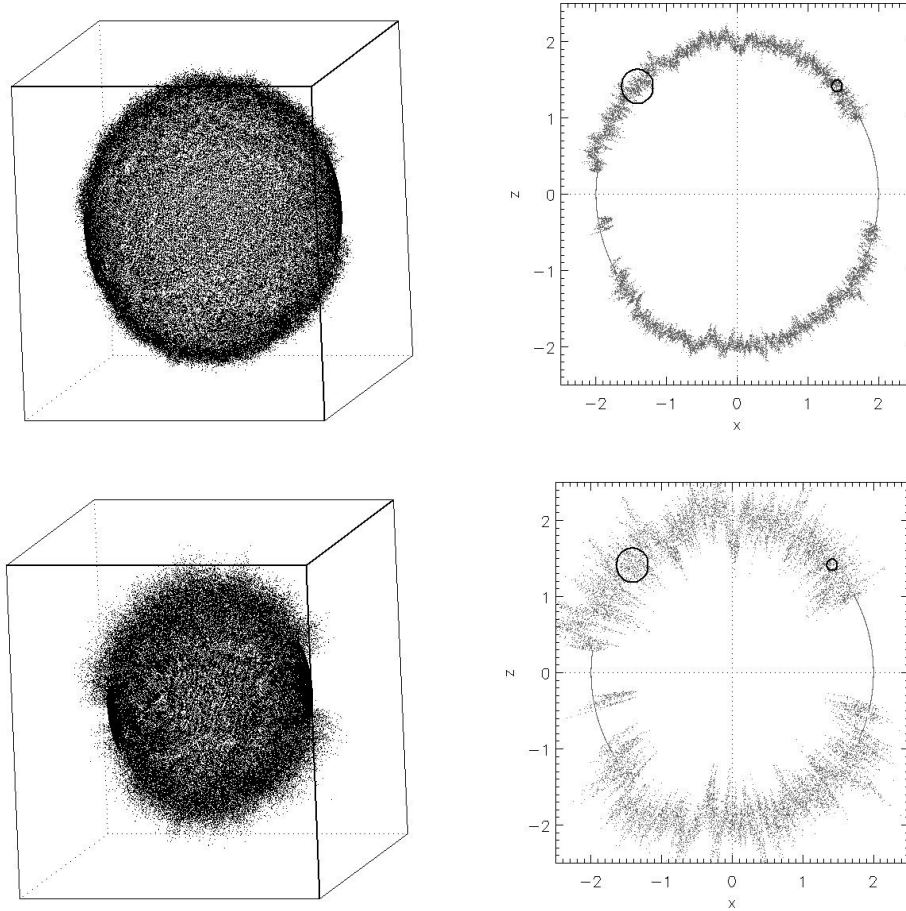


Figure 2.6: Left-hand panel: WMAP data represented as a 3D point distribution. Right-hand panel:  $x, z$ -projection of all points with  $|y| < 0.05$ . Above:  $a = 0.075$ , below:  $a = 0.225$ . The black circles indicate the scaling ranges  $r = 0.075$  and  $0.225$ , respectively. A good sensitivity to the temperature fluctuations at a given scale  $r$  is obtained for  $r = a$ . Source: [Räth et al. \(2007\)](#).

represented as a point distribution in a  $d$ -dimensional embedding space the scaling indices can fully describe the properties of this point set. To apply the SIM on the spherical CMB data, the temperature anisotropies  $\Delta T/T(\mathbf{x}_i)$  with its pixels at positions  $\mathbf{x}_i = (\theta_i, \phi_i)$ ,  $i = 1, \dots, N_{pix}$  on the sphere have to be transformed to a three-dimensional point distribution of  $N_{pix}$  points  $P = \{\mathbf{p}_i\}$  in an artificial embedding space as illustrated in Figure 2.6, for which the local scaling properties are then assessed with the SIM.

For each point the local weighted cumulative point distribution  $\rho$  is calculated as

$$\rho(\mathbf{p}_i, r) = \sum_{j=1}^{N_{pix}} s_r[d(\mathbf{p}_i, \mathbf{p}_j)] \quad (2.14)$$

where  $s_r(\bullet)$  denotes a shaping function depending on a scale parameter  $r$  and a distance measure  $d(\bullet)$ . In principle, any differentiable shaping function and any measure can be used for calculating the scaling indices. Throughout this work, the Euclidian norm and set of Gaussian

shaping functions are used as distance measures, which leads to

$$\rho(\mathbf{p}_i, r) = \sum_{j=1}^{N_{pix}} e^{-\frac{d_{ij}^2}{r}}, d_{ij} = \|\mathbf{p}_i - \mathbf{p}_j\|. \quad (2.15)$$

The weighted scaling indices  $\alpha(\mathbf{p}_i, r)$  are then obtained by calculating the logarithmic derivative of  $\rho(\mathbf{p}_i, r)$  with respect to  $r$ :

$$\alpha(\mathbf{p}_i, r) = \frac{\partial \log \rho(\mathbf{p}_i, r)}{\partial \log(r)}. \quad (2.16)$$

With the definition in Equation 2.15 the weighted scaling indices are expressed by

$$\alpha(\mathbf{p}_i, r) = \frac{\sum_{j=1}^{N_{pix}} q \left(\frac{d_{ij}}{r}\right)^q e^{-\left(\frac{d_{ij}}{r}\right)^q}}{\sum_{j=1}^{N_{pix}} e^{-\left(\frac{d_{ij}}{r}\right)^q}}. \quad (2.17)$$

### 2.3.3 Alternatives

Alternative global measures such as **skewness** or **kurtosis** (e.g. Bernui & Rebouças 2012), genus statistics (e.g. Colley & Gott 2003), the **length of the skeleton** (e.g. Hou et al. 2010) or **multipole vector analysis** (e.g. Copi et al. 2004) have been applied in several studies testing the random phase hypothesis of the CMB.

In contrast to the global measures, local measures estimate the characteristics of the maps in dependence upon the direction. A frequently used local measure is the wavelet filter technique. The **wavelet theory** is applied to the data maps, and decomposes the map into a wavelet series representation, which can help to bring out the underlying structure while localization properties in both pixel and harmonic space are very good. Different wavelet transforms have been considered in CMB analysis as for example the **spherical Mexican hat wavelets** (e.g. Cayón et al. 2001), the **directional spherical wavelets** (e.g. McEwen et al. 2008) and the **steerable wavelets** (e.g. Vielva et al. 2006). Another form of spherical wavelets are the **needlets** (e.g. Marinucci et al. 2008) that provide some advantages over the usual wavelets regarding computation effort but also statistical analysis.

The classical approach of CMB studies focusses on the analysis of real-space n-point correlation functions and their harmonic counterparts, respectively. The analysis of the second-, third- and fourth-order functions and their Fourier transforms given by the **power spectrum**, **bispectrum** and **trispectrum** conduces to the search for nonlinear properties in CMB data sets. The hypothesis of primordial Gaussianity implies a random distribution of the Fourier phases of the CMB and an independent and Gaussian distribution of the  $a_{\ell m}$ , respectively. If the CMB is Gaussian, the power spectrum contains all the information on  $a_{\ell m}$ , the higher-order spectra vanish, higher-order n-point correlation functions with even n can be written in terms of the two-point function, and all n-point correlation functions with odd n are zero. This is not true for non-Gaussian fluctuations for which one needs information on the higher-order content.

The CMB angular bispectrum is given by

$$B_{\ell_1 \ell_2 \ell_3}^{m_1 m_2 m_3} = \langle a_{\ell_1 m_1} a_{\ell_2 m_2} a_{\ell_3 m_3} \rangle. \quad (2.18)$$

It is measured by sampling triangles in Fourier space which can have different configurations formed by the three wave vectors (e.g. Babich et al. 2004). The dependence of the bispectrum

on the different types of triangles encodes important physical information about the shape of non-Gaussianity and the mechanism that generated it in the early Universe. It can also encode the scale dependence, or the so called running of the bispectrum (Chen 2005b). Widely discussed types of NG are the **local type NG** (Komatsu & Spergel 2001; Byrnes & Choi 2010) with maximal signal for squeezed triangles with  $k_1 \ll k_2 \simeq k_3$ . The **equilateral NG** peaks at equilateral configurations with  $k_1 \approx k_2 \approx k_3$  (Babich et al. 2004). **Folded NG** shows itself when the signal is enhanced by triangles with  $k_1 + k_2 \approx k_3$  (Chen et al. 2007). **Orthogonal NG** generates signal which is peaked both at the equilateral configuration and at the folded configuration (with opposite signs) (Senatore et al. 2010).

As specified for example in Komatsu & Spergel (2001) for a flat geometry of space, extendable for an arbitrary geometry, based upon the slow-roll inflationary scenario, the  $a_{\ell m}$  coefficients can be expressed by

$$a_{\ell m} = 4\pi(-i)^\ell \int \frac{d^3\mathbf{k}}{(2\pi)^3} \Phi(\mathbf{k}) g_{T\ell}(k) Y_{\ell m}^*(\hat{\mathbf{k}}), \quad (2.19)$$

if the primordial fluctuations are adiabatic scalar fluctuations, where  $\Phi(\mathbf{k})$  is the primordial curvature perturbation in Fourier space, and  $g_{T\ell}$  is the radiation transfer function. Non-Gaussianity, if any, is encoded in the curvature perturbation  $\Phi$ . The simplest weak nonlinear coupling case in real space is expressed by an expansion of the Bardeen potential by

$$\Phi(\mathbf{x}) = \Phi_L(\mathbf{x}) + f_{NL}[\Phi_L^2(\mathbf{x}) - \langle \Phi_L^2(\mathbf{x}) \rangle], \quad (2.20)$$

where  $\Phi_L$  denotes the linear Gaussian part of the curvature perturbation  $\Phi$ , and  $\Phi_{NL}$  the nonlinear part. Komatsu & Spergel (2001), and others, call  $f_{NL}$  the nonlinear coupling constant, henceforth.  $f_{NL}$ , or to be more precise  $f_{NL}^{local}$  is the dimensionless amplitude of a certain shape of the angular bispectrum that parametrizes non-Gaussianity of the local type in corresponding models. The size and shape of the other types of non-Gaussianity are described by  $f_{NL}^{equil}$ ,  $f_{NL}^{fold}$  and  $f_{NL}^{orthog}$ , respectively.

A convincing detection of  $f_{NL}^{local} \gg 1$  would rule out all single-field inflation models. It has been shown that the trispectrum of primordial fluctuations complements the information about the physics of the early Universe. But the analysis of the trispectrum is even more challenging than that of the bispectrum, due to the increased range of systematic effects and secondary signals which can contribute (Planck Collaboration et al. 2014h).

### 2.3.4 Statistical interpretation

The two image analysis techniques, Minkowski functionals and scaling indices, are applied to scale-dependent full-sky surrogate maps of the first and second order, to the original maps and to simulations, to quantify the higher-order information of the maps and to enable a comparison between the maps.

To shed light on the origin of detected phase correlations, efforts are being made to localize potential sources in real space that cause the Fourier space anomalies. For the analysis, the sky map is therefore separated into 768 overlapping spherical caps as sketched in Figure 2.7. Here, the number 768 is chosen to correspond to a HEALPix resolution of  $N_{\text{side}} = 8$ . The two image analysis techniques are each applied to the individual spherical caps. Varying results among the 768 caps will then indicate asymmetries in the Universe. The size of the caps can optionally be reduced as illustrated in Figure 2.8. Two different sizes for the caps are tested. Their two different solid angles are  $2\pi$  (hemisphere, apex angle  $\pi$ ) and  $\sim 0.6\pi$  for the smaller cap (apex angle  $\pi/2$ ).

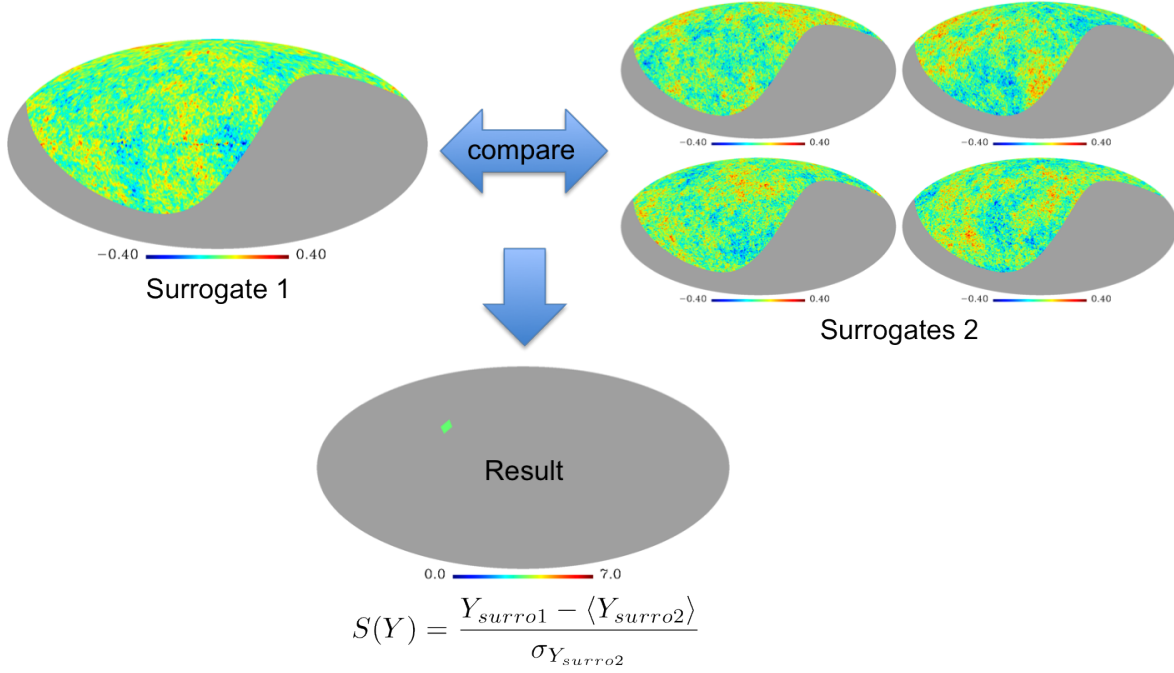


Figure 2.7: Sketch of the hemispherical analysis. Overlapping spherical caps are analyzed separately. The results are presented in so-called  $S$  maps.

To quantify the degree of agreement between the surrogates of different orders with respect to higher-order correlations found with the three Minkowski functionals  $M_0, M_1$  and  $M_2$ , the mean of the Minkowski functional  $M_{\star, surro2}$  of  $N = 500$  realizations of the second-order surrogate is calculated per spherical cap  $h$  and threshold bin  $\mathbf{v}$

$$A := \langle M_{\star, surro2}(\mathbf{v}, h) \rangle = \frac{1}{N} \sum_{m=1}^N M_{\star, surro2}(m, \mathbf{v}, h)$$

and the standard deviation

$$\sigma_{M_{\star, surro2}}(\mathbf{v}, h) = \left( \frac{1}{N-1} \sum_{m=1}^N (M_{\star, surro2}(m, \mathbf{v}, h) - A)^2 \right)^{1/2}$$

for  $m = 1, \dots, N$ . Mean and standard deviation are combined in a diagonal  $\chi^2$  statistic per spherical cap  $h$  for the surrogates of first order

$$\chi_{M_{\star, surro1}}^2(h) = \sum_{j=0}^{\mathbf{v}} \left[ \frac{M_{\star, surro1}(j, h) - A}{\sigma_{M_{\star, surro2}}(j, h)} \right]^2$$

and for the second-order surrogate maps

$$\chi_{M_{\star, surro2}}^2(h, m) = \sum_{j=0}^{\mathbf{v}} \left[ \frac{M_{\star, surro2}(m, j, h) - A}{\sigma_{M_{\star, surro2}}(j, h)} \right]^2.$$

Finally, the degree of agreement between the two types of surrogates is quantified by the  $\sigma$ -normalized deviation  $S$

$$S(\chi_{M_{\star}}^2(h)) = \frac{\chi_{M_{\star, surro1}}^2(h) - \langle \chi_{M_{\star, surro2}}^2(h) \rangle}{\sigma_{\chi_{M_{\star, surro2}}^2}(h)} \quad (2.21)$$

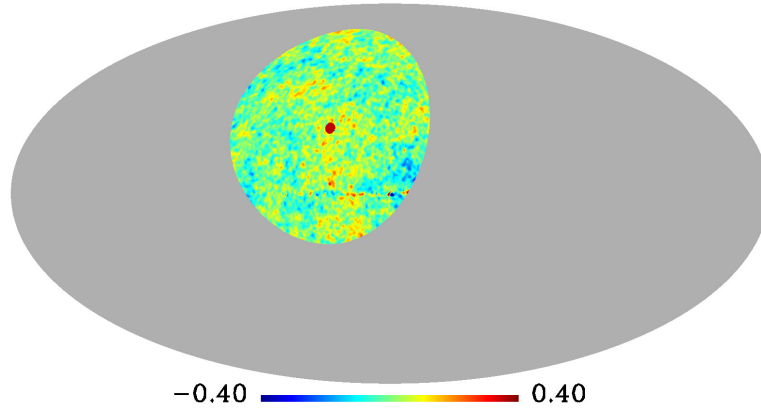


Figure 2.8: For an advanced hemispherical analysis, the size of the caps can arbitrarily be reduced. The red dot marks the pixel that will later represent the  $S$ -value calculated in the analysis.

for each of the 768 spherical caps with  $\langle \chi_{M_*,surro2}^2(h) \rangle$  and  $\sigma_{\chi_{M_*,surro2}^2}(h)$  denoting the mean and the standard deviation of  $\chi_{M_*,surro2}^2(h)$  for the  $N = 500$  second-order surrogates. Thus, the  $\sigma$ -normalized hemispherical deviations  $S(\chi_{M_0}^2(h))$ ,  $S(\chi_{M_1}^2(h))$  and  $S(\chi_{M_2}^2(h))$  for the Area, Perimeter and Euler characteristics are obtained.

Similar to the Minkowski functionals, the mean  $\langle \alpha(r) \rangle$  and standard deviation  $\sigma_{\alpha(r)}$  of the scaling indices  $\alpha(\mathbf{p}_i, r)$  is calculated for the set of 768 hemispherical maps. The scaling indices are calculated with varying scale parameter  $r$ . The differences of the two classes of surrogates are again quantified by the  $\sigma$ -normalized deviation  $S$ :

$$S(Y) = \frac{Y_{surro1} - \langle Y_{surro2} \rangle}{\sigma_{Y_{surro2}}} \quad (2.22)$$

where  $Y$  represents a diagonal  $\chi^2$  statistic

$$\chi_{(\alpha(r), \sigma_{\alpha(r)})}^2 = \sum_{j=1}^2 \left[ \frac{B_j - \langle B_j \rangle}{\sigma_{B_j}} \right]^2, \quad (2.23)$$

as a combination of the mean and the standard deviation where  $B_1(r) = \langle \alpha(r) \rangle$ ,  $B_2(r) = \sigma_{\alpha(r)}$ . See [Räth et al. \(2007\)](#) for a detailed description regarding the scaling indices statistics.

The results obtained by the hemispherical study of the sky are visualized in so-called  $S$ -maps as illustrated in Figure 2.7. Each pixel centre of a full-sky map with a HEALPix resolution of  $N_{\text{side}} = 8$  marks one of the 768 spherical caps' poles. After calculating the deviation  $S$  between one first-order surrogate and 500 realizations of second-order surrogates for each individual cap, the corresponding value is plotted in a sky map at that pixel position where the  $z$ -axis of the rotated cap pierces the sky. This is done for both, the Minkowski functionals and the scaling indices. For one single  $S$ -map with 768 values stemming from the comparison of 500 surrogates of the second order with one first-order surrogate, it is necessary to analyze 384,768 spherical caps with the image analysis techniques.

## 2.4 Analysis in harmonic space

Instead of analyzing phase correlations in CMB maps by means of the method of the surrogates, one can also study the phase distribution directly. The hope is that such methods are

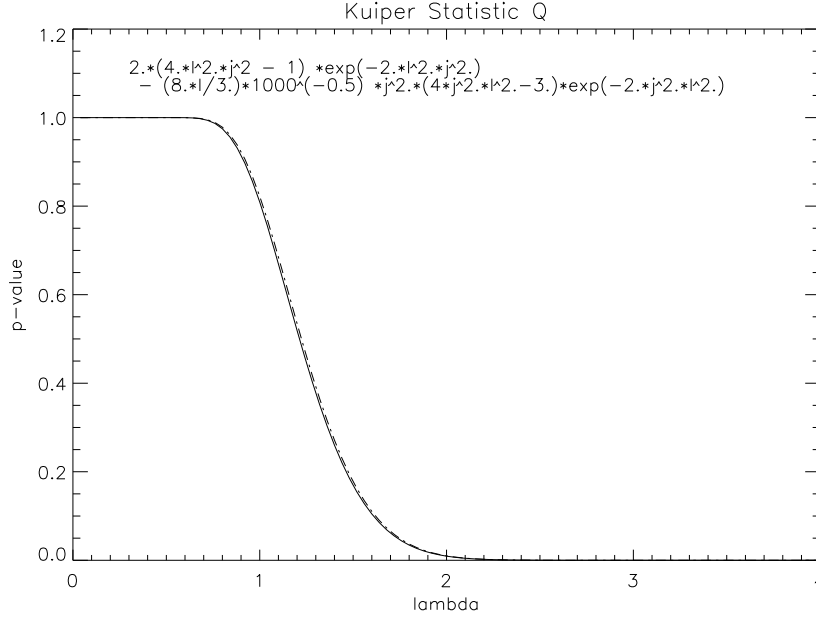


Figure 2.9: The monotonic function  $Q$  that gives information about the  $p$ -value of an observed value  $V$ .

able to isolate higher-order image components that are created by single multipoles or certain combinations of Fourier modes. An advantage of the surrogates is that they enable the localization of sources in real space that cause the phase correlations. However, direct studies on the phase distribution can enable a complementary and more detailed insight into the nature of higher-order image structures in phase space. To test for the independence of the CMB phases we make use of the well suited Kuiper test as explained below.

### 2.4.1 Kuiper statistics

Complementary to the analysis of surrogate maps, the Fourier phases  $\varphi_{\ell m}$  of the maps can be tested for independence in an in-depth analysis of the phase distributions of the maps by means of the Kuiper test. This enables a direct study of the phase distribution and can reveal details about the CMB phase correlations. The Kuiper test can be viewed as a variant of the standard Kolmogorov-Smirnov test, designed to cope with circular data.

After an  $a_{\ell m}$ -decomposition for  $\ell \in [2, 10]$ ,  $m > 0$ , 54 phases  $\varphi_{\ell m}$  with values between  $-\pi$  and  $\pi$  depending on the chosen coordinate system are obtained. The distribution of values is illustrated in Figure 2.10. If these  $\varphi_{\ell m}$  fulfill the random phase hypothesis, i.e. are i.i.d. and follow a uniform distribution, the phase difference taken between these phases are uniformly distributed in  $[0, 2\pi]$ . To test this, subsets of differences with fixed separations  $(\Delta\ell, \Delta m)$  by  $\Delta\varphi(\Delta\ell, \Delta m) = \varphi_{\ell+\Delta\ell, m+\Delta m} - \varphi_{\ell m}$  are defined. The Kuiper statistic (KS) (Kuiper 1960; Press et al. 2007) is then used to test for the null hypothesis by comparing the cumulative distribution function (CDF) of the  $\Delta\varphi(\Delta\ell, \Delta m)$  with a given uniform CDF. The Kuiper test statistic is  $V = D^+ + D^-$ , where  $D^+$  and  $D^-$  represent the absolute sizes of the most positive and most negative difference between the two cumulative distribution functions that are being compared. The  $p$ -value of an observed value  $V$  is given by  $p = Q_{KP}([\sqrt{N_e} + 0.155 + 0.24\sqrt{N_e}] V)$  with respect to the monotonic function  $Q_{KP}(\lambda) = 2\sum_{j=1}^{\infty} (4j^2\lambda^2 - 1)e^{-2j^2\lambda^2}$ , where  $N_e$  is the effective

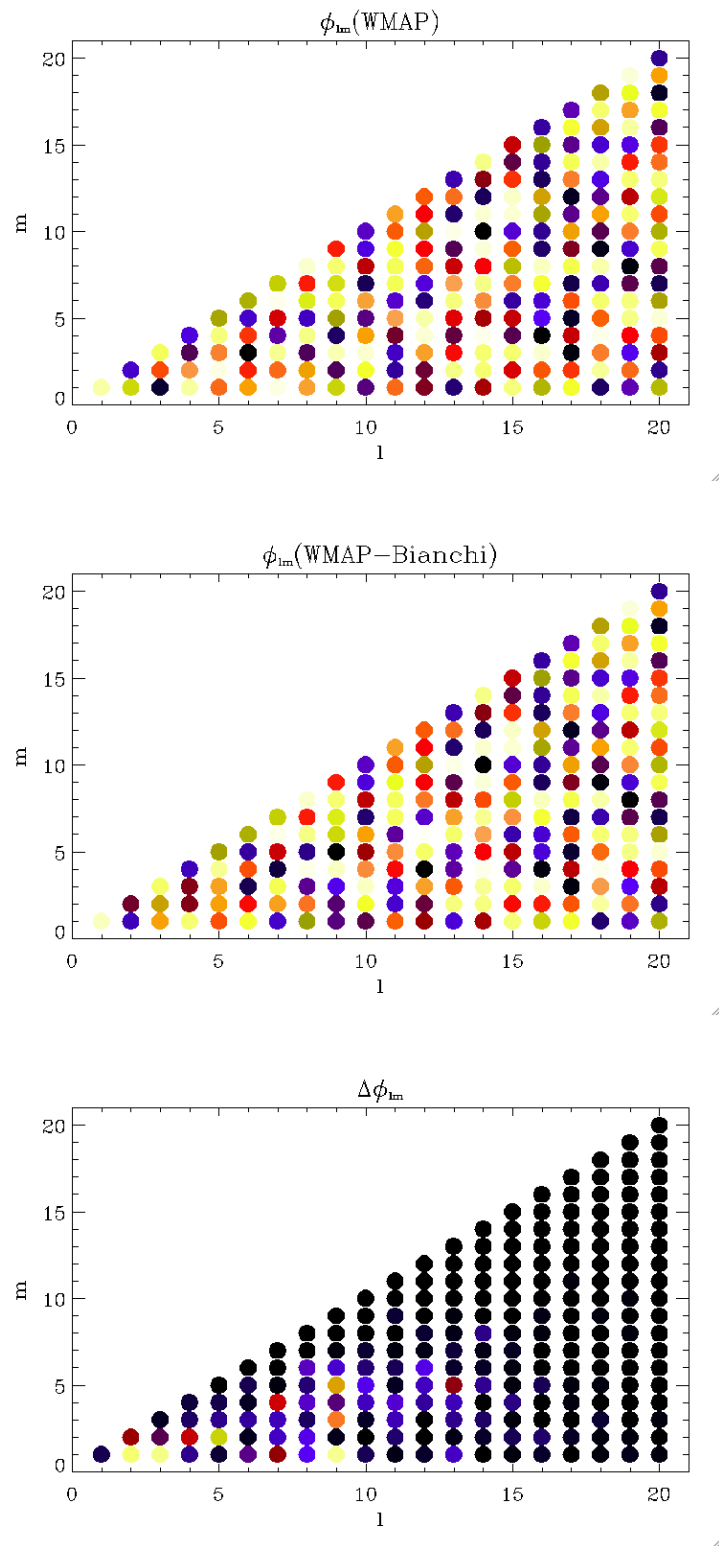


Figure 2.10: The color-coded values of the Fourier phases of WMAP (upper plot), WMAP-Bianchi (middle plot) and the difference of these two plots (lower plot). The values lie in the range of  $[-\pi, +\pi]$  where black corresponds to zero.

number of data points (see Figure 2.9). It is interpreted as the probability the measured value  $V$  has if the null hypothesis were true. High  $p$ -values for a given  $(\Delta\ell, \Delta m)$  separation therefore indicate the absence of phase correlations between mode-pairs separated by  $(\Delta\ell, \Delta m)$  whereas low values indicate their existence. In standard frequentist fashion, values of  $p \leq 0.05$  (5% level) are widely accepted as strong evidence against the null hypothesis. The results depend on the chosen coordinate system. However, averaging over rotated systems will show a global trend of the results.

As described in Chapter 1.1.4, there is a chance that the Bianchi type VII<sub>h</sub> model can account for some of the observed anomalies in CMB maps as for example the suppression of the quadrupole, or the alignment of small multipoles. We will therefore study these Bianchi models in more detail by subtracting them from CMB maps (Planck data) in Chapter 6. Figure 2.10 shows the color-coded values of the phases after an  $a_{\ell m}$ -decomposition for  $\ell \in [2, 20]$ , with respect to a Bianchi subtraction, and for the difference between the original map and the subtraction.

## Chapter 3

# Scale-dependent non-Gaussianities identified by using surrogates and scaling indices

**Original Publication:** C. Räth, A. J. Banday, G. Rossmanith, H. I. Modest, R. Sütterlin, K. M. Górski, J. Delabrouille and G. E. Morfill, *Scale-dependent non-Gaussianities in the WMAP data as identified by using surrogates and scaling indices*, MNRAS, **415**, 2205 (2011)

**Abstract:** We present a model-independent investigation of the *Wilkinson Microwave Anisotropy Probe (WMAP)* data with respect to scale-independent and scale-dependent non-Gaussianities (NGs). To this end, we employ the method of constrained randomization. For generating so-called surrogate maps a well-specified shuffling scheme is applied to the Fourier phases of the original data, which allows to test for the presence of higher order correlations (HOCs) also and especially on well-defined scales.

Using scaling indices as test statistics for the HOCs in the maps we find highly significant signatures for non-Gaussianities when considering all scales. We test for NGs in four different  $l$ -bands  $\Delta l$ , namely in the bands  $\Delta l = [2, 20], [20, 60], [60, 120]$  and  $[120, 300]$ . We find highly significant signatures for both non-Gaussianities and ecliptic hemispherical asymmetries for the interval  $\Delta l = [2, 20]$  covering the large scales. We also obtain highly significant deviations from Gaussianity for the band  $\Delta l = [120, 300]$ . The result for the full  $l$ -range can then easily be interpreted as a superposition of the signatures found in the bands  $\Delta l = [2, 20]$  and  $[120, 300]$ . We find remarkably similar results when analyzing different ILC-like maps based on the WMAP 3-, 5- and 7-year data. We perform a set of tests to investigate whether and to what extent the detected anomalies can be explained by systematics. While none of these tests can convincingly rule out the intrinsic nature of the anomalies for the low- $l$  case, the ILC map making procedure and/or residual noise in the maps can also lead to NGs at small scales.

Our investigations prove that there *are* phase correlations in the WMAP data of the CMB. In the absence of an explanation in terms of Galactic foregrounds or known systematic artefacts, the signatures at low  $l$  must so far be taken to be cosmological at high significance. These findings would strongly disagree with predictions of isotropic cosmologies with single field slow roll inflation.

The task is now to elucidate the origin of the phase correlations and to understand the physical processes leading to these scale-dependent non-Gaussianities – if it turns out that

systematics as cause for them must be ruled out.

### 3.1 Introduction

The Cosmic Microwave Background (CMB) radiation represents the oldest observable signal in the Universe. Since this relic radiation has its origin just 380000 years after the Big Bang when the CMB photons were last scattered off electrons, this radiation is one of the most important sources of information to gain more knowledge about the very early Universe. Estimating the linear correlations of the temperature fluctuations in the CMB as measured e.g. with the WMAP satellite by means of the power spectrum has yielded very precise determinations of the parameters of the standard  $\Lambda$ CDM cosmological model like the age, the geometry and the matter and energy content of the Universe (Komatsu et al. 2009a, 2011).

Analyzing CMB maps by means of the power spectrum represents an enormous compression of information contained in the data from approx.  $10^6$  temperature values to roughly 1000 numbers for the power spectrum. It has often been pointed out (Komatsu et al. 2009b and references therein) that this data compression is lossless and thus fully justified, if and *only if* the statistical distribution of the observed fluctuations is a Gaussian distribution with random phases. Any information that is contained in the phases and the correlations among them, is not encoded in the power spectrum, but has to be extracted from measurements of higher-order correlation (HOC). Thus, the presence of phase correlations may be considered as an unambiguous evidence of non-Gaussianity (NG). Otherwise, non-Gaussianity can only be defined by the negation of Gaussianity.

Primordial NG represents one way to test theories of inflation with the ultimate goal to constrain the shape of the potential of the inflaton field(s) and their possible (self-)interactions. While the simplest single field slow roll inflationary scenario predicts that fluctuations are nearly Gaussian (Guth 1981; Linde 1982; Albrecht & Steinhardt 1982), a variety of more complex models predict deviations from Gaussianity (Linde & Mukhanov 1997; Peebles 1997; Bernardeau & Uzan 2002; Acquaviva et al. 2003). Models in which the Lagrangian is a general function of the inflaton and powers of its first derivative (Armendáriz-Picón et al. 1999; Garriga & Mukhanov 1999) can lead to scale-dependent non-Gaussianities, if the sound speed varies during inflation. Similarly, string theory models that give rise to large non-Gaussianity have a natural scale dependence (Chen 2005b; Lo Verde et al. 2008). Also, NGs put strong constraints on alternatives to the inflationary paradigm (Buchbinder et al. 2008; Lehnert & Steinhardt 2008).

Given the plethora of conceivable scenarios for the very early Universe, it is worth first checking what is in the data in a model-independent way. Further, such a model-independent approach has a large discovery potential to detect yet unexpected fingerprints of nonlinear physics in the early universe. Thus, a detection of possibly scale-dependent non-Gaussianity being encrypted in the phase correlations in the WMAP data would be of great interest. While a detection of non-Gaussianity could be indicative of an experimental systematic effect or of residual foregrounds, it could also point to new cosmological physics.

The investigations of deviations from Gaussianity in the CMB (see Komatsu et al. (2009a) and references therein) and claims for the detection of non-Gaussianity and a variety of other anomalies like hemispherical asymmetries, lack of power at large angular scales, alignment of multipoles, detection of the Cold Spot etc. (see e.g. de Oliveira-Costa et al. 2004; Eriksen et al. 2004b, 2005, 2007; Hansen et al. 2004; Park 2004; Vielva et al. 2004; Räth et al. 2007; McEwen et al. 2008; Copi et al. 2009, 2010; Hansen et al. 2009; Rossmanith et al. 2009; Yoho et al. 2011) have been made, where the statistical significance of some of the detected signatures

is still subject to discussion (Zhang & Huterer 2010; Bennett et al. 2011). These studies have in common that the level of non-Gaussianity is assessed by comparing the results for the measured data with simulated CMB-maps which were generated on the basis of the standard cosmological model and/or specific assumptions about the nature of the non-Gaussianities as parametrized with e.g. the scalar, scale-independent parameter  $f_{nl}$ . Other studies focused on the detection of signatures in the distribution of Fourier phases (Chiang et al. 2003; Coles et al. 2004; Naselsky et al. 2005; Chiang et al. 2007) representing deviations from the random phase hypothesis for Gaussian random fields. These model-independent tests also revealed signatures of NGs. Pursuing this approach one can go one step further and investigate possible phase correlations and their relation to the morphology of the CMB maps by means of so-called surrogate maps.

This technique of surrogate data sets (Theiler et al. 1992) was originally developed for nonlinear time series analysis. In this field of research complex systems like the climate, stock-market, heart-beat variability, etc. are analyzed (see e.g. Bunde et al. (2002) and references therein). For those systems a full modeling is barely or not possible. Therefore, statistical methods of constrained randomization involving surrogate data sets were developed to infer some information about the nature of the underlying physical process in a completely data-driven, i.e. model-independent way. One of the first and most basic question here is whether a (quasi-periodic) process is completely linear or whether also weak nonlinearities can be detected in the data. The basic formalism to answer this question is to compute statistics sensitive to HOCs for the original data set and for an ensemble of surrogate data sets, which mimic the linear properties of the original time series while wiping out all phase correlations. If the computed measure for the original data is significantly different from the values obtained for the set of surrogates, one can infer that the data contain HOCs.

Extensions of this formalism to three-dimensional galaxy distributions (Räth et al. 2002) and two-dimensional simulated flat CMB maps (Räth & Schuecker 2003) have been proposed and discussed. By introducing a more sophisticated two-step surrogatization scheme for full-sky CMB observations it has become possible to also test for scale-dependent NG in a model-independent way (Räth et al. 2009). Probing NG on the largest scales ( $l < 20$ ) yielded highly significant signatures for both NG and ecliptic hemispherical asymmetries.

In this paper, we apply the method of constrained randomization to the WMAP 5-year and 7-year data in order to test for scale-independent and scale-dependent non-Gaussianity up to  $l = 300$  as encoded in the Fourier phase correlations. Further, this work fully recognizes the need to rule out foregrounds and systematic artefacts as the origin of the detections (as advised by Bennett et al. (2011)). Therefore, a large part of our analyses is dedicated to various checks on systematics to single out possible causes of the detected anomalies.

The paper is organized as follows: In Section 2 we briefly describe the observational and simulated data we use in our study. The method of constrained randomization is reviewed in some detail in Section 3. Scaling indices, which we use as test statistic, and the statistics derived out of them are discussed in Section 4. In Section 5 we present our results and we draw our conclusions in Section 6.

## 3.2 Data Sets

We used the 7-year foreground-cleaned internal linear combination (ILC) map (Gold et al. 2011) generated and provided by the WMAP team<sup>1</sup> (in the following: ILC7). For comparison

---

<sup>1</sup><http://lambda.gsfc.nasa.gov>

we also included the map produced by [Delabrouille et al. \(2009\)](#), namely the 5-year needlet-based ILC map, which has been shown to be significantly less contaminated by foreground and noise than other existing maps obtained from WMAP data (in the following: NILC5).

To check for systematics we also analyzed the following set of maps:

1) *Uncorrected ILC map*

The ILC map is a weighted linear combination of the 5 frequency channels that recovers the CMB signal. The weights are derived by requiring minimum variance in a given region of the sky under the constraint that the sum of the weights is unity. Such weights, however, cannot null an arbitrary foreground signal with a non-blackbody frequency spectrum, thus some residuals due to Galactic emission will remain. The WMAP team attempts to correct for this "bias" with an estimation of the residual signal based on simulations and a model of the foreground sky. Our uncorrected map (UILC7 in the following) is simply the ILC without applying this correction, computed from the weights provided in [Gold et al. \(2011\)](#) and the 1-degree smoothed WMAP data.

2) *Asymmetric beam map*

Beam asymmetries may result in statistically anisotropic CMB maps. To assess these effects on the signatures of scale-dependent NGs and their (an-)isotropies we make use of the publicly available CMB sky simulations including the effects of asymmetric beams ([Wehus et al. 2009](#)). Specifically we analyze a simulated map of the V1-band, because this band is considered to have the least foreground contamination.

3) *Simulated co-added VW-band map*

To make sure that neither systematic effects are induced by the method of constrained randomization nor the WMAP-like beam and noise properties lead to systematic deviations from Gaussianity we include in our analysis a co-added VW-map as obtained using the standard  $\Lambda$ CDM best fit power spectrum and WMAP-like beam and noise properties. Note that this map did not undergo the ILC-map making procedure.

4) *Simulated ILC map*

Simulated sky maps result from processing a simulated differential time-ordered data (TOD) stream through the same calibration and analysis pipeline that is used for the flight data. The TOD is generated by sampling a reference sky that includes both CMB and Galactic foregrounds with the actual flight pointings, and adding various instrumental artefacts. We have then processed the individual resulting data into 7 separate simulated yearly ILC maps, plus a 7-year merge. It is worth noting that, if the yearly frequency-averaged maps are combined into ILCs using the [Gold et al. \(2011\)](#) 7-year weights per region, then the resulting ILCs show clear Galactic plane residuals. This reflects the fact that the simulated data has a different CMB realization to the observed sky, and may additionally represent a mismatch between the simulated foreground properties and the true sky in the Galactic plane. Instead, we analyze the 7-year merged simulated data to compute the ILC weights for the simulations, then apply to all yearly data sets separately. However, the derived weights are quite different from the WMAP7 ones, which would imply different noise properties in the simulated ILC data compared to the real data. Care should be exercised for any results that are sensitive to the specific noise pattern.

5) *Difference ILC map*

Finally, we consider the difference map (year 7 - year 6) from yearly ILC-maps computed using the same weights and regions as the 7-year data set from [Gold et al. \(2011\)](#). No debiasing has been applied. With this map we estimate what effect possible ILC-residuals may have on the detection of NGs.

### 3.3 Generating Surrogate Maps

To test for scale-dependent non-Gaussianities in a model-independent way we apply a two-step procedure that has been proposed and discussed in R  th et al. (2009). Let us describe the various steps for generating surrogate maps in more detail:

Consider a CMB map  $T(\theta, \phi)$ , where  $T(\theta, \phi)$  is Gaussian distributed and its Fourier transform. The Fourier coefficients  $a_{lm}$  can be written as  $a_{lm} = |a_{lm}|e^{i\phi_{lm}}$  with  $\phi_{lm} = \arctan(\text{Im}(a_{lm})/\text{Re}(a_{lm}))$ . The linear or Gaussian properties of the underlying random field are contained in the absolute values  $|a_{lm}|$ , whereas all HOCs – if present – are encoded in the phases  $\phi_{lm}$  and the correlations among them. Having this in mind, a versatile approach for testing for scale dependent non-Gaussianities relies on a scale-dependent shuffling procedure of the phase correlations followed by a statistical comparison of the so-generated surrogate maps.

However, the Gaussianity of the temperature distribution and the randomness of the set of Fourier phases in the sense that they are uniformly distributed in the interval  $[-\pi, \pi]$ , are a necessary prerequisite for the application of the surrogate-generating algorithm, which we propose in the following. To fulfill these two conditions, we perform the following preprocessing steps. First, the maps are remapped onto a Gaussian distribution in a rank-ordered way. This means that the amplitude distribution of the original temperature map in real space is replaced by a Gaussian distribution in a way that the rank-ordering is preserved, i.e. the lowest value of the original distribution is replaced with the lowest value of the Gaussian distribution etc. By applying this remapping we automatically focus on HOCs induced by the spatial correlations in the data while excluding any effects coming from deviations of the temperature distribution from a Gaussian one.

To ensure the randomness of the set of Fourier phases we performed a rank-ordered remapping of the phases onto a set of uniformly distributed ones followed by an inverse Fourier transformation. These two preprocessing steps only have marginal influence to the maps. The main effect is that the outliers in the temperature distribution are removed. Due to the large number of temperature values (and phases) we did not find any significant dependence of the specific Gaussian (uniform) realization used for remapping of the temperatures (phases). The resulting maps may already be considered as a surrogate map and we named it zeroth order surrogate map. The first and second order surrogate maps are obtained as follows:

We first generate a first order surrogate map, in which any phase correlations for the scales, which are not of interest, are randomized. This is achieved by a random shuffle of the phases  $\phi_{lm}$  for  $l \notin \Delta l = [l_{min}, l_{max}]$ ,  $0 < m \leq l$  and by performing an inverse Fourier transformation.

In a second step,  $N$  ( $N = 500$  throughout this study) realizations of second order surrogate maps are generated for the first order surrogate map, in which the remaining phases  $\phi_{lm}$  with  $l \in \Delta l$ ,  $0 < m \leq l$  are shuffled, while the already randomized phases for the scales, which are not under consideration, are preserved. Note that the Gaussian properties of the maps, which are given by  $|a_{lm}|$ , are *exactly* preserved in all surrogate maps.

So far, we have applied the method of surrogates only to the  $l$ -range  $\Delta l = [2, 20]$ . In this paper we will repeat the investigations for this  $l$ -interval but using newer CMB maps. Furthermore, we extend the analysis to smaller scales. Namely, we consider three more  $l$ -intervals  $\Delta l = [20, 60]$ ,  $\Delta l = [60, 120]$  and  $\Delta l = [120, 300]$ . The choice of 60 as  $l_{min}$  and  $l_{max}$  is somewhat arbitrary, whereas the  $l_{min} = 120$  and  $l_{max} = 300$  for the last  $l$ -interval was selected in such a way that the first peak in the power spectrum is covered. Going to even higher  $l$ 's doesn't make much sense, because the ILC7 map is smoothed to 1 degree FWHM. Some other maps which we included in our study – especially NILC5 – are not smoothed and we could

in principle go to higher  $l$ 's. But to allow for a consistent comparison of the results obtained with the different observed and simulated input maps we restrict ourselves to only investigate  $l$ -intervals up to  $l_{max} = 300$  in this study.

Besides this two-step procedure aiming at a dedicated scale-dependent search of non-Gaussianity, we also test for non-Gaussianity using surrogate maps without specifying certain scales. In this case there are no scales, which are not of interest, and the first step in the surrogate map making procedure becomes dispensable. The zeroth order surrogate map is to be considered here as first order surrogate and the second order surrogates are generated by shuffling all phases with  $0 < m \leq l$  for all available  $l$ 's, i.e. in our case  $\Delta l = [2, 1024]$ .

Finally, for calculating scaling indices to test for higher order correlations the surrogate maps were degraded to  $N_{side} = 256$  and residual monopole and dipole contributions were subtracted. The statistical comparison of the two classes of surrogates will reveal, whether possible HOCs on certain scales have left traces in the first order surrogate maps, which were then deleted in the second order surrogates. Before the results of such a comparison of the surrogate maps are shown in detail, we review the formalism of scaling indices.

### 3.4 Weighted Scaling Indices and Test Statistics

As test statistics for detecting and assessing possible scale-dependent non-Gaussianities in the CMB data weighted scaling indices are calculated (Räth et al. 2002; Räth & Schuecker 2003). The basic ideas of the scaling index method (SIM) stem from the calculation of the dimensions of attractors in nonlinear time series analysis (Grassberger & Procaccia 1983). Scaling indices essentially represent one way to estimate the local scaling properties of a point set in an arbitrary  $d$ -dimensional embedding space. The technique offers the possibility of revealing local structural characteristics of a given point distribution. Thus, point-like, string-like and sheet-like structures can be discriminated from each other and from a random background. The alignment of e.g. string-like structures can be detected by using a proper metric for calculating the distances between the points (Räth et al. 2008; Sütterlin et al. 2009).

Besides the countless applications in time series analysis the use of scaling indices has been extended to the field of image processing for texture discrimination (Räth & Morfill 1997) and feature extraction (Jamitzky et al. 2001; Räth et al. 2008) tasks. Following further this line we performed several non-Gaussianity studies of the CMB based on WMAP data using scaling indices in recent years (Räth & Schuecker 2003; Räth et al. 2007, 2009; Rossmanith et al. 2009).

Let us review the formalism for calculating this test statistic for assessing HOCs:

In general, the SIM is a mapping that calculates for every point  $\vec{p}_i, i = 1, \dots, N_{pix}$  of a point set  $P$  a single value, which depends on the spatial position of  $\vec{p}_i$  relative to the group of other nearby points, in which the point under consideration is embedded in. Before we go into the details of assessing the local scaling properties, let us first of all outline the steps of generating a point set  $P$  out of observational CMB-data. To be able to apply the SIM on the spherical CMB data, we have to transform the pixelized sky  $S$  with its pixels at positions  $(\theta_i, \phi_i), i = 1, \dots, N_{pix}$ , on the unit sphere to a point-distribution in an artificial embedding space. One way to achieve this is by transforming each temperature value  $T(\theta_i, \phi_i)$  to a radial jitter around a sphere of radius  $R$  at the position of the pixel center  $(\theta_i, \phi_i)$ . Formally, the three-dimensional position

vector of the point  $\vec{p}_i$  reads as

$$x_i = (R + dR) \cos(\phi_i) \sin(\theta_i) \quad (3.1)$$

$$y_i = (R + dR) \sin(\phi_i) \sin(\theta_i) \quad (3.2)$$

$$z_i = (R + dR) \cos(\theta_i) \quad (3.3)$$

with

$$dR = a \left( \frac{T(\theta_i, \phi_i) - \langle T \rangle}{\sigma_T} \right). \quad (3.4)$$

Hereby,  $R$  denotes the radius of the sphere while  $a$  describes an adjustment parameter. The mean temperature and its standard deviation are characterized by  $\langle T \rangle$  and  $\sigma_T$ , respectively. By the use of the normalization we obtain for  $dR$  zero mean and a standard deviation of  $a$ . Both  $R$  and  $a$  should be chosen properly to ensure a high sensitivity of the SIM with respect to the temperature fluctuations at a certain spatial scale. For the analysis of WMAP-like CMB data, it turned out that this requirement is provided using  $R = 2$  for the radius of the sphere and coupling the adjustment parameter  $a$  to the value of the below introduced scaling range parameter  $r$  via  $a = r$  (Räth et al. 2007). Now that we obtained our point set  $P$ , we can apply the SIM. For every point  $\vec{p}_i$  we calculate the local weighted cumulative point distribution which is defined as

$$\rho(\vec{p}_i, r) = \sum_{j=1}^{N_{pix}} s_r(d(\vec{p}_i, \vec{p}_j)) \quad (3.5)$$

with  $r$  describing the scaling range, while  $s_r(\bullet)$  and  $d(\bullet)$  denote a shaping function and a distance measure, respectively. The scaling index  $\alpha(\vec{p}_i, r)$  is then defined as the logarithmic derivative of  $\rho(\vec{p}_i, r)$  with respect to  $r$ :

$$\alpha(\vec{p}_i, r) = \frac{\partial \log \rho(\vec{p}_i, r)}{\partial \log r}. \quad (3.6)$$

As mentioned above,  $s_r(\bullet)$  and  $d(\bullet)$  can in general be chosen arbitrarily. For our analysis we use a quadratic gaussian shaping function  $s_r(x) = e^{-\left(\frac{x}{r}\right)^2}$  and an isotropic euclidian norm  $d(\vec{p}_i, \vec{p}_j) = \|\vec{p}_i - \vec{p}_j\|$  as distance measure. With this specific choice of  $s_r(\bullet)$  and  $d(\bullet)$  we obtain the following analytic formula for the scaling indices

$$\alpha(\vec{p}_i, r) = \frac{\sum_{j=1}^{N_{pix}} 2 \left(\frac{d_{ij}}{r}\right) e^{-\left(\frac{d_{ij}}{r}\right)^2}}{\sum_{j=1}^{N_{pix}} e^{-\left(\frac{d_{ij}}{r}\right)^2}}, \quad (3.7)$$

where we used the abbreviation  $d_{ij} := d(\vec{p}_i, \vec{p}_j)$ . As becomes obvious from equation (3.7), the calculation of scaling indices depends on the scale parameter  $r$ . Therefore, we can investigate the structural configuration in the underlying CMB-map in a scale-dependent manner. For our analysis, we use the ten scaling range parameters  $r_k = 0.025, 0.05, \dots, 0.25$ ,  $k = 1, 2, \dots, 10$ , which (roughly) correspond to sensitive  $l$ -ranges from  $\Delta l = [83; 387]$ ,  $\Delta l = [41; 193]$ ,  $\dots$ ,  $\Delta l = [8; 39]$  (Rossmanith et al. 2009).

In order to quantify the degree of agreement between the surrogates of different orders with respect to their signatures left in distribution of scaling indices, we calculate the mean

$$\langle \alpha(r_k) \rangle = \frac{1}{N_p} \sum_{i=1}^{N_p} \alpha(\vec{p}_i, r_k) \quad (3.8)$$

and the standard deviation

$$\sigma_{\alpha(r_k)} = \left( \frac{1}{N_p - 1} \sum_{i=1}^{N_p} (\alpha(\vec{p}_i, r_k) - \langle \alpha(r_k) \rangle)^2 \right)^{1/2} \quad (3.9)$$

of the scaling indices  $\alpha_i$  derived from  $N_p$  considered pixels for the different scaling ranges  $r_k$ .  $N_p$  becomes the number of all pixels  $N_{pix}$  for a full sky analysis. To investigate possible spatial variations of signatures of NG and to be able to measure asymmetries we also consider the moments as derived from the pixels belonging to rotated hemispheres. In these cases the number  $N_p$  of the pixels halves and their positions defined by the corresponding  $\phi$ - and  $\theta$ -intervals vary according to the part of the sky being considered. Furthermore, we combine these two test statistics by using  $\chi^2$  statistics. There is an ongoing discussion, whether a diagonal  $\chi^2$  statistic or the ordinary  $\chi^2$  statistic, which takes into account correlations among the different random variables through the covariance matrix is the better suited measure. On the one hand it is of course important to take into account correlations among the test statistics, on the other hand it has been argued (Eriksen et al. 2004b) that the calculation of the inverse covariance matrix may become numerically unstable when the correlations among the variables are strong making the ordinary  $\chi^2$  statistic sensitive to fluctuations rather than to absolute deviations. Being aware of this we calculated both  $\chi^2$  statistics, namely the scale dependent diagonal  $\chi^2$  combining the mean and the standard deviation at a given scale  $r_k$ , and the scale-independent  $\chi^2$  combining the mean or/and the standard deviation calculated at all scales  $r_k, k = 1, \dots, 10$  (see Rossmanith et al. (2009)).

Further, we calculate the corresponding ordinary  $\chi^2$  statistics, which is obtained by summing over the full inverse correlations matrix  $\mathbf{C}^{-1}$ . In general, this is expressed by the bilinear form

$$\chi^2 = (\vec{M} - \langle \vec{M} \rangle)^T \mathbf{C}^{-1} (\vec{M} - \langle \vec{M} \rangle), \quad (3.10)$$

where the test statistics to be combined are comprised in the vector  $\vec{M}$  and  $\mathbf{C}$  is obtained by cross correlating the elements of  $\vec{M}$ . Specifically, for obtaining the scale dependent  $\chi_{full, \langle \alpha(r_k) \rangle, \sigma_{\alpha(r_k)}}^2$  combining the mean and the standard deviation at a given scale  $r_k$  the vector  $\vec{M}^T$  becomes  $\vec{M}^T = (M_1, M_2)$  with  $M_1 = \langle \alpha(r_k) \rangle$ ,  $M_2 = \sigma_{\alpha(r_k)}$ . Similarly, the full scale-independent  $\chi^2$  statistics  $\chi_{full, \langle \alpha \rangle}^2$ ,  $\chi_{full, \sigma_\alpha}^2$  and  $\chi_{full, \langle \alpha \rangle, \sigma_\alpha}^2$  are derived from the vectors  $\vec{M}^T$  consisting of  $\vec{M}^T = (\langle \alpha(r_1) \rangle, \dots, \langle \alpha(r_{10}) \rangle)$ ,  $\vec{M}^T = (\sigma_{\alpha(r_1)}, \dots, \sigma_{\alpha(r_{10})})$  and  $\vec{M}^T = (\langle \alpha(r_1) \rangle, \dots, \langle \alpha(r_{10}) \rangle, \sigma_{\alpha(r_1)}, \dots, \sigma_{\alpha(r_{10})})$ , respectively. For all our investigations we calculated both  $\chi^2$  statistics and found out that the results are only marginally dependent from the chosen  $\chi^2$  statistics. Thus, in the following we will only list explicit numbers for the full  $\chi^2$  statistics, if not stated otherwise, because this measure yielded overall slightly more conservative results.

### 3.5 Results

To test for NGs and asymmetries in the ILC7 map and the NILC5 map, we compare the different surrogate maps in the following way:

For each scale we calculate the mean  $\langle \alpha(r_k) \rangle$  and standard deviation  $\sigma_{\alpha(r_k)}$  of the map of scaling indices  $\alpha(\theta, \phi; r_k)$  of the full sky and a set of 768 rotated hemispheres. The northern pole of the different hemispheres is located at every pixel centre of the full sky with  $N_{side} = 8$  in the HEALPix<sup>2</sup> (Górski et al. 2005) pixelization scheme. The differences of the two classes

<sup>2</sup><http://healpix.jpl.nasa.gov/>

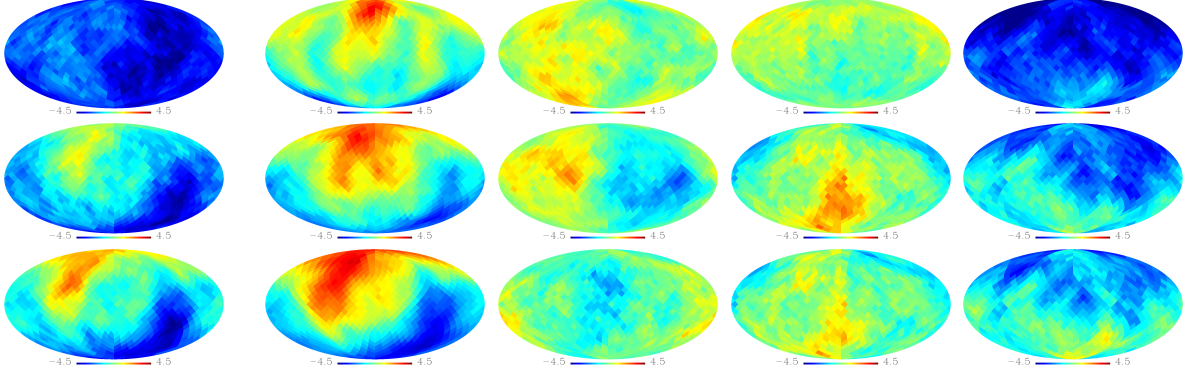


Figure 3.1: Deviations  $S(\langle\alpha(r_k)\rangle)$  of the rotated hemispheres for three scales  $r_k, k = 2, 6, 10$  (from top to bottom) for the ILC7 map and for (from left to right) the shuffling intervals  $\Delta l = [2, 1024]$ ,  $\Delta l = [2, 20]$ ,  $\Delta l = [20, 60]$ ,  $\Delta l = [60, 120]$  and  $\Delta l = [120, 300]$ . The expected correspondence between the shuffling range  $\Delta l$  and the scales  $r_k$  of the scale-dependent higher order statistics  $\langle\alpha(r_k)\rangle$ , for which the largest deviations are detected, becomes apparent. While the ecliptic hemispherical asymmetries for  $\Delta l = [2, 20]$  are most pronounced for the largest scaling range  $r_{10}$  (second column), the deviation  $S$  becomes largest for  $r_2$  when shuffling the phases of the smallest scales  $\Delta l = [120, 300]$  (rightmost column).

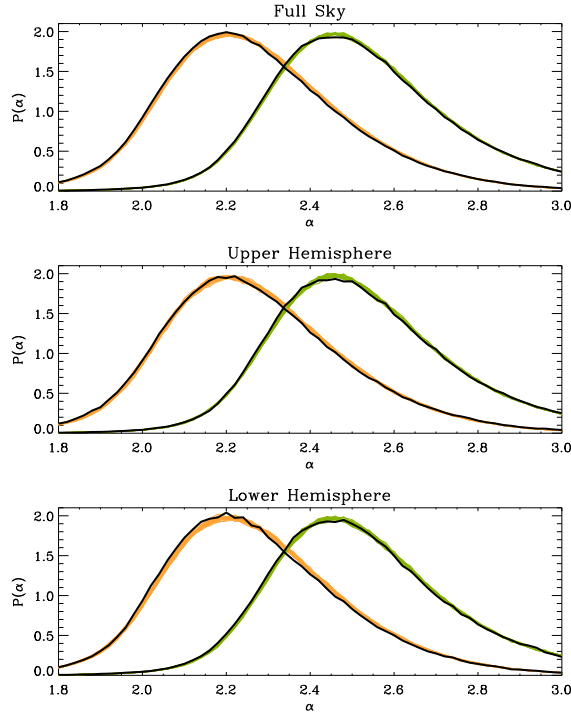


Figure 3.2: Probability density  $P(\alpha)$  of the first and second order surrogates for the scaling indices calculated for the largest scaling range  $r_{10}$  and for the  $l$ -interval  $\Delta l = [2, 20]$ . Yellow (green) curves denote the densities for 20 realizations of second order surrogates derived from the ILC7 (NILC5) map. The black lines are the corresponding first order surrogates. The reference frame for defining the upper and lower hemispheres is chosen such that the difference  $\Delta S = S_{up} - S_{low}$  becomes maximal for  $\langle\alpha\rangle$  of the respective map and respective scale  $r$ .

of surrogates are quantified by the  $\sigma$ -normalized deviation  $S$

$$S(Y) = \frac{Y_{\text{surro1}} - \langle Y_{\text{surro2}} \rangle}{\sigma_{Y_{\text{surro2}}}} \quad (3.11)$$

with,  $Y = \langle \alpha(r_k) \rangle, \sigma_{\alpha(r_k)}, \chi^2$ . Every hemisphere of the set of 768 hemispheres delivers one deviation value  $S$ , which is then plotted on a sky map at that pixel position where the z-axis of the rotated hemisphere pierces the sky. Fig. 3.1 shows the deviations  $S$  for the mean value  $S(\langle \alpha(r_k) \rangle), k = 2, 6, 10$  for the ILC7 map as derived from the comparison of the different classes of surrogates for the scale-independent surrogate test and for the four selected  $l$ -ranges. The following striking features become immediately obvious:

First, various deviations representing features of non-Gaussianity and asymmetries are can be found in the  $S$ -maps for the ILC7 map. These features can nearly exactly be reproduced when the NILC5 map is taken as input map (results not shown).

Secondly, we find for the scale-independent surrogate test (leftmost column in figs. 3.1) large isotropic deviations for the scaling indices calculated for the smallest scale shown in the figure. The negative values for  $S$  indicate that the mean of the scaling indices for the first order surrogate is smaller than for the second order surrogate maps. This systematic trend can be interpreted such that there's more structure detected in the first order surrogate than in the second order surrogate maps. Obviously, the random shuffle of all phases has destroyed a significant amount of structural information at small scales in the maps.

Thirdly, for the scale-dependent analysis we obtain for the largest scales ( $\Delta l = [2, 20]$ ) highly significant signatures for non-Gaussianities and ecliptic hemispherical asymmetries at the largest  $r$ -values (second column in figs. 3.1). These results are perfectly consistent with those obtained for the WMAP 5-year ILC map and the foreground removed maps generated by Tegmark et al. (2003) on the basis of the WMAP 3-year data (see Räth et al. (2009)). The only difference between this study and our previous one is that we now obtain higher absolute values for  $S$  ranging now from  $-4.00 < S < 3.72$  for the ILC7 map and  $-4.36 < S < 4.50$  for the NILC5 map as compared to  $-3.87 < S < 3.51$  for the WMAP 5-year ILC map. Thus, the cleaner the map becomes due to better signal-to-noise ratio and/or improved map making techniques the higher the significances of the detected anomalies get which suggests that the signal is of intrinsic CMB origin.

Fourthly, we also find for the smallest considered scales ( $\Delta l = [150, 300]$ ) large isotropic deviations for the scaling indices calculated for a small scaling range  $r$  very similar to those observed for the scale-independent test.

Fifthly, we do not observe very significant anomalies for the two other bands ( $\Delta l = [20, 60]$  and  $\Delta l = [60, 120]$ ) being considered in this study. Thus, the results obtained for the scale independent surrogate test can clearly be interpreted as a superposition of the signals identified in the two  $l$ -bands covering the largest ( $\Delta l = [2, 20]$ ) and smallest ( $\Delta l = [120, 300]$ ) scales.

Let us investigate the observed anomalies in more details. We begin with a closer look at the most significant deviations. Fig. 3.2 shows the probability densities derived for the full sky and for (rotated) hemispheres for the scaling indices at the largest scaling range  $r_{10}$  for the first and second order surrogates for the  $l$ -interval  $\Delta l = [2, 20]$ . We recognize the systematic shift of the whole density distribution towards higher values for the upper hemisphere and to lower values for the lower hemisphere. As these two effects cancel each other for the full sky, we do no longer see significant differences in the probability densities in this case. Since the densities as a whole are shifted, the significant differences between first and second order surrogates found for the moments cannot be attributed to some salient localizable features leading to an excess

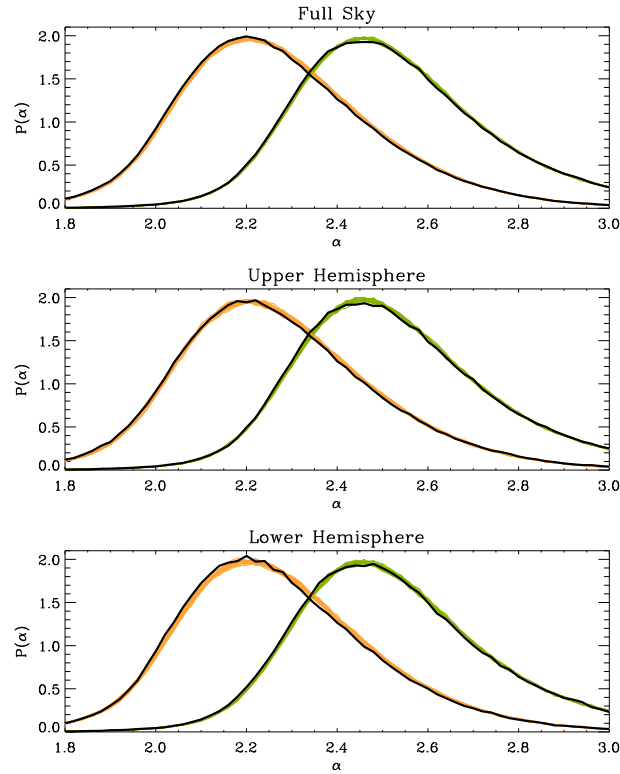


Figure 3.3: Same as figure 3.2 but the second smallest scaling range  $r_2$  and the  $l$ -interval  $\Delta l = [120, 300]$ .

(e.g. second peak) at very low or high values in otherwise very similar  $P(\alpha)$ -densities. Rather, the shift to higher (lower) values for the upper (lower) hemisphere must be interpreted as a global trend indicating that the first order surrogate map has less (more) structure than the respective set of second order surrogates. The seemingly counterintuitive result for the upper hemisphere is on the other hand consistent with a linear hemispherical structure analysis by means of a power spectrum analysis, where also a lack of power in the northern hemisphere and thus a pronounced hemispherical asymmetry was detected (Hansen et al. 2004, 2009). However, it has to be emphasized that the effects contained in the power spectrum are – by construction – exactly preserved in both classes of surrogates, so that the scaling indices measure effects that can solely be induced by HOCs thus being of a new, namely non-Gaussian, nature. Interestingly though, the linear and nonlinear hemispherical asymmetries seem to be correlated with each other.

Fig. 3.3 is very similar to fig. 3.2 and shows the probability densities for the scaling indices calculated for the second smallest scaling range  $r_2$  for the first and second order surrogates for the  $l$ -interval  $\Delta l = [120, 300]$ . The systematic shift towards smaller values for the first order surrogate for both hemispheres and thus for the full sky is visible. It is interesting to note that all densities derived from the ILC7 and NILC5 map differ significantly from each other. These differences can be attributed to e.g. the smoothing of the ILC7 map. However, the systematic differences between first and second order surrogates induced by the phase manipulations prevailed in all cases – irrespective of the input map.

The results for the deviations  $|S(r)|$  for the full sky and rotated upper and lower hemisphere

| $\Delta l$                                       | Full Sky      | Upper Hemisphere | Lower Hemisphere |
|--|---------------|------------------|------------------|
| $\langle \alpha(r_2) \rangle$ :                  | ( $S/\%$ )    | ( $S/\%$ )       | ( $S/\%$ )       |
| [2,1024]   | 7.73 / > 99.8 | 4.53 / >99.8     | 1.87 / 96.0      |
| [2,20]   | 0.14 / 56.6   | 3.54 / >99.8     | 3.44 / >99.8     |
| [20,60]  | 0.88 / 80.6   | 1.84 / 96.4      | 1.08 / 85.2      |
| [60,120]   | 0.26 / 60.4   | 0.32 / 64.8      | 0.64 / 71.6      |
| [120,300]  | 6.97 / >99.8  | 5.36 / >99.8     | 0.92 / 83.0      |
| $\sigma_{\alpha(r_2)}$ :                         |               |                  |                  |
| [2,1024]   | 4.16 / >99.8  | 3.77 / >99.8     | 0.25 / 61.8      |
| [2,20]   | 0.48 / 69.2   | 0.48 / 69.8      | 0.19 / 58.0      |
| [20,60]  | 1.70 / 95.2   | 3.18 / >99.8     | 1.02 / 84.8      |
| [60,120]   | 0.88 / 80.0   | 2.35 / 98.8      | 1.25 / 88.2      |
| [120,300]  | 3.54 / >99.8  | 1.03 / 83.4      | 3.69 / >99.8     |
| $\chi^2_{(\alpha(r_2)), \sigma_{\alpha(r_2)}}$ : |               |                  |                  |
| [2,1024]   | 24.55 / >99.8 | 14.44 / >99.8    | 0.94 / 84.4      |
| [2,20]   | 0.90 / 85.2   | 7.67 / >99.8     | 8.47 / 99.8      |
| [20,60]  | 0.82 / 83.4   | 4.03 / 99.2      | 0.31 / 50.4      |
| [60,120]   | 0.51 / 61.4   | 3.63 / 98.6      | 1.00 / 85.2      |
| [120,300]  | 19.62 / >99.8 | 17.17 / >99.8    | 4.15 / 99.2      |

Table 3.1: Deviations  $S$  and empirical probabilities  $p$  of the mean, standard deviation and their  $\chi^2$ -combination as derived for the scaling indices at the second smallest scale  $r_2$ . The results of the ILC7 map are shown for the different  $l$ -bands as well as for the full sky and the upper and lower hemispheres. Corresponding to the small scale  $r_2$  the largest values for  $S$  are calculated for small scale non-Gaussianities in the  $l$ -range [120,300] and for the scale-independent NGs, where the phases of all  $l$ 's ( $\Delta l = [2,1024]$ ) are included.

are shown for all considered  $l$ -ranges and all scales  $r$  in figs. 3.4. The corresponding values for  $r_2$  and  $r_{10}$  are listed in the tables 3.1 and 3.2. In table 3.3 we further summarize the results for the scale-independent  $\chi^2$ -measures  $\chi^2_{\langle \alpha \rangle}$ ,  $\chi^2_{\sigma_\alpha}$  and  $\chi^2_{\langle \alpha \rangle, \sigma_\alpha}$ .

The main results which were already briefly discussed on the basis of figs. 1 become much more apparent when interpreting fig. 3.4 and tables 3.1 to 3.3. We find stable  $3.7 - 12\sigma$  deviations for all  $r$ -values for  $S(\langle \alpha(r_k) \rangle)$  and the scale-independent surrogate test when considering the full sky. This yields  $S$ -values of  $S(\langle \alpha(r_2) \rangle) = 7.73$  (ILC7 map) and  $S(\langle \alpha(r_2) \rangle) = 11.06$  (NILC5 map) for the scaling indices calculated for the small value  $r_2$  and  $S(\langle \alpha(r_{10}) \rangle) = 3.75$  (ILC7 map) and  $S(\langle \alpha(r_{10}) \rangle) = 5.77$  (NILC5 map) for the largest radius  $r_{10}$ . This stable  $r$ -independent effect leads to very high values of the deviations  $S$  for the scale-independent  $\chi^2$ -statistics  $S(\chi^2_{\langle \alpha \rangle})$ , where we find  $S(\chi^2_{\langle \alpha \rangle}) = 5.73$  (ILC7 map) and  $S(\chi^2_{\langle \alpha \rangle}) = 27.93$  (NILC5 map). It is interesting to compare these results with those obtained for the diagonal  $\chi^2$ -statistics. In this case we find  $S(\chi^2_{\langle \alpha \rangle}) = 57.32$  (ILC7 map) and  $S(\chi^2_{\langle \alpha \rangle}) = 119.16$  (NILC5 map), which is up to an order of magnitude larger than the values for the full  $\chi^2$ -statistics. These results

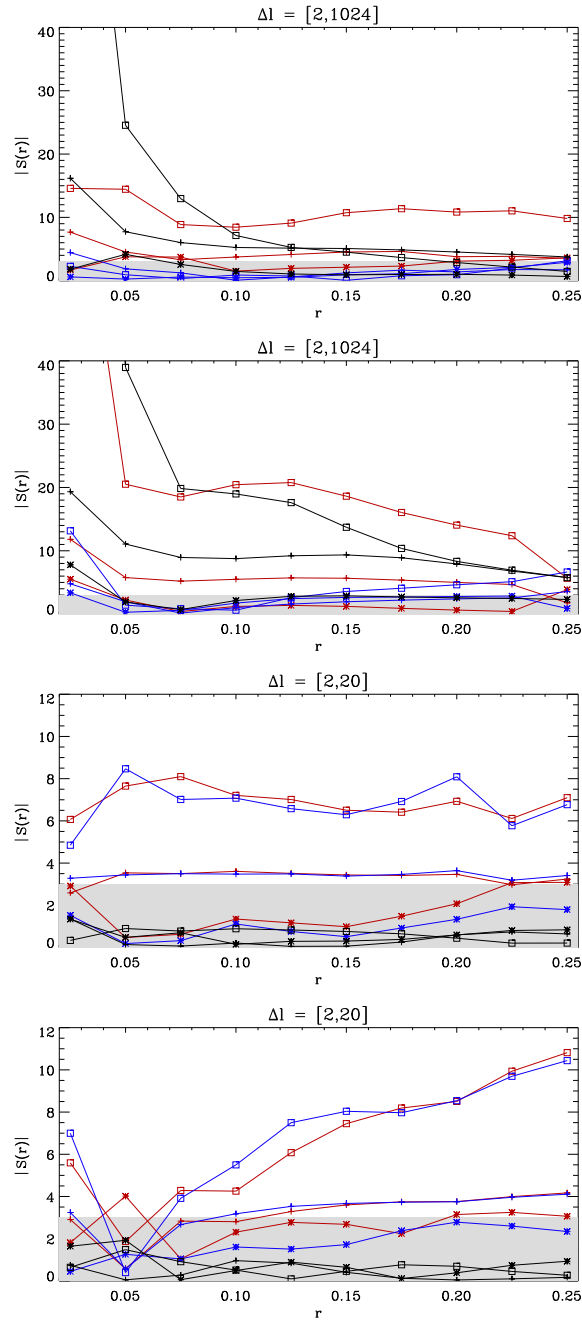


Figure 3.4: Deviations  $|S(r)|$  for the ILC7 (left) and NILC5 (right) map as a function of the scale parameter  $r$  for the full sky (black) and the upper (red) and lower (blue) hemisphere. The plus signs denote the results for the mean  $\langle\alpha(r_k)\rangle$ , the star-signs for the standard deviation  $\sigma_{\alpha(r_k)}$  and the boxes for the  $\chi^2$ -combination of  $\langle\alpha(r_k)\rangle$  and  $\sigma_{\alpha(r_k)}$ . The shaded region indicates the  $3\sigma$  significance interval.

| $\Delta l$   | Full Sky     | Upper Hemisphere | Lower Hemisphere |
|--|--------------|------------------|------------------|
| $\langle \alpha(r_{10}) \rangle$ :                                   | ( $S/\%$ )   | ( $S/\%$ )       | ( $S/\%$ )       |
| [2, 1024]  | 3.75 / >99.8 | 3.53 / >99.8     | 1.72 / 95.4      |
| [2, 20]  | 0.64 / 74.2  | 3.24 / >99.8     | 3.41 / >99.8     |
| [20, 60]   | 0.67 / 74.2  | 1.41 / 91.6      | 2.04 / 98.0      |
| [60, 120]  | 0.01 / 50.5  | 2.28 / 99.0      | 2.19 / 98.6      |
| [120, 300]   | 2.45 / 99.4  | 3.58 / >99.8     | 1.38 / 92.2      |
| $\sigma_{\alpha(r_{10})}$ :  |              |                  |                  |
| [2, 1024]  | 0.66 / 74.4  | 3.60 / >99.8     | 2.90 / >99.8     |
| [2, 20]  | 0.84 / 80.0  | 3.09 / >99.8     | 1.79 / 96.4      |
| [20, 60]   | 2.27 / 98.6  | 2.94 / 99.8      | 0.13 / 55.0      |
| [60, 120]  | 0.77 / 79.0  | 1.63 / 94.6      | 0.47 / 67.6      |
| [120, 300]   | 0.60 / 73.6  | 1.61 / 95.8      | 0.81 / 79.6      |
| $\chi^2_{\langle \alpha(r_{10}) \rangle, \sigma_{\alpha(r_{10})}}$ : |              |                  |                  |
| [2, 1024]  | 1.46 / 90.4  | 9.83 / >99.8     | 3.15 / 98.0      |
| [2, 20]  | 0.21 / 54.8  | 7.10 / >99.8     | 6.77 / 99.8      |
| [20, 60]   | 2.74 / 97.2  | 5.27 / 99.6      | 0.29 / 73.6      |
| [60, 120]  | 0.38 / 50.2  | 2.09 / 94.2      | 0.43 / 75.8      |
| [120, 300]   | 0.26 / 57.2  | 2.23 / 96.2      | 0.19 / 60.4      |

Table 3.2: Same as table 3.1 but for the scaling indices at the largest scale  $r_{10}$ . The largest values for  $S$  are found for large scales non-Gaussianities in the  $l$ -range [2, 20].

are very remarkable, since they represent – to the best of our knowledge – by far the most significant detection of non-Gaussianities in the WMAP data to date. Note that we used here only the mean value of the distribution of scaling indices, which is a robust statistics not being sensitive to contributions of some spurious outliers. Further, the scale-independent statistics  $\chi^2_{\langle \alpha \rangle}$  calculated for the full sky represents a rather unbiased statistical approach.

The hemispherical asymmetry for NGs on large scales ( $\Delta l = [2, 20]$ ) finds its reflection in the results of  $S(r)$ . While we calculate significant and stable deviations  $S$  for the upper and lower hemispheres separately (red and blue lines) in fig. 3.4, the results for the full sky (black lines) are not significant, because the deviations detected in the two hemispheres are complementary and thus cancel each other. Therefore, we obtain only for the hemispheres high values for  $S$  ranging from  $S = 3.24$  up to  $S = 7.10$  ( $S = 4.11$  up to  $S = 10.82$ ) for the ILC7 (NILC5) map when considering the statistics derived from the scaling indices for the largest scales  $r_{10}$  and  $S = 4.01$  up to  $S = 9.76$  for the scale-independent  $\chi^2$ -statistics.

For the smallest scales considered so far ( $\Delta l = [120, 300]$ ) we also find significant deviations from non-Gaussianity being much more isotropic and naturally more pronounced at smaller scaling ranges  $r < 0.15$ . Thus, we obtain  $S = 6.97$  (ILC7 map) and  $S = 5.30$  (NILC5 map) for  $S(\langle \alpha(r_2) \rangle)$  considering the full sky. For the scale-independent  $\chi^2$ -statistics the most significant signatures of NGs are detected for the respective upper hemispheres ranging from  $S = 5.16$  to

| $\Delta l$                           | Full Sky     | Upper Hemisphere | Lower Hemisphere |
|--------------------------------------|--------------|------------------|------------------|
| $\chi^2_{(\alpha)}$ :                | ( $S/\%$ )   | ( $S/\%$ )       | ( $S/\%$ )       |
| [2, 1024]                            | 5.73 / >99.8 | 9.35 / >99.8     | 0.33 / 55.2      |
| [2, 20]                              | 0.97 / 95.0  | 4.57 / 99.6      | 4.01 / 99.2      |
| [20, 60]                             | 1.81 / 94.2  | 2.57 / 97.4      | 2.42 / 97.0      |
| [60, 120]                            | 1.41 / 99.0  | 1.53 / 99.6      | 0.91 / 83.8      |
| [120, 300]                           | 3.17 / 92.8  | 10.53 / >99.8    | 1.19 / 87.8      |
| $\chi^2_{\sigma_\alpha}$ :           |              |                  |                  |
| [2, 1024]                            | 5.50 / >99.8 | 11.50 / >99.8    | 0.66 / 79.6      |
| [2, 20]                              | 0.32 / 52.8  | 4.03 / 98.6      | 4.04 / 99.6      |
| [20, 60]                             | 2.15 / 95.8  | 4.00 / 99.8      | 2.18 / 96.4      |
| [60, 120]                            | 1.40 / 98.2  | 3.26 / 99.4      | 2.01 / 95.6      |
| [120, 300]                           | 3.10 / 99.0  | 8.90 / >99.8     | 1.90 / 95.8      |
| $\chi^2_{(\alpha), \sigma_\alpha}$ : |              |                  |                  |
| [2, 1024]                            | 1.89 / 94.2  | 8.38 / >99.8     | 3.03 / 98.8      |
| [2, 20]                              | 0.73 / 77.4  | 5.64 / >99.8     | 6.01 / 99.8      |
| [20, 60]                             | 1.60 / 92.8  | 3.42 / 99.2      | 1.49 / 91.0      |
| [60, 120]                            | 0.26 / 52.4  | 2.15 / 96.6      | 0.53 / 75.6      |
| [120, 300]                           | 1.68 / 92.8  | 5.34 / 99.8      | 0.22 / 63.2      |

Table 3.3: Same as table 3.1 but for the scale-independent  $\chi^2$ -statistics. Also for this statistics the largest values for  $S$  are found for the largest  $\Delta l = [2, 20]$  and smallest scales  $\Delta l = [120, 300]$  and for the scale-independent NGs.

$S = 10.53$ .

To test whether all these signatures are of intrinsic cosmic origin or more likely due to foregrounds or systematics induced by e.g. asymmetric beams or map making, we performed the same surrogate and scaling indices analysis for the five additional maps described in Section 2. Figs. 3.5 and 3.6 show the significance maps for the two  $l$ -ranges  $\Delta l = [2, 20]$  and  $\Delta l = [120, 300]$ , for which we found the most pronounced signatures in the ILC7 and NILC5 map. For the large scale NGs we find essentially the same results for the UILC7 map. The difference map, shows some signs of NGs and asymmetries, especially for large  $r$ -values. A closer look reveals, however, that both the numerator and denominator in the equation for  $S$  are an order of magnitude smaller than the values obtained for the ILC7 (NILC5) maps. Thus the signal of the difference map can be considered to be subdominant. And even if it were not subdominant, the signal coming from the residuals would rather diminish the signal in the ILC map than increase its significance, because the foreground signal is spatially anticorrelated with the CMB-signal. Both the asymmetric beam map and the simulated co-added VW-map do not show any significant signature for NGs and asymmetries. Finally, the simulated ILC map does show some signs of (galactic) north-south asymmetries which become smaller and therefore insignificant for increasing  $r$ , where we find the largest signal in the CMB maps.

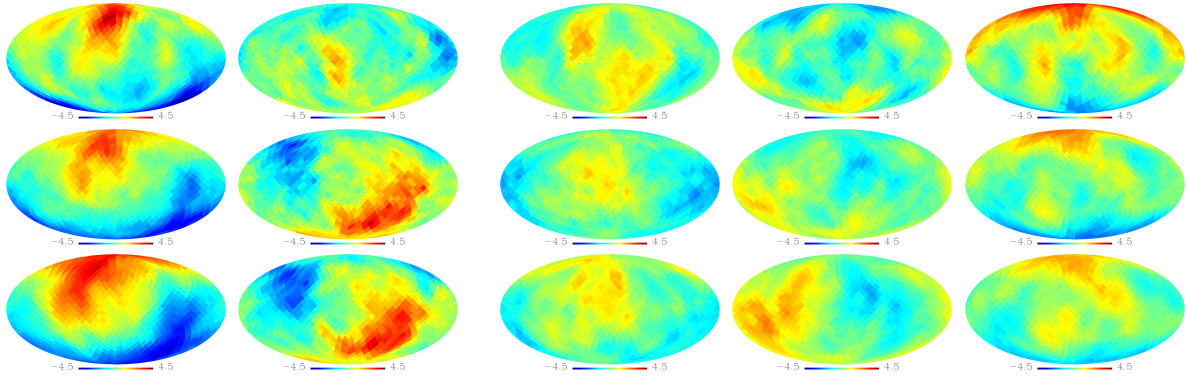


Figure 3.5: Deviations  $S(\langle\alpha(r_k)\rangle)$  for the three scales  $r_k, k = 2, 6, 10$  (from top to bottom) for  $\Delta l = [2, 20]$ . The results are shown for (from left to right) the UILC7 map, the difference map 7-year ILC - 6-year ILC map, the asymmetric beam map, the co-added V and W-band from a standard simulation and the simulated ILC-like map (for more detailed information about the different maps see text).

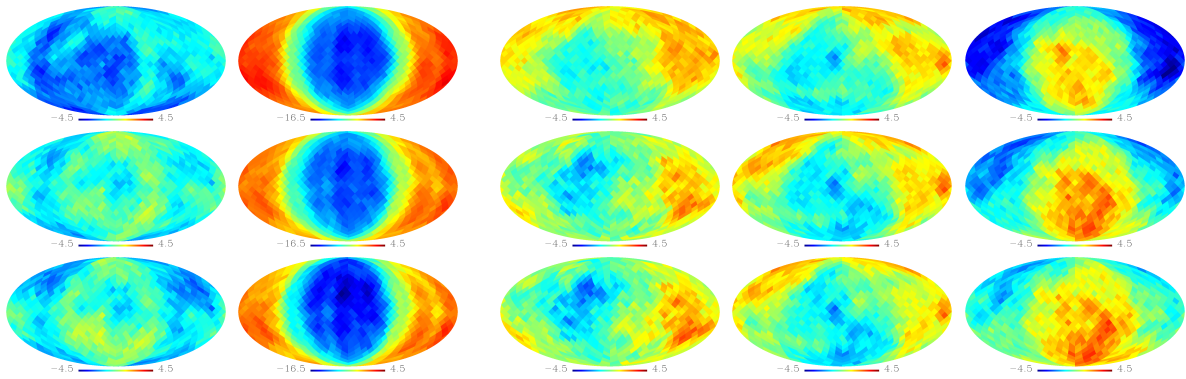


Figure 3.6: Same as Fig. 3.5 but for  $\Delta l = [120, 300]$ . Note that the scale for the color coding has significantly changed for the difference map (second column).

For the small scale NGs ( $\Delta l = [120, 300]$ ) we also find that the UILC7-map yields similar results as the ILC7 and NILC5 map with smaller significance. Once again the asymmetric beam map and the simulated co-added VW-map do not show significant signature for NGs and asymmetries. This is not the case for the simulated ILC map. Here, we find highly significant signatures for NGs and asymmetries, which show some similarities with significance patterns observed in the ILC7 (NILC5) map. Even much more striking features are detected in the difference map, where we find deviations as high as  $|S| \approx 15$  forming a very peculiar pattern in the significance maps for all  $r$ . One of us (G.R.) named this pattern 'Eye of Sauron', which we think is a nice and adequate association. It is worth noticing that we found the same pattern when analyzing other difference maps, e.g. year 7 - year 1 or year 2 - year 1.

To better understand, where these features may come from we had a closer look at the zeroth, first and second order surrogate maps. It became immediately obvious that for the difference maps the fluctuations are systematically smaller in the regions in the galactic plane used for the ILC-map making than in the rest of the sky. This effect persists in the first order surrogate map and is only destroyed in the second order surrogates. This more (less) structure

in first order surrogate map leads to lower (higher) values for the scaling indices, which can qualitatively explain the observed patterns in the significance maps.

A much more detailed study of these high  $l$  effects and their possible origins is part of our current work but is beyond the scope of this paper. The results for the difference map shown here point, however, already towards a very interesting application of the surrogate technique. It may become a versatile tool to define criteria of the cleanness of maps in the sense of e.g. absence of artificially induced (scale-dependent) NGs in the map of the residual signal. Such a criterion may then in turn be implemented in the map making procedure so that ILC-like maps are not only minimizing the overall quadratic error in the map, but also e.g. the amount of unphysical NGs of the foregrounds.

### 3.6 Conclusions

To the best of our knowledge this work represents the first comprehensive study of scale-dependent non-Gaussianities in full sky CMB data as measured with the WMAP satellite. By applying the method of surrogate maps, which explicitly relies on the scale-dependent shuffling of Fourier phases while preserving all other properties of the map, we find highly significant signatures of non-Gaussianities for very large scales and for the  $l$ -interval covering the first peak in the power spectrum. In fact, our analyses yield by far the most significant evidence of non-Gaussianities in the CMB data to date. Thus, it is no longer the question whether there are phase correlations in the WMAP data. It is rather to be figured out what the origin of these scale-dependent non-Gaussian signatures is. The checks on systematics we performed so far revealed that no clear candidate can be found to explain the low- $l$  signal, which we take to be cosmological at high significance. These findings would strongly disagree with predictions of isotropic cosmologies with single field slow roll inflation.

The picture is not that clear for the signatures found at smaller scales, i.e. at higher  $l$ 's. In this case we found that NGs can also easily be induced by the ILC map making procedure so that it is difficult to disentangle possible intrinsic anomalies from effects induced by the preprocessing of the data. More tests are required to further pin down the origin of the detected high  $l$  anomalies and to probably uncover yet unknown systematics being responsible for the low  $l$  anomalies. Another way of ruling out effects of unknown systematics is to perform an independent observation preferably via a different instrument as we are now able to do with the Planck satellite.

In any case our study has shown that the method of surrogates in conjunction with sensitive higher order statistics offers the potential to become an important tool not only for the detection of scale-dependent non-Gaussianity but also for the assessment of possibly induced artefacts leading to NGs in the residual map which in turn may have important consequences for the map making procedures.

### Acknowledgments

Many of the results in this paper have been derived using the HEALPix ([Górski et al. 2005](#)) software and analysis package. We acknowledge use of the Legacy Archive for Microwave Background Data Analysis (LAMBDA). Support for LAMBDA is provided by the NASA Office of Space Science.



## Chapter 4

# Non-Gaussianities identified with Minkowski Functionals and Scaling Indices

**Original publication:** H. I. Modest, C. Räth, A. J. Banday, G. Rossmannith, R. Sütterlin, S. Basak, J. Delabrouille, K. M. Górski and G. E. Morfill, *Scale-dependent non-Gaussianities in the CMB data identified with Minkowski functionals and scaling indices*, MNRAS, **428**, 551 (2013)

**Abstract:** We present further investigations of the *Wilkinson Microwave Anisotropy Probe* (WMAP) data by means of the Minkowski functionals and the scaling index method. In order to test for non-Gaussianities (NGs) with respect to scale-dependencies we use so-called surrogate maps, in which possible phase correlations of the Fourier phases of the original WMAP data and the simulations, respectively, are destroyed by applying a shuffling scheme to the maps. A statistical comparison of the original maps with the surrogate maps then allows to test for the existence of higher order correlations (HOCs) in the original maps, also and especially on well-defined Fourier modes.

We calculate the  $\sigma$ -normalized deviation between the Minkowski functionals of original data and 500 surrogates for different hemispheres in the sky and find ecliptic hemispherical asymmetries between the northern and southern ecliptic sky. Using Minkowski functionals as an image analysis technique sensitive to HOCs we find deviations from Gaussianity in the WMAP data with an empirical probability  $p > 99.8\%$  when considering the low- $\ell$  range with  $\Delta\ell = [2, 20]$ . The analysis technique of the scaling indices leads to the same results for this  $\ell$  interval with a slightly lower deviation but still at  $p > 99.8\%$ . Although the underlying foreground reduction methods of the maps differ from each other, we find similar results for the WMAP seven-year ILC map and the WMAP seven-year (needlet-based) NILC map for deviations from Gaussianity in the low- $\ell$  range. Our results point once more to a cosmological nature of the signal. For a higher  $\ell$  range with  $\Delta\ell = [120, 300]$  the results differ between the two image analysis techniques and between the two maps which makes an intrinsic nature of the signal on this  $\ell$  range less likely. When we decrease the size of the analyzed sky regions for the low- $\ell$  study, we do not find signatures of NG in the northern ecliptic sky. In the south we find individual spots which show deviations from Gaussianity.

In addition, we investigate non-Gaussian CMB simulations that depend on the  $f_{\text{NL}}$ -parameter

of the local type. These simulations with  $f_{\text{NL}}^{\text{local}} = [0, \pm 100, \pm 1000]$  cannot account for the detected signatures on the low- $\ell$  range.

## 4.1 Introduction

The primary anisotropies of the Cosmic Microwave Background (CMB) are caused by the primordial inhomogeneities of the Universe. They are assumed to be generated during a period of cosmic inflation and became the seeds for the structure of the density distribution in the Universe we observe today. The CMB was emitted from the surface of last scattering about 380,000 years after the Big Bang and the analysis of its  $\Delta T/T \simeq 10^{-5}$  temperature fluctuations help unraveling the mysteries of inflation.

The WMAP high resolution maps of the CMB allow detailed tests on the nature of the primordial density perturbations. The analysis of the CMB power spectrum is allowing for a high-precision determination of the fundamental cosmological parameters. However, any cosmological information that is encoded in the phases and correlations among them is not contained in the power spectrum and has to be extracted from measurements of higher-order correlations (HOCs).

Evidence for the existence or non-existence of non-Gaussianity (NG) is necessary to choose the correct class of scenarios for the very early Universe. The inflationary scenario (Guth 1981; Linde 1982; Albrecht & Steinhardt 1982) was proposed about 30 years ago to solve the flatness, monopole and horizon problems of standard Big Bang cosmology. It endorses homogeneity and isotropy of the Universe, provides a mechanism for the generation of primordial, approximately scale-invariant and approximately Gaussian density perturbations and its predictions are consistent with the observed power spectrum (Komatsu et al. 2011).

The Gaussian distribution of scalar (density) and tensor (metric) perturbations is a generic prediction of single-field slow-roll inflationary models. Yet, it has been shown that single field as well as two-/multi-field models (Linde & Mukhanov 1997; Bartolo et al. 2002; Bernardeau & Uzan 2002; Vernizzi & Wands 2006) generate a small amount of non-Gaussianity, below our current experimental limits though (Maldacena 2003; Acquaviva et al. 2003). Models where the primordial density perturbations are generated by a curvaton field may predict a high level of NG (Moroi & Takahashi 2001; Enqvist & Sloth 2002; Lyth et al. 2003). There are many more alternative inflationary scenarios which could generate NG at an observable level, e.g. Dirac-Born-Infeld inflation (Silverstein & Tong 2004; Alishahiha et al. 2004) or ghost inflation (Arkani-Hamed et al. 2004). See also review articles on NGs from inflationary models written by Bartolo et al. (2004) and Chen (2010). The determination of non-Gaussianity would make it possible to distinguish between these different inflationary models. However, inflation still remains as a paradigm and a determination of NGs would also constrain alternatives, e.g. ekpyrotic and cyclic models (Buchbinder et al. 2008; Lehnert & Steinhardt 2008), and help unraveling the nature of the primordial density perturbations in general.

Various methods of statistical analysis of the WMAP data claim the detection of non-Gaussianity and different anomalies like hemispherical asymmetries, lack of power at large angular scales, alignment of multipoles, detection of the Cold Spot, etc. (Park 2004; Eriksen et al. 2004a, 2005, 2007; Hansen et al. 2004, 2009; de Oliveira-Costa et al. 2004; Vielva et al. 2004; Rossmanith et al. 2009). In these studies, the level of NG is assessed by comparing WMAP data with simulated model-dependent CMB maps based on cosmological models and/or specific assumptions about the nature of non-Gaussianities as parametrized with e.g. the scale-independent scalar parameters  $f_{\text{NL}}$  and  $g_{\text{NL}}$ . Fewer studies are testing the random phase hypothesis for Gaussian random fields analyzing the distribution of the Fourier phases

of the data (Chiang et al. 2003; Coles et al. 2004; Naselsky et al. 2005; Chiang et al. 2007). These model-independent tests also show signatures of anomalies and non-Gaussianities.

In this paper, we apply the well established method of surrogate data sets to analyze Fourier phase correlations in the WMAP data. The method of the surrogates has first been established in Theiler et al. (1992) in order to detect weak nonlinearities in time series. For given possibly nonlinear data, so-called surrogate data sets are generated, which mimic the linear properties of the original time series. A comparison of original data set and surrogates through statistical measures sensitive to higher order correlations (HOCs) can reveal a significant deviation from linearity in the data. Extensions to this formalism to three-dimensional galaxy distributions (Räth et al. 2002) and two-dimensional simulated flat CMB maps (Räth & Schuecker 2003) have been proposed and discussed. In a prior report, we introduced a two-step surrogatization scheme for full sky CMB observations which allows for a scale-dependent analysis of the data (Räth et al. 2009). This method yields significant signatures for both NG and ecliptic hemispherical asymmetries (Räth et al. 2009, 2011), especially on largest scales ( $\ell \leq 20$ ). In these papers, the HOCs are measured with the weighted scaling index method (SIM) introduced in Räth et al. (2002), Räth & Schuecker (2003) and Räth et al. (2007). The image data is represented as a point distribution comprising the spatial and scalar information of each pixel. The scaling indices then offer the possibility to estimate the local scaling properties of such a point distribution and depend on a scale parameter  $r$ .

We concentrate on the set of statistics known as Minkowski Functionals (MFs) as a comparative measure sensitive to HOCs. A general theorem of integral geometry states that three Minkowski Functionals quantify the integrated geometry and topology and therefore morphology of a two-dimensional density field. For a pixelized temperature map  $\Delta T/T(n)$ , we consider the excursion sets of the map, defined as the set of all map pixels with value of  $\Delta T/T(n)$  greater than some threshold level  $v$ . The Minkowski functionals of these excursion sets completely describe the morphological properties of the underlying temperature map  $\Delta T/T(n)$ . These measures embody the information from all orders of the correlation functions. They are additive measures which allows us to calculate them efficiently by summing up their local contributions. The calculation of n-point correlation functions is much more expensive computationally (Eriksen et al. 2005; Szapudi 2009). In comparison to the SIM the Minkowski functionals are scale-independent, i.e. they do not depend on any scale parameter.

We apply our methods to WMAP seven-year ILC and NILC maps. Furthermore, we simulate and analyze non-Gaussian CMB maps that depend on the scale-independent  $f_{\text{NL}}^{\text{local}}$  parameter and serve as first toy models for further tests on inflationary models.

The paper is organized as follows. In Section 2 we briefly describe the observational and simulated data we use in our study. The method of generating surrogate maps is reviewed in Section 3. A discussion and comparison of the used test statistics, Minkowski functionals and scaling indices, can be found in Section 4. In Section 5 we present our results and we draw our conclusions in Section 6.

## 4.2 Data Sets and Simulations

For our studies we use the WMAP seven-year foreground-cleaned internal linear combination map (in the following: ILC7) generated and provided by Gold et al. (2011). This map can be directly downloaded from the LAMBDA-website<sup>1</sup> with a HEALPix<sup>2</sup> (Górski et al. 2005) resolution parameter of  $N_{\text{side}} = 512$ , corresponding to 3,145,728 sky pixels. The ILC7 map

<sup>1</sup><http://lambda.gsfc.nasa.gov>

<sup>2</sup><http://healpix.jpl.nasa.gov>

has one degree FWHM. For comparison we also include the seven-year needlet-based ILC map (in the following: NILC7) produced by [Basak & Delabrouille \(2012\)](#) pursuing a different approach for foreground removal. Because the needlet implementation of the ILC allows for optimizing weights both as a function of sky direction and as a function of scale, the NILC7 is significantly less contaminated by foregrounds than other existing maps obtained from WMAP, in particular at low Galactic latitude (see [Delabrouille et al. \(2009\)](#) for a description of the needlet ILC method). It features a better total resolution, corresponding to the WMAP W-band resolution, and has an original HEALPix resolution of  $N_{\text{side}} = 1024$ . We downgrade the map to  $N_{\text{side}} = 512$  in the employed HEALPix software. The ILC7 as well as the NILC7 map are weighted linear combinations of the five frequency channels  $K, Ka, Q, V$  and  $W$  that recover the CMB signal even in heavily foreground affected regions. The weights are calculated by requiring minimum variance in a given region of the sky under the constraint that the sum of the weights is unity. Full sky maps ensure the required orthogonality of the set of basis functions  $Y_{\ell m}$  when generating surrogates.

For our comparison of the ILC7 and NILC7 maps on larger scales,  $120 \leq \ell \leq 300$ , we choose to decrease the resolution of the original NILC7 map down to one degree FWHM before downgrading to a HEALPix resolution of  $N_{\text{side}} = 512$ . In these higher  $\ell$ -ranges the beam effects have stronger influences. For our studies of the low- $\ell$  ranges with  $0 \leq \ell \leq 20$  this influence is negligible.

The primordial non-Gaussianity that might arise during cosmic inflation has often been parametrized by the  $f_{\text{NL}}$  parameter in the following simple form of the curvature perturbation  $\Phi$  ([Bardeen 1980](#)) with quadratic correction

$$\Phi(x) = \Phi_L(x) + f_{\text{NL}} \Phi_{\text{NL}}(x) \quad (4.1)$$

where  $\Phi_L$  are Gaussian linear perturbations and  $\Phi_{\text{NL}}(x)$  is defined as

$$\Phi_{\text{NL}}(x) = \Phi_L^2(x) - \langle \Phi_L^2(x) \rangle \quad (4.2)$$

and  $f_{\text{NL}}$  characterizes the dimensionless amplitude of quadratic correction. This form of  $f_{\text{NL}}$  describes non-Gaussianity of the local type. In order to test for possible impacts of local type NG on the data, we compare the results obtained from the original data to models based on a scale-independent  $f_{\text{NL}}^{\text{local}}$  parameter. Therefore, we compute temperature maps as constrained realizations of non-linear fields with varying  $f_{\text{NL}}^{\text{local}}$ .

The spherical harmonic coefficients  $a_{\ell m}$  of the CMB temperature ( $i = T$ ) and polarisation ( $i = E$ ) anisotropies in harmonic space are related to the primordial fluctuations  $\Phi_{\ell m}(x)$  via

$$a_{\ell m}^i = \int dx x^2 \Phi_{\ell m}(x) \alpha_{\ell}^i(x) \quad (4.3)$$

as a function of comoving distance  $x$ , where  $\alpha_{\ell}^i(x)$  is the real space transfer function. A set of linear and non-linear spherical harmonic coefficients are a valid realization of temperature and polarization fluctuations for a given cosmological model, in this case  $\Lambda$ CDM model. The total  $a_{\ell m}$  coefficients and a desired level of  $f_{\text{NL}}^{\text{local}}$  NG are then calculated as

$$a_{\ell m} = a_{\ell m}^{\text{linear}} + f_{\text{NL}} * a_{\ell m}^{\text{non-linear}}, \quad (4.4)$$

where the linear and non-linear  $a_{\ell m}$  coefficients are provided by [Elsner & Wandelt \(2009\)](#).

To explore the plausibility of  $f_{\text{NL}}$  as an explanation for the observed large-scale NGs, we use these  $a_{\ell m}$  coefficients to simulate five co-added VW-band maps with  $f_{\text{NL}}^{\text{local}} = [0, \pm 100, \pm 1000]$ .

As shown in [Räth et al. \(2011\)](#) the results for the method of surrogates of the simulated VW-band maps are similar to those of ILC-like simulations on large scales. The specific beam properties of the WMAP satellite are taken into account using the respective window functions for each differencing assembly ( $V1 - V2, W1 - W4$ ), being available again on the LAMBDA-website<sup>1</sup>. For every assembly, we add Gaussian noise to these maps with a particular variance for every pixel of the sphere. This variance depends on the number of observations  $N_i(\boldsymbol{\theta}, \boldsymbol{\phi})$  in the respective direction and the noise dispersion per observation per different assembly,  $\sigma_{0,i}$ . After this procedure, we accumulate the V- and W-bands to a co-added VW-band via a noise-weighted sum ([Bennett et al. 2003](#)):

$$T(\boldsymbol{\theta}, \boldsymbol{\phi}) = \frac{\sum_{i \in \mathcal{A}} T_i(\boldsymbol{\theta}, \boldsymbol{\phi}) / \sigma_{0,i}^2}{\sum_{i \in \mathcal{A}} 1 / \sigma_{0,i}^2} \quad (4.5)$$

In this equation,  $\mathcal{A}$  characterizes the set of required assemblies, for the co-added VW-map  $\mathcal{A} = \{V1, V2, W1, W2, W3, W4\}$ . The parameters  $\boldsymbol{\theta} = [0, \pi]$  and  $\boldsymbol{\phi} = [0, 2\pi]$  correspond to the co-latitude and the longitude on the sphere, while the seven-year noise per observation of the different assemblies is denoted by  $\sigma_0$ , given by [Jarosik et al. \(2011\)](#). Again, the maps are decreased to a HEALPix resolution of  $N_{\text{side}} = 512$ . Finally, we remove the residual monopole and dipole by means of the appropriate HEALPix routine.

### 4.3 Method of Surrogates

In order to constrain possible phase-correlations of the Fourier phases of the cosmic microwave background, we generate so-called surrogate maps as proposed in [Räth & Schuecker \(2003\)](#). We destroy possible phase correlations in the data by applying a shuffling scheme to the phases. In order to test for the scale-dependence of non-Gaussianity this is done with a two-step procedure.

The full sky CMB temperature anisotropy map of the celestial sphere with  $\Delta T / T(\mathbf{n}) \equiv \Delta T / T(\boldsymbol{\theta}, \boldsymbol{\phi})$  can be expanded in orthonormal spherical harmonics  $Y_{\ell m}$  as

$$\Delta T / T(\boldsymbol{\theta}, \boldsymbol{\phi}) = \sum_{l=0}^{\infty} \sum_{m=-l}^l a_{\ell m} Y_{\ell m}(\boldsymbol{\theta}, \boldsymbol{\phi}) \quad (4.6)$$

with the complex spherical harmonic coefficients

$$a_{\ell m} = \int d\mathbf{n} T(\mathbf{n}) Y_{\ell m}^*(\mathbf{n}) \quad (4.7)$$

where  $\mathbf{n}$  is the unit direction vector and  $a_{\ell m} = |a_{\ell m}| e^{i\phi_{\ell m}}$ . The linear properties of the underlying density field are contained in the absolute values  $|a_{\ell m}|$ , whereas all HOCs - if existent - are encoded in the phases  $\phi_{\ell m}$  and the correlations among them. If the spherical harmonic coefficients are independent Gaussian random variables their probability density is

$$P(a_{\ell m}) da_{\ell m} = \frac{1}{\sqrt{2\pi C_\ell}} e^{-\frac{a_{\ell m}^2}{2C_\ell}} da_{\ell m} \quad (4.8)$$

(e.g. [Rubakov & Vlasov \(2012\)](#)) and the orthonormality relation holds:

$$\langle a_{\ell m} a_{\ell' m'}^* \rangle = \delta_{\ell\ell'} \delta_{mm'} C_\ell, \quad (4.9)$$

where  $C_\ell$  is the angular power spectrum and  $\delta$  is the Kronecker delta. In this case, the amplitude  $|a_{\ell m}|$  would be Rayleigh-distributed and the phase  $\phi_{\ell m} = \arctan(\text{Im}(a_{\ell m}) / \text{Re}(a_{\ell m}))$  would

be independent and identically distributed (i.i.d.) and follow a uniform distribution in the interval  $[-\pi, \pi]$ . The temperature values themselves would be normally distributed as well. The measured angular power spectrum  $C_\ell^{\text{obs}}$  depends on the  $a_{\ell m}$  coefficients by

$$C_\ell^{\text{obs}} = \frac{1}{2\ell + 1} \sum_{m=-\ell}^{\ell} |a_{\ell m}|^2, \quad (4.10)$$

where  $\langle C_\ell^{\text{obs}} \rangle = C_\ell$ . In case the CMB variables  $a_{\ell m}$  are independent and Gaussian distributed and their phases are therefore i.i.d. (independent and identically distributed) and consequentially uncorrelated, it is adequate (Komatsu et al. (2009b) and references therein) to only investigate the linear properties of the data described by the power spectrum  $C_\ell$ . In this paper, we focus on the non-linear information and test for possible *phase correlations* of  $\phi_{\ell m}$  in the data, which we define as non-Gaussianities of the CMB, to check if the above requirements are fulfilled.

To test the hypothesis of independent Fourier phases we try to exclude further features of the data as e.g. artefacts due to experimental constraints. Therefore, we make sure that the data meets the following two requirements before generating the surrogate maps. The temperature distribution is Gaussian and the set of phases is uniformly distributed in the interval  $[-\pi, \pi]$ . To fulfill these conditions we perform two preprocessing steps. First, the almost Gaussian distributed temperature values of the original map in real space are replaced by an exact Gaussian distribution in a rank-ordered way, i.e. the lowest value of the original distribution is replaced with the lowest value of the Gaussian distribution etc. Second, in order to guarantee that the phases  $\phi_{\ell m}$  are identically distributed the Fourier phases are remapped on to a set of uniformly distributed ones. No significant dependence on the specific Gaussian or uniform realization, respectively, was found in these preprocessing steps.

The scale dependent surrogate maps that are later analyzed are obtained as follows. In our scale-dependent analysis we focus on the two  $\ell$ -ranges  $\Delta\ell_1 = [2, 20]$  and  $\Delta\ell_2 = [120, 300]$ . The interval  $\Delta\ell_1$  covers the largest spatial scales of the CMB, while the first peak of the power spectrum lies in the interval  $\Delta\ell_2$ . Our previous results have shown that findings of an almost scale-independent analysis with a shuffling range  $\Delta\ell = [2, 1024]$  are only the superposition of signals from the analysis with  $\Delta\ell_1$  and  $\Delta\ell_2$  shuffling ranges (Räth et al. 2011). Therefore, we assume that the results of these two intervals are of special interest in the analysis of phase correlations. We first generate a first order surrogate map, in which any correlation of phases  $\phi_{\ell m}$  with  $\ell$  outside the certain  $\Delta\ell$ -range of interest is destroyed: The phases  $\phi_{\ell m}$  with  $2 \leq \ell \leq 1024$  and  $\ell \notin \Delta\ell = [\ell_{\min}, \ell_{\max}]$ ,  $0 < m \leq \ell$ , are randomized through a shuffling procedure. In a second step,  $N$  ( $N = 500$  throughout this study) realizations of second order surrogate maps are generated from the first order surrogate map: The remaining phases  $\phi_{\ell m}$  with  $\ell \in \Delta\ell = [\ell_{\min}, \ell_{\max}]$  are shuffled, while the already randomized phases in the first order surrogate for the scales not under consideration are preserved. Note that the Gaussian properties of the maps, which are given by  $|a_{\ell m}|$ , are exactly preserved for all surrogate maps.

The first order surrogate preserves phase correlations in the  $\Delta\ell$  range, if they were present in the original maps. In the second order surrogate map, where all phases are randomly distributed, all original correlations will be completely destroyed. The statistical comparison of the two classes of surrogates will thus reveal possible higher order correlations in the original maps on defined Fourier modes and uncover signatures for deviations from Gaussianity.

One might argue that the above discussed phase shuffling is not the intuitive approach, since it is also possible to construct surrogates (of first as well as of second order) by just replacing the respective Fourier phases with randomly generated ones. In order to account for

this aspect, we additionally investigate surrogates (for selected data sets) that were constructed by replacing the phases with a completely new set of uniform distributed values in the interval  $[-\pi, \pi]$ . Note that for this replacement approach, one has to generate a new set of phases for the relative  $\ell$ -interval. It might be preferable to only rely on the information which is given in the underlying data set, instead of adding something new.

Before analyzing the maps with different image analysis techniques we decrease the HEALPix resolution of the maps from  $N_{\text{side}} = 512$  to  $N_{\text{side}} = 256$  for the data analysis and  $N_{\text{side}} = 64$  for the simulated maps.

## 4.4 Test Statistics

### 4.4.1 Minkowski Functionals

A full morphological specification of an image requires geometrical as well as topological descriptors to characterize not only the shape and content but also the connectivity of spatial patterns. Hadwiger's theorem (Hadwiger 1957) in the field of integral-geometry states that any complete morphological descriptor of a set  $Q$  in  $d$ -dimensional Euclidian space  $\mathbb{E}^d$  is a linear combination of only  $d + 1$  functionals which meet some simple requirements; the so-called Minkowski Functionals  $M_j$  with  $j$  ranging from 0 to  $d$ . Functional  $M_0$  and  $M_1$  in two-dimensional space can be interpreted as the familiar geometric quantities surface area and perimeter, respectively. Functional  $M_2$  is the topological Euler characteristic. In spherical, two-dimensional CMB sky map space  $\mathbb{S}^2$  of radius  $R$  and a constant curvature  $K = R^{-2}$  they are formally defined as

$$\begin{aligned} M_0 &= \int_Q da \\ M_1 &= \frac{1}{4} \int_{\partial Q} dl \\ M_2 &= \frac{1}{2\pi} \int_{\partial Q} dl k_g, \end{aligned}$$

where  $da$  and  $dl$  denote the surface element of  $\mathbb{S}^2$  and the line element along the smooth boundary  $\partial Q$ , respectively, as explained in Schmalzing & Górski (1998). The factor  $k_g$  is the geodesic curvature. The Minkowski functionals have been introduced into cosmology as descriptors for the morphological properties of large-scale structure by Mecke et al. (1994) and of CMB sky maps by Winitzki & Kosowsky (1998) and Schmalzing & Górski (1998).

In order to study the morphology of the temperature anisotropies  $\Delta T/T(n)$ , which can be considered as a smooth scalar field on  $\mathbb{S}^2$ , we calculate the three Minkowski Functionals (MFs) of excursion sets  $Q_v$  in the pixelised spherical two-dimensional maps of original data, surrogates and simulations.  $Q_v$  is defined as the set of all map pixels with value of  $\Delta T/T$  greater than or equal to some temperature threshold  $v$  by  $Q_v = \{n \in \mathbb{S}^2 | \Delta T/T(n) \geq v\}$ .

The maps we are analyzing are pixelised according to the HEALPix pixelisation scheme. HEALPix produces a partition of a spherical surface into exactly equal area quadrilateral pixels of varying shape which simplifies the calculation of the Minkowski functionals. The pixel size depends on the HEALPix resolution parameter of the grid equal to  $N_{\text{side}} = 1, 2, 4, 8, \dots$  corresponding to a total number of pixels of  $N_{\text{pix}} = 12 \times N_{\text{side}}^2 = 12, 48, 192, 768, \dots$ . In this work we use a resolution parameter of  $N_{\text{side}} = 256$  and  $N_{\text{side}} = 64$ , respectively.

The temperature maps we want to analyze are divided into an active and a non-active part by running over 200 threshold steps  $v_i$  with  $-4\sigma_T \leq v_i \leq +4\sigma_T$ . At the first threshold step  $v_0$

nearly every pixel is included in the active part besides few outliers with  $T < -4\sigma_T$ . The last step  $v_{199}$  excludes most of the pixels.

We adapted an algorithm of [Michielsen & De Raedt \(2001\)](#) to compute the Minkowski functionals of the pixelized maps. Conceptually, each active pixel is decomposed into 4 vertices, 4 edges and the interior of the pixel. We count the total number of active squares  $n_s$  and edges  $n_e$  and vertices  $n_v$  between active and non-active pixels and compute the area  $M_0$ , the integral mean curvature or perimeter  $M_1$  and the Euler characteristic  $M_2$  from

$$\begin{aligned} M_0 &= n_s \\ M_1 &= -4n_s + 2n_e \\ M_2 &= n_s - n_e + n_v. \end{aligned}$$

A technical difficulty with this procedure is to avoid counting an edge or vertex more than once. As suggested by [Michielsen & De Raedt \(2001\)](#) we build up the original image by adding active pixels to an initially empty temporary image one by one. Depending on whether the surrounding pixels have already been activated in the temporary image or not, we then add up edges and vertices to their total numbers. The number of arithmetic operations required to compute  $M_0$ ,  $M_1$ , and  $M_2$  scales linearly with the number of active pixels and the total number of pixels of the image.

#### 4.4.2 Weighted Scaling Indices

For comparison we assess possible scale-dependent NGs in the CMB with the scaling indices method (SIM) as done in our series of earlier papers ([Räth et al. 2002](#); [Räth & Schuecker 2003](#); [Räth et al. 2007, 2009](#); [Rossmannith et al. 2009](#); [Räth et al. 2011](#); [Rossmannith et al. 2011](#)). The basic idea for this test statistic comes from the calculation of the dimensions of attractors in non-linear time series analysis ([Grassberger & Procaccia 1983](#)). The scaling indices have been extended to the field of image processing for texture discrimination. If the image data is represented as a point distribution in a  $d$ -dimensional embedding space the scaling indices represent one way to estimate the local morphological properties of this point set. Point-like, ring-like and sheet-like structures can be discriminated from each other and from a random background.

In order to apply the SIM on the spherical CMB data, we have to transform the temperature anisotropies  $\Delta T/T(n_i)$  with its pixels at positions  $n_i = (\theta_i, \phi_i)$ ,  $i = 1, \dots, N_{pix}$  on the sphere to a three-dimensional point distribution of  $N_{pix}$  points  $P = \{\mathbf{p}_i\}$  in an artificial embedding space, for which then the local scaling properties are assessed with the SIM.

For each point the local weighted cumulative point distribution  $\rho$  is calculated as

$$\rho(\mathbf{p}_i, r) = \sum_{j=1}^{N_{pix}} s_r[d(\mathbf{p}_i, \mathbf{p}_j)] \quad (4.11)$$

where  $s_r(\bullet)$  denotes a shaping function depending on a scale parameter  $r$  and a distance measure  $d(\bullet)$ . In principle any differentiable shaping function and any measure can be used for calculating the scaling indices. We use the Euclidian norm as distance measure and set of Gaussian shaping functions, which leads to

$$\rho(\mathbf{p}_i, r) = \sum_{j=1}^{N_{pix}} e^{-\frac{d_{ij}^2}{r}}, d_{ij} = \|\mathbf{p}_i - \mathbf{p}_j\|. \quad (4.12)$$

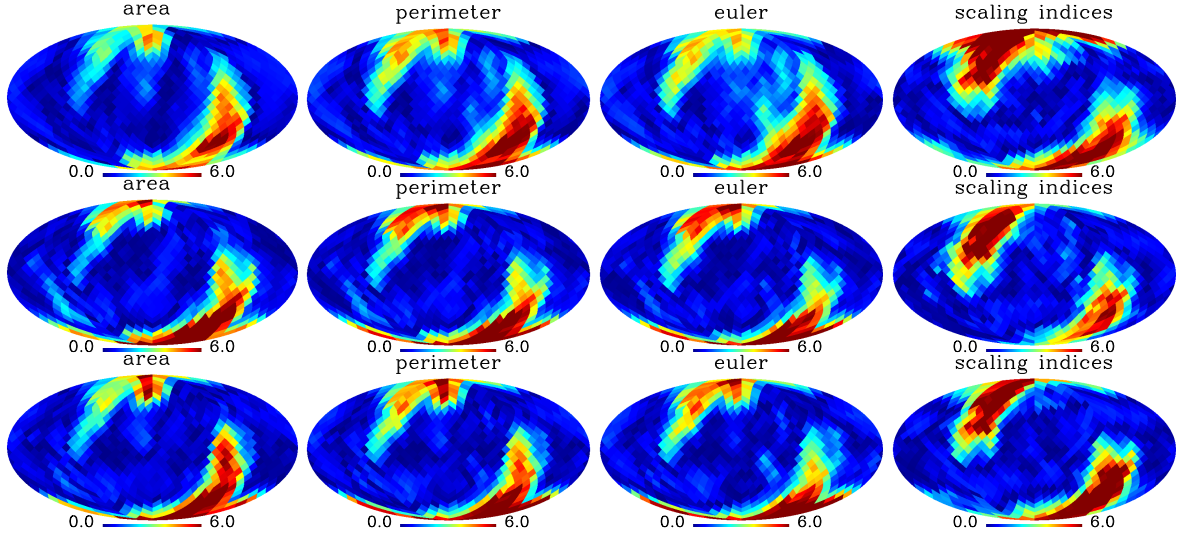


Figure 4.1: Deviations  $S(\chi^2)$  of Minkowski Functionals  $M_0$ ,  $M_1$  and  $M_2$  of the rotated hemispheres for the ILC7 (upper row) and NILC7 map (middle row) in Galactic coordinates. In the lower row we show the results of the phase replacement method for NILC7. The plots to the very right show the corresponding results  $S(\chi^2)$  for the respective maps gained by the scaling index method. The  $\ell$ -range for the method of the surrogates is  $\Delta\ell = [2, 20]$ .

The weighted scaling indices  $\alpha(\mathbf{p}_i, r)$  are then obtained by calculating the logarithmic derivative of  $\rho(\mathbf{p}_i, r)$  with respect to  $r$ :

$$\alpha(\mathbf{p}_i, r) = \frac{\partial \log \rho(\mathbf{p}_i, r)}{\partial \log(r)}. \quad (4.13)$$

With the definition in Equation 4.12 the weighted scaling indices are expressed by

$$\alpha(\mathbf{p}_i, r) = \frac{\sum_{j=1}^{N_{pix}} q \left( \frac{d_{ij}}{r} \right)^q e^{-\left( \frac{d_{ij}}{r} \right)^q}}{\sum_{j=1}^{N_{pix}} e^{-\left( \frac{d_{ij}}{r} \right)^q}}. \quad (4.14)$$

#### 4.4.3 Statistical Interpretation

The two image analysis techniques, Minkowski functionals and scaling indices, are applied to scale-dependent full sky surrogate maps and 768 overlapping hemispherical maps, with two different solid angles: a solid angle of  $2\pi$  (apex angle  $\pi$ ) and  $\sim 0.6\pi$  (apex angle  $\pi/2$ ). These hemispherical maps are rotated around the full sky to study possible scale-dependent phase-correlations in the Fourier space of the maps with a certain spatial localization of the phenomena. In this paper we focus on the analysis of the Minkowski functionals and compare our results to the scaling index method.

In order to quantify the degree of agreement between the surrogates of different orders with respect to higher order correlations found with the three Minkowski functionals  $M_0, M_1$  and  $M_2$  we calculate the mean of each Minkowski functional  $M_{\star, surro2}$  for  $N = 500$  realizations of the second order surrogate per hemisphere  $h$  and threshold bin  $\mathbf{v}$

$$A := \langle M_{\star, surro2}(\mathbf{v}, h) \rangle = \frac{1}{N} \sum_{m=1}^N M_{\star, surro2}(m, \mathbf{v}, h)$$

and the standard deviation

$$\sigma_{M_{\star, \text{surro2}}}(\mathbf{v}, h) = \left( \frac{1}{N-1} \sum_{m=1}^N (M_{\star, \text{surro2}}(m, \mathbf{v}, h) - A)^2 \right)^{1/2}$$

for  $m = 1, \dots, N$ . We combine mean and standard deviation in a diagonal  $\chi^2$  statistic per hemisphere  $h$  for the surrogates of first order

$$\chi_{M_{\star, \text{surro1}}}^2(h) = \sum_{j=0}^{\mathbf{v}} \left[ \frac{M_{\star, \text{surro1}}(\mathbf{v}, h) - A}{\sigma_{M_{\star, \text{surro2}}}(\mathbf{v}, h)} \right]^2$$

and for the second order surrogate maps

$$\chi_{M_{\star, \text{surro2}}}^2(h, m) = \sum_{j=0}^{\mathbf{v}} \left[ \frac{M_{\star, \text{surro2}}(m, \mathbf{v}, h) - A}{\sigma_{M_{\star, \text{surro2}}}(\mathbf{v}, h)} \right]^2.$$

Finally, the degree of agreement between the two types of surrogates is quantified by the  $\sigma$ -normalized deviation  $S$

$$S(\chi_{M_{\star}}^2(h)) = \frac{\chi_{M_{\star, \text{surro1}}}^2(h) - \langle \chi_{M_{\star, \text{surro2}}}^2(h) \rangle}{\sigma_{\chi_{M_{\star, \text{surro2}}}^2}(h)} \quad (4.15)$$

for each of the 768 hemispheres with  $\langle \chi_{M_{\star, \text{surro2}}}^2(h) \rangle$  and  $\sigma_{\chi_{M_{\star, \text{surro2}}}^2}(h)$  denoting the mean and the standard deviation of  $\chi_{M_{\star, \text{surro2}}}^2(h)$  for the  $N = 500$  second order surrogates. Thus, we obtain the  $\sigma$  normalized hemispherical deviations  $S(\chi_{M_0}^2(h))$ ,  $S(\chi_{M_1}^2(h))$  and  $S(\chi_{M_2}^2(h))$  for the Area, Perimeter and Euler characteristics.

As for the Minkowski functionals, we calculate the mean  $\langle \alpha(r) \rangle$  and standard deviation  $\sigma_{\alpha(r)}$  of the scaling indices  $\alpha(\mathbf{p}_i, r)$  for the set of 768 hemispherical maps. The scaling indices are calculated with a scale parameter  $r = 0.25$ , which corresponds to  $r_{10}$  as defined in our earlier works, e.g in [Rossmanith et al. \(2009\)](#). The differences of the two classes of surrogates are again quantified by the  $\sigma$ -normalized deviation  $S$ :

$$S(Y) = \frac{Y_{\text{surro1}} - \langle Y_{\text{surro2}} \rangle}{\sigma_{Y_{\text{surro2}}}} \quad (4.16)$$

where  $Y$  represents a diagonal  $\chi^2$  statistic

$$\chi_{\langle \alpha(r) \rangle, \sigma_{\alpha(r)}}^2 = \sum_{j=1}^2 \left[ \frac{B_j - \langle B_j \rangle}{\sigma_{B_j}} \right]^2, \quad (4.17)$$

as a combination of the mean and the standard deviation where  $B_1(r) = \langle \alpha(r) \rangle$ ,  $B_2(r) = \sigma_{\alpha(r)}$ . See [Räth et al. \(2007\)](#) for a detailed description regarding the scaling indices statistics.

The results we obtain with the hemispherical study of the sky are visualized in so-called  $S$ -maps. Each pixel centre of a full sky map with a HEALPix resolution of  $N_{\text{side}} = 8$  marks one of the 768 hemispheres' poles. After calculating the deviation  $S$  between one first order surrogate and 500 realizations of second order surrogates for each individual hemisphere, we plot the respective value in a sky map at that pixel position where the  $z$ -axis of the rotated hemisphere pierces the sky. This is done for both, the Minkowski functionals and the scaling indices. For one single  $S$ -map with 768 values stemming from the comparison of 500 surrogates of second order with one first order surrogate we need to calculate 384,768 hemispherical maps.

## 4.5 Results and Discussion

### 4.5.1 ILC and NILC Maps

Figure 4.1 shows the  $S$ -values per hemisphere for a deviation from Gaussianity in ILC7 and NILC7 data on largest scales with  $\Delta\ell = [2, 20]$ , found with the method of surrogates by using a shuffling approach and a phase replacement procedure, respectively, and analyzed by the Minkowski functionals as well as the scaling index method. The  $\chi^2$ -statistics of the two image analysis techniques yield consistent results on largest scales and show significant signatures for ecliptic hemispherical asymmetries and non-Gaussianity in CMB sky maps. The signal for the Minkowski functionals is maximal in the southern ecliptic sky whereas for the SIM we find the maximum in the northern ecliptic sky. In Table 4.1 and 4.2 we summarized the deviations  $S$  and the empirical probabilities  $p$  of the three Minkowski functionals and the SIM. The results are shown for the full sky and a pair of hemispheres which consists of the hemisphere with maximum  $S(\chi^2)$  and its opposing hemisphere on the other side of the sky.

The two CMB maps, ILC7 and NILC7, are different enough in their implementation that the presence of residual foregrounds and noise, if important in the present analysis, is not expected to result in similar NG detections. The needlet ILC is, in principle, less contaminated by foregrounds and noise, as shown on 5-year data by Delabrouille et al. (2009). However, the pattern in the  $S$ -maps of these two maps are almost identical to each other. The  $\sigma$ -normalized deviations  $S$  are higher for the NILC map and range up to 9.97 for the perimeter with an empirical probability above 99.8%. The stronger signatures for NGs in the NILC map can further be attributed to the fact that this map did not undergo the one-degree smoothing of the ILC7 map.

Expectedly, the replacement of the original phase distribution by a distribution of random values in NILC7 during the surrogates generating process yields the same pattern in the  $S$ -maps as for the shuffling procedure. However, the shuffling approach avoids any dependence on additional data and is therefore preferable for generating surrogates.

We show that the scale-dependence of the scaling index method is not a limitation to that measure since the scale-independent  $\chi^2$  statistic of the Minkowski functionals still yields the same results as the scale-dependent  $\chi^2$  statistic of the scaling indices, that depends on scale parameter  $r$ .

All three Minkowski functionals area, perimeter and Euler as well as the SIM detect phase correlations and therefore non-Gaussianities in the data with almost identical spatial signatures. However, the single values in the  $S$ -maps do not demonstrate local NGs but must be interpreted as an overall signal per hemisphere. Note that in this hemispherical study large overlapping sky patches have been analyzed.  $S$ -values in the upper sky also account for signal from the lower sky and the other way around.

In Figure 4.2 and 4.3, the three Minkowski functionals area, perimeter and Euler characteristic of the ILC7 and NILC7 map, respectively, are plotted as a function of threshold values  $v_i$ . We compare one surrogate of first order with 20 realizations of second order surrogates generated for the  $\ell$ -range of interest, here  $\Delta\ell = [2, 20]$ . The full sky Minkowski functionals do not show differences between the two classes of surrogates. Single hemispheres though show clear deviations between first and second order surrogate maps. For the plots we choose again the pair of pixels as defined above: the hemisphere with the highest  $S(\chi^2)$ -value and its opposing hemisphere. In general, we refer to hemispheres mainly located in the northern Galactic sky as upper hemispheres, southern sky hemispheres are called lower hemispheres.

The first order surrogate functionals of the upper or lower hemisphere differ from the re-

|           | Full Sky    | hemisphere   | hemisphere   |
|-----------|-------------|--------------|--------------|
|           |             | $S_{max}$    | Opposite $S$ |
| $\chi^2$  | ( $S \%$ )  | ( $S \%$ )   | ( $S \%$ )   |
| Area      | 0.62   86.4 | 6.72   99.6  | 3.05   98.8  |
| Perimeter | 0.93   88.6 | 7.33   >99.8 | 4.52   99.4  |
| Euler     | 1.44   92.2 | 7.24   >99.8 | 3.62   99.0  |
| SIM       | 0.41   57.0 | 8.9   >99.8  | 6.1   99.8   |

Table 4.1: Deviations  $S$  calculated for the ILC7 map at a shuffling range of  $\Delta\ell = [2, 20]$  from Equation 4.15 and the empirical probabilities  $p$  of the scale-independent diagonal  $\chi^2$ -statistics for full sky functionals and two selected single hemispheres for the three Minkowski Functionals and the scaling index method. This table corresponds to the first row of Figure 4.1.

|           | Full Sky    | hemisphere   | hemisphere   |
|-----------|-------------|--------------|--------------|
|           |             | $S_{max}$    | Opposite $S$ |
| $\chi^2$  | ( $S \%$ )  | ( $S \%$ )   | ( $S \%$ )   |
| Area      | 1.03   88.2 | 9.51   >99.8 | 5.98   99.8  |
| Perimeter | 0.89   86.4 | 9.97   >99.8 | 7.31   99.8  |
| Euler     | 0.77   84.4 | 9.50   >99.8 | 7.22   >99.8 |
| SIM       | 0.29   51.4 | 7.53   >99.8 | 6.23   >99.8 |

Table 4.2: The same as Table 4.1, but for the NILC7 surrogate maps. This table corresponds to the second row of Figure 4.1.

spective second order surrogates for most of the threshold levels  $\mathbf{v}$ . These deviations between the two classes of surrogates lead to the assumption that phase correlations of Fourier phases  $\phi_{\ell m}$  with  $2 \leq l \leq 20$ , manifested as certain morphological structures in the temperature distribution in real space, are existent in the first order surrogates, in which only phases outside  $\Delta\ell = [2, 20]$  are randomized, but are destroyed in the second order surrogate maps.

The first order surrogates of area, perimeter and Euler functionals show contrary behavior comparing the upper and lower sky. Where the surrogates of first order of the chosen upper sky hemisphere lie above the second order surrogates it is the lower sky first order surrogates' Minkowski functionals that lie below. The algebraic sign of the deviations between the two classes of surrogates depends on the analyzed sky region. The results of NILC7 in Figure 4.3 show in principle the same deviations of the two surrogates and between northern and southern sky. The absolute amplitude of the Minkowski functional  $M_2$  (Euler) for the NILC7 map though is larger for negative thresholds compared to positive thresholds. In the case of the ILC7 map the two amplitudes are nearly equal.

Figure 4.4 shows the probability densities  $P(\alpha)$  of the scaling index method of one first and 20 second order surrogate maps for the  $\ell$ -interval  $\Delta\ell = [2, 20]$ , again for the full sky analysis as well as for two opposing hemispheres for comparison. The density distributions of the second order surrogates with fully randomized phases are shifted towards lower (higher)  $\alpha$  values for

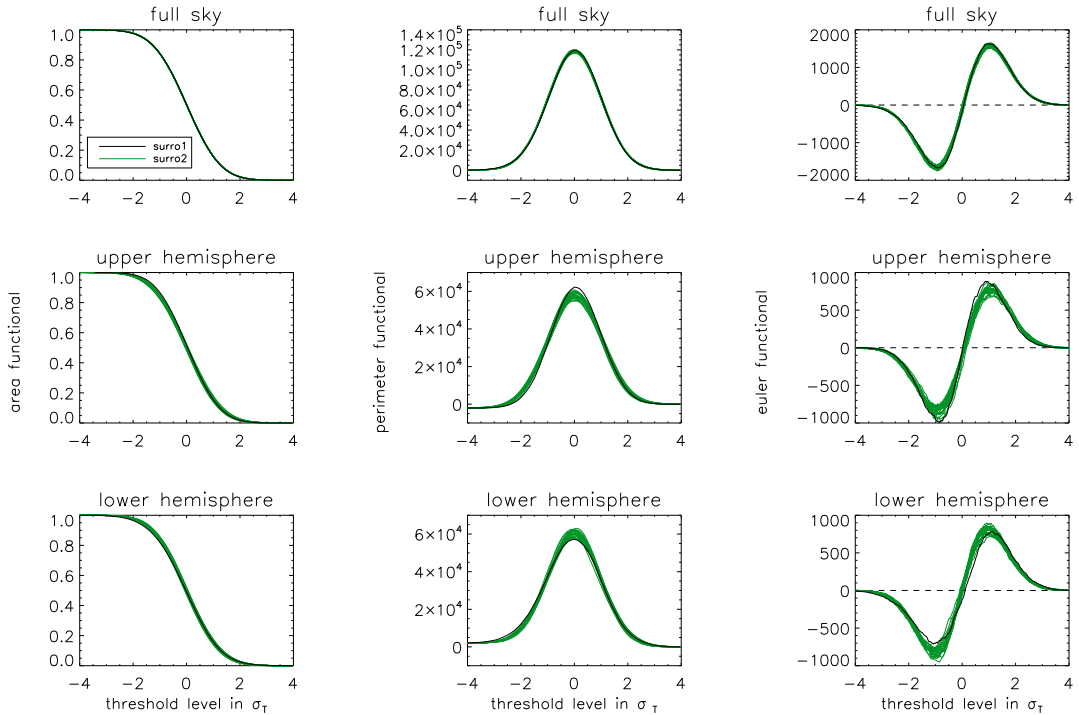


Figure 4.2: Minkowski Functionals  $M_0$  (left),  $M_1$  (middle) and  $M_2$  (right) of the first (black) and 20 second order surrogate maps (green), calculated for  $\Delta\ell = [2, 20]$ . The surrogate maps were derived from the ILC7 map. The upper row shows the Minkowski functionals for the full sky, the middle row for an ecliptic northern sky hemisphere and the lower row for an ecliptic southern sky hemisphere as selected from the  $S$ -maps. The coordinates are given in Table 4.1.

the upper (lower) hemisphere. This shift must be interpreted as a global trend indicating that the first order surrogate map has less (more) structure than the respective set of second order surrogates. As these deviations of different algebraic sign cancel each other for the full sky, we do no longer see significant differences in the probability densities in the full sky analysis. The SIM applied to the NILC7 map shows again that the morphology of the temperature distribution depends on the analyzed sky region and differs in algebraic sign between northern and southern Galactic sky, as was the case with the Minkowski functionals. The deviations between first and second order surrogates demonstrate the existence of HOCs in the WMAP Fourier phases. In our earlier works we found similar results for the ILC7 and NILC5 (five-year needlet-based ILC) map (see R ath et al. (2011)).

The  $\chi^2$  results discussed above do not depend on the algebraic sign anymore. In order to visualize the sign-dependence we plot the deviation  $S$  per hemisphere between first and second order surrogates calculated with the Minkowski functionals for only one chosen threshold, shown in Figure 4.5, and keep the algebraic signs of the deviations with this calculation. The chosen thresholds correspond to the minima or maxima of perimeter and Euler functional. For the SIM we choose to plot  $S(Y)$  with  $Y = \langle \alpha \rangle$  corresponding to Equation 4.16 to keep the algebraic sign, as was done in previous works. For the Euler characteristic we see that the sign of the deviation depends on the threshold level  $v$ .

An analysis of different  $\ell$ -ranges was also performed in Hansen et al. (2009). In their work,

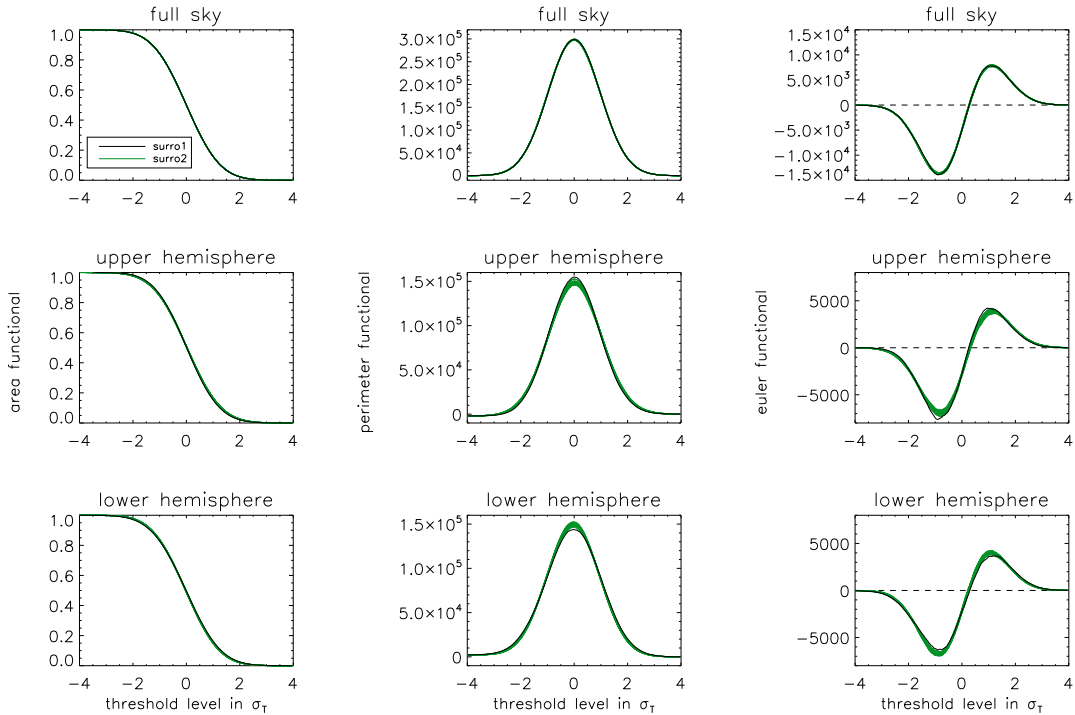


Figure 4.3: Same as Figure 4.2, but for the NLC7 surrogate maps.

the dipole directions of the power distributions of different multipole blocks of 100 multipoles each were calculated. It was shown that for the 6 multipole blocks in  $\ell = [2, 600]$  the dipole directions lie very close to each other. We compare our non-linear statistics for the method of surrogates with  $\Delta\ell = [2, 20]$  with these linear findings in Figure 4.6. We show our coordinates of the hemispherical pairs defined above and add the directions of the 6 dipoles of the power distributions. Note that the linear and non-linear statistics can have different scale sensitivity. Although it is not clear to what extent the results can be reconciled in detail, interestingly, our large-scale investigations with Minkowski functionals and scaling indices as well as the results of Hansen et al. (2009) show evidence of asymmetry. As mentioned above, the original power spectrum is exactly preserved for all our surrogate maps. The dipole direction of the multipole block  $\ell = 2 - 100$  lies close to our large-scale SIM results for ILC7 and close to the Minkowski (Area, Perimeter) results for NLC7. Furthermore, these three pixels are close to the southern ecliptic pole.

In Rossmanith et al. (2012) we introduced the method of surrogates for an incomplete sky. We find that even when the complete Galactic plane is removed, NGs and hemispherical asymmetries can still be detected in the CMB and conclude that the Galactic plane cannot be the dominant source for the found anomalies. Our results point in general towards a violation of statistical isotropy of the Universe and disfavor single-field slow roll inflation.

Supplemental to the results on largest scales, Figure 4.7 shows the deviations  $S(\chi^2)$  per hemisphere of the ILC7 and NLC7 map obtained by the Minkowski functionals for the surrogates  $\Delta\ell$ -range  $[120, 300]$ , which is covering the first peak of the power spectrum. The three Minkowski functionals show indications for phase correlations for both maps. Yet the directions of these deviations on the sky totally differ from each other. Since the two compared maps

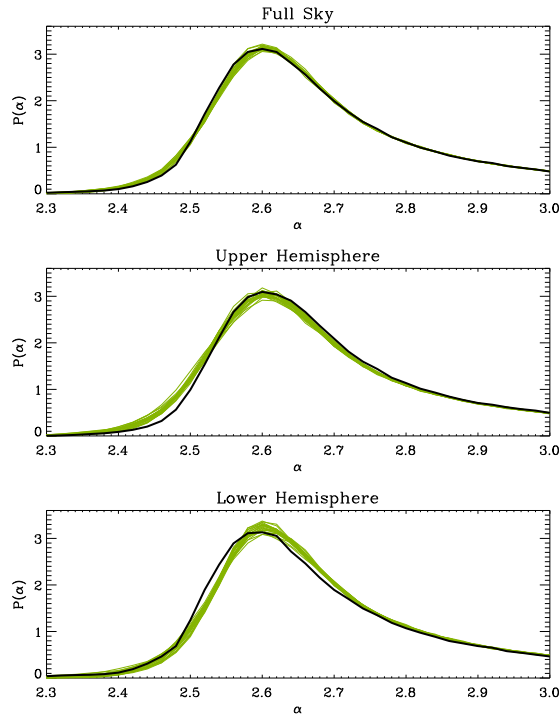


Figure 4.4: Probability density  $P(\alpha)$  of the first and second order surrogates for the scaling indices calculated for surrogate maps with the  $\ell$  interval  $\Delta\ell = [2, 20]$ . The black lines denote the first order surrogates derived from the NILC7 map. The green lines are the densities for the corresponding 20 realizations of second order surrogates.

differ in their resolution we extend the tests with a comparison of the NILC7 at a resolution decreased to one degree FWHM (not shown here). We generate the corresponding surrogate maps of first and second order and calculate the statistics for the Minkowski functionals and the scaling indices. The signatures for phase correlations detected by the Minkowski functionals differ from the results of the fully resolved NILC7 map and they do not resemble the signatures of the ILC7 map. For the SIM there is more concordance between the findings of the differing resolutions of NILC7. We claim that the reason for disparities between the ILC and NILC maps on intermediate length-scales,  $120 \leq l \leq 300$ , is not only the difference in beam resolutions but even more the difference in the foreground cleaning. As explained in [Räth et al. \(2011\)](#) foreground removal can induce phase correlations, especially on these intermediate  $\ell$ -ranges. The detected phase correlations in the  $\Delta\ell$ -range of  $[120, 300]$  depend on the foreground cleaning, the map resolutions and the response of the image analysis techniques. If there are additional deviations from Gaussianity with cosmological origin in the maps on these  $\ell$ -ranges we cannot distinguish them from systematics so far. Our findings clearly show that the found non-Gaussianities in WMAP data are scale-dependent and can have different origin.

So far, we have analyzed the deviations from Gaussianity in areas of apex angle  $\pi$  around the sky which leads to a solid angle of  $2\pi$ , so a full hemispherical analysis. We decrease the apex angle to  $\pi/2$  and calculate the Minkowski functionals and scaling indices for areas with a size of only 30% (solid angle  $0.6\pi$ ) of the former hemispheres. The corresponding  $\mathcal{S}$ -maps are shown in Figure 4.8 for the  $\chi^2$  statistic of the three Minkowski functionals and the SIM. The

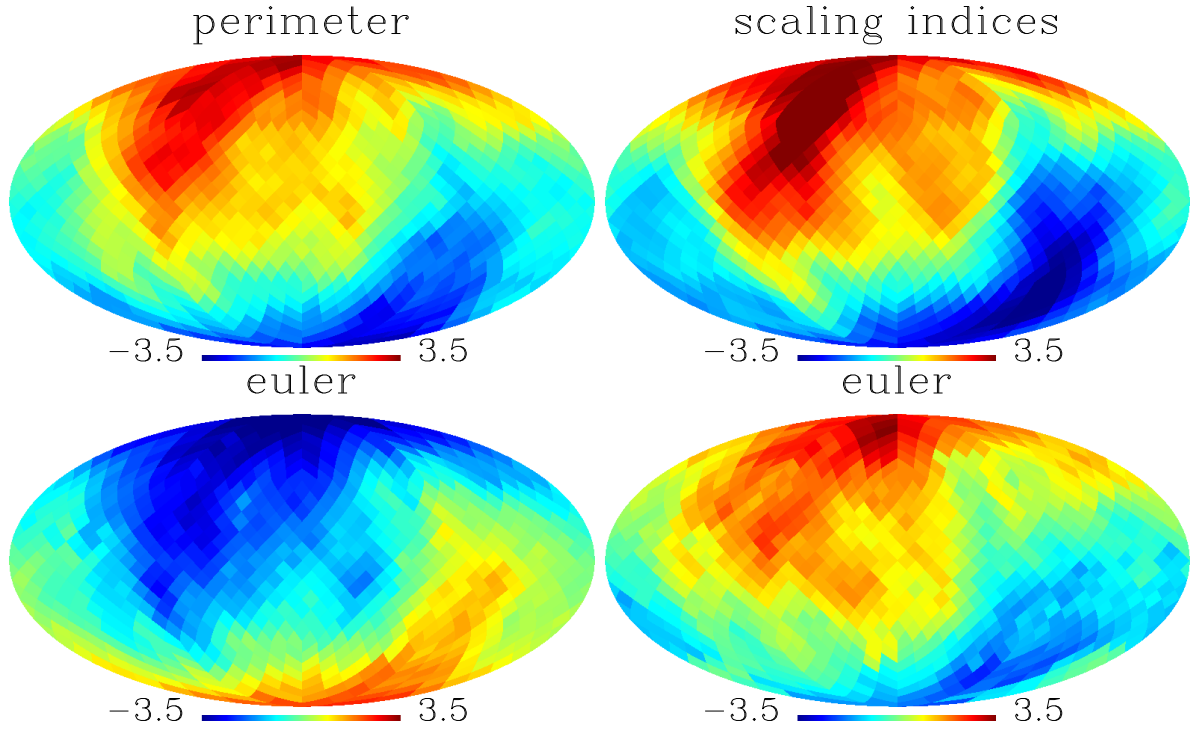


Figure 4.5: Significance  $S$  per hemisphere between surrogate of first and second order of NILC7 calculated for one threshold value  $v_i$ . For perimeter,  $S$  is calculated at the threshold value where  $M_{1,surro1}$  becomes maximal (upper left). For Euler, we chose the threshold values where  $M_{2,surro1}$  becomes minimal (lower left) and maximal (lower right), respectively. For comparison, we show the deviations  $S(\langle\alpha\rangle)$  for the mean of the scaling indices (upper right). The  $\ell$ -range for the method of the surrogates is  $\Delta\ell = [2, 20]$ .

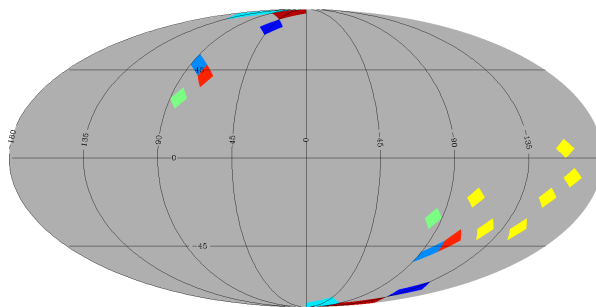


Figure 4.6: A sky map in Galactic coordinates with the directions of maximal signal for NGs found in ILC7 (red) and NILC7 (blue) with Minkowski functionals (Area, Perimeter: blue, Euler: dark blue, Area, Perimeter, Euler: dark red) and SIM (light blue, light red). The yellow pixels show the dipole directions of the power distribution in 6 blocks of 100 multipoles each taken from Hansen et al. (2009). The green pixels correspond to the ecliptic northern and southern pole, respectively.

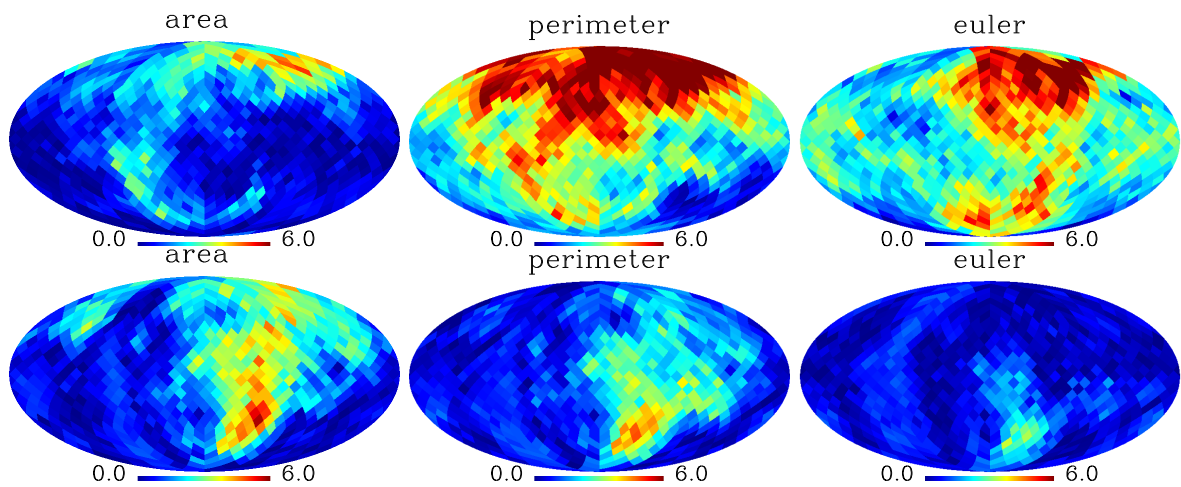


Figure 4.7: Deviations of the Minkowski Functionals  $M_0$ ,  $M_1$  and  $M_2$  of the rotated hemispheres for the ILC7 (upper row) and NILC7 (lower row) map. The  $\ell$ -range for the method of the surrogates is  $\Delta\ell = [120, 300]$ .

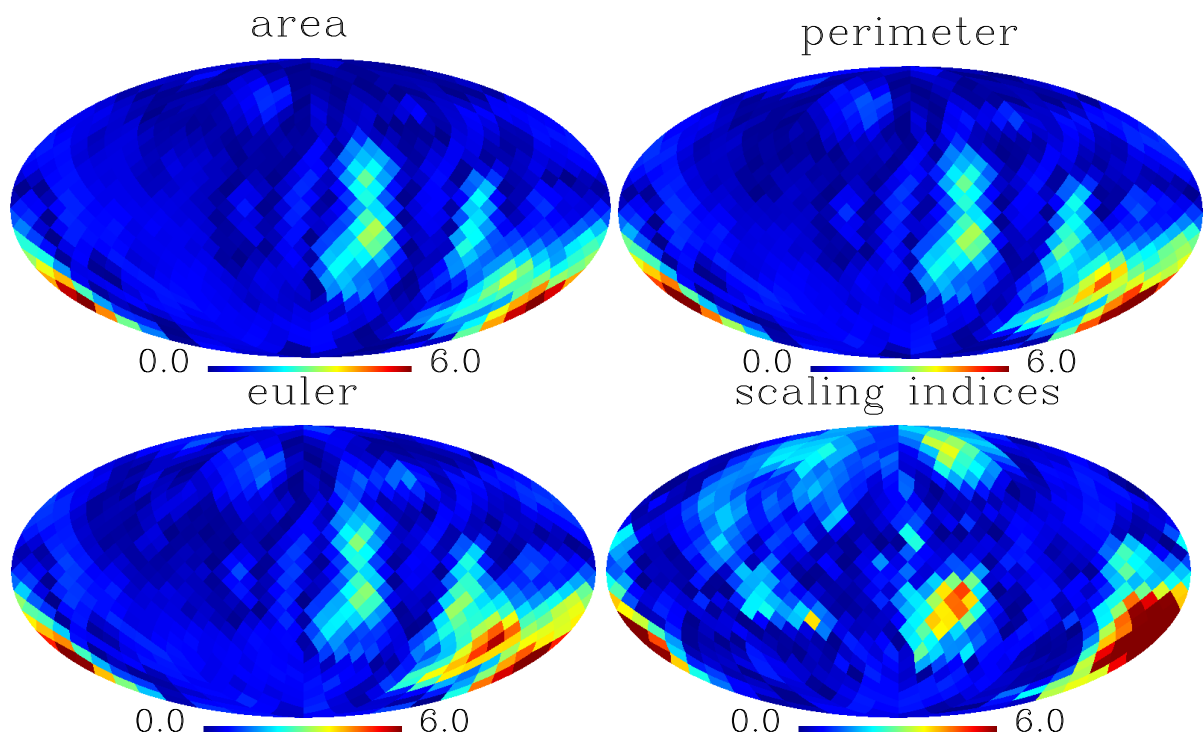


Figure 4.8: Deviations  $S(\chi^2)$  of the Minkowski Functionals  $M_0$ ,  $M_1$  and  $M_2$  and the scaling indices (from left to right and top to bottom) of the rotated hemispheres for the NILC7 map for the smaller apex angle  $\pi/2$ . The  $\ell$ -range for the method of the surrogate is  $\Delta\ell = [2, 20]$ .

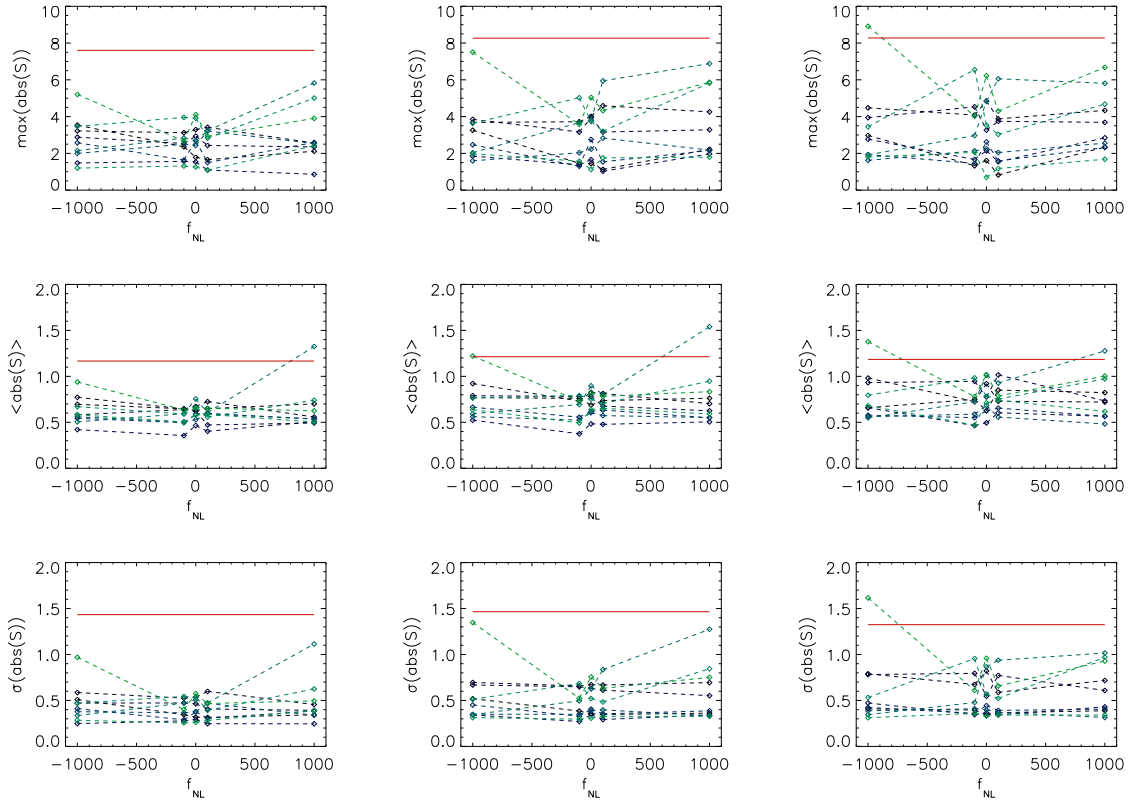


Figure 4.9: Maximum, mean and standard deviation of the absolute values of  $S(\chi^2)_{M_*}$  of ten  $f_{\text{NL}}^{\text{local}}$  simulations compared to the NILC7 original map (red line) for area (left column), perimeter (middle) and Euler (right). The HEALPix resolution of the maps is  $N_{\text{side}} = 64$ . The  $\ell$ -range for the method of the surrogates is  $\Delta\ell = [2, 20]$ .

$\pi/2$  study analyzes smaller sky patches of the CMB. It can feature a better spatial localization of the phase correlations. However, a smaller number of pixels might constrict the detection of a weaker signal. Comparing between the two classes of surrogates on smaller areas of the sky maps, we find no signal for non-Gaussianity in the northern ecliptic sky, whereas we detect individual spots in the southern sky which indicate phase correlations in these parts of the sky. The fact that we do not detect these spots in the northern sky makes ecliptic systematics from observations less likely. However, it cannot be ruled out that the detected spots are correlated with unknown foregrounds. Further study on the origin of the found spots and comparison with other detected anomalous spots in the CMB is needed.

#### 4.5.2 $f_{\text{NL}}$ -dependent Simulations

The analysis of the ILC and NILC7 surrogate maps with the Minkowski functionals as well as the scaling indices reveals HOCs in the original maps. In order to test whether these phase correlations can be reproduced by  $f_{\text{NL}}^{\text{local}}$ -models we analyze constrained realizations of the temperature maps with varying  $f_{\text{NL}}^{\text{local}}$ -parameter with values  $f_{\text{NL}}^{\text{local}} = [0, \pm 100, \pm 1000]$  by means of the surrogate method for  $\Delta\ell = [2, 20]$ . Figure 4.9 shows the results for the corresponding  $S(\chi^2)$  statistics for the three Minkowski functionals. We plot the maximum, mean and standard deviation of  $S(\chi^2)$  for ten simulations and the NILC7 original map. The HEALPix resolution

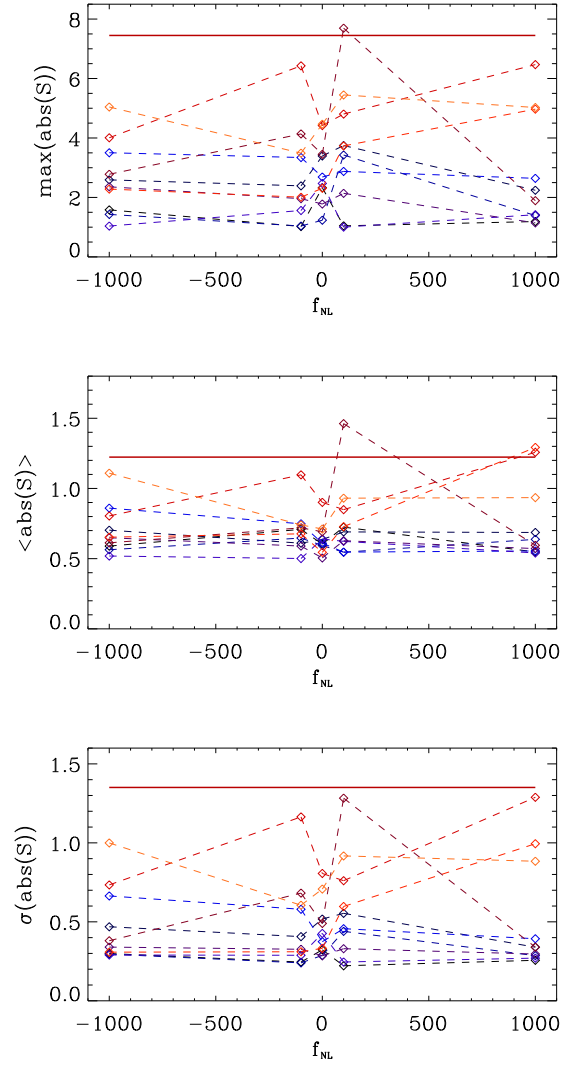


Figure 4.10: Maximum, mean and standard deviation of the absolute values of  $S(\chi^2)_\alpha$  of ten  $f_{\text{NL}}^{\text{local}}$  simulations compared to one NILC7 original map (red line). The HEALPix resolution of the maps is  $N_{\text{side}} = 64$ . The  $\ell$ -range for the method of the surrogates is  $\Delta\ell = [2, 20]$ .

parameter of the maps is decreased to  $N_{\text{side}} = 64$  which does not change the results for low- $\ell$  ranges. One can immediately see that the  $S$ -values of the  $f_{\text{NL}}^{\text{local}}$ -simulations are nearly always smaller compared to the original data set. The few exceptions where the signal of the simulations lies close to the NILC7 data feature a value of  $f_{\text{NL}}^{\text{local}} = \pm 1000$ . These extreme values are already ruled out by recent analyses that resulted in current constraints for  $|f_{\text{NL}}^{\text{local}}|$  well below 100 (e.g.  $f_{\text{NL}}^{\text{local}} = 32 \pm 21$  (68% CL), Komatsu et al. (2011)). For the scaling indices, we obtain similar results, which are shown in Figure 4.10. For the maximum plot, only one simulation lies above the results for the NILC7 map, which is at  $f_{\text{NL}}^{\text{local}} = 100$ . For the mean, we obtain three points with a slightly higher value than the data, and none for the standard deviation.

One has to conclude that the CMB simulations with  $f_{\text{NL}}^{\text{local}}$  cannot reproduce the low- $\ell$  anomalies we found in the WMAP data. This means that the detected large-scale NGs and asymmetries in the data do not correspond to the type of NG which is described by  $f_{\text{NL}}^{\text{local}}$  but stem from a different origin. The search for the source of the deviations from Gaussianity has to be continued in future analyses.

## 4.6 Conclusions

In addition to our previous work based on the use of surrogate maps we analyzed latest WMAP experiment CMB maps with respect to asymmetries and scale-dependent non-Gaussianity. The surrogates are generated by a scale-dependent shuffling of Fourier phases while all other properties of the maps are preserved. In this work we focus on the Minkowski functionals calculated for the ILC7 and NILC7 maps as a scale-independent measure being sensitive on the HOCs of the maps. We compare these new results with the scale-dependent scaling index method calculated for the NILC7 map in this work and for the ILC7 map in previous works. We find that both measures detect highly significant signatures for phase-correlations and therefore deviations from Gaussianity, and furthermore ecliptic hemispherical asymmetries for the interval  $\Delta\ell = [2, 20]$  in both ILC and NILC maps. The reduction of the analyzed sky region down to 30% of the former hemispheres shows no signal for NG in the northern ecliptic sky. In the south we detect individual spots of NG.

If the findings are indeed of intrinsic nature they would disagree with the predictions of isotropic cosmologies with single-field slow-roll inflation.

The two different image analysis techniques reveal very consistent results on the low- $\ell$  range for both maps. The signatures we find for  $\Delta\ell = [120, 300]$  show less agreement between ILC and NILC and differ from the low- $\ell$  range results. They also depend on the image analysis technique and the resolution of the map. As discussed in our earlier works NGs on these scales can be induced by foreground cleaning and can be subject to secondary anisotropies.

The constrained realizations of the CMB with varying  $f_{\text{NL}}^{\text{local}}$  cannot parametrise the detected NGs and asymmetries on largest scales.  $f_{\text{NL}}^{\text{local}}$  might still be a suitable parametrization for smaller scales (larger- $\ell$  ranges). Also, other types of  $f_{\text{NL}}$ , as the equilateral and orthogonal type, also the  $g_{\text{NL}}$  parameter could characterize the found NGs. A deeper study of different inflationary models, as for example Bianchi type models, that represent appropriate test candidates for the found anomalies, is required.

Future investigations, e.g. of upcoming data of the Planck satellite, will shed more light on the open questions regarding instrumental constraints, observational systematics, map making influences and resolution problems.

## 4.7 Acknowledgements

Many of the results in this paper have been derived using the HEALPix ([Górski et al. 2005](#)) software and analysis package. The WMAP data are taken from the Legacy Archive for Microwave Background Data Analysis (LAMBDA). Support for LAMBDA is provided by the NASA Office of Space Science. HM thanks the Christiane Nüsslein-Volhard (CNV) foundation for financial support and acknowledges the support of the International Max Planck Research School.



## Chapter 5

# Probing non-Gaussianities on an incomplete sky

**Original Publication:** G. Rossmanith, H. I. Modest, C. R ath, A. J. Banday, K. M. G orski and G. E. Morfill, *Probing non-Gaussianities in the CMB on an incomplete sky using surrogates*, Phys. Rev. D, **86**, 083005 (2012)

**Abstract:** We demonstrate the feasibility to generate surrogates by Fourier-based methods for an incomplete data set. This is performed for the case of a CMB analysis, where astrophysical foreground emission, mainly present in the Galactic plane, is a major challenge. The shuffling of the Fourier phases for generating surrogates is now enabled by transforming the spherical harmonics into a new set of basis functions that are orthonormal on the cut sky. The results show that non-Gaussianities and hemispherical asymmetries in the CMB as identified in several former investigations, can still be detected even when the complete Galactic plane ( $|b| < 30^\circ$ ) is removed. We conclude that the Galactic plane cannot be the dominant source for these anomalies. The results point towards a violation of statistical isotropy.

### 5.1 Introduction

The search for primordial non-Gaussianities in the Cosmic Microwave Background (CMB) is one of the most important yet challenging tasks in modern cosmology. Any convincing detection of intrinsic non-Gaussianities as well as their characteristics and scaling behavior would directly support or reject different models of inflation, and therefore affect a fundamental part of the standard cosmological model.

The currently still favored inflationary model is single-field slow-roll inflation (Guth 1981; Linde 1982; Albrecht & Steinhardt 1982), which should result in (nearly) Gaussian and isotropic temperature fluctuations of the CMB. However, deviations from Gaussianity, preferred directions, and other kinds of asymmetries have been repeatedly detected (Eriksen et al. 2004b, 2007; Hansen et al. 2007; Dickinson et al. 2009; Hoftuft et al. 2009; Hansen et al. 2009; Rossmanith et al. 2009; R ath et al. 2009, 2011; Vielva & Sanz 2010; Pietrobon et al. 2010; Paci et al. 2010; Cay on 2010; Copi et al. 2010), already questioning the simplest picture of inflation. It is under discussion, if these asymmetries are connected to foreground influences (Copi et al. 2009; Naselsky et al. 2011), which appear particularly in the direction of the Galactic plane.

For investigations of CMB data sets, e.g. WMAP data, the analysis of Fourier phases has proven to be a useful method (Chiang et al. 2003; Coles et al. 2004; Naselsky et al. 2005;

(Chiang et al. 2007), since all potential higher order correlations, which directly point to non-Gaussianities, are contained in the phases and the correlations among them. The method of surrogate maps with shuffled Fourier phases (Räth et al. 2009, 2011) represents one way of analyzing the phases. Originally, this idea stems from the field of time series analysis (Theiler et al. 1992; Schreiber 1998; Bunde et al. 2002; Gliozzi et al. 2010) and describes the construction of data sets, so-called surrogates, which are similar to the original, except for a few modified characteristics. The validation of these characteristics in the original data can then be tested by comparing them to the set of surrogates with appropriate measures. The method used in Räth et al. (2009, 2011) tests the hypothesis that the coefficients  $a_{\ell m} = |a_{\ell m}| e^{i\phi_{\ell m}}$  of the Fourier transform of the temperature values  $T(\theta, \phi)$  have independent and uniform distributed phases  $\phi_{\ell m} \in [-\pi, \pi]$  calculated for the complete sphere  $S$ . The phases of the original map are shuffled, which can be done within some previously chosen interval of interest,  $\Delta\ell = [\ell_1, \ell_2]$ , or simply for the complete range  $\Delta\ell = [2, \ell_{max}]$  for some given  $\ell_{max}$ . Every realization of this shuffling results in a new set of  $a_{\ell m}$ 's, which then represents (after transforming back) one surrogate map. Note that every surrogate still has by construction exactly the same power spectrum as the original map. If the original map contained any phase correlations, these are now destroyed due to the shuffling. Thus, any detected differences between the original and a set of surrogate maps reveals higher order correlations and therefore deviations from Gaussianity.

One major problem in CMB analyses is the treatment of the Galactic plane, which strongly influences the microwave signal. It is possible to cut out the foreground affected regions (Gold et al. 2011), but this procedure itself can affect the subsequent analyses. When applying a sky cut, orthonormality of the spherical harmonics no longer holds on this new incomplete sky, which leads to a coupling of the  $a_{\ell m}$ 's, making a naive phase shuffling impossible. However, one can transform the spherical harmonics into a new set of harmonics, which forms an orthonormal basis on the incomplete sky (Gorski 1994; Gorski et al. 1994; Mortlock et al. 2002), where phase manipulation can then take place again.

The problem of incomplete data also occurs in time series analysis by means of surrogates. Here, gaps can be overcome e.g. by the use of simulated annealing for reproducing the auto-correlation function (Schreiber & Schmitz 1997; Schreiber & Schmitz 2000). Still, the quality of surrogates constructed with this method seems to be questionable, since it is not ensured that no phase correlations are induced.

In this work, we combine the cut-sky methods with phase shuffling, thus enabling investigations by means of surrogates on an incomplete sky. Our method can also be extended for use on incomplete data sets in general.

## 5.2 Methods

### 5.2.1 Cut Sky Surrogates

On a complete sphere  $S$ , an orthonormal basis is given by the spherical harmonics  $Y_{\ell m}(s)$  with  $\ell \geq 0, -\ell \leq m \leq \ell$  and  $s \in S$ . Let the number of harmonics be limited by some given  $\ell_{max} \in \mathbb{N}^+$ . Now, for any map  $f(s) = \sum_{\ell, m}^{\ell_{max}} a_{\ell m} Y_{\ell m}(s)$ ,  $\forall s \in S$  with  $a_{\ell m} \in \mathbb{C}$ , and for any new incomplete sky  $S^{cut}$ , we want to know the corresponding  $a_{\ell m}^{cut}$  and  $Y_{\ell m}^{cut}$  for representing the map on the remaining regions of the sphere:  $f(s) = \sum_{\ell, m}^{\ell_{max}} a_{\ell m}^{cut} Y_{\ell m}^{cut}(s)$ ,  $\forall s \in S^{cut}$ , with  $Y_{\ell m}^{cut}$  being orthonormal on  $S^{cut}$  and thus  $a_{\ell m}^{cut}$  being unique. For real valued spherical harmonics, this was performed in Gorski (1994) and Gorski et al. (1994), and later on extended in Mortlock et al. (2002). The methods presented there can be easily adapted to complex valued spherical harmonics as well.

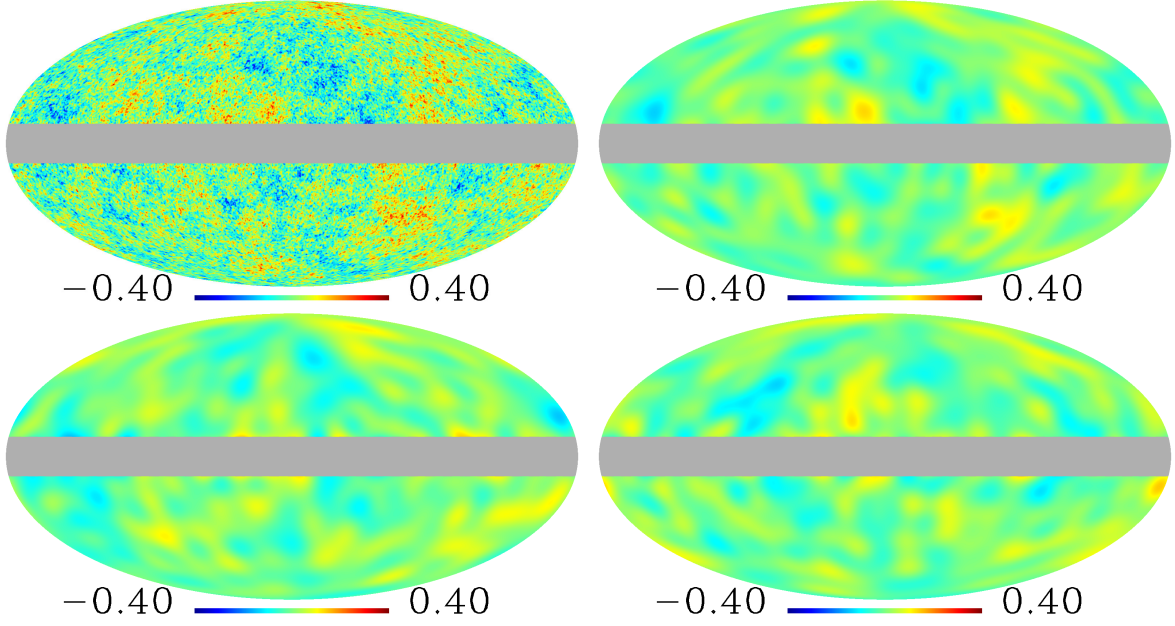


Figure 5.1: Example for the method of surrogates on a cut sky: A simulated CMB map in its original form (upper left), after reconstruction with cut-sky harmonics corresponding to the sky cut  $|b| < 10^\circ$  and the limitation  $\ell_{\max} = 20$  (upper right), and after two realizations of a phase shuffling of these harmonics for the complete range of  $\Delta\ell = [2, 20]$  (lower row).

At first, we define the vectors

$$Y(s) := [Y_{0,0}(s), Y_{1,0}(s), Y_{1,1}(s), \dots, Y_{\ell_{\max}, \ell_{\max}}(s)]^T,$$

$$a := [a_{0,0}, a_{1,0}, a_{1,1}, \dots, a_{\ell_{\max}, \ell_{\max}}]^T$$

containing all harmonics and coefficients with  $m \geq 0$ , respectively, of the given map on the complete sphere. Both have a length of  $i_{\max} := (\ell_{\max} + 1)(\ell_{\max} + 2)/2$ . Analogously, we define  $Y^{\text{cut}}(s)$  and  $a^{\text{cut}}$ . Our objective is to determine two transformation matrices  $B_1, B_2 \in \mathbb{C}^{i_{\max} \times i_{\max}}$ , that fulfill the following equations:

$$Y^{\text{cut}}(s) = B_1 Y(s) \quad (5.1)$$

$$a^{\text{cut}} = B_2 a \quad (5.2)$$

To identify them, we need to define the coupling matrix

$$C := \int_R Y(s) Y^*(s) d\Omega$$

as well as analogously its counterpart  $C^{\text{cut}}$ , with  $R$  being a given region on the sphere. Hereby,  $Y^*$  denotes the hermitian transposed of  $Y$ . When working with a pixelized sky, one uses a sum over the pixels of  $R$  instead of the integral. For  $R = S^{\text{cut}}$ , an orthonormal set of harmonics  $Y_{\ell m}^{\text{cut}}$  needs to fulfill the condition  $C^{\text{cut}} = I_{i_{\max}}$ , with  $I_{i_{\max}}$  being the unit matrix of size  $i_{\max}$ . We can use equation (5.1) on  $C^{\text{cut}}$  to change this condition to  $B_1 C B_1^* = I_{i_{\max}}$ . It is possible to apply different matrix decompositions to obtain  $C = A A^*$  with  $A \in \mathbb{C}^{i_{\max} \times i_{\max}}$ . Consequently, the above equation now reads as  $(B_1 A)(B_1 A)^* = I_{i_{\max}}$  and offers the simple solution  $B_1 = A^{-1}$ .

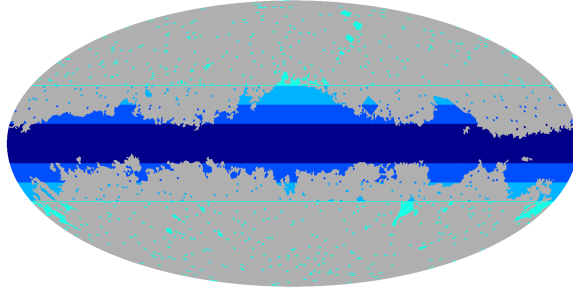


Figure 5.2: The latest KQ75-mask provided by the WMAP-team (Gold et al. 2011), that cuts out the highly foreground affected regions, compared to the three central latitude cuts applied in this work. The smallest cut is  $\pm 10^\circ$  (dark blue), which removes already a large amount of the highly foreground affected regions of the Galactic plane but presumes nearly all non-affected regions. The second,  $\pm 20^\circ$  (blue), removes more regions, while the largest,  $\pm 30^\circ$  (light blue) cuts out almost the entire Galactic Plane. Only minor point sources (turquoise) remain.

For the evaluation of  $B_2$ , let us recall that the coefficient vector  $a$  can be expressed by

$$a = \int_S \bar{Y}(s) f(s) d\Omega$$

or, respectively,

$$a^{cut} = \int_{S^{cut}} \bar{Y}^{cut}(s) f(s) d\Omega .$$

Inserting (5.1) and the expression  $f(s) = a^T Y(s)$  into the latter leads to  $a^{cut} = \bar{B}_1 C^T a$ . Now we use the above matrix decomposition again and obtain  $a^{cut} = \bar{B}_1 (AA^*)^T a = A^T a$ . Thus, it follows that  $B_2 = A^T$ .

To obtain the  $a_{\ell m}^{cut}$  and  $Y_{\ell m}^{cut}$  with  $m < 0$ , we make use of the following equations, that hold for full sky and that we assume to be valid also on incomplete skies:

$$Y_{\ell, -m}^{cut} = (-1)^{|m|} \bar{Y}_{\ell m}^{cut}$$

and

$$a_{\ell, -m}^{cut} = (-1)^{|m|} \bar{a}_{\ell m}^{cut} .$$

For the sky cuts and  $\ell$ -ranges used throughout our study, the cut-sky harmonics were tested and confirmed to be orthogonal.

For constructing  $C = AA^*$  as above, one can make use of different matrix decomposition methods. Since the coupling matrix  $C$  is hermitian and can be treated as positive definite for low  $\ell$  by construction, a Cholesky decomposition is applicable. This is the easiest and fastest way, although numerical problems only allow usage for lower  $\ell_{max}$  (Mortlock et al. 2002). Another possibility is the eigendecomposition (ED): We obtain  $C = VWV^*$ , with the columns of  $V$  containing the eigenvectors, and  $W$  being diagonal and containing the eigenvalues of  $C$ . Because of the properties of the coupling matrix, these values are real and positive, allowing therefore a simple decomposition of  $W$  by taking the square root of every element,  $W = W^{1/2} (W^*)^{1/2}$ . Thus, we obtain  $A = VW^{1/2}$ . Since  $C$  is hermitian, the ED is formally similar to a singular value decomposition (SVD), which is also applied in this paper, with the eigenvalues corresponding to the singular values. For both the ED and the SVD we apply

a householder transformation similar to [Mortlock et al. \(2002\)](#) to make  $A$  lower triangular. For the Cholesky decomposition, this is already the case by definition. Thus, due to equation (5.2), it is ensured that the mono- and dipole contributions of the underlying maps – often considered as non-cosmological – are kept separate from the  $\ell \geq 2$  modes.

With the help of the new cut-sky harmonics  $Y_{\ell m}^{cut}$ , we can now generate the surrogates on a cut sky  $S^{cut}$  as well. Similar to above, we shuffle the phases  $\phi_{\ell m}^{cut}$  of the cut-sky coefficients  $a_{\ell m}^{cut}$ , which is in this work performed for the full cut-sky range  $\Delta\ell^{cut} = [2, \ell_{max}]$ . We obtain new sets of  $a_{\ell m}^{cut}$ ’s, which are transformed back to pixel space to form the cut-sky surrogate (CSS) maps. Figure 5.1 shows as an example a simulated CMB map, its reconstruction with cut-sky harmonics and two corresponding cut-sky surrogates. As we did in the case of a complete sphere, we now search for deviations between the original data as well as its surrogates. However, one has to take care about the above mentioned properties. While the uniform distribution still holds for  $\phi_{\ell m}^{cut}$ , the single phases in the sets are no longer independent from each other due to equation (5.2). In other words, the cut-sky transformation induces phase correlations to the underlying map. To account for these systematic effects, we create for each of the input maps  $N_{FSS} = 20$  full-sky surrogate (FSS) maps as explained above, with  $\ell_{max} = 1024$  and by shuffling the phases within  $\Delta\ell = [2, 1024]$ . By comparing the results of the surrogate analysis for an input map and its FSS, we evade systematically induced phase correlations, since the original map as well as the FSS are subject to the same cut-sky transformation process. Thus, we only search for additional signatures possibly contained in the phases.

Even though the input map might feature induced phase correlations, it has to be pointed out that the cut-sky transformation is reasonable. Only with a new set of cut-sky harmonics, analysis techniques that depend on the orthonormality (like the method of surrogates) are feasible on an incomplete sky. The transformation into the new regime only induces a phase coupling to the data set, whose consequences can be eliminated as explained above. The method of cut-sky surrogates itself is firmly constructed.

We construct the cut-sky harmonics for three different central latitude sky cuts, that remove  $|b| < 10^\circ$ ,  $20^\circ$  and  $30^\circ$  of latitude in the centre of the maps. While the smallest cut ( $|b| < 10^\circ$ ) removes already a large amount of the highly foreground affected regions but retains nearly all non-affected regions, the largest ( $|b| < 30^\circ$ ) excludes almost the entire Galactic plane, with only minor point sources remaining. This is illustrated in figure 5.2. We choose an upper bound of  $\ell_{max} = 20$  and set  $a_{\ell m} = 0$  for  $\ell > \ell_{max}$ . To check for consistency with [Räth et al. \(2009, 2011\)](#), we applied the cut-sky formalism also to the complete sphere with no points excluded. To compare the different matrix decomposition methods, all three approaches (Cholesky, ED, SVD) were applied. For every sky cut, the phases of the coefficients  $a_{\ell m}^{cut}$  were shuffled a hundred times to generate  $N_{CSS} = 100$  cut-sky surrogates for each input map. The same was done for the corresponding FSS maps.

### 5.2.2 Measures for comparison

In general, the comparison of the original data and its surrogate maps can be accomplished with any higher order statistics. For our study, we chose the *scaling index method* (SIM) ([Rossmannith et al. 2009](#); [Räth et al. 2011](#)) as well as *Minkowski functionals* ([Eriksen et al. 2004b](#); [Michielsen & De Raedt 2001](#)) as test statistics.

The SIM is a local measure that is able to detect structural characteristics of a given data set by estimating its local scaling properties. Briefly, the temperature anisotropies  $T(\theta, \phi)$  are transformed to variations in radial direction around the sphere, therefore leading to a point distribution  $\vec{p}_i$ ,  $i = 1, \dots, N_{pix}$ , in three-dimensional space. Then, the weighted cumulative point

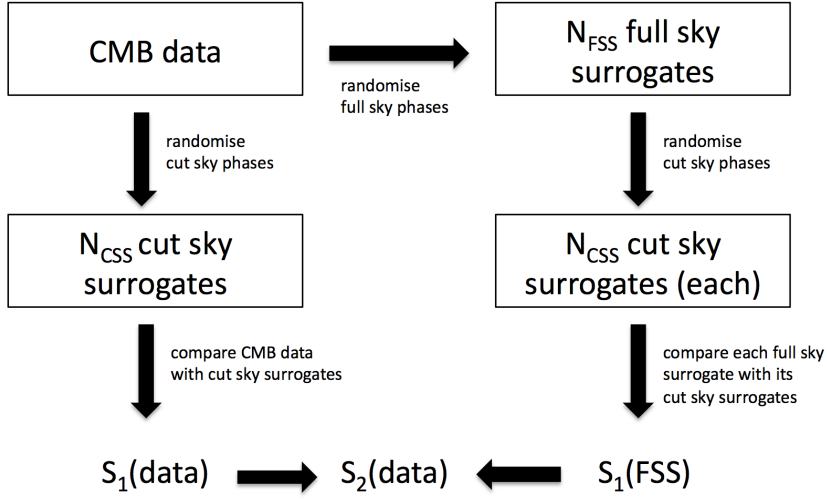


Figure 5.3: Sketch of the method of surrogates on a cut sky.

distribution  $\rho(\vec{p}_i, r)$  is calculated for every point  $\vec{p}_i$  and a freely chosen scaling parameter  $r$ . Since we will only investigate the large scales in our study, we choose the free parameter  $r$  to be  $r_{10} = 0.25$  (in the notation of [Rossmannith et al. \(2009\)](#)), which is appropriate for these scales. Eventually, the scaling indices are obtained by calculating the logarithmic derivative of  $\rho(\vec{p}_i, r)$  with respect to  $r$ .

The three Minkowski functionals measure the behavior of a given map with respect to different threshold values  $\nu$ . The fraction of the sky where the temperature value is larger than  $\nu$  is denoted as the excursion set  $R(\nu)$ , its smooth boundary is identified by  $\partial R(\nu)$ , and  $da$  and  $dl$  describe the surface element of  $R(\nu)$  and the line element of  $\partial R(\nu)$ , respectively. Then, we can define the three Minkowski functionals as

$$\begin{aligned}
 M_{area}(\nu) &= \int_{R(\nu)} da \\
 M_{perim}(\nu) &= \int_{\partial R(\nu)} dl \\
 M_{euler}(\nu) &= \int_{\partial R(\nu)} dl \kappa,
 \end{aligned}$$

with  $\kappa$  being the geodesic curvature of  $\partial R(\nu)$ . For more details, we refer to [Eriksen et al. \(2004b\)](#); [Michielsen & De Raedt \(2001\)](#). Eventually, we sum up over all thresholds with the help of the appropriate cut-sky surrogates by means of a  $\chi^2$ -measure

$$\chi^2 = \sum_{\nu} \left[ (M_{\bullet}^{map}(\nu) - \langle M_{\bullet}^{CSS}(\nu) \rangle) / \sigma_{M_{\bullet}^{CSS}(\nu)} \right]^2$$

for  $M_{area}(\nu)$ ,  $M_{perim}(\nu)$  and  $M_{euler}(\nu)$ , respectively.

For computational reasons, the resolution of the input maps in the corresponding HEALPix<sup>1</sup> scheme ([Górski et al. 2005](#)) was chosen to be  $N_{side} = 256$  for the scaling index analysis and

<sup>1</sup><http://healpix.jpl.nasa.gov>

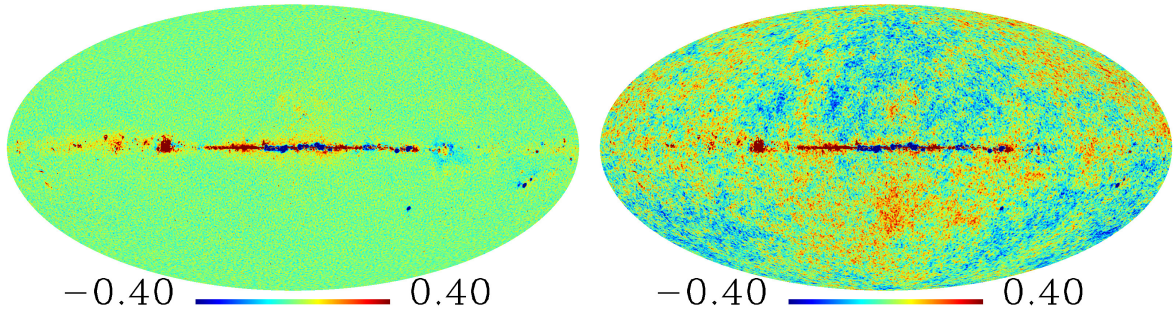


Figure 5.4: The foreground residuals resulting from the subtraction of the WMAP ILC map from the full seven-year foreground reduced co-added VW-band in its original form (left) and added to a Gaussian simulation (right). The latter represents the map that is used in section 5.3.1.

$N_{side} = 64$  for the Minkowski functionals. By testing several subsets, we assured ourselves that the results are only marginally affected when choosing a lower resolution.

### 5.2.3 Statistical interpretation

The results for the different maps of both the scaling indices and the Minkowski functionals are then evaluated in terms of *rotated hemispheres*: For 768 different angles we rotate the underlying maps and calculate the  $\sigma$ -normalized deviations

$$S_1(Y) = (Y^{map} - \langle Y^{CSS} \rangle) / \sigma_{Y^{CSS}}$$

of the pixels included in the new upper hemisphere between the input map and its cut-sky surrogates, by means of the measure  $Y$ . In our case,  $Y = \langle \alpha \rangle, \sigma_\alpha, \chi_{area}^2, \chi_{perim}^2, \chi_{euler}^2$ , with  $\langle \alpha \rangle$  and  $\sigma_\alpha$  being the mean and the standard deviation of the scaling index response  $\alpha(\vec{p}_i, r)$ , respectively. The result is then shown as color-coded pixel, whose centre is pierced by the  $z$ -axis of the respective rotated reference frame (see R ath et al. (2009); Rossmannith et al. (2009); R ath et al. (2011)). To separate traces of possibly intrinsic phase correlations from those induced by the transition to incomplete sky, and thus to account for systematic effects, we calculate the statistics

$$S_2(Y) = \left( S_1^{data}(Y) - \langle S_1^{FSS}(Y) \rangle \right) / \sigma_{S_1^{FSS}(Y)}$$

for comparing the results of  $S_1(Y)$  for the original and the full-sky surrogate maps. Figure 5.3 illustrates the concept of this statistical interpretation of the method of cut-sky surrogates.

An important advantage of the rotated hemispheres  $S_2(Y)$  is the possibility to identify not only a global difference between the original map and its surrogates, but also the directions where these differences occur. Thus, one can make a statement about possible deviations from statistical isotropy. One example for such anisotropies are asymmetries, that have been detected in numerous previous analyses as mentioned above. A difference between a  $S_2(Y)$  map that detected asymmetries and a statistical isotropic map is reflected in a difference in the empirical distributions: For the latter, one would expect a histogram with a narrow range of values for  $S_2(Y)$  that peaks around zero. But for the first, one expects a broader spectrum and possibly more than one peak, since on the map there are at least two areas with different values. One measure that exactly accounts for the broadness of histograms is the discrete

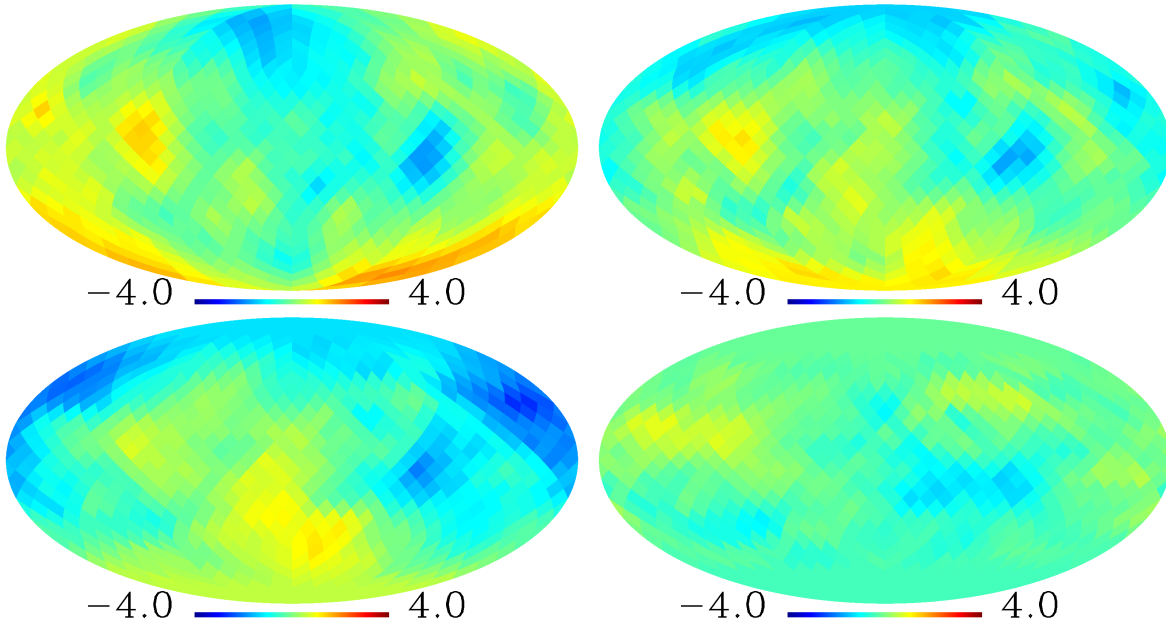


Figure 5.5: The  $\sigma$ -normalized deviations  $S_2(\sigma_\alpha)$  comparing a simulated map and its 20 full-sky surrogates for the complete sphere (upper left) and the three different central latitude sky cuts  $|b| < 10^\circ$  (upper right),  $|b| < 20^\circ$  (lower left), and  $|b| < 30^\circ$  (lower right), that were constructed by means of the singular value decomposition.

entropy  $H(S_2(Y))$ . We define it as

$$H(x) = - \sum_{i=1}^{N_{bins}} p_i \ln p_i ,$$

with  $p_i$  being the empirical probability (that is the relative frequency) of the realizations of  $x$  to occur in the bin  $i$ , with  $N_{bins}$  describing the number of bins in a chosen underlying interval.

The entropy  $H(S_2(Y))$  reaches its maximal value for a uniform distribution, which would correspond to a  $S_2(Y)$  map that consists of all different values of the chosen range, which again would imply that there is no statistical isotropy at all. The (theoretical) minimum of  $H(S_2(Y))$  is zero. This occurs for the special case of a completely isotropic map with a distribution where only for one bin  $i$  the empirical probability  $p_i$  differs from zero. Thus, a statistical anisotropic map, e.g. one with a strong asymmetry, results in a higher value for  $H(S_2(Y))$  than an isotropic one.

## 5.3 Validation

### 5.3.1 Underlying Data Sets

To test the new approach, we generate two types of Gaussian simulations of the co-added VW-band of the WMAP satellite via a noise-weighted sum. The difference between these two is simply that for the one type we add Gaussian noise with a particular variance, given by  $N_{obs}$ , for every pixel of the sphere and for the other we do not. The procedure is the same as in [Rossmannith et al. \(2009\)](#), but note that we now apply the more recent WMAP 7-year parameters. We include the simulation without the noise, since only there one can be absolutely

sure that the results are not distorted by any influences coming from the input map: The map is created by only using a given power spectrum and completely random phases, and should therefore be resistant against phase shuffling in a statistical sense. In addition to these two clean simulations, we applied the cut-sky surrogate approach to another simulated Gaussian map, to which we added typical foreground residuals that are still present after the template cleaning of the WMAP data. With the help of this second simulation, one can examine the impact of possible aliasing effects due to the chosen  $\ell_{max}$ , that could be caused by strong foregrounds which are cut out. The required residuals were computed by subtracting the WMAP ILC map from the full seven-year foreground reduced co-added VW-band. However, when performing this subtraction, one has to bear two things in mind: First, not only the co-added VW-band but also the ILC map contains influences from the Galactic plane, although with a lower amplitude. Second, the resulting map is slightly noisier compared to the original foreground cleaned WMAP band-wise maps. Still, both remarks should not have a significant impact on the intention of the test. The residuals resulting from the subtraction as well as the corresponding simulation with the typical foreground pattern are shown in figure 5.4.

### 5.3.2 Results

For the clean simulated Gaussian maps, the significances  $S_2(\sigma_\alpha)$  and  $S_2(\chi^2_{area})$  calculated for the rotated hemispheres are illustrated in the figures 5.5 and 5.6. The differences between the original and the FSS maps are insignificant (nearly always  $S_2(Y) < 2.5$ ) for the complete sphere and all sky cuts. This holds for the results of the scaling indices ( $Y = \langle \alpha \rangle, \sigma_\alpha$ ) as well as for the Minkowski functionals ( $Y = \chi^2_{area}, \chi^2_{perim}, \chi^2_{euler}$ ). There are only marginal differences when one adds the Gaussian noise to the map, which shows that these noise fluctuations alone are not responsible for non-Gaussianities or anisotropies on the large scales. The results of the assembled map are very similar as well, except for the full sky, where phase correlations are obviously present. These results clearly demonstrate the validity of the approach. Although phase correlations were induced by the cut-sky transformation, these are subtracted away by using  $S_2(Y)$ . The results of the assembled map show that the impact of aliasing effects, even when strong foregrounds are present in the Galactic plane, is negligible.

Only minimal differences were detected for the three used matrix decomposition methods, that are likely to be due to the random shuffle of the phases. When going to larger  $\ell$ -ranges or more irregular sky cuts, this technical part of the investigation will become more important, especially for making the transition to the cut-sky possible.

## 5.4 Application to WMAP data

### 5.4.1 Underlying Data Sets

For the application of the cut-sky method to observations, we make use of several data maps. Two of them are linear combinations of the different frequency bands and based on the WMAP results<sup>2</sup> (Jarosik et al. 2011): First, the 7-year Internal Linear Combination map (ILC7) provided by the WMAP team (Gold et al. 2011) and second the 5-year needlet based ILC map (NILC5) (Delabrouille et al. 2009). In addition to these two data sets, we examine three maps based on the 7-year co-added VW-band: For the first (VW7m), the galactic plane and several point sources of the co-added VW-band map are cut out by means of the KQ75-mask (Jarosik et al. 2011). These empty regions are then filled with Gaussian noise, whose mean and standard deviation correspond to the values of the remaining map, while preserving the spatial noise

<sup>2</sup><http://lambda.gsfc.nasa.gov/>

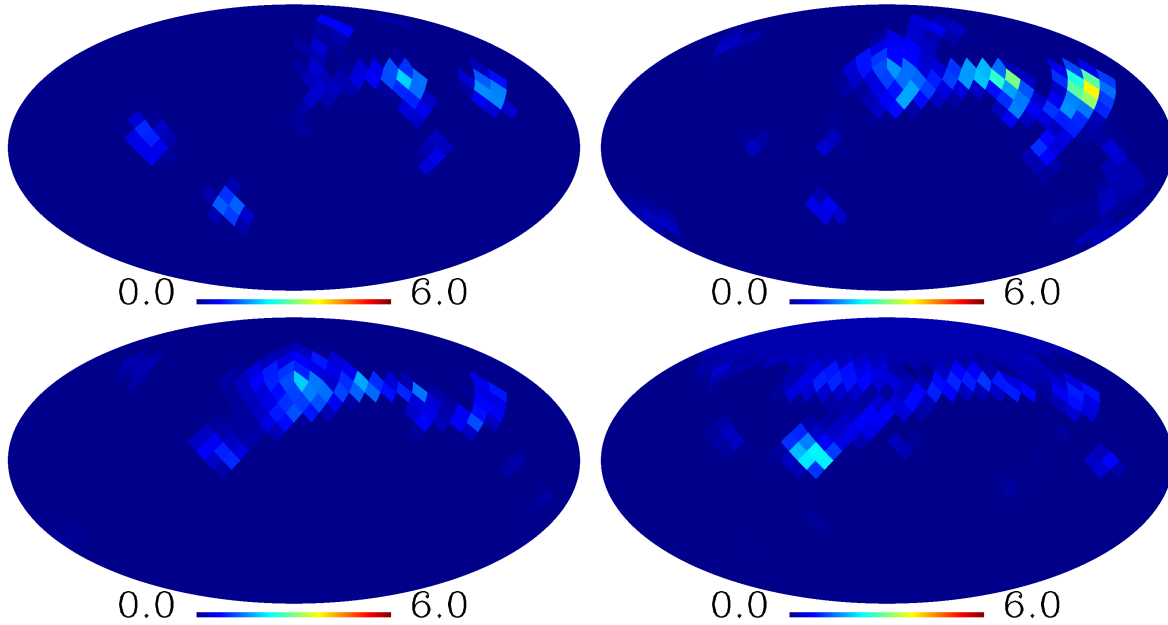


Figure 5.6: Same as figure 5.5 but for  $S_2(\chi^2_{area})$ . Note the different color scaling.

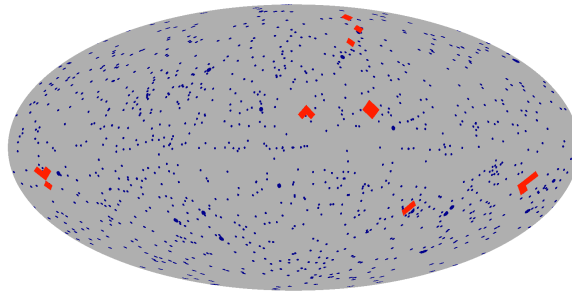


Figure 5.7: The temperature point source mask of the WMAP team in its original (blue spots) and in its extended form (additional red regions), used to obtain the VW7p and the VW7pe data map, respectively.

patterns. As above, this procedure is similar to [Rossmanith et al. \(2009\)](#). The second map (VW7p) is obtained by applying the same method but cutting out the point sources outside the Galactic Plane only. The temperature point source mask of the WMAP team is used for this purpose ([Jarosik et al. 2011](#)). Since some of the point sources correspond to larger sources that might not always be completely masked out, it can be advantageous to extend the previous mask with the help of the high-latitude regions of the WMAP processing mask ([Jarosik et al. 2011](#)). This leads to the third VW-band based map (VW7pe) used in this paper. The regions that were cut out to obtain the VW7p and VW7pe maps are illustrated in figure 5.7. For all data maps, the monopole and dipole were removed.

The three maps based on the co-added VW-band map will be treated slightly different to the analysis process from above: Instead of using the usual 20 FSS maps, we compare the VW7m, the VW7p, and the VW7pe map with 20 simulations of the VW-band, where we likewise excluded the respective mask or point sources and filled it with Gaussian noise. In

doing so, we avoid to detect deviations that are only due to the structural differences inside the masked regions or to the peculiar boundary between the masks and the rest of the map. These unintentional deviations might occur when applying the FSS method. However, for the VW7m map, a comparison with FSS was tested as well, leading to similar results as the approach with the masked simulations.

The ILC7 and NILC5 data sets are maps that can also be used in a full-sky surrogate analysis. The maps were nevertheless analyzed in this work, on the one hand to check for consistency with the full-sky surrogates method, and on the other hand to elucidate the influence of the different map making procedures on the phase correlations. Apparently, effects of these map making procedures should in particular be present in the Galactic Plane.

For the VW7m map, a full-sky surrogate analysis would not be applicable, since obviously the filling of the mask has a severe influence on the phase correlations. However, it could be used in a regular full-sky analysis, e.g. in comparison with simulated CMB maps of the VW band, for which the same mask filling method is applied.

The remaining two maps (VW7p and VW7pe) represent data sets that do not attempt to remove the foreground influences of the Milky Way. These maps would not produce reasonable results when analyzed with the full-sky surrogates approach. Thus, they are a perfect example to demonstrate the usage of the method of cut-sky surrogates. By applying the method on these maps, we are consistent with the statement that the removal of foreground affected regions is to be preferred to an reconstruction of these areas (Copi et al. 2011).

### 5.4.2 Results

When evaluating the scaling index results  $S_2(\langle\alpha\rangle)$  and  $S_2(\sigma_\alpha)$  for the  $|b| < 10^\circ$  cut for the rotated hemispheres of all data maps described above, we detect significant non-Gaussianities and an asymmetry. Both features were already found in corresponding full-sky analyses (Räth et al. 2009, 2011). The signal for  $S_2(\langle\alpha\rangle)$  becomes less clear for larger cuts. But for  $S_2(\sigma_\alpha)$ , a significant asymmetry with a clear north-south direction persists for all maps when excluding the Galactic plane. As examples, the significances  $S_2(\sigma_\alpha)$  determined for the rotated hemispheres of the NILC5 and the VW7pe map for the different sky cuts are shown in the figures 5.8 and 5.9, respectively.

The Minkowski functionals show similar results: For  $M_{area}(\mathbf{v})$ , one detects similar deviations between all the data sets and its related full-sky surrogates. The only exception is the VW7pe map, where the asymmetries are less pronounced than in the other maps. For the VW7m map, that cuts out even larger areas of foreground affected data, a clear asymmetric behaviour is found again. As examples, the results for  $M_{area}(\mathbf{v})$  are illustrated for the NILC5 and VW7pe maps in the figures 5.10 and 5.11.

For  $M_{perim}(\mathbf{v})$  and  $M_{euler}(\mathbf{v})$ , the results agree for the full sky, but get less definite for larger cuts. However, experience shows that this could likely be due to the limited amount of pixels that is present especially when applying the  $|b| < 20^\circ$  or  $30^\circ$  cuts. The decreasing number of pixels on the incomplete skies leads to an increasing influence of noise and a lower influence of the intrinsic signal. Due to discreteness, possible effects on the tails of the Minkowski functionals may vanish, which in turn might damp the respective  $\chi^2$ . This especially holds for the two Minkowski functionals  $M_{perim}(\mathbf{v})$  and  $M_{euler}(\mathbf{v})$  that examine complex pixel formations and thus need enough data points to produce statistically reliable results.

The detected north-south asymmetry is reflected in the empirical distribution functions of the result maps  $S_2(\sigma_\alpha)$ . We compare the results of the ILC7 and the NILC5 maps with 10 simulations without noise. These simulated maps undergo the same processes as the data

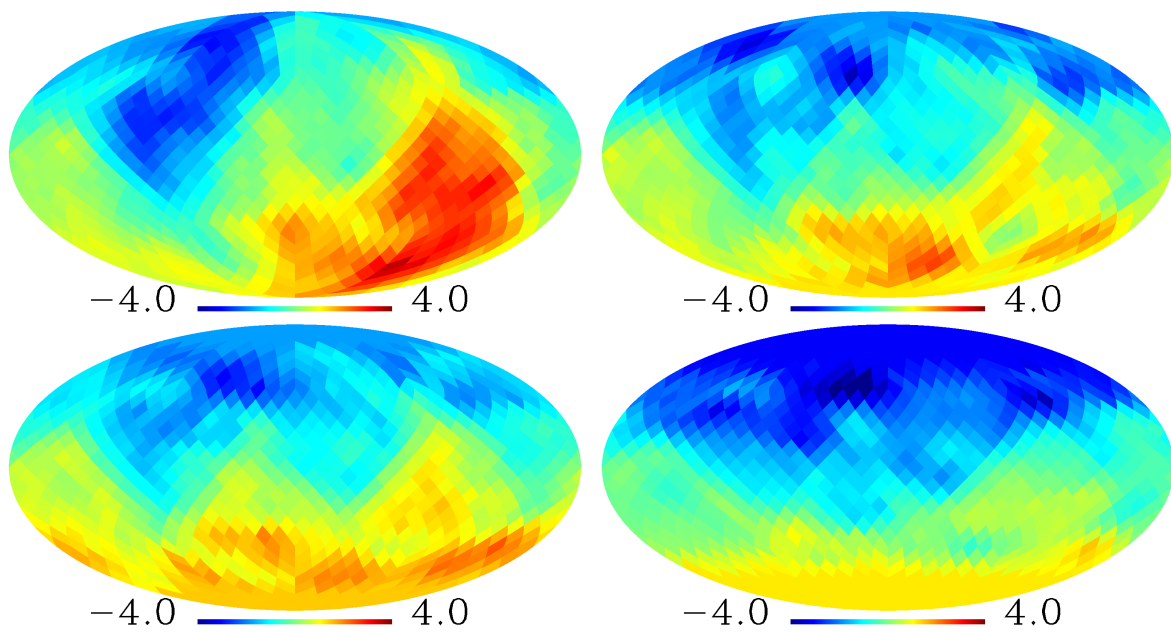


Figure 5.8: Same as figure 5.5 for the NILC5 map.

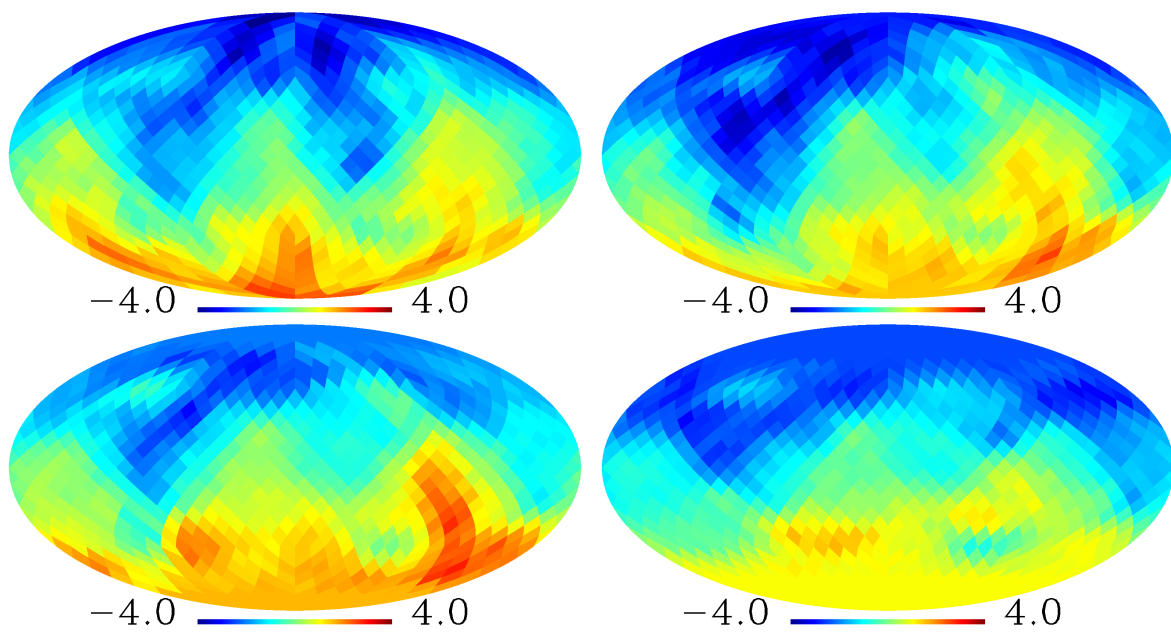


Figure 5.9: Same as figure 5.5 for the VW7pe map.

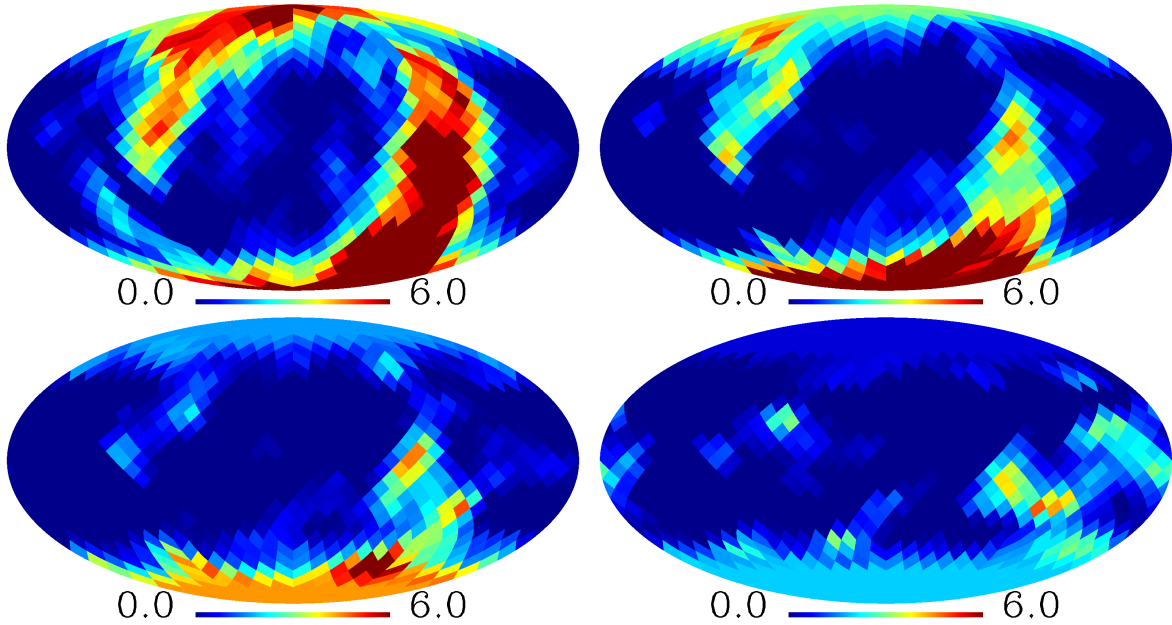


Figure 5.10: Same as figure 5.6 for the NILC5 map.

maps. That means we constructed for each simulation 20 FSS, and again for each FSS and the original map 100 CSS for all different sky cuts. The results are illustrated in figure 5.12. Clearly, the histograms of the data maps show a much broader spectrum than the respective output of the simulations, which underlines the detection of statistical anisotropies.

This aspect is in turn quantified by the empirical entropy  $H(S_2(\sigma_\alpha))$ . Figure 5.13 presents the corresponding results of the twelve above mentioned histograms and additional ten simulations with Gaussian noise. The results of the data maps offer higher values than the ones of the simulations. Also, it is remarkable that these values are nearly not decreasing when moving to a larger sky cut. As above in section 5.3.2, the differences between the two types of simulations are negligible.

In summary, both the scaling indices and Minkowski functionals detect higher order correlations and thus non-Gaussianities, as well as a clear north-south asymmetry in all data sets even when large parts of the Galactic Plane are removed. Only the output of the Minkowski functionals of the VW7pe map shows a weaker significance. Nevertheless, the scaling indices detect an asymmetry in the VW7pe map. To investigate this particularity a bit further, we repeated the CSS analysis of the NILC5 map where we removed the masked regions of the VW7pe map. For simplicity reasons, no new FSS were generated. A comparison of this new NILC5pe map with the FSS of the NILC5 data lead to the same results as the analysis of the NILC5 map itself.

The different signs in the opposite hemispheres of the findings for  $S_2(\sigma_\alpha)$  that appear for all data maps reflect a lower (higher) variability of the scaling index results for the northern (southern) hemisphere of the original maps compared to their surrogates. A higher variability implies the presence of different types of structure. Thus, the lower variability in the north can also be interpreted as a lack of power in the northern hemisphere, which is in agreement with former results (Eriksen et al. 2004a,b; Hansen et al. 2004, 2009; Rossmannith et al. 2009; Räth et al. 2009, 2011). The regions with large deviations from isotropy become very broad

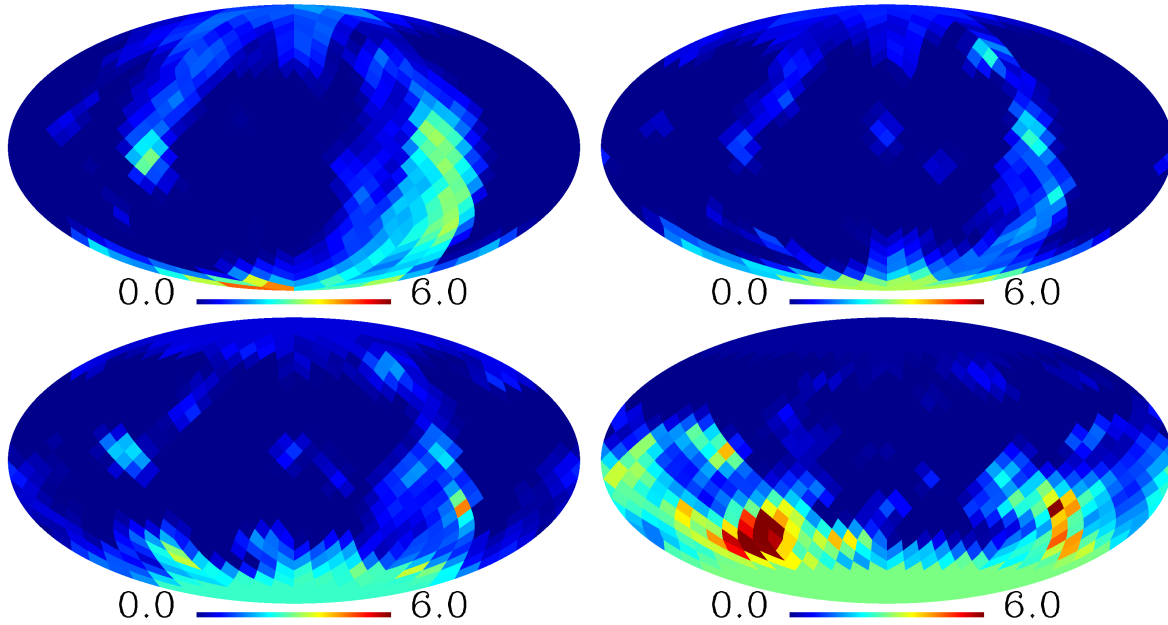


Figure 5.11: Same as figure 5.6 for the VW7pe map.

for the larger cuts, which makes it difficult to draw a clear statement about a more accurate direction of the detected asymmetry, e.g. if it was aligned with the ecliptic plane or not.

The above results also clearly indicate that both the detected non-Gaussianity and asymmetry on the large scales cannot mainly be attributed to foreground influences of the Galactic plane. This verifies the results of the full-sky surrogate analyses of R ath et al. (2009, 2011), where foreground effects could in principle have played a role, and confirms previous findings of other analyses (e.g. Hansen et al. (2009)). In combination with the multitude of checks on systematics performed for the cut-sky transformation in section 5.3 and for the technique of surrogates in R ath et al. (2009, 2011), the results point towards the conclusion that the signatures are of cosmological origin. This would represent a strong violation of the Gaussian hypothesis and of statistical isotropy. Both assumptions are fundamental parts of single-field slow-roll inflation, which is therefore rejected at high significance by this analysis.

A lot of effort as well as knowledge about the cut-sky transformation process will be necessary to be able to extend the method of cut-sky surrogates to higher resolutions. A naive approach results in an  $O(\ell^4)$  scaling. As usual in CMB analysis, this includes both calculations in Fourier as well as in real space. It is important to remove the restrictions of a low  $\ell_{max}$  to enable investigations of higher  $\ell$ -ranges, as it was already done for the full-sky case (R ath et al. 2009, 2011). When going to higher  $\ell$ -values, it is of course helpful to work with a higher resolution in pixel space as well. The upcoming data sets of the Planck satellite will offer a better resolution for both Fourier and pixel space.

## 5.5 Conclusions

We demonstrated the feasibility of generating surrogates by Fourier-based methods also for an incomplete data set. This was worked out for the case of a CMB analysis on an incomplete sphere. Three different constant latitude sky cuts were applied. For this purpose, three different cut-sky transformations were calculated. We generated 100 cut-sky surrogates for every input

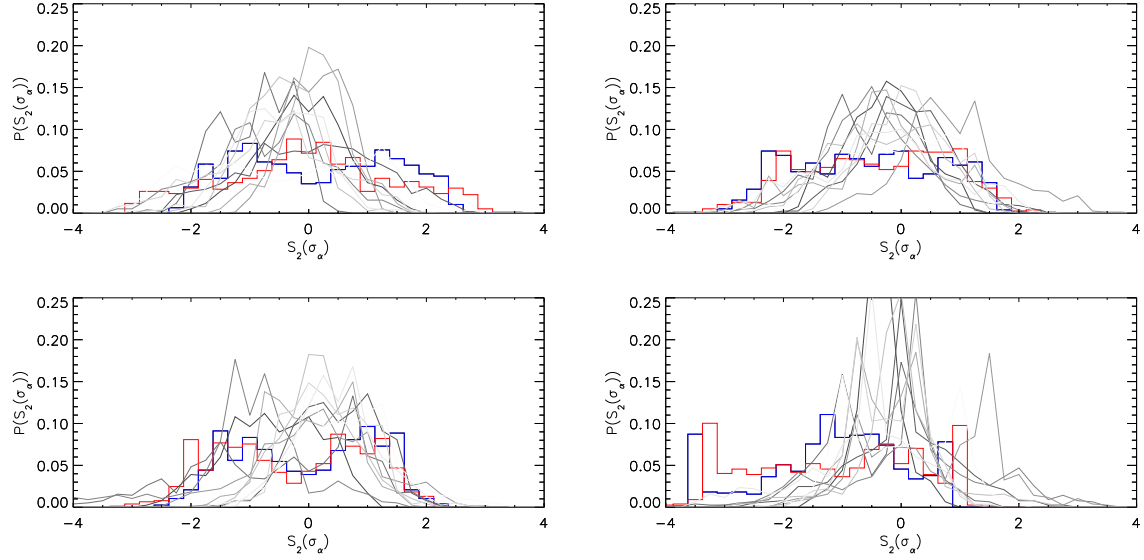


Figure 5.12: The histograms of  $S_2(\sigma_\alpha)$  for the complete sphere and the three different central latitude sky cuts  $|b| < 10^\circ$ ,  $|b| < 20^\circ$ , and  $|b| < 30^\circ$  (from top to bottom), for the ILC7 (blue) and NILC5 (red) maps as well as for 10 simulated Gaussian random fields without noise (grey).

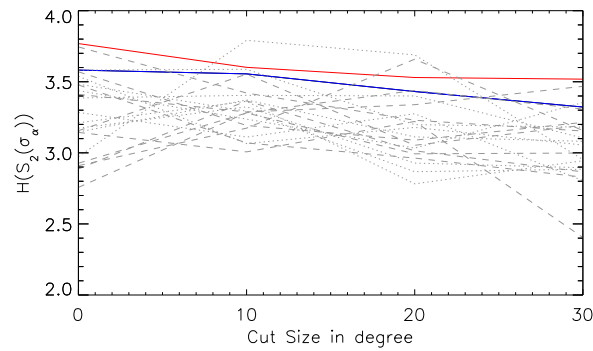


Figure 5.13: The empirical discrete entropy  $H(S_2(\sigma_\alpha))$  corresponding to the histograms of figure 5.12. The blue and red lines represent the ILC7 and NILC5 maps, while the results of the simulated Gaussian random fields with and without noise (10 realizations each) are illustrated by the dotted and dashed grey lines.

map, sky cut and matrix decomposition method, which were analyzed by means of scaling indices and Minkowski functionals. To remove systematic effects, a second analysis compared the results of the original with the ones of 20 full-sky surrogate maps for each of the input maps. For simulated maps, no anomalies could be detected. The findings for the data maps show strong signatures of non-Gaussianities and pronounced asymmetries, which persist even when removing larger parts of the sky. This confirms that the influence of the Galactic plane is not responsible for these deviations from Gaussianity and isotropy. Together with former full-sky analyses, the results point towards a violation of statistical isotropy.

The forthcoming Planck data offers the opportunity to test an independently measured data set. This will help to yield more information about the origin of the detected anomalies, since the new measurement might feature systematic effects different from WMAP. In addition, the better signal-to-noise ratio, the unprecedented accuracy, and the supply of higher  $\ell$ -bands will improve the value of the analyses, especially when extending the investigations to smaller scales.

Many of the results in this paper have been obtained using HEALPix ([Górski et al. 2005](#)). We acknowledge the use of LAMBDA. Support for LAMBDA is provided by the NASA Office of Space Science. We want to thank the referees for their comments and suggestions.

## Chapter 6

# Correlating Fourier phase information with real-space higher order statistics in CMB data

**Original Publication:** H. I. Modest, C. Räth, A. J. Banday, K. M. Górski and G. E. Morfill, *Correlating Fourier phase information with real-space higher order statistics in CMB data*, Phys. Rev. D, **89**, 123004, (2014)

**Abstract:** We present a heuristic study on the correlations between harmonic space phase information and higher order statistics. Using the spherical full-sky maps of the cosmic microwave background as an example we demonstrate that known phase correlations at large spatial scales can gradually be diminished when subtracting a suitable best-fit (Bianchi-)template map of given strength. The weaker phase correlations are attended by a vanishing signature of anisotropy when measuring the Minkowski functionals and scaling indices in real-space with the aid of surrogate maps being free of phase correlations. Those investigations can open a new road to a better understanding of signatures of non-Gaussianities in complex spatial structures, especially by elucidating the meaning of Fourier phase correlations and their influence on higher-order statistics.

### 6.1 Introduction

Great advances in imaging techniques nowadays allow for a visualization of spatial structures in medicine, biochemistry, solid-state physics, or astronomy, ranging from the atomic nanometer scale ([Binnig et al. 1986](#)) to megaparsec for the large scale structure of the Universe ([Ahn et al. 2012](#)) with the largest and oldest observable structure being the cosmic microwave background (CMB) ([Smoot et al. 1992](#); [Bennett et al. 2003](#); [Planck Collaboration et al. 2014a](#)). These images of complex natural structures contain a wealth of information about the origin and often nonlinear formation process of structure. As known from the field of signal processing and imaging science, for example, in optics, cybernetics or time-series analysis, a comprehensive analysis of signals stemming from systems with nonlinear dynamics must go beyond a linear analysis (autocorrelation function in real-space or the power spectrum in Fourier/harmonic space). In image analysis by higher-order statistics (HOS) this is only achieved when the phase information is included. A detailed understanding of this phase information has become very important in natural sciences in recent years and can improve existing methods of image

analysis, image reconstruction and also image compression [Rodenburg et al. \(2007\)](#). Examples for studies on phase information and their application can be found in the development of the first phase retrieval methods in X-ray imaging ([Gerchberg & Saxton 1972](#); [Fienup 1982](#); [Hauptman 1991](#)) or in studies of the phase distribution in CMB data ([Coles et al. 2004](#); [Chiang & Naselsky 2007](#); [Chiang et al. 2007](#)), inter alia.

The higher order  $n$ -point correlation functions with  $n > 2$  in real space or their equivalent polyspectra in Fourier space, however, do not allow direct conclusions on the distribution of the phases yet. If the signal is Gaussian, the Fourier phases are independent and identically uniform distributed. In this case, the second-order measures are anyway sufficient to understand the underlying physics. In generic cases, though, in which the underlying random fields are non-Gaussian, the phases are correlated and contain information that must not be neglected. One of the next steps on the way to a more profound understanding of images in general is a detailed description of the phase distribution and the investigation of the relation between phase information and real-space HOS.

In cosmology, the search for primordial non-Gaussian random fields has attracted great attention since their detection and identification allows for a differentiation between various models of inflation. While, e.g., multi-field inflation or self-interactions of the inflaton field generally yield measurable non-Gaussianity (NG), the standard isotropic cosmology with the simple single-field slow-roll inflationary scenario and a Friedmann-Robertson-Walker (FRW) metric predicts a Gaussian distribution for the first density perturbations of the Universe ([Guth 1981](#); [Albrecht & Steinhardt 1982](#); [Linde 1982](#)). The latest, most precise measurements of parametrized NGs of the local, equilateral and orthogonal type by the Planck team did not reveal significant deviations from Gaussianity ([Planck Collaboration et al. 2014h](#)). A model independent test using the well-established method of surrogates ([Theiler et al. 1992](#)) applied to the Planck CMB maps revealed, however, NGs and hemispherical asymmetries for higher-order statistics ([Planck Collaboration et al. 2014g](#)), which can be traced back to harmonic space phase correlations on large spatial scales at low spherical harmonic modes  $\ell$  with  $\ell < 20$ , confirming previous findings in Wilkinson Microwave Anisotropy Probe (WMAP) data ([R ath et al. 2011](#); [Rossmanith et al. 2012](#); [Modest et al. 2013](#)).

Evidence was found that a best-fit Bianchi type VII<sub>h</sub> template (BT) correlates with the large-scale anomalies in the CMB sky ([Jaffe et al. 2005](#); [Cay on et al. 2006](#); [McEwen et al. 2006](#)), although it is clear the best-fit Bianchi model itself is not compatible with the parameters of the cosmological concordance model (see, e.g., [Jaffe et al. \(2006b\)](#)). Bianchi models provide a generic description of anisotropic homogeneous cosmologies ([Barrow et al. 1985](#)) that are only asymptotically close to a FRW universe. Applying a BT correction to CMB data yields a sky that is statistically isotropic for several subsets of statistical measures, e.g., the local power estimates ([Jaffe et al. 2005](#)). In [Planck Collaboration et al. \(2014g\)](#), it was found that the signal stemming from low- $\ell$  phase correlations can also be significantly reduced if the best-fitting BT is subtracted from the Planck maps. These results could hint at the properties of fully compliant cosmological models, especially when the behavior of the data is studied as a function of the BT correction and on isolated scales.

This work aims at the systematic investigation of the fundamental relation between the Fourier phase distribution in harmonic-space and real-space higher-order statistics, comparable to the Wiener-Khinchin theorem ([Wiener 1930](#); [Khinchin 1957](#)). To do so, we analyze the distributions of Fourier phases directly using the non-parametric statistical Kuiper test and compare these results to real-space signatures from higher-order correlations involving surrogates maps. The investigations are carried out using the CMB as an example of a spherical

data set where no boundary conditions have to be met. We find that our previous real-space results studying the phase correlations of CMB data on the large scales with  $\ell$ -modes of  $\ell < 20$  are reproduced in a study with  $\ell < 10$ . With this even stricter choice of  $\ell$ -interval we make sure that our analysis of the phase distribution is comparable to the phase analysis in [Chiang et al. \(2007\)](#) where they have used exactly the same range. To modify the strength of phase correlations contained in the data, we make use of anisotropic Bianchi type VII<sub>h</sub> best-fit templates. We compare full-sky CMB maps of the WMAP experiment ([Bennett et al. 2013](#)) and the Planck mission ([Planck Collaboration et al. 2014a](#)).

## 6.2 Methods

Assuming that an image  $I(x, y)$  can be represented in terms of linear superposition of (not necessarily orthogonal) basis functions  $\beta_i(x, y)$  by  $I(x, y) = \sum_i a_i \beta_i(x, y)$ , the CMB map with its temperature anisotropies  $\Delta T/T(\theta, \phi)$  at angular position  $(\theta, \phi)$  can be expanded in orthonormal spherical harmonics  $Y_{\ell m}$  as

$$\Delta T/T(\theta, \phi) = \sum_{l=0}^{\infty} \sum_{m=-l}^l a_{\ell m} Y_{\ell m}(\theta, \phi) \quad (6.1)$$

with the complex spherical harmonic coefficients

$$a_{\ell m} = \int d\mathbf{n} T(\mathbf{n}) Y_{\ell m}^*(\mathbf{n}),$$

where  $\mathbf{n}$  is the unit direction vector,  $T$  is the CMB temperature anisotropy,  $Y_{\ell m}^*$  are the complex conjugates of the spherical harmonics, and  $a_{\ell m} = |a_{\ell m}| e^{i\varphi_{\ell m}}$ . The phases  $\varphi_{\ell m}$  of the harmonic coefficients are not rotational invariant. The set of the spherical harmonics is defined with respect to a particular coordinate system. For the CMB the usual system is in Galactic coordinates.

Gaussianity of the CMB implies a Gaussian distribution of its independent complex spherical harmonic coefficients  $a_{\ell m}$ . According to theory, the harmonic space phases are then independent and identically distributed (i.i.d.) and follow a uniform distribution in the interval  $[-\pi, \pi]$ . We test for this null hypothesis of uncorrelated phases with two complementary methods to enable a comparison between them. Method A directly explores the distribution of the phases in harmonic space and is motivated by the findings in [Chiang et al. \(2007\)](#). Method B is based on a real-space analysis and is supported by the method of surrogates. Generating the surrogate maps, we destroy only a single characteristic of the original map, which is a possible correlation of the phases. We gradually diminish the strength of phase correlations by subtracting a Bianchi type VII<sub>h</sub> best-fit template (taken from [Jaffe et al. \(2006a\)](#) for WMAP, taken from [McEwen et al. \(2013\)](#); [Planck Collaboration et al. \(2014j\)](#) for Planck) multiplied by a strength factor of  $f = 0.1, 0.3, 0.5, 0.7, 0.9$  and 1.0 from the original map to enable a comparison of the response in method A and B as a function of the correction. Tests reveal so far that remaining Galactic plane foreground residuals and inpainting techniques in Planck SMICA and SEVEM and WMAP-9 ILC do not influence the low- $\ell$  phase correlations which corresponds to findings in [Räth et al. \(2011\)](#); [Rossmannith et al. \(2012\)](#); [Planck Collaboration et al. \(2014g\)](#). We will therefore use full-sky maps in our analysis.

### 6.2.1 Method A – phase space

For a precise analysis of the phase distributions of the maps, we calculate the  $a_{\ell m}$  coefficients of Planck SMICA and SEVEM<sup>1</sup> and WMAP-9 ILC<sup>2</sup> full-sky maps and test their phases  $\varphi_{\ell m}$  for independence. We obtain 54 phases  $\varphi_{\ell m}$  with values between  $-\pi$  and  $\pi$  depending on the chosen coordinate system after an  $a_{\ell m}$ -decomposition for  $\ell \in [2, 10]$ ,  $m > 0$ . If these  $\varphi_{\ell m}$  fulfill the random phase hypothesis, i.e., are i.i.d. and follow a uniform distribution, the phase difference taken between these phases should be uniformly distributed in  $[0, 2\pi]$ . To test this, we define subsets of differences with fixed separations  $(\Delta\ell, \Delta m)$  by  $\Delta\varphi(\Delta\ell, \Delta m) = \varphi_{\ell+\Delta\ell, m+\Delta m} - \varphi_{\ell m}$ . The Kuiper statistic (Kuiper 1960; Press et al. 2007) is then used to test for the null-hypothesis by comparing the cumulative distribution function (CDF) of the  $\Delta\varphi(\Delta\ell, \Delta m)$  with a given uniform CDF. The Kuiper test statistic is  $V = D^+ + D^-$ , where  $D^+$  and  $D^-$  represent the absolute sizes of the most positive and most negative difference between the two cumulative distribution functions that are being compared. For  $N_e > 4$ , the  $p$  value of an observed value  $V$  is given by

$$p = Q_{KP}([\sqrt{N_e} + 0.155 + 0.24\sqrt{N_e}]V) \quad (6.2)$$

with respect to the monotonic function

$$Q_{KP}(\lambda) = 2 \sum_{j=1}^{\infty} (4j^2\lambda^2 - 1)e^{-2j^2\lambda^2}, \quad (6.3)$$

where  $N_e$  is the effective number of data points. The  $p$  value can be interpreted as the probability of measuring a value at least equal to the observed value  $V$  or even more extreme when the test statistic is applied to data that satisfies the null hypothesis. The smaller the  $p$  value is, the more convincing evidence is against the null hypothesis. High  $p$  values for a given  $(\Delta\ell, \Delta m)$  separation therefore indicate the absence of phase correlations between mode pairs separated by  $(\Delta\ell, \Delta m)$ , whereas low values indicate their existence. Values of  $p \leq 0.05$  (5% level) are widely accepted as strong evidence against the null hypothesis.

Our results depend on the chosen coordinate system. However, averaging over rotated systems will show a global trend of the results.

### 6.2.2 Method B – real space

Using a shuffling approach, we generate surrogate maps by randomizing the potentially correlated phases  $\varphi_{\ell m}$  of the original map while preserving the full-sky power spectrum of the map. In a prestep, we apply an initial Gaussian remapping of the temperature field, and a uniform remapping of the phases to avoid any influence of data outliers on the measurement of phase correlations. If the original phases are independent, the shuffling process will statistically not influence the real-space higher-order statistics of the maps. Phase correlations that are contained in the original data are destroyed by the shuffling process. In order to enable a scale-dependent analysis of the maps, we generate one first order surrogate and 200 second-order surrogate maps. In the first-order surrogate, only the phases with  $\ell$  outside the  $\ell$ -range of  $[2, 10]$  are randomized. In a second step, we shuffle the remaining phases inside that  $\ell$ -range. Significant deviations between these two classes of surrogates reveal phase correlations in the original data among  $\varphi_{\ell m}$  with  $\ell \in [2, 10]$ .

To quantify the higher-order content of the surrogate maps, we use two comparable real-space image analysis methods sensitive to HOS, namely, the scaling index method, which

<sup>1</sup><http://www.cosmos.esa.int/web/planck/pla>

<sup>2</sup><http://lambda.gsfc.nasa.gov/product/map/current/>

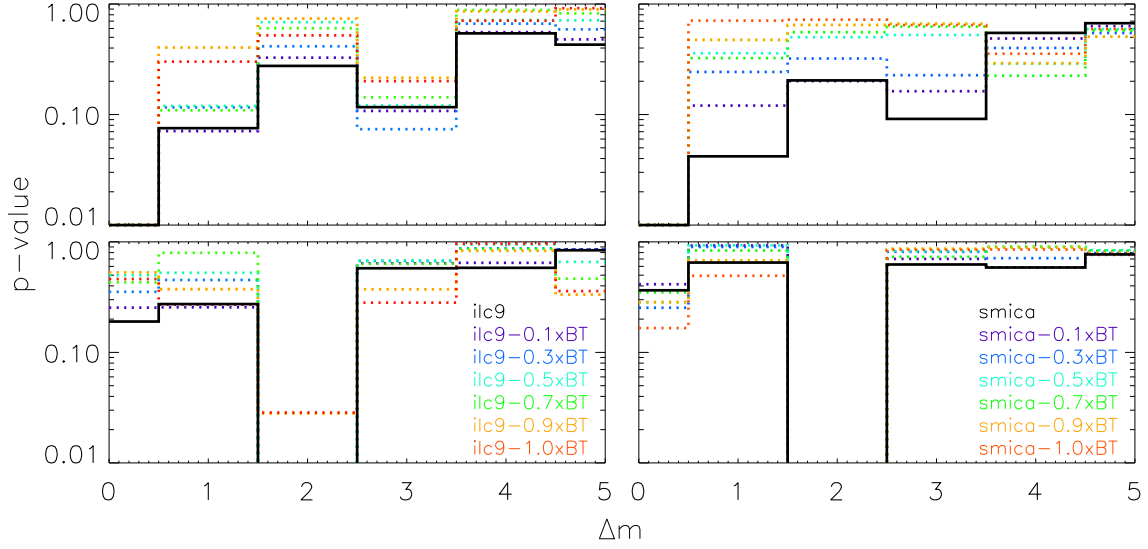


Figure 6.1:  $p$  values of the Kuiper statistic for the WMAP-9 ILC (left) and Planck SMICA map (right) (black solid line) and the corresponding Bianchi-corrected maps (colored dotted lines) for  $\Delta\ell = 0$  (top) and  $\Delta\ell = 1$  (bottom), calculated in the Galactic coordinate system. The Planck SEVEM map (not shown here) resembles the SMICA results. Note that subtracting the corresponding BTs does not significantly reduce the dip at  $(\Delta\ell, \Delta m) = (1, 2)$ .

calculates the weighted scaling indices  $\alpha$  of the three-dimensional point distribution  $P = \{\mathbf{p}_i\}$  of the CMB expressed by

$$\alpha(\mathbf{p}_i, r) = \frac{\sum_{j=1}^{N_{\text{pix}}} q \left( \frac{d_{ij}}{r} \right)^q e^{-\left( \frac{d_{ij}}{r} \right)^q}}{\sum_{j=1}^{N_{\text{pix}}} e^{-\left( \frac{d_{ij}}{r} \right)^q}}, \quad (6.4)$$

as developed in R ath & Morfill (1997); R ath et al. (2012), and a set of three statistics known as the Minkowski functionals (Minkowski 1903),

$$\begin{aligned} M_0 &= \int_Q da \\ M_1 &= \frac{1}{4} \int_{\partial Q} d\ell \\ M_2 &= \frac{1}{2\pi} \int_{\partial Q} d\ell k_g, \end{aligned}$$

which were introduced into cosmology by Mecke et al. (1994); Winitzki & Kosowsky (1998); Schmalzing & G orski (1998). For details and former results see Modest et al. (2013).

Calculating the Minkowski functionals, the surrogate temperature maps are divided into active and a non-active parts by running over 200 threshold steps  $v_i$  with  $-4\sigma_T \leq v_i \leq +4\sigma_T$ . Temperature values of the surrogate maps are counted as active if they lie above the temperature threshold step, whereas the other values are taken as non-active. We then calculate area, perimeter and Euler characteristic of the active pixels. These three Minkowski functionals are calculated for 768 overlapping hemispheres in the sky. To quantify the degree of agreement between the surrogates of the two different orders with respect to higher order correlations found with the three Minkowski functionals  $M_0$  (area),  $M_1$  (perimeter) and  $M_2$  (Euler), we calculate

the mean of each Minkowski functional  $M_{\star, \text{surro2}}$  for  $N = 200$  realizations of the second-order surrogate, per hemisphere  $h$  and threshold bin  $\mathbf{v}$ ,

$$A := \langle M_{\star, \text{surro2}}(\mathbf{v}, h) \rangle = \frac{1}{N} \sum_{m=1}^N M_{\star, \text{surro2}}(m, \mathbf{v}, h)$$

and the standard deviation

$$\sigma_{M_{\star, \text{surro2}}}(\mathbf{v}, h) = \left( \frac{1}{N-1} \sum_{m=1}^N (M_{\star, \text{surro2}}(m, \mathbf{v}, h) - A)^2 \right)^{1/2}$$

for  $m = 1, \dots, N$ . We combine mean and standard deviation in a diagonal  $\chi^2$  statistic, per hemisphere  $h$ , for the surrogates of first order

$$\chi_{M_{\star, \text{surro1}}}^2(h) = \sum_{j=0}^{\mathbf{v}} \left[ \frac{M_{\star, \text{surro1}}(j, h) - A}{\sigma_{M_{\star, \text{surro2}}}(j, h)} \right]^2$$

and for the second-order surrogate maps

$$\chi_{M_{\star, \text{surro2}}}^2(h, m) = \sum_{j=0}^{\mathbf{v}} \left[ \frac{M_{\star, \text{surro2}}(m, j, h) - A}{\sigma_{M_{\star, \text{surro2}}}(j, h)} \right]^2.$$

Plots of the  $\chi^2$  statistic can be found in Fig. 6.3.

Finally, the degree of agreement between the two types of surrogates is quantified by the  $\sigma$ -normalized deviation  $S$

$$S(\chi_{M_{\star}}^2(h)) = \frac{\chi_{M_{\star, \text{surro1}}}^2(h) - \langle \chi_{M_{\star, \text{surro2}}}^2(h) \rangle}{\sigma_{\chi_{M_{\star, \text{surro2}}}^2}(h)} \quad (6.5)$$

for each of the 768 hemispheres with  $\langle \chi_{M_{\star, \text{surro2}}}^2(h) \rangle$  and  $\sigma_{\chi_{M_{\star, \text{surro2}}}^2}(h)$  denoting the mean and the standard deviation of  $\chi_{M_{\star, \text{surro2}}}^2(h)$ . We obtain the  $\sigma$ -normalized hemispherical deviations  $S(\chi_{M_0}^2(h))$ ,  $S(\chi_{M_1}^2(h))$  and  $S(\chi_{M_2}^2(h))$  (called  $S$  values) between the surrogates of first and second order for the area, perimeter and Euler characteristics. As for the Minkowski functionals, we calculate the mean  $\langle \alpha(r) \rangle$  and standard deviation  $\sigma_{\alpha(r)}$  of the scaling indices  $\alpha(\mathbf{p}_i, r)$  for the set of 768 hemispherical maps. The differences of the two classes of surrogates are again quantified by the  $\sigma$ -normalized deviation  $S$ :

$$S(Y) = \frac{Y_{\text{surro1}} - \langle Y_{\text{surro2}} \rangle}{\sigma_{Y_{\text{surro2}}}} \quad (6.6)$$

where  $Y$  represents a diagonal  $\chi^2$  statistic

$$\chi_{\langle \alpha(r) \rangle, \sigma_{\alpha(r)}}^2 = \sum_{j=1}^2 \left[ \frac{B_j - \langle B_j \rangle}{\sigma_{B_j}} \right]^2, \quad (6.7)$$

as a combination of the mean and the standard deviation where  $B_1(r) = \langle \alpha(r) \rangle$ ,  $B_2(r) = \sigma_{\alpha(r)}$ .

It can be shown that method B is rotational invariant. Regardless of the chosen coordinate system, the  $S$ -value pattern on the sphere is preserved.

## 6.3 Results

Comparing the results from the Kuiper statistic of 36  $(\Delta\ell, \Delta m)$ -combinations with  $\Delta\ell = 0 - 5$  and  $\Delta m = 0 - 5$  in different coordinate systems, we find the trend that gradually subtracting the corresponding BT from the original map leads to increasing Kuiper  $p$  values with increasing Bianchi factor  $f$  if  $p < 0.1$  in the original data. This behavior is a strong indication for vanishing phase correlations due to BT correction in certain phase separation subsets depending on the chosen coordinate system. Figure 6.1 shows the significance levels for 12 combinations of  $\Delta\ell = 0, 1$  and  $\Delta m = 0, 1, 2, 3, 4, 5$  for all steps of BT corrections with respect to the Galactic coordinate system. The majority of the  $(\Delta\ell, \Delta m)$ -mode-pairs has  $p$ -values that lie well above 0.05 and even above 0.1 in the original map as well as after the BT corrections. These results have a relatively high probability of above 10% to arise under the null-hypothesis of random phases.

In rare cases, we find higher  $p$  values in the original map and values below 0.1 after the BT correction. In the Galactic coordinate system, e.g., this is the case at  $(\Delta\ell, \Delta m) = (5, 0)$  in the original ILC9 map, where the full BT correction leads to  $p = 0.064$ . For SMICA, this behavior is found for the correction with  $0.3 \times \text{BT}$  and  $0.5 \times \text{BT}$ , for SEVEM at correction steps 0.1, 0.3, 0.5 and 0.7. The mode-pair  $(\Delta\ell, \Delta m) = (1, 2)$  is another exception: The subtraction of the BT is almost not increasing the  $p$  values which remain below the 3% level for SMICA and ILC9, and below 6% for SEVEM, with respect to the Galactic coordinate system. In Table 6.1, we list the  $p$ -values of the original maps and the fully BT corrected maps for all subsets with at least one value  $< 0.1$  either in the original map or after the full BT correction with  $1.0 \times \text{BT}$ . The findings in the original maps are consistent with those for the WMAP-3 year data tested by Chiang et al. (2007) and reveal an overall consistent picture of the different maps and experiments.

Averaging over 768 rotated coordinate systems reveals phase correlations for  $\Delta\ell = 0, 1$  and  $\Delta m = 0, 1, 2$  but none for larger phase separations, as shown in the supplemental material in section 6.6.

| $(\Delta\ell, \Delta m)$ | ILC9         |              | SMICA        |              | SEVEM        |              |
|--------------------------|--------------|--------------|--------------|--------------|--------------|--------------|
|                          | orig         | corr         | orig         | corr         | orig         | corr         |
| (0,1)                    | <b>0.075</b> | 0.301        | <b>0.042</b> | 0.707        | 0.160        | 0.853        |
| (0,2)                    | 0.275        | 0.520        | 0.204        | 0.722        | <b>0.096</b> | 0.916        |
| (0,3)                    | 0.117        | 0.201        | <b>0.091</b> | 0.645        | 0.242        | 0.526        |
| (1,2)                    | <b>0.003</b> | <b>0.029</b> | <b>0.002</b> | <b>0.005</b> | <b>0.008</b> | <b>0.060</b> |
| (2,5)                    | <b>0.090</b> | 0.193        | <b>0.087</b> | 0.471        | 0.151        | 0.454        |
| (5,0)                    | 0.321        | <b>0.064</b> | 0.148        | 0.126        | 0.132        | 0.196        |
| (5,4)                    | 0.364        | 0.218        | 0.220        | 0.328        | <b>0.078</b> | 0.139        |

Table 6.1: Combinations of  $(\Delta\ell, \Delta m)$  with  $p$  values  $< 0.1$  (bold) for at least one of the three maps SMICA, SEVEM and ILC9. We show  $p$  before and after the full BT correction.

In Fig. 6.2, we show the inverse  $|p - 1|$  values with respect to the Bianchi factor  $f$  for  $\Delta\ell = 0, 1$  to visualize the trend in individual subsets (for the Galactic system). The mode-pairs  $(0, 1), (0, 2), (0, 3)$  and  $(2, 5)$  (not shown) show a mostly monotonic decrease in the  $p$  value with increasing  $a$ . The analysis of  $(5, 0)$  and  $(5, 4)$  (not shown) yields rather constant  $p$  values above 0.75. Mode-pairs with  $(1, 2)$  remain correlated in all maps.

The  $\chi^2$  statistic of the Minkowski functionals for 768 different hemispheres of the sky

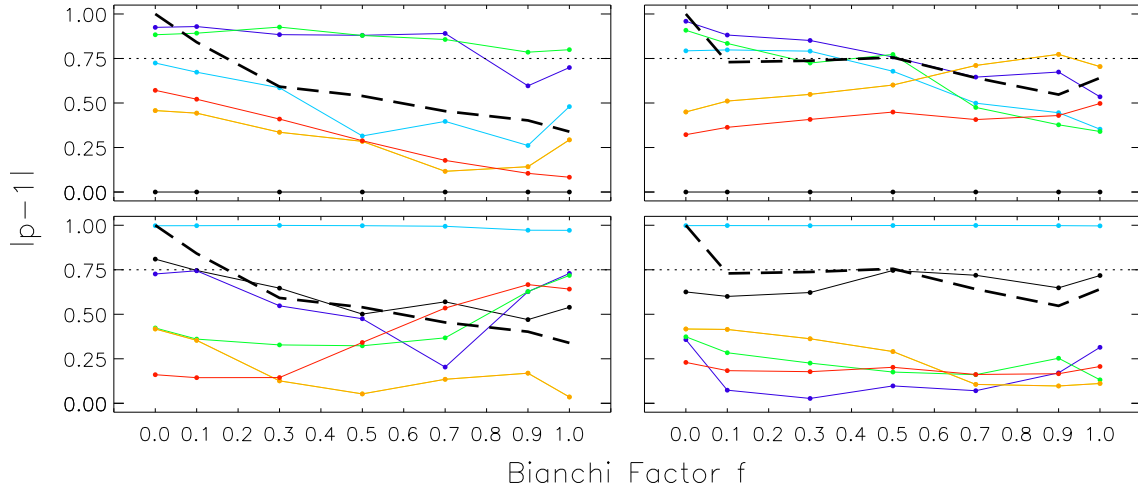


Figure 6.2:  $|p-1|$ -values of the ILC9 (left) and SMICA (right) map for  $\Delta\ell = 0$  (top) and  $\Delta\ell = 1$  (bottom). The colored lines mark the different  $\Delta m$  with black=0, purple=1, blue=2, green=3, orange=4, red=5. The black dashed line shows the normalized mean  $S$ -value of the output maps from method B (Figure 6.4).

shows strong deviations between the first and 200 second-order surrogates generated from the original maps as can be seen in Fig. 6.3. The  $\chi^2$  distribution of 768 first-order surrogate maps, generated from the Planck SMICA map, is after a BT correction very similar to the distribution of the second-order surrogates which indicates that the originally contained phase correlations of the CMB are strongly reduced due to the subtraction of a Bianchi template. Analyzing the  $\chi^2$  statistics of the Minkowski functionals and scaling indices by a comparison of surrogates 1 and 2 with respect to the local hemispherical contributions, method B reveals that both image analysis techniques detect similar asymmetries and deviations from Gaussianity in the CMB sky. This is true for the latest release of the SMICA and SEVEM map of Planck as well as for the WMAP-9 ILC data and does not depend on the chosen coordinate system. In Fig. 6.4, we show the color-coded  $S$  values from a Minkowski Euler analysis for the 768 hemispheres, where a red pixel indicates strong deviations from Gaussianity in the hemisphere surrounding that pixel, and blue none. Subtracting the corresponding Bianchi type VII<sub>h</sub> best-fit templates from the Planck SMICA map diminishes phase correlations and gives an increasing isotropic Gaussian sky, which can be confirmed by an analysis with the scaling indices in Fig. 6.5. For the used SMICA map, the minimum signal of deviations is particularly detected at  $a = 0.9$ , not at 1.0. This is interesting in itself and requires further interpretation with respect to Bianchi template fitting and here especially to its  $\ell$ -range dependency.

To quantify the overall strength of deviation from the random phase hypothesis in method B, we calculate the mean of all  $S$  values from the Minkowski analysis and show the result in Fig. 6.2. The comparison of method A and B reveals that the normalized mean of the real-space method B decreases with  $a$ , likewise to the decrease for several pairs  $(\Delta\ell, \Delta m) = (0, 1), (0, 2), (0, 3), (2, 5)$  in the Galactic system. Although method B reveals that the strength of the phase correlations is highly reduced after subtracting  $1.0 \times BT$ , the  $p$  value of  $(\Delta\ell, \Delta m) = (1, 2)$  remains almost constant.

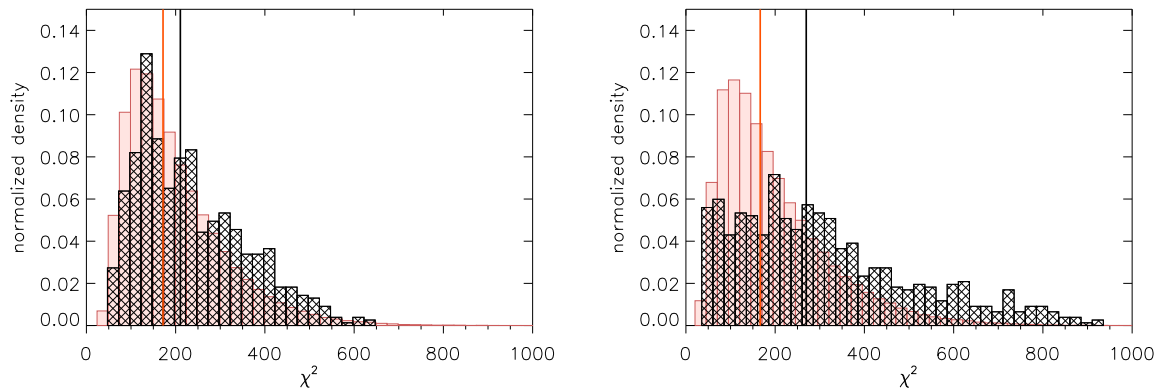


Figure 6.3:  $\chi^2$ -distribution of the surrogates of first (black) and second (red) order generated from the Planck SMICA map, before (left) and after (right) the BT correction. The black and red lines indicate the corresponding median values of the histograms.

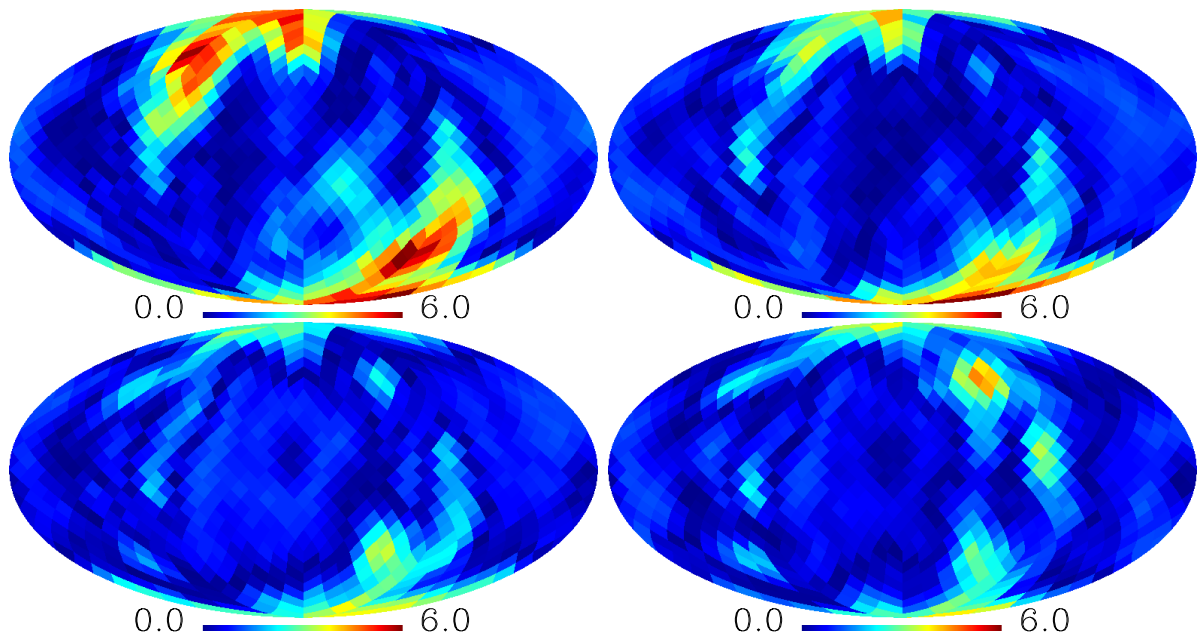


Figure 6.4: Mollweide projection in Galactic coordinates of the  $S$ -value distribution of method B using the Minkowski Euler characteristic for the Planck SMICA map. The BT is subtracted with a factor of  $f = 0.0, 0.3, 0.7, 1.0$  (upper left to lower right), respectively.

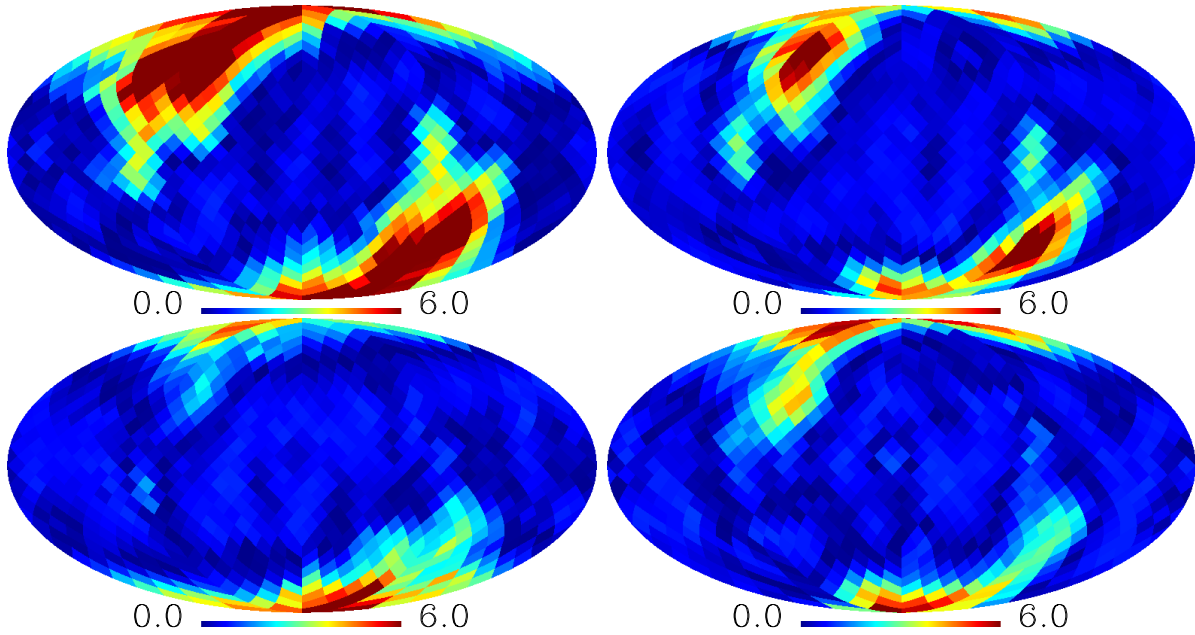


Figure 6.5: Same as Fig. 6.4 but for the the scaling index method.

## 6.4 Conclusions & Outlook

In a comparative study of the important and so far not understood relation between real-space higher-order statistics and the Fourier space phase information, we provide for the first time heuristic results using the example of the spherical CMB data. Analyzing the phase distribution of CMB maps on low  $\ell$  modes, we detect a clear trend, but with low statistical significance, for gradually diminished phase correlations due to the subtraction of a Bianchi type VII<sub>h</sub> anisotropic cosmological template. This is especially true when looking at the subsets of “close-by” phase differences with  $\Delta\ell = 0 - 1$  and  $\Delta m = 0 - 3$  in the Galactic coordinate system. In comparison, we confirm a significantly vanishing higher-order signal of hemispherical asymmetries in the CMB sky for Bianchi-corrected maps. We suggest that the detected signatures of non-Gaussianities and hemispherical asymmetries in real space due to phase correlations in the CMB can partly be explained by correlations between phases  $\varphi_{\ell m}$  separated by small  $\Delta\ell$  and  $\Delta m$ .

In some subsets, the phase-correlations are not diminished when subtracting the Bianchi template. Furthermore, the BT correction can induce phase correlations for individual mode pairs, depending on the chosen coordinate system of the map. However, the statistic of the Kuiper test with such small effective numbers as used in this work is not strongly significant. The Bianchi template is not fully compatible with standard cosmological parameters, that fit very well to observations, and we cannot expect a perfect reduction of all existing anomalies, whether in real space or phase space. It is not solved yet whether individual phases  $\varphi_{\ell m}$  are responsible for the signatures of phase correlations or whether the relation between certain subsets plays a dominant role. On the studied very low  $\ell$  range, instrumental noise is not an issue and our method is neither influenced by residual foregrounds nor experimental systematics as shown in our earlier works. We therefore expect a cosmological explanation for the detected anomalies.

Low- $\ell$  anomalies are also detected in the linear regime of the data as e.g. the power

asymmetry (e.g. [Hansen et al. 2009](#)), parity asymmetry (e.g. [Ben-David et al. 2012](#)), multipole alignment (e.g. [Copi et al. 2013b](#)) or the lack of large-angle correlations (e.g. [Copi et al. 2013a](#)). For an overview of the latest Planck results see [Planck Collaboration et al. \(2014g\)](#). It might point to a common physical origin of low- $\ell$  anomalies that they manifest themselves in the linear as well as non-linear regime of the data.

Our results can contribute to an understanding of non-Gaussian signals, which in cosmology may be due to Early Universe physics. However, those signals can also indicate the detection of later cosmological events affecting the CMB. The existence of anomalies detected in the WMAP and Planck maps at large angular scales may even point to new fundamental physics. A detailed scale-dependent analysis of latest CMB data and a study of the coordinate system dependencies with respect to anisotropic cosmologies can give further insight into the constraints of fully compliant cosmological models. In summary, the combined analysis of phase statistics including their variations due to either template subtraction or refined surrogate generating methods, and of the respective response of higher-order statistics, offers a new statistical framework to disentangle the information content of images.

## 6.5 Acknowledgements

We greatly thank Theresa Jaffe and Jason McEwen for providing us with the latest WMAP and Planck Bianchi templates, respectively. For the calculations we employ the HEALPix software [Górski et al. \(2005\)](#). HIM acknowledges the support of the Christiane Nüsslein-Volhard (CNV) foundation and the International Max Planck Research School.

## 6.6 Supplemental Material

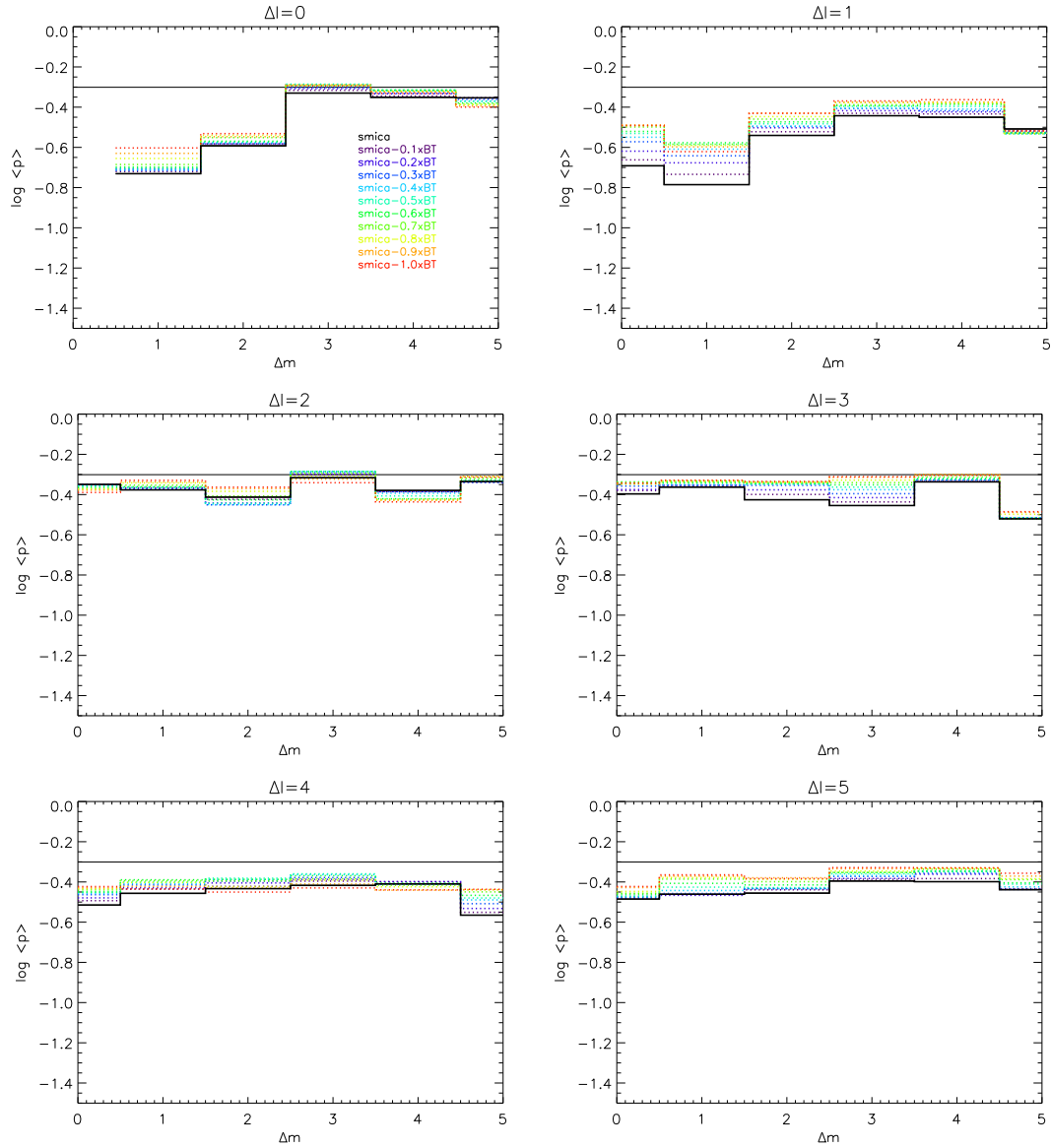


Figure 6.6: Mean  $p$  values of the Kuiper statistic for Planck SMICA map and the corresponding Bianchi-corrected maps (colored dotted lines) for  $\Delta \ell = 0$  to  $\Delta \ell = 5$  (left to right and top to bottom), averaged over 768 coordinate systems, shown in base 10 logarithm.

## Chapter 7

# Significance of the results

Distinct anomalies in the large-scale properties of the cosmic microwave background have been detected in WMAP and Planck data over the last years, as pointed out in this work. The anomalies are detected by a huge variety of probes, the method of the surrogates used here is one example. Other higher-order studies in the nonlinear regime, and even the power spectrum analysis in the linear regime of CMB data, reveal deviations from the assumptions of the standard model of cosmology, too. It is difficult to understand in detail where the detected anomalies stem from. They could be induced by the experiment itself or by foreground sources. Yet, several carefully designed studies, including this one here, suggest that the anomalies are likely primordial. If the anomalies, such as the power asymmetry, the multipole alignment or the phase correlations, are in fact primordial, then understanding their origin is fundamental and will revise the standard model of cosmology, or even disclose new physics.

The relevance of the result but also the consistency of the large-scale anomalies within analysis techniques, experiments and data releases totally motivates a detailed examination of their origin. However, as e.g. [Bunn \(2010\)](#) has stated, the large-angle CMB anomalies remain controversial, largely because of the difficulty in interpreting a posteriori statistics which can amplify statistical fluctuations and might thus produce misleading results. In general, it is necessary that the methods used in a statistical data analysis to qualify and quantify deviations from Gaussianity or the cosmological principle are

- based on a priori statistics,
- not significantly influenced by astrophysical foreground sources,
- and significant over cosmic variance.

The methods in this work try to take this into account when testing for the standard hypothesis of a Gaussian CMB, that is deduced from the standard model of inflation. To this end, the Gaussian hypothesis is mimicked by constructing surrogate maps of the second order by randomizing the Fourier phases of the original CMB maps. The first order surrogate maps keep their possible phase correlations (for a scale-dependent analysis at least on predefined length scales). Two different measures (Minkowski functionals and scaling indices) are then chosen to quantify the higher-order information of these maps. The two measures each provide distribution functions for the first- and second-order surrogates that are then compared with each other by a  $\chi^2$  statistic. The second-order surrogate map is generated in 500 realizations throughout this work.

This method allows one to predefine  $\ell$ -ranges that will be analyzed within the studies to test for the scale-dependence of the anomalies. This is a great advantage of the method, and it is strictly enforced to avoid a posteriori bias here. The ranges are also physically motivated. Regarding the influence of foregrounds, several tests here and elsewhere have shown that remaining Galactic plane bias and point sources in the maps do not affect the results on the largest scales.

The significance of the results plays an important role when distinguishing the anomalies from statistical fluctuations. However, in many complex studies it is extremely hard or even impossible to assess the general significance of the results. Evaluating the findings in this study, the final step compares the  $\chi^2$  statistic of the first and the mean  $\chi^2$  statistic of the second-order surrogates by normalizing their difference with the standard deviation of the  $\chi^2$  statistic of the second-order surrogates. However, since the exact model for the distribution of the  $\chi^2$  values of the surrogates is unknown, it is not possible to directly determine the statistical significance of the results in a Bayesian sense of probability. In accordance with the frequentist view, this work furthermore determines the empirical probabilities that state how many of the  $\chi^2$  values of the second-order surrogates lie above (or below, respectively, depends) the first-order surrogate values. [Modest et al. \(2013\)](#) for example shows that the empirical probability for a deviation from Gaussianity is 92.2% for the full sky analysis of WMAP ILC7 data with the Minkowski functionals. The probability is even higher with > 99.8% when looking at specific hemispheres. Correspondingly, the latest results for the scaling indices as published in [Planck Collaboration et al. \(2014g\)](#) are obtained with an empirical probability > 99% for the SMICA, SEVEM, NILC and C-R maps. The results give strong hints on hemispherical asymmetries and a scale-dependent deviation from Gaussianity in the large-scale properties of the CMB sky.

# Chapter 8

## Conclusions

The cosmological observations of the last decades, made possible by extensive experiments and the latest techniques, have enhanced our understanding of the Universe and narrowed down the possible scenarios for the very early stages of the Cosmos. However, better data quality and specified cosmological theories have on the other hand also raised new questions on the nature of the primordial density perturbations and on the correct theory for the very early Universe. The idea behind this work was to test the latest cosmological data for the validity of the Gaussian hypothesis for the primordial density perturbations, observable as temperature fluctuations in the cosmic microwave background radiation (CMB).

The Gaussian hypothesis is one of the main predictions from single field slow-roll inflation which is widely accepted as the standard theory for inflation in the cosmological concordance model. In the case of primordial Gaussianity, and only then, two-point correlations comprise the full information content of the primordial perturbations. Gaussianity of the CMB would therefore imply vanishing nonlinear higher-order correlations, and equivalently the non-existence of Fourier phase correlations in harmonic space, i. e. random and uncorrelated phases. The concordance model furthermore comprises the idea of the cosmological principle of homogeneity and statistical isotropy. Depending on the existence, the nature and the strength of a deviation from the Gaussian theorem and/or the axiomatic cosmological principle, these distinct violations of the standard theory can help to distinguish between different alternatives to the standard paradigm, or even stimulate ideas for new cosmological models.

The main approach of my work was the enhancement and the completion of a model-independent test for the Gaussian hypothesis in WMAP and Planck full-sky and cut-sky CMB data sets. In addition, I have studied the characteristics of the phase correlations and developed new techniques for the joint interpretation of real-space higher order statistics and phase-space information. For this purpose, surrogate maps have been generated from the original data sets and were compared with the original maps. By definition, the surrogate maps do not contain any phase correlations anymore since possibly existent phase correlations in the original map have been destroyed by a randomization of the phases. I have quantified the higher-order content of the original maps and the surrogate maps with the help of two different image analysis techniques, the scaling indices and the Minkowski functionals. Significant deviations between the results from the surrogate maps and those gained from the original maps point to a violation of the Gaussian hypothesis for the CMB. Since a couple of alternative theories for inflation suggest the scale-dependence of non-Gaussianity, the surrogate maps were generated as scale-dependent maps in a two-step procedure. The scales can be chosen freely. Throughout this work, I have compared the scales of the lowest  $\ell$ -modes (largest scales in the sky) with

$\Delta\ell = [2, 20]$  and the  $\ell$ -modes corresponding to the first peak in the CMB power spectrum at  $\Delta\ell = [120, 300]$ , and a few other scales in between. To test the CMB sky for isotropy it is necessary to compare different directions in the sky. Hence, I have analyzed single hemispheres of the sky, whose poles are oriented in 768 different directions, with respect to their signal of non-Gaussianity.

For  $\Delta\ell = [2, 20]$  and  $\Delta\ell = [120, 300]$  deviations from Gaussianity were detected using the image analysis technique of the scaling indices and have revealed a hemispherical asymmetry between the northern and southern sky. However, the conclusion in Chapter 3 is that only the largest scales yield significant results which are congruent for the WMAP ILC and NILC maps that differ in their underlying foreground reduction algorithms. The map-making procedure of the ILC map and/or residual noise in the maps might lead to artificial non-Gaussianities at smaller scales. The results remain stable over the different data releases from 3-, 5- and 7-year WMAP data.

I have repeated the analysis of WMAP 7-year ILC and NILC maps for the lower  $\ell$ -range with the complementary technique of the Minkowski functionals in Chapter 4. The results from the Minkowski functionals were similar to the scaling indices results. Both methods have shown strong deviations from Gaussianity in the sky. The higher  $\ell$ -range  $\Delta\ell = [120, 300]$  again showed differences between the ILC and NILC maps as well as between the image analysis techniques, which makes an intrinsic nature of the signal on this range less likely. Decreasing the size of the analyzed sky regions for the low- $\ell$  study, I have found no signature for non-Gaussianity in the northern ecliptic sky but individual spots show deviations from Gaussianity in the south. Furthermore, I have investigated non-Gaussian CMB simulations parametrized by  $f_{\text{NL}}$  that quantifies non-Gaussianity of the local-type based on the bispectrum. The simulations did not reproduce the low- $\ell$  results from the experimental data. It is therefore concluded that  $f_{\text{NL}}$  cannot account for the detected low- $\ell$  anomalies.

Galactic plane foreground effects are suspected of causing CMB non-Gaussianities. It is therefore desirable to fully exclude Galactic plane foreground bias from the data, for example, in a cut-sky analysis. However, the construction of surrogate maps only works for an orthonormal set of Fourier functions. The full-sky spherical harmonics fulfill this constraint but require a transformation into a cut-sky version when parts of the sky are excluded. The feasibility of generating the surrogates for an incomplete data set is demonstrated in Chapter 5. The shuffling of the Fourier phases is enabled by transforming the spherical harmonics into a new set of basis functions. An application of the cut-sky surrogates on 5- and 7-year WMAP data and the analysis with the scaling indices and the Minkowski functionals showed that the detected large-scale non-Gaussianities and hemispherical asymmetries are still detected even when the complete Galactic plane is removed. It is concluded that the Galactic plane cannot be the dominant source for the anomalies.

I have pursued the search for the source of large-scale non-Gaussianities with a direct study of the distribution of the Fourier phases in Chapter 6. Specific anisotropic Bianchi templates are known for their ability to account for some CMB anomalies. I have gradually subtracted best-fit Bianchi type VII<sub>h</sub> anisotropic cosmological templates from the 9-year WMAP ILC as well as Planck SMICA and SEVEM maps. Analyzing the phase distribution for low- $\ell$  modes directly, I found a clear trend for gradually diminished phase correlations. This is especially true when looking at the subsets of “close-by” phase differences with  $\Delta\ell = 0 - 1$  and  $\Delta m = 0 - 3$  in the Galactic coordinate system. The surrogate analysis described above was repeated for Bianchi subtracted maps with the aid of scaling indices and Minkowski functionals measured in real-space. For the first time, it was shown that diminishing the phase correlations is

---

accompanied by a significantly decreasing higher-order signal of hemispherical asymmetries in the CMB sky. Therefore, I claim that the detected signatures of non-Gaussianities and hemispherical asymmetries in real-space due to phase correlations in the CMB can partly be explained by correlations between phases separated by small  $\Delta\ell$  and  $\Delta m$ . These investigations open a new road to a refined understanding of signatures of non-Gaussianities in complex spatial structures especially by elucidating the meaning of Fourier phase correlations and their influence on higher-order statistics.

In summary, this thesis has contributed to modern cosmology by analyzing the information content of the phase distribution of the latest CMB data. The detection of scale-dependent non-Gaussianities on the largest angular scales in WMAP and Planck CMB data sets points to a violation of standard single field slow-roll inflation and challenges the cosmological principle. I have confirmed previous studies based on the scaling indices by an implementation of the Minkowski functionals to the method of the surrogates. The stability of the detected anomalies in WMAP and Planck data was demonstrated. I gained insight into the nature of the phase correlations by studying model-dependent non-Gaussian simulations based on  $f_{\text{NL}}$  and Bianchi template subtracted CMB maps. My combined analysis of phase statistics, surrogates and higher-order statistics offers a new statistical framework to disentangle in particular the nonlinear information content of images. A study of additional cosmological models would contribute to the interpretation of CMB anomalies.

There is already evidence that after the successful studies of the temperature anisotropies, the upcoming Planck polarization data together with the BICEP/Keck data will serve as a second data set that can shed light on the nature of the CMB and its anomalies. The new data will offer new possibilities for further studies on the CMB lensing potential and eventually on primordial gravitational waves especially by analyzing the B-mode polarization, which would constrain cosmological parameters and hint at models for inflation and the corresponding energy scales. The promising application of Minkowski functionals, scaling indices, and further statistical tools to polarization data needs considerable development. A phase analysis describing the polarized sky would be an important and complementary approach to classical studies.



# References

- ACQUAVIVA V., BARTOLO N., MATARRESE S. & RIOTTO A. (2003). *Gauge-invariant second-order perturbations and non-Gaussianity from inflation*. Nuclear Physics B 667:pp. 119–148. [arXiv:astro-ph/0209156](#). 14, 52, 70
- ADAMS W.S. (1941). *Some Results with the COUDÉ Spectrograph of the Mount Wilson Observatory*. ApJ93:p. 11. 1
- ADE P.A.R. et al. (2014). *Detection of B-Mode Polarization at Degree Angular Scales by BICEP2*. Physical Review Letters 112(24):241101. [arXiv:1403.3985](#). 13
- AHN C.P. et al. (2012). *The Ninth Data Release of the Sloan Digital Sky Survey: First Spectroscopic Data from the SDSS-III Baryon Oscillation Spectroscopic Survey*. ApJS203:21. [arXiv:1207.7137](#). 2, 107
- ALBRECHT A. & MAGUEIJO J. (1999). *Time varying speed of light as a solution to cosmological puzzles*. Phys. Rev. D59(4):043516. [arXiv:astro-ph/9811018](#). 8
- ALBRECHT A. & STEINHARDT P.J. (1982). *Cosmology for grand unified theories with radiatively induced symmetry breaking*. Physical Review Letters 48:pp. 1220–1223. URL <http://dx.doi.org/10.1103/PhysRevLett.48.1220>. 6, 52, 70, 91, 108
- ALISHAHIHA M., SILVERSTEIN E. & TONG D. (2004). *DBI in the sky: Non-Gaussianity from inflation with a speed limit*. Phys. Rev. D70(12):123505. [arXiv:hep-th/0404084](#). 15, 70
- ALPHER R.A., BETHE H. & GAMOW G. (1948). *The Origin of Chemical Elements*. Physical Review 73:pp. 803–804. URL <http://journals.aps.org/pr/pdf/10.1103/PhysRev.73.803>. 1
- ALPHER R.A. & HERMAN R. (1948). *Evolution of the Universe*. Nat162:pp. 774–775. URL <http://adsabs.harvard.edu/abs/1948Natur.162..774A>. 1
- ALPHER R.A. & HERMAN R.C. (1950). *Theory of the Origin and Relative Abundance Distribution of the Elements*. Reviews of Modern Physics 22:pp. 153–212. URL <http://link.aps.org/doi/10.1103/RevModPhys.22.153>. 1
- ANDERSON L. et al. (2012). *The clustering of galaxies in the SDSS-III Baryon Oscillation Spectroscopic Survey: baryon acoustic oscillations in the Data Release 9 spectroscopic galaxy sample*. MNRAS427:pp. 3435–3467. [arXiv:1203.6594](#). 7
- ARKANI-HAMED N., CREMINELLI P., MUKOHYAMA S. & ZALDARRIAGA M. (2004). *Ghost inflation*. J. Cosmol. Astropat. Phys.4:p. 1. [arXiv:hep-th/0312100](#). 15, 70

- ARMENDÁRIZ-PICÓN C., DAMOUR T. & MUKHANOV V. (1999). *k-Inflation*. Physics Letters B 458:pp. 209–218. [arXiv:hep-th/9904075](#). 14, 52
- BABICH D., CREMINELLI P. & ZALDARRIAGA M. (2004). *The shape of non-Gaussianities*. J. Cosmol. Astropat. Phys.8:009. [arXiv:astro-ph/0405356](#). 44, 45
- BARDEEN J.M. (1980). *Gauge-invariant cosmological perturbations*. Phys. Rev. D22:pp. 1882–1905. URL <http://link.aps.org/doi/10.1103/PhysRevD.22.1882>. 10, 72
- BARROW J.D., JUSZKIEWICZ R. & SONODA D.H. (1985). *Universal rotation: how large can it be?* MNRAS213(4):pp. 917–943. URL <http://mnras.oxfordjournals.org/content/213/4/917.abstract>. 16, 108
- BARROW J.D. & SONODA D.H. (1986). *Asymptotic stability of Bianchi type universes*. Physics Reports139:pp. 1–49. URL <http://adsabs.harvard.edu/abs/1986PhR...139....1B>. 16
- BARTOLO N., KOMATSU E., MATARRESE S. & RIOTTO A. (2004). *Non-Gaussianity from inflation: theory and observations*. Physics Reports402:pp. 103–266. [arXiv:astro-ph/0406398](#). 70
- BARTOLO N., MATARRESE S. & RIOTTO A. (2002). *Non-Gaussianity from inflation*. Phys. Rev. D65(10):103505. [arXiv:hep-ph/0112261](#). 14, 70
- BASAK S. & DELABROUILLE J. (2012). *A needlet internal linear combination analysis of WMAP 7-year data: estimation of CMB temperature map and power spectrum*. MNRAS419:pp. 1163–1175. [arXiv:1106.5383](#). 22, 72
- BEN-DAVID A., KOVETZ E.D. & ITZHAKI N. (2012). *Parity in the Cosmic Microwave Background: Space Oddity*. ApJ748:39. [arXiv:1108.1702](#). 30, 117
- BENNETT C.L. (2006). *Cosmology from start to finish*. Nat440:pp. 1126–1131. 1, 5
- BENNETT C.L. et al. (1996). *Four-Year COBE DMR Cosmic Microwave Background Observations: Maps and Basic Results*. ApJ464:p. L1. [arXiv:astro-ph/9601067](#). 27
- BENNETT C.L. et al. (2003). *First-Year Wilkinson Microwave Anisotropy Probe (WMAP) Observations: Preliminary Maps and Basic Results*. ApJS148:pp. 1–27. [arXiv:astro-ph/0302207](#). 24, 27, 73, 107
- BENNETT C.L. et al. (2011). *Seven-year Wilkinson Microwave Anisotropy Probe (WMAP) Observations: Are There Cosmic Microwave Background Anomalies?* ApJS192:pp. 17–+. [arXiv:1001.4758](#). 28, 33, 53
- BENNETT C.L. et al. (2013). *Nine-year Wilkinson Microwave Anisotropy Probe (WMAP) Observations: Final Maps and Results*. ApJS208:20. [arXiv:1212.5225](#). 7, 18, 109
- BERERA A. (2006). *The warm inflationary universe*. Contemporary Physics 47:pp. 33–49. [arXiv:0809.4198](#). 15
- BERNARDEAU F. & UZAN J.P. (2002). *Non-Gaussianity in multifield inflation*. Phys. Rev. D66(10):pp. 103506–+. [arXiv:hep-ph/0207295](#). 14, 52, 70

- BERNUI A. (2008). *Anomalous CMB north-south asymmetry*. Phys. Rev. D78(6):pp. 063531–+. [arXiv:0809.0934](#). 30
- BERNUI A. & REBOUÇAS M.J. (2012). *Mapping the large-angle deviation from Gaussianity in simulated CMB maps*. Phys. Rev. D85:p. 023522. [arXiv:1109.6086](#). 44
- BERNUI A., TSALLIS C. & VILLELA T. (2007). *Deviation from Gaussianity in the cosmic microwave background temperature fluctuations*. EPL (Europhysics Letters) 78:p. 19001. [arXiv:astro-ph/0703708](#). 30
- BEUTLER F. et al. (2011). *The 6dF Galaxy Survey: baryon acoustic oscillations and the local Hubble constant*. MNRAS416:pp. 3017–3032. [arXiv:1106.3366](#). 7
- BIANCHI L. (1898). *Sugli spazi a tre dimensioni che ammettono un gruppo continuo di movimenti (On the spaces of three dimensions that admit a continuous group of movements)*. Mem. Mat. Fis. Soc. Ital. Sci. 11:pp. 267–352. 16
- BICEP2/KECK AND PLANCK COLLABORATIONS et al. (2015). *Joint Analysis of BICEP2/Keck Array and Planck Data*. Physical Review Letters 114(10):101301. [arXiv:1502.00612](#). 13
- BIELEWICZ P., ERIKSEN H.K., BANDAY A.J., GÓRSKI K.M. & LILJE P.B. (2005). *Multipole Vector Anomalies in the First-Year WMAP Data: A Cut-Sky Analysis*. ApJ635:pp. 750–760. [arXiv:astro-ph/0507186](#). 28
- BINNIG G., QUATE C.F. & GERBER C. (1986). *Atomic Force Microscope*. Phys. Rev. Lett. 56:pp. 930–933. URL <http://link.aps.org/doi/10.1103/PhysRevLett.56.930>. 107
- BOND J.R., JAFFE A.H. & KNOX L. (1998). *Estimating the power spectrum of the cosmic microwave background*. Phys. Rev. D57:pp. 2117–2137. [arXiv:astro-ph/9708203](#). 27
- BRANDENBERGER R. (2012). *Do we have a Theory of Early Universe Cosmology?* ArXiv e-prints [arXiv:1204.6108](#). 1, 8
- BRANDENBERGER R.H. (2013). *Unconventional Cosmology*. In G. Calcagni, L. Papantonopoulos, G. Siopsis & N. Tsamis (eds.), *Lecture Notes in Physics, Berlin Springer Verlag*, vol. 863 of *Lecture Notes in Physics, Berlin Springer Verlag*, p. 333. [arXiv:1203.6698](#). 14, 15
- BRIDGES M. et al. (2008). *Bianchi VIIh models and the cold spot texture*. MNRAS390(4):pp. 1372–1376. [arXiv:0712.1789](#). 27
- BUCHBINDER E.I., KHOURY J. & OVRUT B.A. (2008). *Non-Gaussianities in New Ekpyrotic Cosmology*. Physical Review Letters 100(17):171302. [arXiv:0710.5172](#). 15, 52, 70
- BUNDE A., KROPP J. & SCHELLNHUBER H. (eds.) (2002). *The science of disasters: Climate disruptions, heart attacks and market crashes*. Physics and astronomy online library (Springer, Berlin [u.a.]). ISBN 3540413243. URL [http://gso.gbv.de/DB=2.1/CMD?ACT=SRCHA&SRT=YOP&IKT=1016&TRM=ppn+341772518&sourceid=fbw\\_bibsonomy](http://gso.gbv.de/DB=2.1/CMD?ACT=SRCHA&SRT=YOP&IKT=1016&TRM=ppn+341772518&sourceid=fbw_bibsonomy). 35, 42, 53, 92
- BUNN E.F. (2010). *Large-Angle Anomalies in the Microwave Background*. ArXiv e-prints [arXiv:1006.2084](#). 33, 119

- BUNN E.F., FERREIRA P.G. & SILK J. (1996). *How Anisotropic is Our Universe?* Physical Review Letters 77:pp. 2883–2886. [arXiv:astro-ph/9605123](#). 16
- BYRNES C.T. & CHOI K.Y. (2010). *Review of Local Non-Gaussianity from Multifield Inflation*. Advances in Astronomy 2010. [arXiv:1002.3110](#). 14, 45
- CABELLA P. & KAMIONKOWSKI M. (2004). *Theory of Cosmic Microwave Background Polarization*. ArXiv Astrophysics e-prints [arXiv:astro-ph/0403392](#). 13
- CARDOSO J.F., LE JEUNE M., DELABROUILLE J., BETOULE M. & PATANCHON G. (2008). *Component Separation With Flexible Models – Application to Multichannel Astrophysical Observations*. IEEE Journal of Selected Topics in Signal Processing 2:pp. 735–746. [arXiv:0803.1814](#). 24
- CAYÓN L. (2010). *Variograms of the cosmic microwave background temperature fluctuations: confirmation of deviations from statistical isotropy*. MNRAS405:pp. 1084–1088. [arXiv:1001.4680](#). 91
- CAYÓN L., JIN J. & TREASTER A. (2005). *Higher Criticism statistic: detecting and identifying non-Gaussianity in the WMAP first-year data*. MNRAS362:pp. 826–832. [arXiv:astro-ph/0507246](#). 26
- CAYÓN L. et al. (2001). *Spherical Mexican hat wavelet: an application to detect non-Gaussianity in the COBE-DMR maps*. MNRAS326:pp. 1243–1248. [arXiv:astro-ph/0105111](#). 44
- CAYÓN L. et al. (2006). *No Higher Criticism of the Bianchi-corrected Wilkinson Microwave Anisotropy Probe data*. MNRAS369:pp. 598–602. [arXiv:astro-ph/0602023](#). 108
- CHEN X. (2005a). *Multithroat brane inflation*. Phys. Rev. D71(6):063506. [arXiv:hep-th/0408084](#). 15
- CHEN X. (2005b). *Running non-Gaussianities in Dirac-Born-Infeld inflation*. Phys. Rev. D72(12):123518. [arXiv:astro-ph/0507053](#). 15, 45, 52
- CHEN X. (2010). *Primordial Non-Gaussianities from Inflation Models*. Advances in Astronomy 2010:638979. [arXiv:1002.1416](#). 70
- CHEN X., HUANG M.x., KACHRU S. & SHIU G. (2007). *Observational signatures and non-Gaussianities of general single-field inflation*. J. Cosmol. Astropat. Phys.1:002. [arXiv:hep-th/0605045](#). 14, 45
- CHIANG L.Y. & NASELSKY P.D. (2007). *Phase analysis of the cosmic microwave background from incomplete sky coverage*. MNRAS380:pp. L71–L74. [arXiv:0705.1626](#). 108
- CHIANG L.Y., NASELSKY P.D. & COLES P. (2007). *Departure from Gaussianity of the Cosmic Microwave Background Temperature Anisotropies in the Three-Year WMAP Data*. ApJ664:pp. 8–13. [arXiv:astro-ph/0603662](#). 31, 53, 71, 92, 108, 109, 113
- CHIANG L.Y., NASELSKY P.D., VERKHODANOV O.V. & WAY M.J. (2003). *Non-Gaussianity of the Derived Maps from the First-Year Wilkinson Microwave Anisotropy Probe Data*. ApJ590:pp. L65–L68. [arXiv:astro-ph/0303643](#). 30, 53, 71, 91

- CLOWES R.G. et al. (2013). *A structure in the early Universe at  $z \sim 1.3$  that exceeds the homogeneity scale of the  $R$ - $W$  concordance cosmology.* MNRAS429:pp. 2910–2916. [arXiv:1211.6256](#). 2
- COLES P. & CHIANG L.Y. (2001). *Non-Linearity and Non-Gaussianity Through Phase Information.* In A.J. Banday, S. Zaroubi & M. Bartelmann (eds.), *Mining the Sky*, p. 289. [arXiv:astro-ph/0010521](#). 31
- COLES P., DINEEN P., EARL J. & WRIGHT D. (2004). *Phase correlations in cosmic microwave background temperature maps.* MNRAS350:pp. 989–1004. [arXiv:astro-ph/0310252](#). 31, 53, 71, 91, 108
- COLLEY W.N. & GOTT J.R. (2003). *Genus topology of the cosmic microwave background from WMAP.* MNRAS344:pp. 686–695. [arXiv:astro-ph/0303020](#). 44
- COLLEY W.N. & GOTT J.R. (2015). *Genus topology and cross-correlation of BICEP2 and Planck 353 GHz B-modes: further evidence favouring gravity wave detection.* MNRAS447:pp. 2034–2045. [arXiv:1409.4491](#). 13
- CONLEY A. et al. (2011). *Supernova Constraints and Systematic Uncertainties from the First Three Years of the Supernova Legacy Survey.* ApJS192:1. [arXiv:1104.1443](#). 7
- COPI C.J., HUTERER D., SCHWARZ D.J. & STARKMAN G.D. (2006). *On the large-angle anomalies of the microwave sky.* MNRAS367:pp. 79–102. [arXiv:astro-ph/0508047](#). 28
- COPI C.J., HUTERER D., SCHWARZ D.J. & STARKMAN G.D. (2007). *Uncorrelated universe: Statistical anisotropy and the vanishing angular correlation function in WMAP years 1–3.* Phys. Rev. D75(2):pp. 023507–+. [arXiv:astro-ph/0605135](#). 27, 28
- COPI C.J., HUTERER D., SCHWARZ D.J. & STARKMAN G.D. (2009). *No large-angle correlations on the non-Galactic microwave sky.* MNRAS399:pp. 295–303. [arXiv:0808.3767](#). 27, 52, 91
- COPI C.J., HUTERER D., SCHWARZ D.J. & STARKMAN G.D. (2010). *Large-Angle Anomalies in the CMB.* Advances in Astronomy 2010:847541. [arXiv:1004.5602](#). 25, 28, 29, 52, 91
- COPI C.J., HUTERER D., SCHWARZ D.J. & STARKMAN G.D. (2011). *Bias in low-multipole cosmic microwave background reconstructions.* MNRAS418:pp. 505–515. 101
- COPI C.J., HUTERER D., SCHWARZ D.J. & STARKMAN G.D. (2013a). *Lack of large-angle  $TT$  correlations persists in WMAP and Planck.* ArXiv e-prints [arXiv:1310.3831](#). 27, 28, 117
- COPI C.J., HUTERER D., SCHWARZ D.J. & STARKMAN G.D. (2013b). *Large-scale alignments from WMAP and Planck.* ArXiv e-prints [arXiv:1311.4562](#). 117
- COPI C.J., HUTERER D. & STARKMAN G.D. (2004). *Multipole vectors: A new representation of the CMB sky and evidence for statistical anisotropy or non-Gaussianity at  $2 \leq l \leq 8$ .* Phys. Rev. D70(4):043515. [arXiv:astro-ph/0310511](#). 28, 44
- CRUZ M., CAYÓN L., MARTÍNEZ-GONZÁLEZ E., VIELVA P. & JIN J. (2007a). *The Non-Gaussian Cold Spot in the 3 Year Wilkinson Microwave Anisotropy Probe Data.* ApJ655:pp. 11–20. [arXiv:astro-ph/0603859](#). 26

- CRUZ M., MARTÍNEZ-GONZÁLEZ E., VIELVA P. & CAYÓN L. (2005). *Detection of a non-Gaussian spot in WMAP*. MNRAS356:pp. 29–40. [arXiv:astro-ph/0405341](#). 26
- CRUZ M., TUCCI M., MARTÍNEZ-GONZÁLEZ E. & VIELVA P. (2006). *The non-Gaussian cold spot in Wilkinson Microwave Anisotropy Probe: significance, morphology and foreground contribution*. MNRAS369:pp. 57–67. [arXiv:astro-ph/0601427](#). 26
- CRUZ M., TUROK N., VIELVA P., MARTÍNEZ-GONZÁLEZ E. & HOBSON M. (2007b). *A Cosmic Microwave Background Feature Consistent with a Cosmic Texture*. Science 318:pp. 1612–. [arXiv:0710.5737](#). 27
- CRUZ M. et al. (2008). *The CMB cold spot: texture, cluster or void?* MNRAS390:pp. 913–919. [arXiv:0804.2904](#). 27
- DE OLIVEIRA-COSTA A., TEGMARK M., ZALDARRIAGA M. & HAMILTON A. (2004). *Significance of the largest scale CMB fluctuations in WMAP*. Phys. Rev. D69(6):pp. 063516–+. [arXiv:astro-ph/0307282](#). 27, 28, 52, 70
- DELABROUILLE J., CARDOSO J.F. & PATANCHON G. (2003). *Multidetector multicomponent spectral matching and applications for cosmic microwave background data analysis*. MNRAS346:pp. 1089–1102. [arXiv:astro-ph/0211504](#). 24
- DELABROUILLE J. et al. (2009). *A full sky, low foreground, high resolution CMB map from WMAP*. A&A493:pp. 835–857. [arXiv:0807.0773](#). 22, 54, 72, 79, 99
- DICKE R.H., PEEBLES P.J.E., ROLL P.G. & WILKINSON D.T. (1965). *Cosmic Black-Body Radiation*. ApJ142:pp. 414–419. URL <http://adsabs.harvard.edu/abs/1965ApJ...142..414D>. 1
- DICKINSON C. et al. (2009). *Bayesian Component Separation and Cosmic Microwave Background Estimation for the Five-Year WMAP Temperature Data*. ApJ705:pp. 1607–1623. [arXiv:0903.4311](#). 91
- DORÉ O. et al. (2007). *Signature of patchy reionization in the polarization anisotropy of the CMB*. Phys. Rev. D76(4):043002. [arXiv:astro-ph/0701784](#). 13
- DUPAC X. & TAUBER J. (2005). *Scanning strategy for mapping the Cosmic Microwave Background anisotropies with Planck*. A&A430:pp. 363–371. [arXiv:astro-ph/0409405](#). 19
- DURRER R. (2001). *The theory of CMB anisotropies*. Journal of Physical Studies 5:pp. 177–215. [arXiv:astro-ph/0109522](#). 9
- DVALI G. & TYE S.H.H. (1999). *Brane inflation*. Physics Letters B 450:pp. 72–82. [arXiv:hep-ph/9812483](#). 15
- EINSTEIN A. (1915). *Die Feldgleichungen der Gravitation*. Sitzungsberichte der Königlich Preußischen Akademie der Wissenschaften (Berlin), Seite 844-847. pp. 844–847. URL <http://adsabs.harvard.edu/abs/1915SPAW.....844E>. 2
- EINSTEIN A. (1916). *Die Grundlage der allgemeinen Relativitätstheorie*. Annalen der Physik 354:pp. 769–822. URL <http://adsabs.harvard.edu/abs/1916AnP...354..769E>. 2

- EINSTEIN A. (1917). *Kosmologische Betrachtungen zur allgemeinen Relativitätstheorie*. Sitzungsberichte der Königlich Preußischen Akademie der Wissenschaften (Berlin), Seite 142-152. pp. 142–152. URL <http://adsabs.harvard.edu/abs/1917SPAW.....142E>. 2
- ELLIS G.F.R. & MAARTENS R. (2004). *The emergent universe: inflationary cosmology with no singularity*. *Classical and Quantum Gravity* 21:pp. 223–232. [arXiv:gr-qc/0211082](https://arxiv.org/abs/gr-qc/0211082). 15
- ELSNER F. & WANDELT B.D. (2009). *Improved Simulation of Non-Gaussian Temperature and Polarization Cosmic Microwave Background Maps*. *ApJS*184:pp. 264–270. [arXiv:0909.0009](https://arxiv.org/abs/0909.0009). 72
- ENQVIST K. & SLOTH M.S. (2002). *Adiabatic CMB perturbations in pre-Big-Bang string cosmology*. *Nuclear Physics B* 626:pp. 395–409. [arXiv:hep-ph/0109214](https://arxiv.org/abs/hep-ph/0109214). 15, 70
- ERICKCEK A.L., KAMIONKOWSKI M. & CARROLL S.M. (2008). *A hemispherical power asymmetry from inflation*. *Phys. Rev. D*78(12):123520. [arXiv:0806.0377](https://arxiv.org/abs/0806.0377). 16
- ERIKSEN H.K., BANDAY A.J., GÓRSKI K.M., HANSEN F.K. & LILJE P.B. (2007). *Hemispherical Power Asymmetry in the Third-Year Wilkinson Microwave Anisotropy Probe Sky Maps*. *ApJ*660:pp. L81–L84. [arXiv:astro-ph/0701089](https://arxiv.org/abs/astro-ph/0701089). 30, 52, 70, 91
- ERIKSEN H.K., BANDAY A.J., GÓRSKI K.M. & LILJE P.B. (2005). *The N-Point Correlation Functions of the First-Year Wilkinson Microwave Anisotropy Probe Sky Maps*. *ApJ*622:pp. 58–71. [arXiv:astro-ph/0407271](https://arxiv.org/abs/astro-ph/0407271). 52, 70, 71
- ERIKSEN H.K., HANSEN F.K., BANDAY A.J., GÓRSKI K.M. & LILJE P.B. (2004a). *Asymmetries in the Cosmic Microwave Background Anisotropy Field*. *ApJ*605:pp. 14–20. [arXiv:astro-ph/0307507](https://arxiv.org/abs/astro-ph/0307507). 30, 70, 103
- ERIKSEN H.K., NOVIKOV D.I., LILJE P.B., BANDAY A.J. & GÓRSKI K.M. (2004b). *Testing for Non-Gaussianity in the Wilkinson Microwave Anisotropy Probe Data: Minkowski Functionals and the Length of the Skeleton*. *ApJ*612:pp. 64–80. [arXiv:astro-ph/0401276](https://arxiv.org/abs/astro-ph/0401276). 30, 52, 58, 91, 95, 96, 103
- ERIKSEN H.K. et al. (2008). *Joint Bayesian Component Separation and CMB Power Spectrum Estimation*. *ApJ*676:pp. 10–32. [arXiv:0709.1058](https://arxiv.org/abs/0709.1058). 23
- FEENEY S.M., JOHNSON M.C., MCEWEN J.D., MORTLOCK D.J. & PEIRIS H.V. (2013). *Hierarchical Bayesian detection algorithm for early-universe relics in the cosmic microwave background*. *Phys. Rev. D*88(4):043012. [arXiv:1210.2725](https://arxiv.org/abs/1210.2725). 27
- FENG J.L. (2005). *Supersymmetry and cosmology*. *Annals of Physics* 315:pp. 2–51. [arXiv:hep-ph/0405215](https://arxiv.org/abs/hep-ph/0405215). 16
- FERNÁNDEZ-COBOS R., VIELVA P., BARREIRO R.B. & MARTÍNEZ-GONZÁLEZ E. (2012). *Multiresolution internal template cleaning: an application to the Wilkinson Microwave Anisotropy Probe 7-yr polarization data*. *MNRAS*420:pp. 2162–2169. [arXiv:1106.2016](https://arxiv.org/abs/1106.2016). 23
- FIENUP J.R. (1982). *Phase retrieval algorithms: a comparison*. *Appl. Opt.* 21(15):pp. 2758–2769. URL <http://ao.osa.org/abstract.cfm?URI=ao-21-15-2758>. 108

- FINELLI F. & BRANDENBERGER R. (2002). *Generation of a scale-invariant spectrum of adiabatic fluctuations in cosmological models with a contracting phase.* Phys. Rev. D65(10):103522. [arXiv:hep-th/0112249](#). 15
- FIXSEN D.J. (2009). *The Temperature of the Cosmic Microwave Background.* ApJ707:pp. 916–920. [arXiv:0911.1955](#). 1, 10
- FIXSEN D.J. et al. (1996). *The Cosmic Microwave Background Spectrum from the Full COBE FIRAS Data Set.* ApJ473:p. 576. [arXiv:astro-ph/9605054](#). 10
- GAMOW G. (1946). *Expanding Universe and the Origin of Elements.* Physical Review 70:pp. 572–573. URL <http://adsabs.harvard.edu/abs/1946PhRv...70..572G>. 1
- GAMOW G. (1961). *The creation of the universe.* (Penguin Group (USA) Incorporated, New York, Viking Press [1961]). ISBN 978-0670246007. 1
- GARRIGA J. & MUKHANOV V.F. (1999). *Perturbations in k-inflation.* Physics Letters B 458:pp. 219–225. [arXiv:hep-th/9904176](#). 14, 52
- GASPERINI M. & VENEZIANO G. (1993). *Pre-big-bang in string cosmology.* Astroparticle Physics 1:pp. 317–339. [arXiv:hep-th/9211021](#). 15
- GASPERINI M. & VENEZIANO G. (2003). *The pre-big bang scenario in string cosmology.* Physics Reports373:pp. 1–212. [arXiv:hep-th/0207130](#). 15
- GERCHBERG R.W. & SAXTON W.O. (1972). *Practical algorithm for determination of phase from image and diffraction plane pictures.* OPTIK 35(2):pp. 237–246. ISSN 0030-4026. 108
- GLIOZZI M., PAPADAKIS I.E. & RÄTH C. (2006). *Correlated spectral and temporal changes in 3C 390.3: a new link between AGN and Galactic black hole binaries?* A&A449:pp. 969–983. [arXiv:astro-ph/0512026](#). 42
- GLIOZZI M., RÄTH C., PAPADAKIS I.E. & REIG P. (2010). *Characterizing black hole variability with nonlinear methods: the case of the X-ray Nova 4U 1543-47.* A&A512:A21. [arXiv:0912.4676](#). 35, 42, 92
- GLIOZZI M. et al. (2002). *On the nature of X-ray variability in Ark 564.* A&A391:pp. 875–886. [arXiv:astro-ph/0206190](#). 42
- GOLD B. et al. (2011). *Seven-year Wilkinson Microwave Anisotropy Probe (WMAP) Observations: Galactic Foreground Emission.* ApJS192:pp. 15–+. [arXiv:1001.4555](#). 27, 53, 54, 71, 92, 94, 99
- GORDON C. (2007). *Broken Isotropy from a Linear Modulation of the Primordial Perturbations.* ApJ656:pp. 636–640. [arXiv:astro-ph/0607423](#). 16
- GORDON C., HU W., HUTERER D. & CRAWFORD T. (2005). *Spontaneous isotropy breaking: A mechanism for CMB multipole alignments.* Phys. Rev. D72(10):103002. [arXiv:astro-ph/0509301](#). 28
- GORSKI K.M. (1994). *On determining the spectrum of primordial inhomogeneity from the COBE DMR sky maps: Method.* ApJ430:pp. L85–L88. [arXiv:astro-ph/9403066](#). 92

- GORSKI K.M. et al. (1994). *On determining the spectrum of primordial inhomogeneity from the COBE DMR sky maps: Results of two-year data analysis*. ApJ430:pp. L89–L92. [arXiv:astro-ph/9403067](#). 92
- GÓRSKI K.M. et al. (2005). *HEALPix: A Framework for High-Resolution Discretization and Fast Analysis of Data Distributed on the Sphere*. ApJ622:pp. 759–771. [arXiv:astro-ph/0409513](#). 20, 58, 67, 71, 89, 96, 106, 117
- GOTT J.R. III, DICKINSON M. & MELOTT A.L. (1986). *The sponge-like topology of large-scale structure in the universe*. ApJ306:pp. 341–357. URL <http://adsabs.harvard.edu/abs/1986ApJ...306..341G>. 40
- GOTT J.R. III et al. (2005). *A Map of the Universe*. ApJ624:pp. 463–484. [arXiv:astro-ph/0310571](#). 2
- GRASSBERGER P. & PROCACCIA I. (1983). *Characterization of strange attractors*. Physical Review Letters 50:pp. 346–349. URL <http://adsabs.harvard.edu/abs/1983PhRvL...50..346G>. 56
- GRASSBERGER P. & PROCACCIA I. (1983). *Measuring the strangeness of strange attractors*. Physica D: Nonlinear Phenomena 9:pp. 189–208. ISSN 0167-2789. URL <http://www.sciencedirect.com/science/article/pii/0167278983902981>. 42, 76
- GURZADYAN V.G. et al. (2009). *Kolmogorov cosmic microwave background sky*. A&A497:pp. 343–346. [arXiv:0811.2732](#). 26
- GUTH A.H. (1981). *Inflationary universe: A possible solution to the horizon and flatness problems*. Phys. Rev. D23:pp. 347–356. URL <http://adsabs.harvard.edu/abs/1981PhRvD...23..347G>. 6, 52, 70, 91, 108
- GUTH A.H. & KAISER D.I. (2005). *Inflationary Cosmology: Exploring the Universe from the Smallest to the Largest Scales*. Science 307(5711):pp. 884–890. [arXiv:astro-ph/0502328](#). 6, 14
- HADWIGER H. (1957). *Vorlesungen über Inhalt, Oberfläche und Isoperimetrie* (Springer-Verlag, Berlin). ISBN 978-3-642-94703-2. URL <http://link.springer.com/book/10.1007%2F978-3-642-94702-5>. 40, 75
- HANSEN F.K., BANDAY A.J. & GÓRSKI K.M. (2004). *Testing the cosmological principle of isotropy: local power-spectrum estimates of the WMAP data*. MNRAS354:pp. 641–665. [arXiv:astro-ph/0404206](#). 30, 52, 61, 70, 103
- HANSEN F.K., BANDAY A.J., GÓRSKI K.M., ERIKSEN H.K. & LILJE P.B. (2009). *Power Asymmetry in Cosmic Microwave Background Fluctuations from Full Sky to Sub-Degree Scales: Is the Universe Isotropic?* ApJ704:pp. 1448–1458. [arXiv:0812.3795](#). 30, 52, 61, 70, 81, 82, 84, 91, 103, 104, 117
- HANSEN F.K., ERIKSEN H.K., BANDAY A.J., GORSKI K.M. & LILJE P.B. (2007). *Cosmic Microwave Background Challenges to the Standard Model*. In N. Metcalfe & T. Shanks (ed.), *Cosmic Frontiers*, vol. 379 of *Astronomical Society of the Pacific Conference Series*, pp. 16–+. URL <http://adsabs.harvard.edu/abs/2007ASPC...379...16H>. 30, 91

- HANSON D. et al. (2013). *Detection of B-Mode Polarization in the Cosmic Microwave Background with Data from the South Pole Telescope*. Physical Review Letters 111(14):141301. [arXiv:1307.5830](#). 12
- HAUPTMAN H.A. (1991). *The phase problem of X-ray crystallography*. Reports on Progress in Physics 54(11):p. 1427. URL <http://stacks.iop.org/0034-4885/54/i=11/a=002>. 108
- HINSHAW G. et al. (1996). *Band Power Spectra in the COBE DMR Four-Year Anisotropy Maps*. ApJ464:p. L17. [arXiv:astro-ph/9601058](#). 27
- HINSHAW G. et al. (2003). *First-Year Wilkinson Microwave Anisotropy Probe (WMAP) Observations: Data Processing Methods and Systematic Error Limits*. ApJS148:pp. 63–95. [arXiv:astro-ph/0302222](#). 19
- HINSHAW G. et al. (2007). *Three-Year Wilkinson Microwave Anisotropy Probe (WMAP) Observations: Temperature Analysis*. ApJS170:pp. 288–334. [arXiv:astro-ph/0603451](#). 22, 25
- HINSHAW G. et al. (2009). *Five-Year Wilkinson Microwave Anisotropy Probe Observations: Data Processing, Sky Maps, and Basic Results*. ApJS180:pp. 225–245. [arXiv:0803.0732](#). 10
- HOFTUFT J. et al. (2009). *Increasing Evidence for Hemispherical Power Asymmetry in the Five-Year WMAP Data*. ApJ699:pp. 985–989. [arXiv:0903.1229](#). 30, 91
- HOU Z., BANDAY A.J. & GÓRSKI K.M. (2009). *The hot and cold spots in five-year WMAP data*. MNRAS396:pp. 1273–1286. [arXiv:0903.4446](#). 26
- HOU Z., BANDAY A.J., GÓRSKI K.M., ELSNER F. & WANDELT B.D. (2010). *The primordial non-Gaussianity of local type ( $f_{NL}^{local}$ ) in the WMAP 5-year data: the length distribution of CMB skeleton*. MNRAS407:pp. 2141–2156. [arXiv:1005.5568](#). 44
- HU W., SUGIYAMA N. & SILK J. (1997). *The physics of microwave background anisotropies*. Nat386:pp. 37–43. [arXiv:astro-ph/9504057](#). 11
- HUBBLE E. (1929). *A Relation between Distance and Radial Velocity among Extra-Galactic Nebulae*. Proceedings of the National Academy of Science 15:pp. 168–173. URL <http://adsabs.harvard.edu/abs/1929PNAS...15..168H>. 2
- INOUE K.T. & SILK J. (2006). *Local Voids as the Origin of Large-Angle Cosmic Microwave Background Anomalies. I*. ApJ648:pp. 23–30. [arXiv:astro-ph/0602478](#). 28
- INOUE K.T. & SILK J. (2007). *Local Voids as the Origin of Large-Angle Cosmic Microwave Background Anomalies: The Effect of a Cosmological Constant*. ApJ664:pp. 650–659. [arXiv:astro-ph/0612347](#). 28
- JAFFE T.R., BANDAY A.J., ERIKSEN H.K., GORSKI K.M. & HANSEN F.K. (2005). *Evidence of Vorticity and Shear at Large Angular Scales in the WMAP Data: A Violation of Cosmological Isotropy?* ApJ629:pp. L1–L4. [arXiv:astro-ph/0503213](#). 16, 28, 108
- JAFFE T.R., BANDAY A.J., ERIKSEN H.K., GÓRSKI K.M. & HANSEN F.K. (2006a). *Bianchi type VIIh models and the WMAP 3-year data*. A&A460:pp. 393–396. [arXiv:astro-ph/0606046](#). 16, 109

- JAFFE T.R., HERVIK S., BANDAY A.J. & GÓRSKI K.M. (2006b). *On the Viability of Bianchi Type VII<sub>h</sub> Models with Dark Energy*. ApJ644:pp. 701–708. [arXiv:astro-ph/0512433](#). 108
- JAMITZKY F. et al. (2001). *Scaling index method as an image processing tool in scanning probe microscopy*. Ultramicroscopy 86(241). 42, 56
- JAROSIK N. et al. (2011). *Seven-year Wilkinson Microwave Anisotropy Probe (WMAP) Observations: Sky Maps, Systematic Errors, and Basic Results*. ApJS192:pp. 14–+. [arXiv:1001.4744](#). 27, 73, 99, 100
- KHINCHIN A.I. (1957). *Mathematical Foundations of Information Theory* (Dover Publications). ISBN 0486604349. URL <http://www.worldcat.org/oclc/544970>. 108
- KHLEBNIKOV S.Y. & TKACHEV I.I. (1996). *Classical Decay of the Inflaton*. Physical Review Letters 77:pp. 219–222. [arXiv:hep-ph/9603378](#). 9
- KHOURY J., OVRUT B.A., STEINHARDT P.J. & TUROK N. (2001). *Ekpyrotic universe: Colliding branes and the origin of the hot big bang*. Phys. Rev. D64(12):p. 123522. [arXiv:hep-th/0103239](#). 15
- KIM J. & NASELSKY P. (2010a). *Anomalous Parity Asymmetry of the Wilkinson Microwave Anisotropy Probe Power Spectrum Data at Low Multipoles*. ApJ714:pp. L265–L267. [arXiv:1001.4613](#). 30
- KIM J. & NASELSKY P. (2010b). *Anomalous parity asymmetry of WMAP 7-year power spectrum data at low multipoles: Is it cosmological or systematics?* Phys. Rev. D82(6):063002. [arXiv:1002.0148](#). 30
- KODAMA H. & SASAKI M. (1984). *Cosmological Perturbation Theory*. Progress of Theoretical Physics Supplement 78:p. 1. URL <http://ptps.oxfordjournals.org/content/78/1.abstract>. 10
- KOFMAN L., LINDE A. & STAROBINSKY A.A. (1994). *Reheating after Inflation*. Phys. Rev. Lett. 73:pp. 3195–3198. URL <http://link.aps.org/doi/10.1103/PhysRevLett.73.3195>. 6
- KOGUT A., HINSHAW G. & BANDAY A.J. (1997). *Limits to global rotation and shear from the COBE DMR four-year sky maps*. Phys. Rev. D55:pp. 1901–1905. [arXiv:astro-ph/9701090](#). 16
- KOGUT A. et al. (1993). *Dipole Anisotropy in the COBE Differential Microwave Radiometers First-Year Sky Maps*. ApJ419:p. 1. [arXiv:astro-ph/9312056](#). 10
- KOMATSU E. (2010). *Hunting for primordial non-Gaussianity in the cosmic microwave background*. Classical and Quantum Gravity 27(12):124010. [arXiv:1003.6097](#). 14
- KOMATSU E. (2011). *Lecture Notes - Some Basics of the Expansion of the Universe, CMB and LSS*. URL [http://www.mpa-garching.mpg.de/~komatsu/cmb/lecture\\_cosmo\\_iucaa\\_2011.pdf](http://www.mpa-garching.mpg.de/~komatsu/cmb/lecture_cosmo_iucaa_2011.pdf). 2
- KOMATSU E. & SPERGEL D.N. (2001). *Acoustic signatures in the primary microwave background bispectrum*. Phys. Rev. D63(6):pp. 063002–+. [arXiv:astro-ph/0005036](#). 14, 45

- KOMATSU E. et al. (2003). *First-Year Wilkinson Microwave Anisotropy Probe (WMAP) Observations: Tests of Gaussianity*. ApJS148:pp. 119–134. [arXiv:astro-ph/0302223](#). 24
- KOMATSU E. et al. (2009a). *Five-Year Wilkinson Microwave Anisotropy Probe Observations: Cosmological Interpretation*. ApJS180:pp. 330–376. [arXiv:0803.0547](#). 52
- KOMATSU E. et al. (2009b). *Non-Gaussianity as a Probe of the Physics of the Primordial Universe and the Astrophysics of the Low Redshift Universe*. In *astro2010: The Astronomy and Astrophysics Decadal Survey*, vol. 2010 of *ArXiv Astrophysics e-prints*, p. 158. [arXiv:0902.4759](#). 35, 52, 74
- KOMATSU E. et al. (2011). *Seven-year Wilkinson Microwave Anisotropy Probe (WMAP) Observations: Cosmological Interpretation*. ApJS192:18. [arXiv:1001.4538](#). 34, 52, 70, 88
- KOVETZ E.D. & KAMIONKOWSKI M. (2013). *21-cm Lensing and the Cold Spot in the Cosmic Microwave Background*. Physical Review Letters 110(17):171301. [arXiv:1211.4610](#). 27
- KUIPER N.H. (1960). *Tests concerning random points on a circle*. Koninklijke Nederlandse Akademie Van Wetenschappen Proceedings Series A 63:pp. 38–47. 48, 110
- LAND K. & MAGUEIJO J. (2005a). *Examination of Evidence for a Preferred Axis in the Cosmic Radiation Anisotropy*. Physical Review Letters 95(7):pp. 071301–+. [arXiv:astro-ph/0502237](#). 27, 28
- LAND K. & MAGUEIJO J. (2005b). *Is the Universe odd?* Phys. Rev. D72(10):101302. [arXiv:astro-ph/0507289](#). 29
- LAND K. & MAGUEIJO J. (2007). *The Axis of Evil revisited*. MNRAS378:pp. 153–158. [arXiv:astro-ph/0611518](#). 28
- LEACH S.M. et al. (2008). *Component separation methods for the PLANCK mission*. A&A491:pp. 597–615. [arXiv:0805.0269](#). 23
- LEHNERS J.L. (2010). *Ekpyrotic Nongaussianity: A Review*. Advances in Astronomy 2010:903907. [arXiv:1001.3125](#). 15
- LEHNERS J.L. & STEINHARDT P.J. (2008). *Intuitive understanding of non-Gaussianity in ekpyrotic and cyclic models*. Phys. Rev. D78(2):023506. [arXiv:0804.1293](#). 15, 52, 70
- LI L.F., CAI R.G., GUO Z.K. & HU B. (2012). *Non-Gaussian features from the inverse volume corrections in loop quantum cosmology*. Phys. Rev. D86(4):044020. [arXiv:1112.2785](#). 15
- LIDDLE A. (2003). *An Introduction to Modern Cosmology, Second Edition* (Wiley). ISBN 978-0470848357. URL <http://adsabs.harvard.edu/abs/2003imcs.book.....L>. 5
- LIDDLE A.R. & LYTH D.H. (2000). *Cosmological Inflation and Large-Scale Structure* (Cambridge University Press). ISBN 978-0521575980. URL <http://adsabs.harvard.edu/abs/2000cils.book.....L>. 1, 2, 7
- LINDE A. & MUKHANOV V. (1997). *Non-Gaussian isocurvature perturbations from inflation*. Phys. Rev. D56:pp. 535–+. [arXiv:astro-ph/9610219](#). 14, 52, 70

- LINDE A.D. (1982). *A new inflationary universe scenario: A possible solution of the horizon, flatness, homogeneity, isotropy and primordial monopole problems*. Physics Letters B 108:pp. 389–393. URL <http://adsabs.harvard.edu/abs/1982PhLB..108..389L>. 6, 52, 70, 91, 108
- LIU H. & LI T.P. (2011). *Observational Scan-induced Artificial Cosmic Microwave Background Anisotropy*. ApJ732:125. [arXiv:1101.2720](https://arxiv.org/abs/1101.2720). 25
- LO VERDE M., MILLER A., SHANDERA S. & VERDE L. (2008). *Effects of scale-dependent non-Gaussianity on cosmological structures*. J. Cosmol. Astropat. Phys.4:p. 14. [arXiv:0711.4126](https://arxiv.org/abs/0711.4126). 15, 52
- LYTH D.H., UNGARELLI C. & WANDS D. (2003). *Primordial density perturbation in the curvaton scenario*. Phys. Rev. D67(2):023503. [arXiv:astro-ph/0208055](https://arxiv.org/abs/astro-ph/0208055). 14, 70
- MALDACENA J. (2003). *Non-gaussian features of primordial fluctuations in single field inflationary models*. Journal of High Energy Physics 5:p. 13. [arXiv:astro-ph/0210603](https://arxiv.org/abs/astro-ph/0210603). 14, 70
- MARINUCCI D. et al. (2008). *Spherical needlets for cosmic microwave background data analysis*. MNRAS383:pp. 539–545. [arXiv:0707.0844](https://arxiv.org/abs/0707.0844). 44
- MARTIN J. (2012). *Everything you always wanted to know about the cosmological constant problem (but were afraid to ask)*. Comptes Rendus Physique 13:pp. 566–665. [arXiv:1205.3365](https://arxiv.org/abs/1205.3365). 8
- MARTÍNEZ-GONZÁLEZ E., DIEGO J.M., VIELVA P. & SILK J. (2003). *Cosmic microwave background power spectrum estimation and map reconstruction with the expectation-maximization algorithm*. MNRAS345:pp. 1101–1109. [arXiv:astro-ph/0302094](https://arxiv.org/abs/astro-ph/0302094). 23
- MCEWEN J.D., HOBSON M.P., LASENBY A.N. & MORTLOCK D.J. (2005). *A high-significance detection of non-Gaussianity in the Wilkinson Microwave Anisotropy Probe 1-yr data using directional spherical wavelets*. MNRAS359:pp. 1583–1596. [arXiv:astro-ph/0406604](https://arxiv.org/abs/astro-ph/0406604). 26
- MCEWEN J.D., HOBSON M.P., LASENBY A.N. & MORTLOCK D.J. (2006). *Non-Gaussianity detections in the Bianchi VII<sub>h</sub> corrected WMAP one-year data made with directional spherical wavelets*. MNRAS369:pp. 1858–1868. [arXiv:astro-ph/0510349](https://arxiv.org/abs/astro-ph/0510349). 16, 108
- MCEWEN J.D., HOBSON M.P., LASENBY A.N. & MORTLOCK D.J. (2008). *A high-significance detection of non-Gaussianity in the WMAP 5-yr data using directional spherical wavelets*. MNRAS388:pp. 659–662. [arXiv:0803.2157](https://arxiv.org/abs/0803.2157). 44, 52
- MCEWEN J.D., JOSSET T., FEENEY S.M., PEIRIS H.V. & LASENBY A.N. (2013). *Bayesian analysis of anisotropic cosmologies: Bianchi VII<sub>h</sub> and WMAP*. MNRAS436:pp. 3680–3694. [arXiv:1303.3409](https://arxiv.org/abs/1303.3409). 16, 109
- McKELLAR A. (1940). *Evidence for the Molecular Origin of Some Hitherto Unidentified Interstellar Lines*. PASP52:p. 187. 1
- MECKE K.R., BUCHERT T. & WAGNER H. (1994). *Robust morphological measures for large-scale structure in the Universe*. A&A288:pp. 697–704. [arXiv:astro-ph/9312028](https://arxiv.org/abs/astro-ph/9312028). 40, 75, 111

- MICHELSEN K. & DE RAEDT H. (2001). *Integral-Geometry Morphological Image Analysis*. Physics Reports 347:pp. 461–538. URL [http://www.rug.nl/research/portal/publications/pub\(a315a089-4e96-4275-9ce5-0dd7e18ba818\).html](http://www.rug.nl/research/portal/publications/pub(a315a089-4e96-4275-9ce5-0dd7e18ba818).html). 41, 42, 76, 95, 96
- MINKOWSKI H. (1903). *Volumen und Oberfläche*. Mathematische Annalen 57(4):pp. 447–495. ISSN 0025-5831. URL <http://dx.doi.org/10.1007/BF01445180>. 111
- MODEST H.I., RÄTH C., BANDAY A.J., GÓRSKI K.M. & MORFILL G.E. (2014). *Correlating Fourier phase information with real-space higher order statistics in CMB data*. Phys. Rev. D89(12):123004. [arXiv:1311.5053](https://arxiv.org/abs/1311.5053). xx, 16
- MODEST H.I. et al. (2013). *Scale-dependent non-Gaussianities in the CMB data identified with Minkowski functionals and scaling indices*. MNRAS428:pp. 551–562. [arXiv:1209.5106](https://arxiv.org/abs/1209.5106). xx, 31, 35, 108, 111, 120
- MOFFAT J.W. (2005). *Cosmic microwave background, accelerating universe and inhomogeneous cosmology*. J. Cosmol. Astropat. Phys.10:012. [arXiv:astro-ph/0502110](https://arxiv.org/abs/astro-ph/0502110). 28
- MONETTI R.A., BOEHM H., MÜLLER D., RUMMENY E. & RÄTH C. (2004). *Assessing the biomechanical strength of trabecular bone in vitro using 3D anisotropic nonlinear texture measures: the scaling vector method*. Proc. SPIE 5370(215). URL <http://dx.doi.org/10.1117/12.532708>. 42
- MOROI T. & TAKAHASHI T. (2001). *Effects of cosmological moduli fields on cosmic microwave background*. Physics Letters B 522:pp. 215–221. [arXiv:hep-ph/0110096](https://arxiv.org/abs/hep-ph/0110096). 14, 70
- MORTLOCK D.J., CHALLINOR A.D. & HOBSON M.P. (2002). *Analysis of cosmic microwave background data on an incomplete sky*. MNRAS330:pp. 405–420. [arXiv:astro-ph/0008083](https://arxiv.org/abs/astro-ph/0008083). 92, 94, 95
- MOSS A., SCOTT D. & SIGURDSON K. (2011). *Induced CMB quadrupole from pointing offsets*. J. Cosmol. Astropat. Phys.1:001. [arXiv:1004.3995](https://arxiv.org/abs/1004.3995). 25
- MOSS I.G. & XIONG C. (2007). *Non-Gaussianity in fluctuations from warm inflation*. J. Cosmol. Astropat. Phys.4:007. [arXiv:astro-ph/0701302](https://arxiv.org/abs/astro-ph/0701302). 15
- MUELLER D. et al. (2006). *The 3D-based scaling index algorithm: a new structure measure to analyze trabecular bone architecture in high-resolution MR images in vivo*. Osteoporosis International 17:pp. 1483–1493. ISSN 0937-941X. 10.1007/s00198-006-0130-1, URL <http://dx.doi.org/10.1007/s00198-006-0130-1>. 42
- MUKHANOV V.F. & CHIBISOV G.V. (1981). *Quantum fluctuations and a nonsingular universe*. Soviet Journal of Experimental and Theoretical Physics Letters 33:p. 532. URL <http://adsabs.harvard.edu/abs/1981JETPL..33..532M>. 6
- MUKHERJEE P. & WANG Y. (2004). *Wavelets and Wilkinson Microwave Anisotropy Probe Non-Gaussianity*. ApJ613:pp. 51–60. [arXiv:astro-ph/0402602](https://arxiv.org/abs/astro-ph/0402602). 26
- MUNSHI D., COLES P., COORAY A., HEAVENS A. & SMIDT J. (2011). *Primordial non-Gaussianity from a joint analysis of the cosmic microwave background temperature and polarization*. MNRAS410:pp. 1295–1319. [arXiv:1002.4998](https://arxiv.org/abs/1002.4998). 34

- NASELSKY P., CHIANG L.Y., OLESEN P. & NOVIKOV I. (2005). *Statistics of phase correlations as a test for non-Gaussianity of the CMB maps*. Phys. Rev. D72(6):pp. 063512+. [arXiv:astro-ph/0505011](#). 31, 53, 71, 91
- NASELSKY P., HANSEN M. & KIM J. (2011). *Symmetry of the CMB sky as a new test of its statistical isotropy. Non cosmological octupole?* J. Cosmol. Astropat. Phys.9:012. [arXiv:1105.4426](#). 91
- NASELSKY P.D. et al. (2010). *Understanding the WMAP Cold Spot mystery*. Astrophysical Bulletin 65:pp. 101–120. [arXiv:0712.1118](#). 26
- NEWTON I. Sir (1687). *Philosophiæ Naturalis Principia Mathematica*. 1st edn. (Jussu Societatis Regiæ ac Typis Joseph Streater). 2
- NOVELLO M. & BERGLIAFFA S.E.P. (2008). *Bouncing cosmologies*. Physics Reports463:pp. 127–213. [arXiv:0802.1634](#). 15
- OSTRIKER J.P. & VISHNIAC E.T. (1986). *Generation of microwave background fluctuations from nonlinear perturbations at the ERA of galaxy formation*. ApJ306:pp. L51–L54. URL <http://adsabs.harvard.edu/abs/1986ApJ...306L..51O>. 13
- PACI F. et al. (2010). *Power asymmetries in the cosmic microwave background temperature and polarization patterns*. MNRAS407:pp. 399–404. [arXiv:1002.4745](#). 91
- PACI F. et al. (2013). *Hemispherical power asymmetries in the WMAP 7-year low-resolution temperature and polarization maps*. MNRAS434:pp. 3071–3077. [arXiv:1301.5195](#). 31
- PADMANABHAN N. et al. (2012). *A 2 per cent distance to  $z = 0.35$  by reconstructing baryon acoustic oscillations - I. Methods and application to the Sloan Digital Sky Survey*. MNRAS427:pp. 2132–2145. [arXiv:1202.0090](#). 7
- PARK C.G. (2004). *Non-Gaussian signatures in the temperature fluctuation observed by the Wilkinson Microwave Anisotropy Probe*. MNRAS349:pp. 313–320. [arXiv:astro-ph/0307469](#). 30, 52, 70
- PEACOCK J.A. (1999). *Cosmological Physics*. 1st edn. (Cambridge University Press). ISBN 9780521422703. URL <http://adsabs.harvard.edu/abs/1999coph.book.....P>. 1
- PEEBLES P.J.E. (1997). *An Isocurvature Model for Early Galaxy Assembly*. ApJ483:pp. L1+. URL <http://adsabs.harvard.edu/abs/1997ApJ...483L...1P>. 52
- PEIRIS H.V. et al. (2003). *First-Year Wilkinson Microwave Anisotropy Probe (WMAP) Observations: Implications For Inflation*. ApJS148:pp. 213–231. [arXiv:astro-ph/0302225](#). 24
- PENZIAS A.A. & WILSON R.W. (1965). *A Measurement of Excess Antenna Temperature at 4080 Mc/s*. ApJ142:pp. 419–421. URL <http://adsabs.harvard.edu/abs/1965ApJ...142..419P>. 1
- PERCIVAL W.J. et al. (2010). *Baryon acoustic oscillations in the Sloan Digital Sky Survey Data Release 7 galaxy sample*. MNRAS401:pp. 2148–2168. [arXiv:0907.1660](#). 7
- PERLMUTTER S. et al. (1999). *Measurements of Omega and Lambda from 42 High-Redshift Supernovae*. ApJ517:pp. 565–586. [arXiv:astro-ph/9812133](#). 3

- PIETROBON D. et al. (2008). *Needlet detection of features in the WMAP CMB sky and the impact on anisotropies and hemispherical asymmetries*. Phys. Rev. D78(10):pp. 103504–+. [arXiv:0809.0010](#). 26
- PIETROBON D. et al. (2010). *Needlet bispectrum asymmetries in the WMAP 5-year data*. MNRAS402:pp. L34–L38. [arXiv:0905.3702](#). 30, 91
- PLANCK COLLABORATION et al. (2011). *Planck early results. I. The Planck mission*. A&A536:A1. [arXiv:1101.2022](#). 19
- PLANCK COLLABORATION et al. (2014a). *Planck 2013 results. I. Overview of products and scientific results*. A&A571:A1. [arXiv:1303.5062](#). 23, 107, 109
- PLANCK COLLABORATION et al. (2014b). *Planck 2013 results. XII. Diffuse component separation*. A&A571:A12. [arXiv:1303.5072](#). 23, 24
- PLANCK COLLABORATION et al. (2014c). *Planck 2013 results. XIX. The integrated Sachs-Wolfe effect*. A&A571:A19. [arXiv:1303.5079](#). 23
- PLANCK COLLABORATION et al. (2014d). *Planck 2013 results. XV. CMB power spectra and likelihood*. A&A571:A15. [arXiv:1303.5075](#). 23
- PLANCK COLLABORATION et al. (2014e). *Planck 2013 results. XVI. Cosmological parameters*. A&A571:A16. [arXiv:1303.5076](#). 4, 5, 7
- PLANCK COLLABORATION et al. (2014f). *Planck 2013 results. XVII. Gravitational lensing by large-scale structure*. A&A571:A17. [arXiv:1303.5077](#). 7, 23
- PLANCK COLLABORATION et al. (2014g). *Planck 2013 results. XXIII. Isotropy and statistics of the CMB*. A&A571:A23. [arXiv:1303.5083](#). 23, 24, 26, 27, 30, 31, 108, 109, 117, 120
- PLANCK COLLABORATION et al. (2014h). *Planck 2013 results. XXIV. Constraints on primordial non-Gaussianity*. A&A571:A24. [arXiv:1303.5084](#). 14, 23, 45, 108
- PLANCK COLLABORATION et al. (2014i). *Planck 2013 results. XXV. Searches for cosmic strings and other topological defects*. A&A571:A25. [arXiv:1303.5085](#). 23
- PLANCK COLLABORATION et al. (2014j). *Planck 2013 results. XXVI. Background geometry and topology of the Universe*. A&A571:A26. [arXiv:1303.5086](#). 23, 109
- PLANCK COLLABORATION et al. (2014k). *Planck 2013 results. XXVII. Doppler boosting of the CMB: Eppur si muove*. A&A571:A27. [arXiv:1303.5087](#). 10
- POMPILIO M.P., BOUCHET F.R., MURANTE G. & PROVENZALE A. (1995). *Multifractal Analysis of String-induced Cosmic Microwave Background Radiation Anisotropies*. ApJ449:p. 1. URL <http://adsabs.harvard.edu/abs/1995ApJ...449....1P>. 35
- PRESS W.H., TEUKOLSKY S.A., VETTERLING W.T. & FLANNERY B.P. (2007). *Numerical Recipes: The Art of Scientific Computing*. 3 edn. (Cambridge University Press, New York, NY, USA). ISBN 9780521880688. URL <http://www.worldcat.org/oclc/123285342>. 48, 110

- RAKIĆ A., RÄSÄNEN S. & SCHWARZ D.J. (2006). *The microwave sky and the local Rees-Sciama effect*. MNRAS369:pp. L27–L31. [arXiv:astro-ph/0601445](#). 28
- RAKIĆ A. & SCHWARZ D.J. (2007). *Correlating anomalies of the microwave sky*. Phys. Rev. D75(10):103002. [arXiv:astro-ph/0703266](#). 28
- RASSAT A. & STARCK J.L. (2013). *On preferred axes in WMAP cosmic microwave background data after subtraction of the integrated Sachs-Wolfe effect*. A&A557:L1. [arXiv:1303.5051](#). 25, 29
- RÄTH C., GLIOZZI M., PAPADAKIS I.E. & BRINKMANN W. (2012). *Revisiting Algorithms for Generating Surrogate Time Series*. Physical Review Letters 109(14):144101. [arXiv:1111.1414](#). 35, 111
- RÄTH C. & MORFILL G. (1997). *Texture detection and texture discrimination with anisotropic scaling indices*. Journal of the Optical Society of America A 14(12):pp. 3208–3215. URL <http://adsabs.harvard.edu/abs/1997JOSAA..14.3208R>. 42, 56, 111
- RÄTH C., MORFILL G.E., ROSSMANITH G., BANDAY A.J. & GÓRSKI K.M. (2009). *Model-Independent Test for Scale-Dependent Non-Gaussianities in the Cosmic Microwave Background*. Physical Review Letters 102(13):pp. 131301–+. [arXiv:0810.3805](#). 31, 35, 53, 55, 56, 60, 71, 76, 91, 92, 95, 97, 101, 103, 104
- RÄTH C. & SCHUECKER P. (2003). *Analysing large-scale structure - II. Testing for primordial non-Gaussianity in CMB maps using surrogates*. MNRAS344:pp. 115–128. [arXiv:astro-ph/0305248](#). 35, 36, 42, 53, 56, 71, 73, 76
- RÄTH C., SCHUECKER P. & BANDAY A.J. (2007). *A scaling index analysis of the Wilkinson Microwave Anisotropy Probe three-year data: signatures of non-Gaussianities and asymmetries in the cosmic microwave background*. MNRAS380:pp. 466–478. [arXiv:astro-ph/0702163](#). 26, 42, 43, 47, 52, 56, 57, 71, 76, 78
- RÄTH C. et al. (2002). *Analysing large-scale structure - I. Weighted scaling indices and constrained randomization*. MNRAS337:pp. 413–421. [arXiv:astro-ph/0207140](#). 35, 53, 56, 71, 76
- RÄTH C. et al. (2008). *Strength through structure: visualization and local assessment of the trabecular bone structure*. New Journal of Physics 10(12):p. 125010. URL <http://stacks.iop.org/1367-2630/10/i=12/a=125010>. 42, 56
- RÄTH C. et al. (2011). *Scale-dependent non-Gaussianities in the WMAP data as identified by using surrogates and scaling indices*. MNRAS415:pp. 2205–2214. [arXiv:1012.2985](#). xx, 35, 37, 71, 73, 74, 76, 81, 83, 91, 92, 95, 97, 101, 103, 104, 108, 109
- REES M.J. & SCIAMA D.W. (1968). *Large-scale Density Inhomogeneities in the Universe*. Nat217:pp. 511–516. URL <http://adsabs.harvard.edu/abs/1968Natur.217..511R>. 13
- RIESS A.G. et al. (1998). *Observational Evidence from Supernovae for an Accelerating Universe and a Cosmological Constant*. AJ116:pp. 1009–1038. [arXiv:astro-ph/9805201](#). 2

- RODENBURG J.M. et al. (2007). *Hard-X-Ray Lensless Imaging of Extended Objects*. Physical Review Letters 98:p. 034801. URL <http://link.aps.org/doi/10.1103/PhysRevLett.98.034801>. 108
- ROSSMANITH G., RÄTH C., BANDAY A.J. & MORFILL G. (2009). *Non-Gaussian signatures in the five-year WMAP data as identified with isotropic scaling indices*. MNRAS 399:pp. 1921–1933. [arXiv:0905.2854](https://arxiv.org/abs/0905.2854). 26, 52, 56, 57, 58, 70, 76, 78, 91, 95, 96, 97, 98, 100, 103
- ROSSMANITH G. et al. (2011). *Search for Non-Gaussianities in the WMAP Data with the Scaling Index Method*. Advances in Astronomy 2011:174873. [arXiv:1108.0596](https://arxiv.org/abs/1108.0596). 76
- ROSSMANITH G. et al. (2012). *Probing non-Gaussianities in the cosmic microwave background on an incomplete sky using surrogates*. Phys. Rev. D 86(8):083005. [arXiv:1207.3235](https://arxiv.org/abs/1207.3235). xx, 31, 35, 40, 82, 108, 109
- ROUKEMA B.F. (2010). *On the suspected timing error in Wilkinson microwave anisotropy probe map-making*. A&A 518:A34. [arXiv:1004.4506](https://arxiv.org/abs/1004.4506). 25
- RUBAKOV V. & VLASOV A. (2012). *What do we learn from the CMB observations?* Physics of Atomic Nuclei 75:pp. 1123–1141. ISSN 1063-7788. [arXiv:1008.1704](https://arxiv.org/abs/1008.1704). 34, 73
- SACHS R.K. & WOLFE A.M. (1967). *Perturbations of a Cosmological Model and Angular Variations of the Microwave Background*. ApJ 147:p. 73. URL <http://adsabs.harvard.edu/abs/1967ApJ...147...73S>. 10
- SAKHAROV A.D. (1991). *SPECIAL ISSUE: Violation of CP in variance, C asymmetry, and baryon asymmetry of the universe*. Soviet Physics Uspekhi 34:pp. 392–393. URL <http://adsabs.harvard.edu/abs/1991SvPhU...34..392S>. 9
- SANTOS M.G., COORAY A., HAIMAN Z., KNOX L. & MA C.P. (2003). *Small-Scale Cosmic Microwave Background Temperature and Polarization Anisotropies Due to Patchy Reionization*. ApJ 598:pp. 756–766. [arXiv:astro-ph/0305471](https://arxiv.org/abs/astro-ph/0305471). 13
- SARKAR D., HUTERER D., COPI C.J., STARKMAN G.D. & SCHWARZ D.J. (2011). *Missing power vs low- $l$  alignments in the cosmic microwave background: No correlation in the standard cosmological model*. Astroparticle Physics 34:pp. 591–594. [arXiv:1004.3784](https://arxiv.org/abs/1004.3784). 28
- SCHMALZING J. & GÓRSKI K.M. (1998). *Minkowski functionals used in the morphological analysis of cosmic microwave background anisotropy maps*. MNRAS 297:pp. 355–365. [arXiv:astro-ph/9710185](https://arxiv.org/abs/astro-ph/9710185). 40, 41, 75, 111
- SCHREIBER T. (1998). *Constrained Randomization of Time Series Data*. Physical Review Letters 80:pp. 2105–2108. [arXiv:chao-dyn/9909042](https://arxiv.org/abs/chao-dyn/9909042). 35, 92
- SCHREIBER T. & SCHMITZ A. (1996). *Improved Surrogate Data for Nonlinearity Tests*. Physical Review Letters 77:pp. 635–638. [arXiv:chao-dyn/9909041](https://arxiv.org/abs/chao-dyn/9909041). 35
- SCHREIBER T. & SCHMITZ A. (1997). *Classification of Time Series Data with Nonlinear Similarity Measures*. Physical Review Letters 79:pp. 1475–1478. URL <http://link.aps.org/doi/10.1103/PhysRevLett.79.1475>. 92

- SCHREIBER T. & SCHMITZ A. (2000). *Surrogate time series*. *Physica D: Nonlinear Phenomena* 142:pp. 346–382. [arXiv:chao-dyn/9909037](#). 35, 92
- SCHWARZ D.J., STARKMAN G.D., HUTERER D. & COPI C.J. (2004). *Is the Low- $l$  Microwave Background Cosmic?* *Physical Review Letters* 93(22):pp. 221301–+. [arXiv:astro-ph/0403353](#). 28
- SENATORE L., SMITH K.M. & ZALDARRIAGA M. (2010). *Non-Gaussianities in single field inflation and their optimal limits from the WMAP 5-year data*. *J. Cosmol. Astropat. Phys.*1:028. [arXiv:0905.3746](#). 45
- SILK J. (1968). *Cosmic Black-Body Radiation and Galaxy Formation*. *ApJ*151:p. 459. URL <http://adsabs.harvard.edu/abs/1968ApJ...151..459S>. 12
- SILVERSTEIN E. & TONG D. (2004). *Scalar speed limits and cosmology: Acceleration from D-celeration*. *Phys. Rev. D*70(10):103505. [arXiv:hep-th/0310221](#). 15, 70
- SLOSAR A. & SELJAK U. (2004). *Assessing the effects of foregrounds and sky removal in WMAP*. *Phys. Rev. D*70(8):083002. [arXiv:astro-ph/0404567](#). 30
- SMOOT G.F. et al. (1992). *Structure in the COBE differential microwave radiometer first-year maps*. *ApJ*396:pp. L1–L5. URL <http://adsabs.harvard.edu/abs/1992ApJ...396L...1S>. 1, 16, 107
- SPERGEL D.N. et al. (2003). *First-Year Wilkinson Microwave Anisotropy Probe (WMAP) Observations: Determination of Cosmological Parameters*. *ApJS*148:pp. 175–194. [arXiv:astro-ph/0302209](#). 27
- STAROBINSKY A.A. (1980). *A new type of isotropic cosmological models without singularity*. *Physics Letters B* 91:pp. 99–102. URL <http://adsabs.harvard.edu/abs/1980PhLB...91..99S>. 6
- STEINHARDT P.J. & TUROK N. (2002a). *A Cyclic Model of the Universe*. *Science* 296:pp. 1436–1439. [arXiv:hep-th/0111030](#). 15
- STEINHARDT P.J. & TUROK N. (2002b). *Cosmic evolution in a cyclic universe*. *Phys. Rev. D*65(12):126003. [arXiv:hep-th/0111098](#). 15
- SUNYAEV R.A. & ZELDOVICH Y.B. (1972). *The Observations of Relic Radiation as a Test of the Nature of X-Ray Radiation from the Clusters of Galaxies*. *Comments on Astrophysics and Space Physics* 4:p. 173. URL <http://adsabs.harvard.edu/abs/1972CoASP...4..173S>. 13
- SÜTTERLIN K.R. et al. (2009). *Dynamics of Lane Formation in Driven Binary Complex Plasmas*. *Physical Review Letters* 102(8):085003. [arXiv:0812.3091](#). 56
- SUZUKI N. et al. (2012). *The Hubble Space Telescope Cluster Supernova Survey. V. Improving the Dark-energy Constraints above  $z > 1$  and Building an Early-type-hosted Supernova Sample*. *ApJ*746:85. [arXiv:1105.3470](#). 7
- SZAPUDI I. (2009). *Introduction to Higher Order Spatial Statistics in Cosmology*. In V.J. Martínez, E. Saar, E. Martínez-González & M.J. Pons-Bordería (eds.), *Data Analysis in Cosmology*, vol. 665 of *Lecture Notes in Physics*, Berlin Springer Verlag, pp. 457–492. [arXiv:astro-ph/0505391](#). 71

- TAUBER J.A. et al. (2010). *Planck pre-launch status: The Planck mission*. A&A520:A1. URL <http://adsabs.harvard.edu/abs/2010A%26A...520A...1T>. 19
- TEGMARK M., DE OLIVEIRA-COSTA A. & HAMILTON A.J. (2003). *High resolution foreground cleaned CMB map from WMAP*. Phys. Rev. D68(12):pp. 123523–+. [arXiv:astro-ph/0302496](https://arxiv.org/abs/astro-ph/0302496). 27, 60
- THEILER J., EUBANK S., LONGTIN A., GALDRIKIAN B. & FARMER J.D. (1992). *Testing for nonlinearity in time series: the method of surrogate data*. Physica D: Nonlinear Phenomena 58(1-4):pp. 77 – 94. ISSN 0167-2789. URL <http://www.sciencedirect.com/science/article/pii/016727899290102S>. 35, 53, 71, 92, 108
- VERNIZZI F., MELCHIORRI A. & DURRER R. (2001). *Cosmic microwave background anisotropies from pre-big bang cosmology*. Phys. Rev. D63(6):063501. [arXiv:astro-ph/0008232](https://arxiv.org/abs/astro-ph/0008232). 15
- VERNIZZI F. & WANDS D. (2006). *Non-Gaussianities in two-field inflation*. J. Cosmol. Astropat. Phys.5:p. 19. [arXiv:astro-ph/0603799](https://arxiv.org/abs/astro-ph/0603799). 14, 70
- VIELVA P., MARTÍNEZ-GONZÁLEZ E., BARREIRO R.B., SANZ J.L. & CAYÓN L. (2004). *Detection of Non-Gaussianity in the Wilkinson Microwave Anisotropy Probe First-Year Data Using Spherical Wavelets*. ApJ609:pp. 22–34. [arXiv:astro-ph/0310273](https://arxiv.org/abs/astro-ph/0310273). 26, 30, 52, 70
- VIELVA P. & SANZ J.L. (2010). *Constraints on  $f_{NL}$  and  $g_{NL}$  from the analysis of the  $N$ -pdf of the CMB large-scale anisotropies*. MNRAS404:pp. 895–907. [arXiv:0910.3196](https://arxiv.org/abs/0910.3196). 91
- VIELVA P., WIAUX Y., MARTÍNEZ-GONZÁLEZ E. & VANDERGHEYNST P. (2006). *Steerable wavelet analysis of CMB structures alignment*. New Astronomy Review50:pp. 880–888. [arXiv:astro-ph/0609147](https://arxiv.org/abs/astro-ph/0609147). 44
- VIELVA P., WIAUX Y., MARTÍNEZ-GONZÁLEZ E. & VANDERGHEYNST P. (2007). *Alignment and signed-intensity anomalies in Wilkinson Microwave Anisotropy Probe data*. MNRAS381:pp. 932–942. [arXiv:0704.3736](https://arxiv.org/abs/0704.3736). 26
- VIELVA P. et al. (2011). *Cosmic microwave background polarization as a probe of the anomalous nature of the cold spot*. MNRAS410:pp. 33–38. [arXiv:1002.4029](https://arxiv.org/abs/1002.4029). 34
- WANDS D. (1999). *Duality invariance of cosmological perturbation spectra*. Phys. Rev. D60(2):023507. [arXiv:gr-qc/9809062](https://arxiv.org/abs/gr-qc/9809062). 15
- WANDS D. (2007). *Multiple Field Inflation*. In M. Lemoine, J. Martin & P. Peter (eds.), *Lecture Notes in Physics, Berlin Springer Verlag*, vol. 738 of *Lecture Notes in Physics, Berlin Springer Verlag*, p. 275. ISBN 978-3-540-74352-1. [arXiv:astro-ph/0702187](https://arxiv.org/abs/astro-ph/0702187). 14
- WANDS D. (2009). *Cosmology: Designs for an asymmetric universe*. Nature Physics 5:pp. 89–90. URL <http://adsabs.harvard.edu/abs/2009NatPh...5...89W>. 16
- WANG F., YAMASAKI K., HAVLIN S. & STANLEY H.E. (2008). *Indication of multiscaling in the volatility return intervals of stock markets*. Phys. Rev. E77(1):016109. [arXiv:0707.4638](https://arxiv.org/abs/0707.4638). 35

- WEHUS I.K., ACKERMAN L., ERIKSEN H.K. & GROENEBOOM N.E. (2009). *The Effect of Asymmetric Beams in the Wilkinson Microwave Anisotropy Probe Experiment*. ApJ707:pp. 343–353. [arXiv:0904.3998](#). 54
- WEINBERG S. (2008). *Cosmology* (Oxford University Press). ISBN 978-0-19-852682-7. URL <http://www.worldcat.org/oclc/182779803>. 1, 2, 3, 8
- WHEELER J.A. & FORD K. (2000). *Geons, Black Holes, and Quantum Foam: A Life in Physics* (W. W. Norton & Company). ISBN 0393319911. URL <http://www.worldcat.org/oclc/43618489>. 2
- WIENER N. (1930). *Generalized harmonic analysis*. Acta Mathematica 55(1):pp. 117–258. ISSN 0001-5962. URL <http://dx.doi.org/10.1007/BF02546511>. 108
- WINITZKI S. & KOSOWSKY A. (1998). *Minkowski functional description of microwave background Gaussianity*. New Astronomy3:pp. 75–100. [arXiv:astro-ph/9710164](#). 40, 75, 111
- YADAV A.P.S. & WANDELT B.D. (2010). *Primordial Non-Gaussianity in the Cosmic Microwave Background*. Advances in Astronomy 2010:565248. [arXiv:1006.0275](#). 7
- YADAV J.K., BAGLA J.S. & KHANDAI N. (2010). *Fractal dimension as a measure of the scale of homogeneity*. MNRAS405:pp. 2009–2015. [arXiv:1001.0617](#). 2
- YOHO A., FERRER F. & STARKMAN G.D. (2011). *Degree-scale anomalies in the CMB: Localizing the first peak dip to a small patch of the north ecliptic sky*. Phys. Rev. D83(8):083525. [arXiv:1005.5389](#). 52
- ZHANG R. & HUTERER D. (2010). *Disks in the sky: A reassessment of the WMAP “cold spot”*. Astroparticle Physics 33:pp. 69–74. [arXiv:0908.3988](#). 53



# Acknowledgements

My gratitude goes first to my supervisor Prof. Dr. Gregor Morfill for the continuous support of my Ph.D study and research, for his advice, his humor and his kindness.

Heartfelt thanks go to my co-supervisor Dr. Christoph R ath who always encouraged me to ask questions, helped to find answers and to develop new ideas with his patience, enthusiasm and immense knowledge.

My thanks also go to Prof. Dr. Jochen Weller and my collaborators Gregor Rossmannith, Anthony Banday and Krystof G orski for interesting, helpful and educational discussions on cosmology and CMB analysis in general, and our work in particular.

I would like to thank the members of the former theory group of the MPE for a very friendly atmosphere and the constant technical support. Special thanks go to Angelika Langer for always being on my side. Thanks also go to the International Max-Planck Research School on Astrophysics that accompanied me over the last few years.

I also take this opportunity to express my sincere thanks to Thomas Puzia and Paul Goudfrooij who have deepened my interest in astrophysics a long time ago.

Furthermore, I am very grateful for the support of the Christiane N usslein-Volhard Foundation.

Last but not least, I would like to thank my parents, brothers, grandparents and parents-in-law for their permanent support and their belief in me. Special thanks go to Elisabeth and Andreas and Ursula and Peter for being my Bavarian family. For help, fun and everything I thank Alexandra Wei mann, Lisa W rner, Julia Zimmermann, Gregor Rossmannith, Agata Karska, Janina Benecke, Jan Fr omming, Nina Brenner und Simone Schl mer. Been there from the start, my husband Dominik and our older daughter Elena went with me through thick and thin. Special thanks to them for introducing different perspectives to me. And very special thanks to my youngest supporter, little Antonia.